Angular analysis of $\Lambda_b^0 \to \Lambda\mu^+\mu^-$ and $\Lambda_b^0 \to J/\psi\Lambda$ decays with the LHCb detector

Georgios Chatzikonstantinidis

Thesis submitted for the degree of
Doctor of Philosophy

Particle Physics Group,

School of Physics and Astronomy,

University of Birmingham.

24/05/2019

Abstract

In this thesis the angular analysis of $\Lambda_b^0 \to \Lambda\mu^+\mu^-$ and $\Lambda_b^0 \to J/\psi\,\Lambda$ decays is presented, using data from pp collisions recorded by the LHCb experiment between 2011 and 2016, corresponding to an integrated luminosity of approximately $5\,\text{fb}^{-1}$. For the $\Lambda_b^0 \to \Lambda\mu^+\mu^-$ decay, the angular observables are extracted at low hadronic-recoil using the method of moments. This is the first time that the complete set of the angular observables has been measured; the results are published in Ref. [1]. A measurement of the angular observables of the $\Lambda_b^0 \to J/\psi\,\Lambda$ decays is also performed. The angular observables are extracted using a moment analysis; an interpretation of the results in terms of the production polarisation of Λ_b^0 and the decay amplitudes is also performed. This is the first time that the complete set of the angular observables of the $\Lambda_b^0 \to J/\psi\,\Lambda$ has been measured; the results are preliminary and correspond to the current status of the analysis.

DECLARATION OF AUTHOR'S CONTRIBUTION

I am one of the main authors for both analyses presented in chapters 4 and 5 of this thesis. I also contributed to the development and maintenance of a tool used to validate LHCb simulations, presented in chapter 3.

For the angular analysis of $\Lambda_b^0 \to \Lambda\mu^+\mu^-$ and $\Lambda_b^0 \to J/\psi\,\Lambda$ I collaborated with Michal, Thomas, Nigel and (for the $\Lambda_b^0 \to \Lambda\mu^+\mu^-$ analysis) Christopher. I actively collaborated or was the main contributor in all aspects of the analysis; with the exception of the production of the samples used in both analyses that were provided by Michal, the selection and mass fits for the Run1 for the $\Lambda_b^0 \to \Lambda\mu^+\mu^-$ that was performed by Michal, Thomas and Christopher, the development of the MCMC code and χ^2 fit that was done by Thomas, with me providing code to analyse the results and do validation studies in this framework and the interpretation of the results for the

$\Lambda_b^0 \to \Lambda\mu^+\mu^-$ in terms of SM and NP predictions was done by Michal and Thomas.

For the tools developed to validate the electromagnetic interaction models in the LHCb simulations I heavily collaborated with Peter, Nigel and other members of the simulations working group of the LHCb experiment. The original code that was used for the test was developed by Peter and Nigel. In addition I used the code to validate changes in the software used by the LHCb collaboration and provide the necessary reports. The latter task, together with being a "Monte Carlo liaison" for the Rare Decays working group of the LHCb collaboration, were in a sense my service tasks.

ACKNOWLEDGEMENTS

Firstly I would like to thank my supervisor Nigel who was always available to help me and advise me when I needed. I would like also to thank Michal and Thomas for all their help and assistance during my studies. In addition I would like to thank Simone who was always available to ask him questions about the LHCb experiment, Kwstas who helped me many times with questions that I had about statistics and Peter who was always available to guide me through the use of the simulation software. A special thanks goes to all the Birmingham students and particularly to Elliot, Kristian and Maria for being such a good friends. I would like also to thank all the members of the LHCb collaboration for providing an excellent assistance and high quality tools that where of paramount importance in my studies. I would like finally to thank my parents and my sister, for being always next to me.

Dedicated to my parents.

Contents

CHAPTER 1

Introduction

The forces that we are aware of are the electromagnetic, weak, strong and gravitational forces; the latter can safely be ignored when describing interactions between elementary particles. A model that can integrate all the known fundamental particles and its interactions exists and it is called the Standard Model (SM). The SM is described in the context of relativistic Quantum Field Theory (QFT), where interactions between fundamental particles, *e.g.* $e^+e^- \to e^+e^-$, and composite particles known as hadrons, *e.g.* Λ_b^0, can be described and a prediction for observables of interest such as decay rates can be made. To date, the SM agrees remarkably well with experimental measurements. However, there are several phenomena in nature,

such as the observed asymmetry between matter and anti-matter in the universe, that cannot be explained in the context of the SM [2]. Additionally, other phenomena such as the galactic rotational curves, representing the orbital velocity of visible matter with respect to the radial distance from the galactic centre, exhibit a behaviour that cannot be explained by any of the known particles provided by the SM [3]. At the same time, conceptual issues such as the huge disparities between the masses of the elementary particles, *e.g.* the muon is approximately 200 times heavier than the electron, and also between the forces of nature where gravity appears to be so weak, are examples of well known "hierarchy problems", which still remain very puzzling. In addition, even though the SM unifies electromagnetic and week interactions in the electroweak forces, no attempt is made for further unification with strong interactions. Gravitational forces are still not incorporated in this description which makes it more likely that the SM is an effective version of a more fundamental underlying theory.

The search for New Physics beyond the SM (NP) can be done either directly, by looking for NP, *e.g.* existence of new particles, or indirectly by testing precise predictions of the SM against experimental measurements. The latter approach is used in this thesis where predictions of the angular observables for the decay of $\Lambda_b^0 \to \Lambda\mu^+\mu^-$ are tested against data. Before looking for new physics, it is vital to validate that the existing theoretical tools that are used to make predictions are correct. It is in this spirit that the angular analysis of $\Lambda_b^0 \to J/\psi\,\Lambda$ is performed, where apart from being a necessary ingredient in the process of performing other measurements related with searches of new physics, it provides an insight in the models that are

used to describe the weak decays of b-hadrons.

1.1 The Standard Model

The Standard Model of particle physics is a model that is formulated in the context of QFT, where all particles are described as fields. The fermionic fields are the ones that represent all the fundamental particles that make up matter. These are the quarks and leptons, where only the former contain a colour. Quarks come in six different flavours, u (up), d (down), s (strange), c (charm), t (top) and b (bottom) and they form three families of doublets with, u, c, t and d, s, b being in the first and second rows of the doublets respectively. The up-type quarks have an electric charge of $2/3$ $|e|$ while the down-type quarks have electric charge of $-1/3$ $|e|$. A similar situation arises for leptons, which are the e^- (electron), ν_e (electron neutrino), μ^- (muon), ν_μ (muon neutrino), τ^- (tau) and ν_τ (tau neutrino), with electric charge of $-$ $|e|$ (0 $|e|$). In this picture the e^-, μ^- and τ^- (ν_e, ν_μ, ν_τ) are set as the up-type (down-type) leptons. The equivalent antiparticles also exist with inverted quantum numbers and the same masses. The interactions of quarks and leptons are described by a set of bosonic fields, which are generated by the requirement that the Lagrangian ($\mathcal{L}$) describing the dynamics of particles in the SM, remains invariant under $SU(3)_C \times SU(2)_L \times U(1)_Y$ transformations (see Refs. [4–6] for an extensive discussion on the topic).

The $SU(3)_C$ represents the gauge group for Quantum Chromodynamics (QCD),

where the eight generators of this group represent the gluons that mediate the strong interactions. Quarks and gluons carry a colour charge, which takes the "values" conventionally referred as of Red (R), Green (G) and Blue (B) (including the anti-colours). A direct consequence of the fact that gluons carry colour is the interaction of gluons with each other. An interesting property of QCD is the colour confinement which results in the non-observation of single quarks or gluons [7]. This essentially means that quarks and gluons cannot be observed individually in nature and are hadronised in colourless (white) states called hadrons. Those that consist of a quark and anti-quark are called mesons, while those that consist of three quarks or anti-quarks are called baryons. In this thesis I will frequently discuss the Λ_b^0 and Λ baryons, which consist of udb and uds quarks respectively, and the J/ψ meson that comprises $c\bar{c}$. In must be noted that exotic states beyond the traditional baryons (qqq or $\bar{q}\bar{q}\bar{q}$) and mesons ($q\bar{q}$), but with a richer quark content have been observed [8, 9].

The $SU(2)_L \times U(1)_Y$ describes the gauge group of electroweak interactions [10–12]. This has four generators that mix and result in the four force carriers, the $W^{\pm}$ and Z, and the γ, that mediate the weak and electromagnetic interactions respectively. The experimental observation of the maximum violation of the parity [13] is incorporated in the SM $\mathcal{L}$, with the weak interactions only coupling to left-handed particles. This is better described with the presence of left-handed doublets (families) in the SM $\mathcal{L}$, while leaving the right-handed particles as singlets. A unique feature of the weak forces is the mixing between different families, an example is illustrated in figure 1.1 with the decay of $\Lambda \to p\pi^-$, where the transition of an s to u type quark takes place [7]. A more detailed description of transitions between quarks belonging to

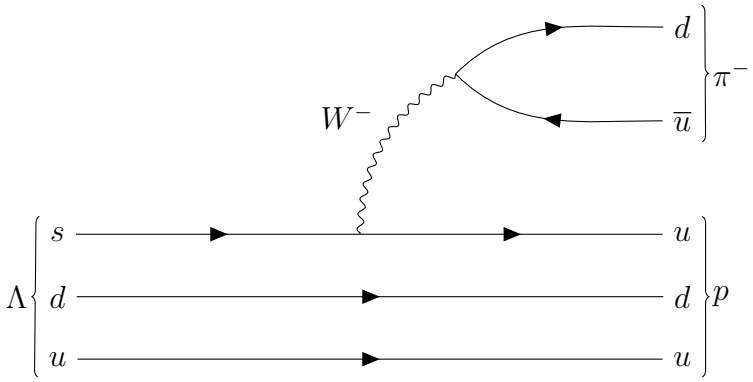

Figure 1.1: Feynman diagram of the decay of $\Lambda \to p\pi^-$.

different families is given in section 1.2.

To preserve the invariance of the SM $\mathcal{L}$ under local gauge transformations, explicit inclusion of a mass term in not allowed. This leaves all particles massless. To solve this issue, a new complex scalar field is introduced, represented by the Higgs field, with a potential that around its minimum leads to non-zero expectation values for the Higgs field [14–16]. This results in breaking spontaneously the electroweak symmetry and consequently generating finite masses to $W^{\pm}$ and Z bosons, while leaving the photon massless. The observation of the Higgs particle was performed by ATLAS [17] and CMS [18] collaborations in 2012. The inclusion of the Higgs field, even though it generates the masses of the weak bosons, leaves all quarks and leptons massless. In order to resolve this issue, the interaction (Yukawa) terms [7] of the leptons and quarks with the Higgs field that generate the masses of quark and leptons are introduced "by hand".

1.2 Flavour physics

In this section I will briefly discuss the mixing between different families focusing only on the quark sector, for more information see Refs. [19,20]. The mixing between different quark families becomes apparent when we write down the part of the SM $\mathcal{L}$ for the charged weak interactions between the quark fields. By expressing the interaction eigenstates in terms of mass eigenstates, the part of the $\mathcal{L}$ responsible for the charged current interactions takes the following form,

$$\mathcal{L}_{cc} = \frac{g}{\sqrt{2}} \bar{u_{iL}} (V_L^u V_L^{d\dagger})_{ij} \gamma_\mu W^{-\mu} d_{iL} + \frac{g}{\sqrt{2}} \bar{d_{iL}} (V_L^d V_L^{u\dagger})_{ij} \gamma_\mu W^{+\mu} u_{iL} + ... \tag{1.1}$$

where $V_L^u V_L^{d\dagger}$, is an element of the so-called Cabibbo-Kobayashi-Maskawa (CKM) matrix, usually refereed as V_{CKM} [7]. The latter has three real elements and one complex phase. The presence of this matrix is responsible for allowing transitions of quarks between different families, while the magnitudes of the elements represent the strength of the coupling between the relevant quark fields and the charged weak bosons. The measured absolute values of the CKM matrix are given in equation 1.2[1], where it becomes apparent that the CKM matrix exhibits an interesting symmetry, forming another type of "hierarchy problem", which is still puzzling. The absolute values of the CKM matrix as given in equation 1.2, are measured by several decays, each of them sensitive to different transitions; a small collection of them is illustrated in figure 1.2. From equation 1.2 it becomes obvious that transitions such as $u \to s$, are suppressed with respect to $u \to d$, which has a direct consequence on the

[1] The equation is adopted from [20], while the numerical values are taken from Ref. [7]

equivalent branching fractions. The presence of *CP*-violation in the SM is a direct consequence of the complex phase in the CKM matrix, which naturally results from the requirement of having three quark families. In other words, for *CP*-violation to be allowed, the V_{CKM}, should contain elements that $V_{ij} \neq V_{ij}^*$. To complete the description of the flavour mixing it must be noted that the only allowed flavour changing processes at tree level in the SM $\mathcal{L}$ are through charged currents, *i.e.* there are no Flavour Changing Neutral Currents (FCNC) in the SM at a tree level. Transitions of this kind do however take place with weak charged currents through more complicated processes (involving loops).

$$|V_{CKM}| = \begin{pmatrix} |V_{ud}| & |V_{us}| & |V_{ub}| \\ |V_{cd}| & |V_{cs}| & |V_{cb}| \\ |V_{td}| & |V_{ts}| & |V_{tb}| \end{pmatrix} = \tag{1.2}$$

$$\begin{pmatrix} 0.97446 \pm 0.00010 & 0.22452 \pm 0.00044 & 0.00365 \pm 0.00012 \\ 0.22438 \pm 0.00044 & 0.97359^{+0.00010}_{-0.00011} & 0.04214 \pm 0.00076 \\ 0.00896^{+0.00024}_{-0.00023} & 0.04133 \pm 0.00074 & 0.999105 \pm 0.000032 \end{pmatrix} \approx$$

$$\begin{pmatrix} 1 & (m_d/m_s)^{1/2} & (m_d/m_s)^{3/2} \\ (m_d/m_s)^{1/2} & 1 & (m_d/m_s) \\ (m_d/m_s)^{3/2} & (m_d/m_s) & 1 \end{pmatrix}$$

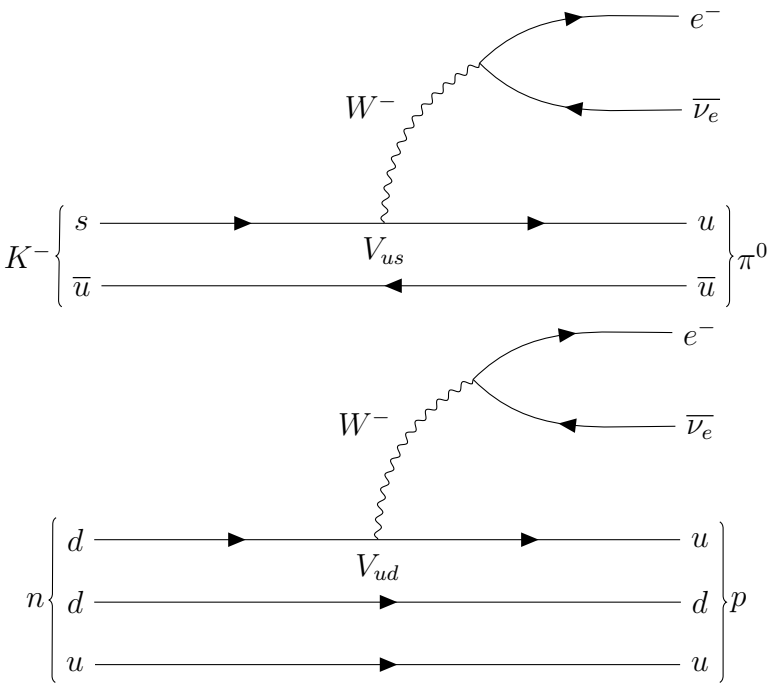

Figure 1.2: Feynman diagrams of the decays $K^- \to \pi^0 e^- \bar{\nu}_e$ (top) and $n \to p e^- \bar{\nu}_e$ (bottom), where the V_{us} and V_{ud} can be measured.

1.3 Theoretical framework

The decays of b-hadrons involve the transition of a b quark to another quark and a radiation of $W^\pm$ where, due to the vast mass difference [7] the $W^\pm$ is produced highly virtual and so can be removed and replaced with an effective vertex. In this spirit the $W^\pm$, Z and heavy quarks such as the top quark, *i.e.* "heavy" degrees of freedom can be integrated out of the description of these transitions. This approximation will result in a low energy effective description of the SM Hamiltonian ($\mathcal{H}_{\text{eff}}$), where the weak decays proceed through point interactions (similar to Fermi's 4-point interaction). The theoretical framework where this idea is formulated is called the Operator Product Expansion (OPE) [21]. In this framework the $\mathcal{H}_{\text{eff}}$ is expressed

as,

$$\mathcal{H}_{\text{eff}} \sim \sum_j \lambda_{CKM}^j C_j O_j \ , \tag{1.3}$$

where the O_j and C_j, represent the operators describing the process and the Wilson coefficients describing the strength with which the equivalent operators enter the effective Hamiltonian, respectively. The λ_{CKM}^j are the CKM elements. Using the OPE framework an amplitude that represents the transition of an initial state (I) to a final state (f) can we written as,

$$A_{I\to f} = \langle f|\mathcal{H}_{\text{eff}}|I\rangle \sim \sum_j \lambda_{CKM}^j C_j \langle f|O_j|I\rangle \ . \tag{1.4}$$

The advantage of the OPE is that it separates the amplitude into two parts: the Wilson Coefficients, which encode the contribution from high-energy scales and potentially new physics effects, including QCD contributions that can be calculated in perturbation theory; and the hadronic matrix elements $\langle f|O_j|I\rangle$ that integrate contributions from low energy scales, which can be calculated using non-perturbative methods.

The contribution of $O_{1,2}$ describes the V-A structure of the tree blocks including corrections, while the $O_{3-6,8}$ terms account for the gluon loops. The $O_{7,9,10}$ terms represent the suppressed operators, where O_7 corresponds to the electromagnetic operator and the O_9, O_{10} operators represent the Z penguin and box diagram involving the W boson. In this thesis I will focus on the FCNC processes, which proceed through the $b\to s\ell^+\ell^-$ transition and so are sensitive mainly to the $O_{9,10}$ operators. The O_7 term mainly dominates the $b\to s\gamma$ transitions. It must be no-

ticed that if the V-A structure is not assumed, right handed currents are allowed, the contribution of which will be encoded into primed operators and equivalent Wilson Coefficients; for more information see, Refs. [19, 22–24].

1.4 Flavour Changing Neutral Currents

The FCNC processes represent transitions between quark families that do not alter the charge of the quarks, and as discussed in section 1.2 do not appear at tree level in the SM. Transitions of these kind, such as the $b \to s$, occur however in more complicated processes, as illustrated in figure 1.3. These transitions which include two leptons in their final state are referred to as $b \to s\ell^+\ell^-$ and are highly suppressed, because there are multiple vertices in the amplitude and due to the Glashow-Iliopoulos-Maiani mechanism (GIM) [25] that will further suppress these processes, resulting in branching fractions of the order of 10^{-6}. The description of these processes is complicated by the dependence of the amplitudes on the invariant mass squared (q^2) of the dilepton system. A typical spectrum of the differential branching fraction versus q^2 is illustrated in figure 1.4. At very low q^2 values, the process is dominated by the contribution of the photon pole and so sensitive to C_7, the latter is mainly constrained from radiative decays, *e.g.* $B^0 \to K^{*0}\gamma$ [26]. Between the photon pole and the J/ψ resonance the q^2 region has sensitivity to the interference between the C_7 and C_9, collectively the region below $q^2 \approx 8\,\mathrm{GeV}^2/c^4$ is usually referred to as low-q^2 (this definition is not always adopted). The preferred region is terms of theory predictions is the $1 < q^2 < 6\ \mathrm{GeV}^2/c^4$ (represented by the

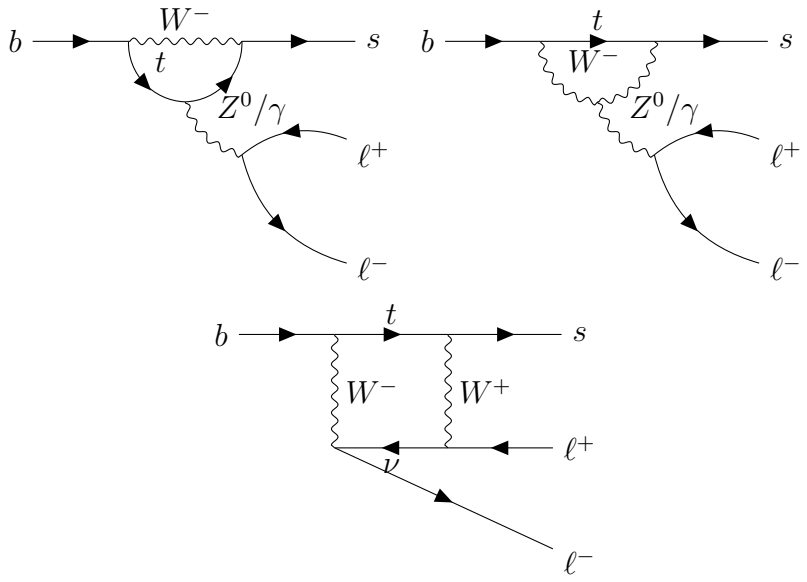

Figure 1.3: One loop (top-left and top-right) and box (bottom) diagrams of the $b \to s\ell^+\ell^-$ transitions.

yellow band in the figure 1.4), while the regions which contain the J/ψ and $\psi(2S)$ resonances are not of interest. Above the $\psi(2S)$ the main contribution comes from the interference between C_9 and C_{10}. The latter q^2 region is usually refereed as high-q^2 and is taken to start above $q^2 \approx 15\,\mathrm{GeV}^2/c^4$. In the high-$q^2$ region there are contributions from very broad resonances, and more caution should be given to theoretical predictions. Usually no attempt is made to disentangle the contribution of these resonances.

Heavy particles beyond the Standard Model that cannot be produced in colliders at present energies can appear in these loops as off-shell states and change observables such as angular distributions and branching fractions. In addition, new particles can contribute in such a way that FCNC processes are allowed at tree level. The decay of $\Lambda_b^0 \to \Lambda\mu^+\mu^-$ is a FCNC decay, and so a very rare decay [27]; one of the possible Feynman diagrams that contributes to this decay is illustrated in figure 1.5.

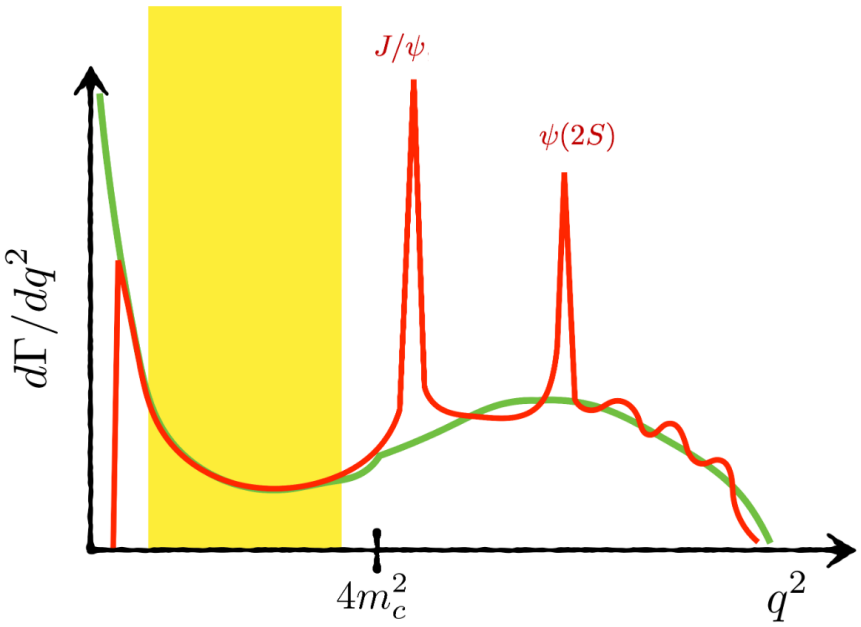

Figure 1.4: An illustration of the q^2 spectrum for the $b \to s\ell^+\ell^-$ transitions. The green line represents the contribution of the SM from the diagrams illustrated in figure 1.3, while the red line includes the contribution from the $c\bar{c}$ resonances (*e.g.* the J/ψ and $\psi(2S)$. The yellow band represents the $1 < q^2 < 6\,\text{GeV}^2/c^4$ region (the figure is adopted and modified from Ref. [22]).

1.5 Flavour anomalies in FCNC processes

In this section I will give a brief overview of a small collection of interesting deviations observed in FCNC processes for the $b \to s\ell^+\ell^-$ transitions, using data from the LHCb detector. The data are collected at centre-of-mass energies ($\sqrt{s}$) of 7 and 8 TeV, during the 2011 and 2012 data-taking periods respectively, corresponding to a total integrated luminosity of $3\,\text{fb}^{-1}$.

The simplest observable that can be measured is the branching fraction of a decay ($\mathcal{B}$). There are several $\mathcal{B}$ measurements performed by the LHCb collaboration. To date there is no single $\mathcal{B}$ measurement that exhibits a significant *i.e.* above 5σ deviation with respect to SM predictions. However, there is a pattern of mild

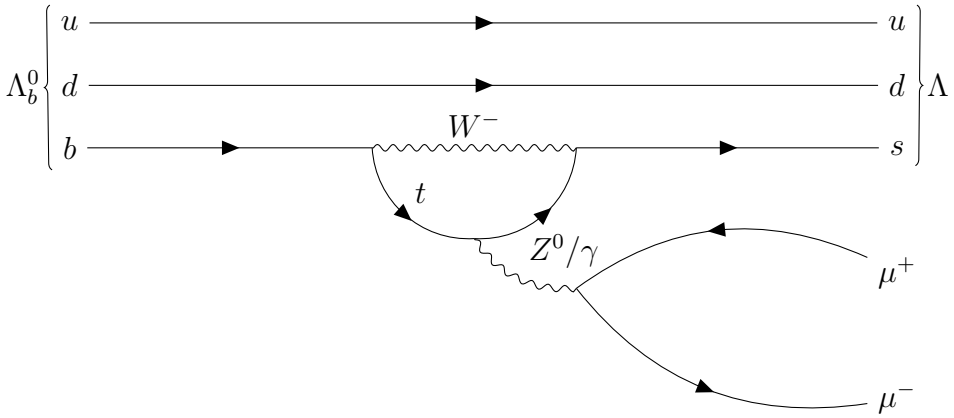

Figure 1.5: One of the Feynman diagrams that contribute to the rare decay of $\Lambda_b^0 \to \Lambda\mu^+\mu^-$.

anomalies observed in the low values of q^2, where data are consistently below the SM predictions. A collection of branching fraction measurements in several bins of q^2 for different decays is presented in figure 1.6. The most significant deviation is observed in the $\mathcal{B}$ of $B^0 \to \phi\mu^+\mu^-$, where a 3.3 σ deviation with respect to the SM prediction is observed in $1 < q^2 < 6\,\mathrm{GeV}^2/c^4$ [28].

The ratio of the $\mathcal{B}$'s for the same decay but using different flavours of leptons can be used to construct observables such as,

$$\mathrm{R_K} \equiv \frac{\mathcal{B}(B^+ \to K^+\mu^+\mu^-)}{\mathcal{B}(B^+ \to K^+e^+e^-)}\,, \qquad \mathrm{R_{K^{*0}}} \equiv \frac{\mathcal{B}(B^0 \to K^{*0}\mu^+\mu^-)}{\mathcal{B}(B^0 \to K^{*0}e^+e^-)}\,, \tag{1.5}$$

both of these parameters are expected to be close to unity in the SM. Interestingly small deviations have been observed in both observables of the order of 2.5 σ [32,33].

Another interesting approach is to perform an angular analysis in these decays and so access observables that provide direct information on the helicity structure of the $\mathcal{H}_{\mathrm{eff}}$ that cannot be accessed otherwise. One example of such a measurement[2] is

[2]This thesis examines in detail the baryonic decay $\Lambda_b^0 \to \Lambda\mu^+\mu^-$, which is complementary to

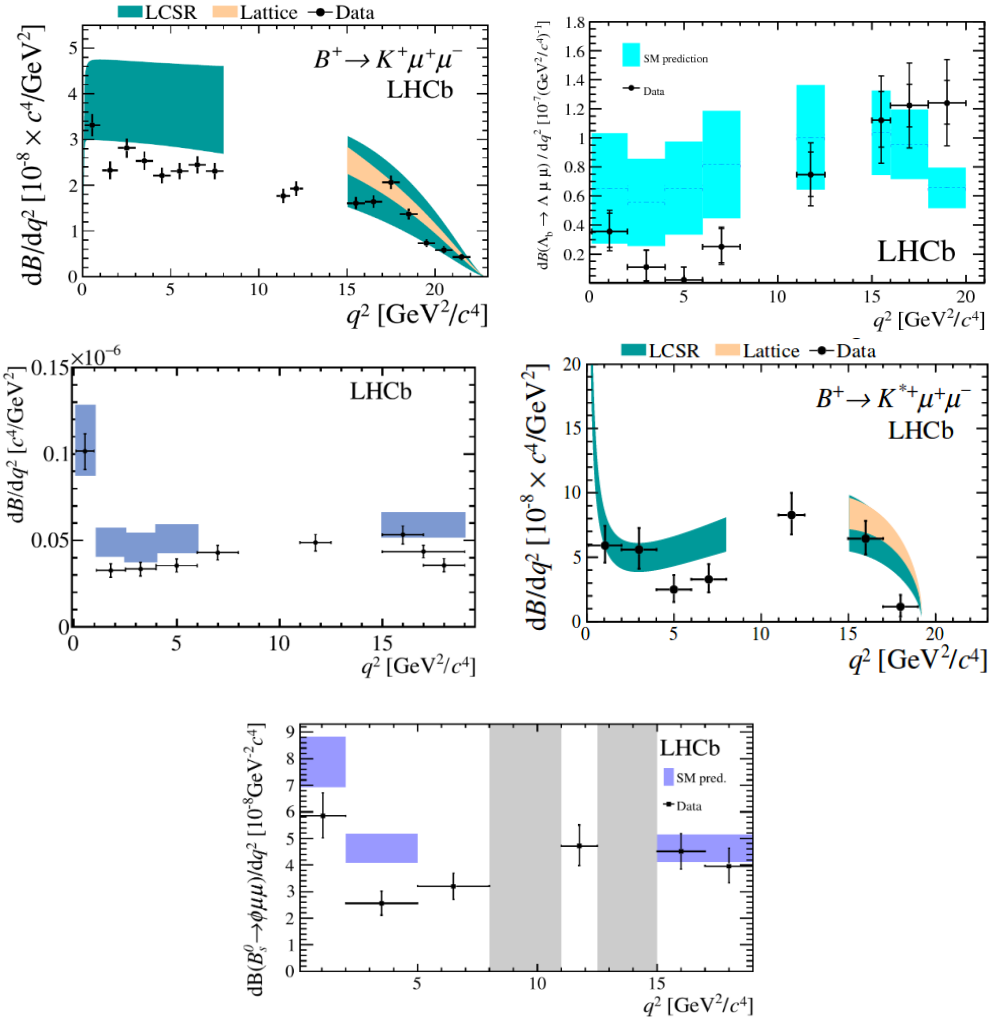

Figure 1.6: A collection of $\mathcal{B}$ measurements in several bins of q^2. The measurements are compared with the SM predictions (coloured bands), for $B^+ \to K^+\mu^+\mu^-$ [29], $\Lambda_b^0 \to \Lambda\mu^+\mu^-$ [27], $B^0 \to K^{*0}\mu^+\mu^-$ [30], $B^+ \to K^{*+}\mu^+\mu^-$ [29], $B^0 \to \phi\mu^+\mu^-$ [28]. The SM prediction of the $\mathcal{B}$ for $\Lambda_b^0 \to \Lambda\mu^+\mu^-$ has significantly improved [31], due to improvements in the calculations of the form factors in the context of Lattice QCD.

the decay $B^0 \to K^{*0}\mu^+\mu^-$, where the K^{*0} decays to $K^+\pi^-$. The latter decay mode involves the decay of a spin zero B^0 to a spin one K^{*0} and two spin one-half particles (μ^+ and μ^-) and so the differential branching fraction of this decay is described by three angles, q^2 and a set of observables that depend on the invariant mass of the dimuon system squared [34], such as the A_{FB} representing the forward-backward

the B^0 meson case.

asymmetry of the dimuon system. The extraction of the angular observables is performed using a maximum-likelihood fit to the three angles and the invariant mass of the $K^+\pi^-\mu^+\mu^-$ system; the latter parameter is used to discriminate signal from background candidates. To further reduce theoretical uncertainties on the definition of the angular observables, a new basis is used, transforming the angular observables to a new optimised set named $P_i^{(\prime)}$. The measurement is performed in several bins of q^2, where local deviations of the order of 3 σ are observed for the P_5' observable, in the bins of $4 < q^2 < 6$ GeV$^2/c^4$ and $6 < q^2 < 8$ GeV$^2/c^4$ [34]. The measurement has been repeated by several collaborations which support these deviations [34–37]. A collection of these results is illustrated in figure 1.7.

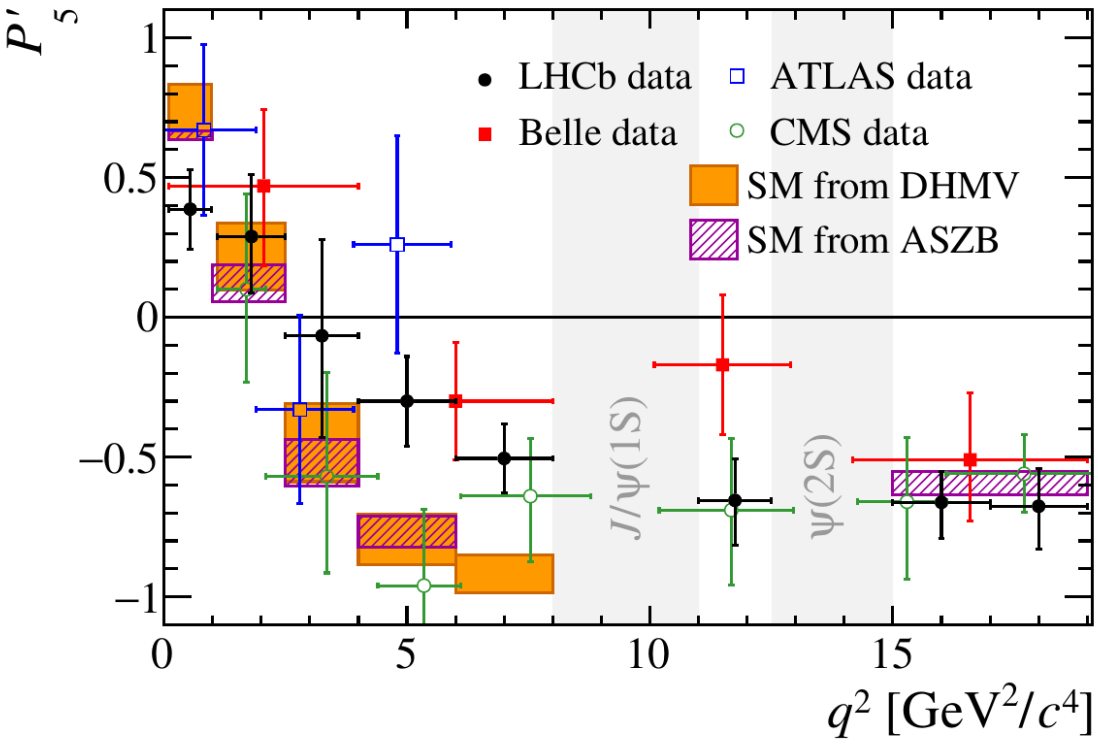

Figure 1.7: A collection of P_5' measurements from several collaborations, where the coloured band represents the SM predictions [34–37].

The various results of branching fractions, the R_K, $R_{K^{*0}}$ ratios and the angular

observables from $b \to s\ell^+\ell^-$ with $\ell \in \mu, e$ transitions (and not only, as discussed before C_7 is constrained mainly from radiative decays), depend on the C_7, C_9 and C_{10} Wilson coefficients; a global fit to the various measurements in a model independent approach can be performed. The Wilson coefficients can be expressed in the global fit as $C_i \equiv C_i^{SM} + C_i^{NP}$, where the superscript NP is referred to as the New Physics contributions. Lepton flavour violating effects can be included by separating the Wilson coefficients to the different lepton flavours. The global fit can be performed in many ways, *e.g.* in 1 dimension (D), *i.e.* fixing all NP physics contributions apart from one to zero, 2D where two C_i^{NP} are floating in the fit, or by allowing all C_i^{NP} to float in the fit. All the previous cases can be repeated by imposing certain constraints in the fit, *e.g.* in the 1D fit $C_9^{NP} = -C_{10}^{NP}$. Depending on the approach that is used and the treatment of the theoretical uncertainties, the deviation with respect to the SM predictions is found to be up to several σ. A few of the well-known scenarios that can explain the $b \to s\ell^+\ell^-$ results are $C_9^{NP} = -C_{10}^{NP} \approx -0.7$ and $C_9^{NP} \approx -1$, which correspond to 4.2 and 4.5 σ deviations from the SM, while an illustration of a 2D fit is presented in figure 1.8. The results of these fits and all the assumptions that are taken into account are described in Ref. [38]; the values of the C_i^{SM} used are $C_{7,9,10}^{SM} = -0.29, 4.07, -4.31$. Several collaborations have attempted to make a global fit to the Wilson coefficients and a small collection of those is given in Refs. [39–43].

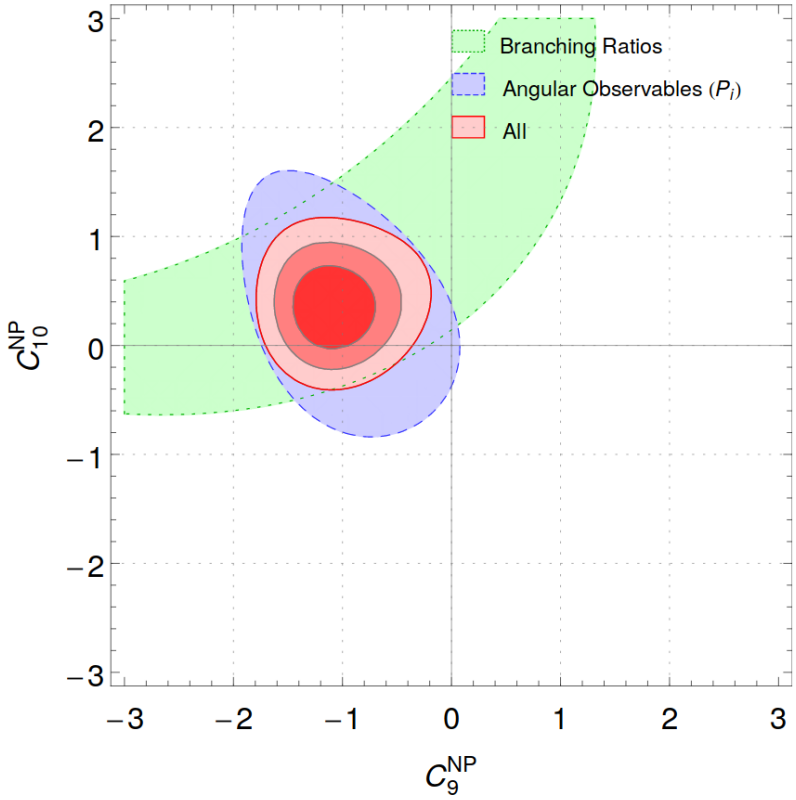

Figure 1.8: A 2D fit to C_9^{NP} and C_{10}^{NP}, which yields a 4.3 σ discrepancy with the SM point (0,0) [38].

1.6 Theoretical framework of $\Lambda_b^0 \to \Lambda\mu^+\mu^-$

The decay $\Lambda_b^0 \to \Lambda(\to p\pi^-)\mu^+\mu^-$ is a rare FCNC decay which proceeds through a $b \to s\ell^+\ell^-$ transition, the angular observables of which are sensitive to the relevant Wilson coefficients. The $\Lambda_b^0 \to \Lambda\mu^+\mu^-$ decay is particularly interesting since the Λ decays weakly (see figure 1.1), resulting in additional angular observables not present in the decay of $B^0 \to K^{*0}\mu^+\mu^-$. In contrast to B^0, the Λ_b^0 has spin one-half, which will result in the Λ_b^0 potentially being produced polarised, increasing significantly the number of angular observables. The production polarisation[3] of Λ_b^0 in pp collisions

[3]The production polarisation of Λ_b^0 in this work corresponds to the transverse polarisation because, due to parity conservation in strong interactions, the Λ_b^0 cannot be produced with longitudinal polarisation [44]. The production polarisation can be realised as the net effect of the fractional contribution of the production cross sections with different orientations of the spin of

has been measured by the LHCb and CMS Collaborations using data collected with $\sqrt{s}$ of 7 TeV and 7+8 TeV, respectively. Both measurements yield a polarisation very close to zero, *i.e.* $P_b^{\rm LHCb} = 0.06 \pm 0.07 \pm 0.02$ and $P_b^{\rm CMS} = 0.00 \pm 0.06 \pm 0.02$ [46,47]. As non-zero values of polarisation cannot be excluded it is also of interest to consider observables that depend on the latter. However, those observables that depend on P_b will have a reduced sensitivity [44]. An additional motivation for exploring the angular distribution of this rare baryon decay is that theoretical calculations of the form factors are very "clean" relative to $B^0 \to K^{*0}\mu^+\mu^-$ and can be calculated with high accuracy in the context of Lattice QCD [31].

1.6.1 Definition of characteristic angles

Before I discuss the $\Lambda_b^0 \to \Lambda(\to p\pi^-)\mu^+\mu^-$ differential decay rate I will introduce the angles used to characterise the observed four-body final state. The differential decay rate is defined by five angles, *i.e.* θ_l (ϕ_l), θ_b (ϕ_b) which are the polar (azimuthal) angles of the μ^+ and p in the dimuon and Λ rest-frame and θ which is defined as the polar angle of the Λ in the rest-frame of the Λ_b^0, with respect to a unit vector $\hat{n}$. The unit vector is defined as $\vec{n} \equiv \vec{p_{inc}} \times \vec{p_{\Lambda_b^0}} \cdot |\vec{p_{inc}} \times \vec{p_{\Lambda_b^0}}|^{-1}$, where the $\vec{p_{\Lambda_b^0}}$ and $\vec{p_{inc}}$ are the momentum of the Λ_b^0 and the incident proton (with direction to $+\hat{Z}$ axis of LHCb coordinate system) in the laboratory frame[4] [44]. For the decay of $\overline{\Lambda}_b^0$, the angles are defined in the same way, *i.e.* using the μ^+ and p, but transforming the $\theta_l \to \pi - \theta_l$, $\phi_l \to \pi - \phi_l$ and $\phi_b \to -\phi_b$, while θ_b and θ remain unchanged. The

the particle with respect to a scattering plane; a more rigorous definition can be found in Ref. [45].

[4]The small crossing angle of the pp beams is not taken into account in the default analysis, but the effect is evaluated as a source of systematic uncertainty.

angular definition is illustrated in figure 1.9.

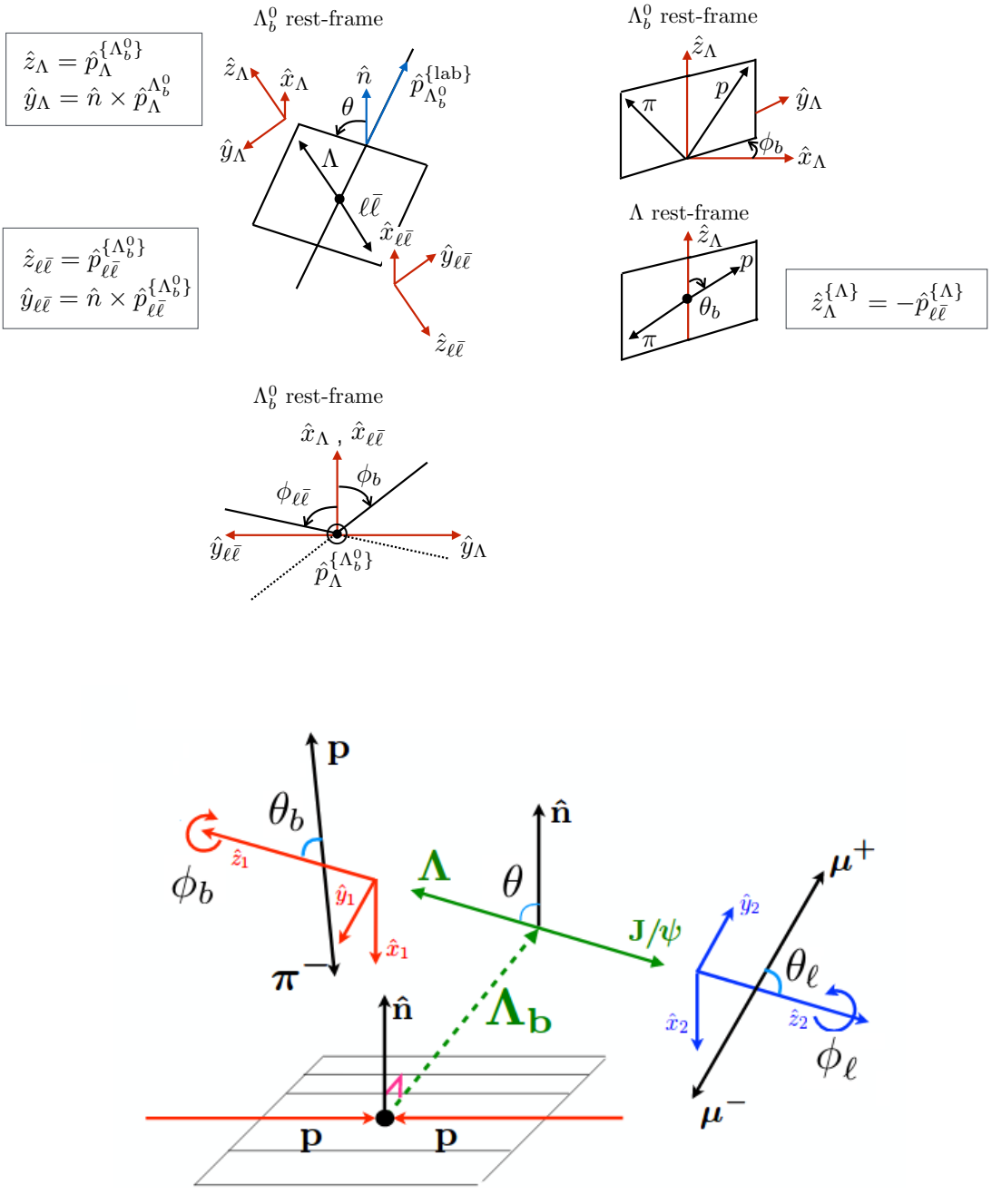

Figure 1.9: Pictorial representation of angles, describing $\Lambda_b^0 \to \Lambda(\to p\pi^-)\mu^+\mu^-$ (top) [44] and $\Lambda_b^0 \to \Lambda(\to p\pi^-)J/\psi(\to \mu^+\mu^-)$ (bottom, adopted and modified by Ref. [47]) decay. The angular definition for both decays is identical.

1.6.2 Differential decay rate

The differential decay rate of $\Lambda_b^0 \to \Lambda\mu^+\mu^-$ can be written in terms of five angles, as defined in section 1.6.1, and q^2 and is expressed in equation 1.7[5]; it must be noted that $J_{29,31}$ are zero in the limit of massless leptons, *i.e.* $\beta_l \equiv \sqrt{1-4m_l^2/q^2} \approx 1$, while $J_{11} - J_{34}$ depend on the production polarisation of the Λ_b^0. Integrating equation 1.7 over all the angles becomes,

$$\frac{\mathrm{d}\Gamma}{\mathrm{d}q^2} = 2J_1 + J_2 \ , \tag{1.6}$$

representing the differential decay rate over q^2. Using equation 1.6, the normalised angular observables can be expressed as $K_i \equiv J_i/(2J_1 + J_2)$, this results in K_1 and K_2 being 100% correlated. Using the normalised angular observables a few simple, well-known observables can be defined, such as, $A_{FB}^{\ell} = 3/2K_3$ (forward-backward asymmetry of the lepton system), $A_{FB}^{h} = K_4 + 1/2K_5$ (forward-backward asymmetry of the hadron system) and $A_{FB}^{\ell h} = 3/4K_6$ (forward-backward asymmetry of the lepton-hadron system) [44,48,49]. The forward-backward asymmetries on the lepton and hadron side are previously measured by LHCb, by performing one dimensional likelihood fits, although without disentangling the contribution of the relevant angular coefficients [27] and providing their associated correlations. It must be noted that the definition of the angles described in section 1.6.1 results in K_i observables that are identical for the CP-conjugate process in the absence of CP-violating effects. For the measurement of the angular observables that will be described in more detail in the following sections the samples of the Λ_b^0 and $\overline{\Lambda}_b^0$ (this is a self-tagging

[5]Equation 1.7 is adopted and modified by Ref. [44], which follows closely the definition given for the unpolarised case in Refs. [31,48].

decay) are merged.

$$
\begin{aligned}
\frac{32\pi^2}{3}\frac{\mathrm{d}^6\Gamma}{\mathrm{d}q^2\ \mathrm{d}\cos\theta_l\ \mathrm{d}\cos\theta_b\ \mathrm{d}\cos\theta\ \mathrm{d}\phi_l\ \mathrm{d}\phi_b} = \\
&\left(J_1 \sin^2\theta_l + J_2 \cos^2\theta_l + J_3 \cos\theta_l\right) + \\
&\left(J_4 \sin^2\theta_l + J_5 \cos^2\theta_l + J_6 \cos\theta_l\right)\cos\theta_b + \\
&\left(J_7 \sin\theta_l \cos\theta_l + J_8 \sin\theta_l\right)\sin\theta_b \cos\left(\phi_b + \phi_l\right) + \\
&\left(J_9 \sin\theta_l \cos\theta_l + J_{10} \sin\theta_l\right)\sin\theta_b \sin\left(\phi_b + \phi_l\right) + \\
\cos\theta\ \{\ &\left(J_{11} \sin^2\theta_l + J_{12} \cos^2\theta_l + J_{13} \cos\theta_l\right) + \\
&\left(J_{14} \sin^2\theta_l + J_{15} \cos^2\theta_l + J_{16} \cos\theta_l\right)\cos\theta_b + \\
&\left(J_{17} \sin\theta_l \cos\theta_l + J_{18} \sin\theta_l\right)\sin\theta_b \cos\left(\phi_b + \phi_l\right) + \\
&\left(J_{19} \sin\theta_l \cos\theta_l + J_{20} \sin\theta_l\right)\sin\theta_b \sin\left(\phi_b + \phi_l\right)\ \} + \\
\sin\theta\ \{\ &\left(J_{21} \cos\theta_l \sin\theta_l + J_{22} \sin\theta_l\right)\sin\phi_l + \\
&\left(J_{23} \cos\theta_l \sin\theta_l + J_{24} \sin\theta_l\right)\cos\phi_l + \\
&\left(J_{25} \cos\theta_l \sin\theta_l + J_{26} \sin\theta_l\right)\sin\phi_l \cos\theta_b + \\
&\left(J_{27} \cos\theta_l \sin\theta_l + J_{28} \sin\theta_l\right)\cos\phi_l \cos\theta_b + \\
&\left(J_{29} \cos^2\theta_l + J_{30} \sin^2\theta_l\right)\sin\theta_b \sin\phi_b + \\
&\left(J_{31} \cos^2\theta_l + J_{32} \sin^2\theta_l\right)\sin\theta_b \cos\phi_b + \\
&\left(J_{33} \sin^2\theta_l\right)\sin\theta_b \cos\left(2\phi_l + \phi_b\right) + \\
&\left(J_{34} \sin^2\theta_l\right)\sin\theta_b \sin\left(2\phi_l + \phi_b\right)\ \}
\end{aligned}
\tag{1.7}
$$

1.6.3 Sensitivity to new physics

As discussed in previous sections, the angular observables depend on the relevant Wilson Coefficients of the $b \to s\ell^+\ell^-$ transitions, contributions of hadronic matrix elements and q^2. The contribution of New Physics in the form of C_i^{NP} is illustrated in figures 1.10 for the regions of $1 < q^2 < 6\,\mathrm{GeV}^2/c^4$ and $15 < q^2 < 20\,\mathrm{GeV}^2/c^4$. The low- and high-$q^2$ are also usually referred to as large- and low-hadronic recoil, respectively. A complete illustration of the variations of the K_i for different C_i^{NP} variations is given in Ref. [44]. Similar variations can be found in the other K_i angular observables. The large number of angular observables and their sensitivity to the C_i^{NP} is particularly important in disentangling the potential NP contribution from different Wilson Coefficients, while the complete information of the angular observables and the covariance matrix is also essential for the full results to be used in the global fits of the Wilson coefficients related to the $b \to s\ell^+\ell^-$ transitions. These aspects make the measurement of the full set of angular observables of the $\Lambda_b^0 \to \Lambda\mu^+\mu^-$ decay an essential tool in the search for NP.

1.7 Theoretical framework for $\Lambda_b^0 \to J/\psi\,\Lambda$

The decay of the $\Lambda_b^0 \to J/\psi\,\Lambda$ has a very similar topology to that of $\Lambda_b^0 \to \Lambda\mu^+\mu^-$, where the Feynman diagram of the decay is illustrated in figure 1.11. The decay now depends on $O_{1...6}$ operators [50]. The branching fraction of the decay is of the order of 10^{-4} [7]; making the decay not particularly interesting for NP searches.

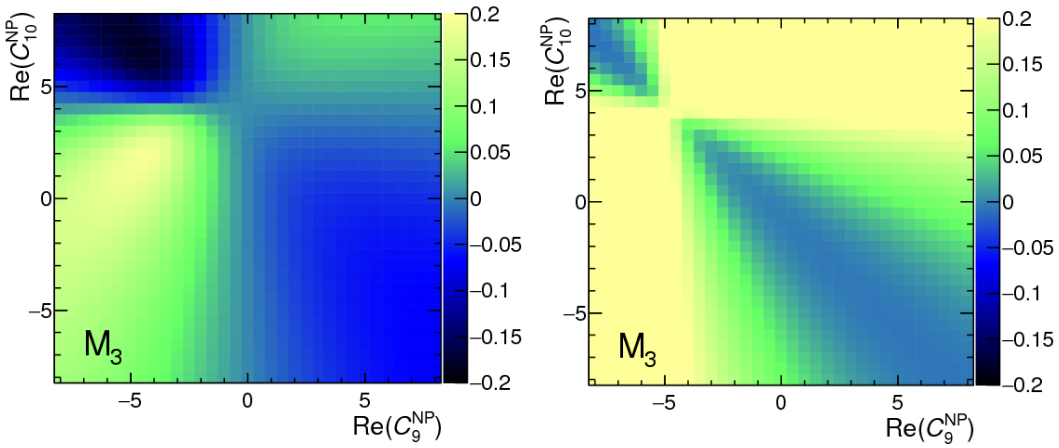

Figure 1.10: Dependence of K_3 (convention used between [44] and this thesis is $K_i \equiv M_i$) with variations in $\mathrm{Re}(C_{10}^{NP})$ and $\mathrm{Re}(C_9^{NP})$, in $1 < q^2 < 6\,\mathrm{GeV}^2/c^4$ (left) and $15 < q^2 < 20\,\mathrm{GeV}^2/c^4$ (right) regions.

However, the study of the angular structure of the decay is of general interest. The angular coefficients that govern the angular distribution of the $\Lambda_b^0 \to J/\psi\,\Lambda$ can be used as inputs for the MC correction, necessary for extracting correct absolute efficiencies. This is a basic ingredient for the future measurement of the branching fraction of the $\Lambda_b^0 \to \Lambda\mu^+\mu^-$ (and other analysis that use the $\Lambda_b^0 \to J/\psi\,\Lambda$ as a normalisation mode) decay (see figure 1.12). In addition, the angular structure of the decay can provide a wealth of information for the strong interactions in the b-hadron decays [45,51–55]. Previous partial measurements of the angular distribution have been made by LHCb [46], CMS [47] and ATLAS [56]; the current work is the first time that the complete angular structure of the decay has ever been measured.

1.7.1 Differential decay rate

The differential decay rate of the $\Lambda_b^0 \to J/\psi\,\Lambda$ is very similar to the one describing the $\Lambda_b^0 \to \Lambda\mu^+\mu^-$ decay, with the difference that the differential decay rate of the former

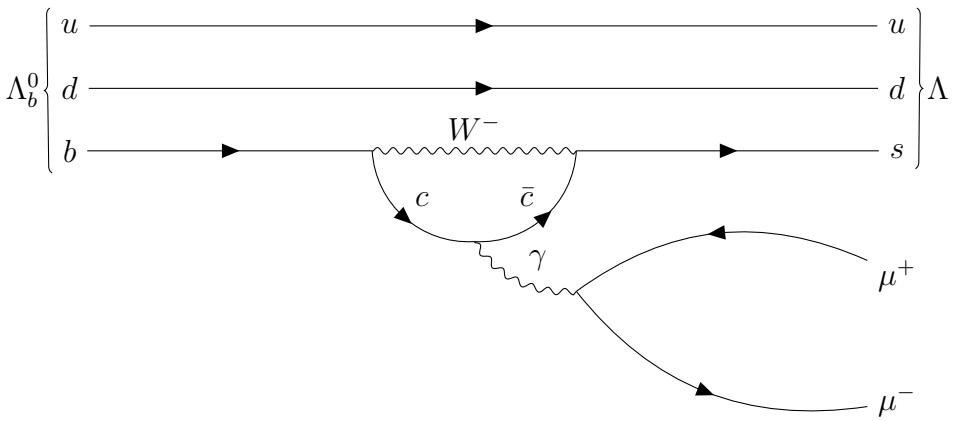

Figure 1.11: Feynman diagram of the $\Lambda_b^0 \to J/\psi\,\Lambda$ decay, where the $c\bar{c}$ resonance represents the J/ψ.

is defined only in terms of the five angles due to the constraint of the q^2 being equal to the invariant mass squared of the J/ψ [7] and in addition $J_{3,6,8,10,13,16,18,20,22,24,26,28} = 0$ [44]. The definition of the angles is identical to those used for the $\Lambda_b^0 \to \Lambda\mu^+\mu^-$ decay. To perform a measurement of the production polarisation of Λ_b^0 and of other parameters such as the amplitudes that govern the decay, it is necessary to expand the definition of the J_i observables in terms of these parameters as illustrated in table 1.1. The differential decay rate now depends on P_b, α_Λ (known as the Λ asymmetry parameter [7]) and four amplitudes which correspond to different configurations of the Λ and J/ψ helicities [44]. It must be noted that there are several parametrisations of the J_i in terms of parameters that can finally be translated to the magnitudes and phases of the amplitudes, *e.g.* LHCb used the following parametrisation; $\alpha_b \equiv |\alpha_+|^2 - |\alpha_-|^2 + |b_+|^2 - |b_-|^2$, $r_0 \equiv |\alpha_+|^2 + |\alpha_-|^2$ and $r_1 \equiv |\alpha_+|^2 - |\alpha_-|^2$ and using as normalisation condition that $|\alpha_+|^2 + |\alpha_-|^2 + |b_+|^2 + |b_-|^2 \equiv 1$. Each of the measurements performed by LHCb [46], CMS [47] and ATLAS [56] used slightly different parametrisations, while none of them extracted the complete set of angular coefficients.

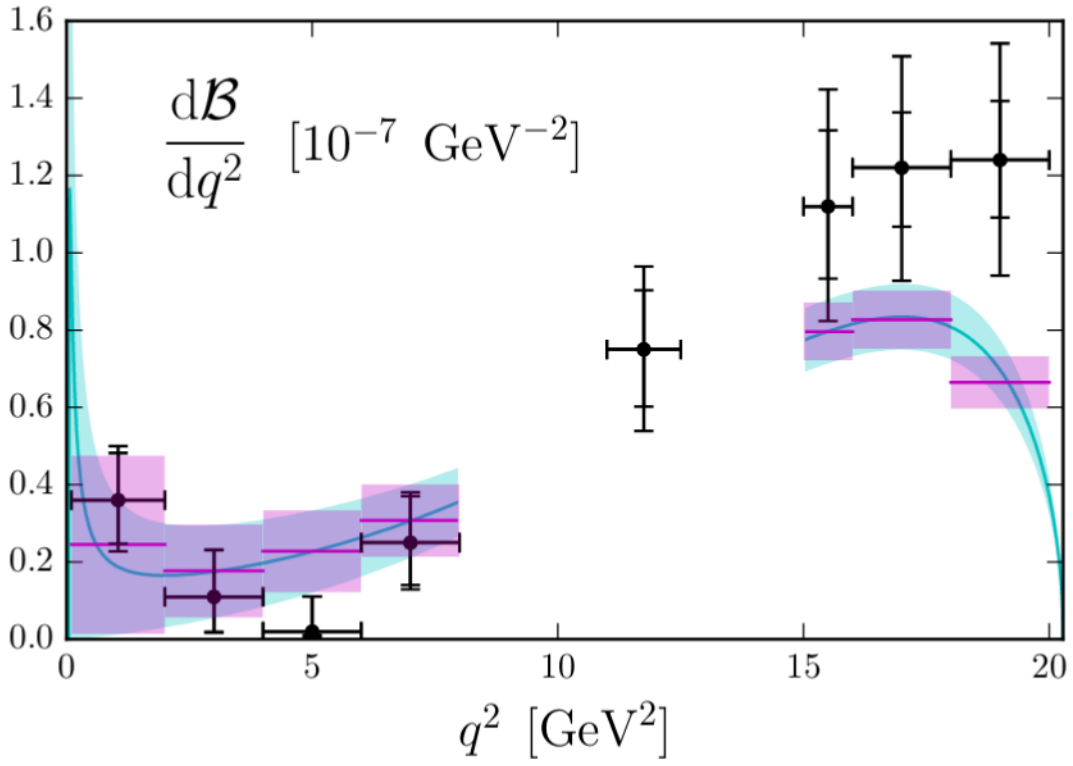

Figure 1.12: The differential branching fraction of $\Lambda_b^0 \to \Lambda\mu^+\mu^-$ as measured by the previous LHCb measurement [27] (black markers, with and without including the uncertainty from the normalisation mode). The coloured cyan band represents the SM prediction, while the magenta band is the SM prediction in several q^2 bins [31].

Observable	Physics parameters
J_1	$\frac{1}{4}(2\|a_+\|^2 + 2\|a_-\|^2 + \|b_+\|^2 + \|b_-\|^2)$
J_2	$\frac{1}{2}(\|b_+\|^2 + \|b_-\|^2)$
J_3	0
J_4	$\frac{\alpha_\Lambda}{4}(\|b_-\|^2 - \|b_+\|^2 + 2\|a_+\|^2 - 2\|a_-\|^2)$
J_5	$\frac{\alpha_\Lambda}{2}(\|b_-\|^2 - \|b_+\|^2)$
J_6	0
J_7	$\frac{\alpha_\Lambda}{\sqrt{2}}\mathrm{Re}(-b_+^* a_+ + b_- a_-^*)$
J_8	0
J_9	$\frac{\alpha_\Lambda}{\sqrt{2}}\mathrm{Im}(b_+^* a_+ - b_- a_-^*)$
J_{10}	0
J_{11}	$P_b\frac{1}{4}(\|b_+\|^2 - \|b_-\|^2 + 2\|a_+\|^2 - 2\|a_-\|^2)$
J_{12}	$P_b\frac{1}{2}(\|b_+\|^2 - \|b_-\|^2)$
J_{13}	0
J_{14}	$P_b\frac{\alpha_\Lambda}{4}(-\|b_-\|^2 - \|b_+\|^2 + 2\|a_+\|^2 + 2\|a_-\|^2)$
J_{15}	$-P_b\frac{\alpha_\Lambda}{2}(\|b_+\|^2 + \|b_-\|^2)$
J_{16}	0
J_{17}	$-P_b\frac{\alpha_\Lambda}{\sqrt{2}}\mathrm{Re}(b_+^* a_+ + b_- a_-^*)$
J_{18}	0
J_{19}	$P_b\frac{\alpha_\Lambda}{\sqrt{2}}\mathrm{Im}(b_+^* a_+ + b_- a_-^*)$
J_{20}	0
J_{21}	$-P_b\frac{1}{\sqrt{2}}\mathrm{Im}(b_+^* a_- - b_- a_+^*)$
J_{22}	0
J_{23}	$P_b\frac{1}{\sqrt{2}}\mathrm{Re}(b_+^* a_- - b_- a_+^*)$
J_{24}	0
J_{25}	$P_b\frac{\alpha_\Lambda}{\sqrt{2}}\mathrm{Im}(b_+^* a_- + b_- a_+^*)$
K_{26}	0
J_{27}	$-P_b\frac{\alpha_\Lambda}{\sqrt{2}}\mathrm{Re}(b_+^* a_- + b_- a_+^*)$
J_{28}	0
J_{29}	0
J_{30}	$P_b\alpha_\Lambda\mathrm{Im}(a_+ a_-^*)$
J_{31}	0
J_{32}	$-P_b\alpha_\Lambda\mathrm{Re}(a_+ a_-^*)$
J_{33}	$-P_b\frac{\alpha_\Lambda}{2}\mathrm{Re}(b_+^* b_-)$
J_{34}	$P_b\frac{\alpha_\Lambda}{2}\mathrm{Im}(b_+^* b_-)$

Table 1.1: Definition of the J_i observables in terms of the physics parameters that govern the $\Lambda_b^0 \to J/\psi\,\Lambda$ decay in the massless limit, *i.e.* $\beta_l = 1$ (see discussion in Ref. [44]). The amplitudes correspond to different helicity combinations of the Λ and J/ψ. Defining in general the amplitudes as $T_{\lambda_\Lambda,\lambda_{J/\psi}}$, then $\alpha_\pm \equiv T_{\pm 1/2,0}$ and $b_\pm \equiv T_{\mp 1/2,\mp 1}$.

CHAPTER 2

The LHCb detector in the Large Hadron Collider complex

The Large Hadron Collider (LHC) [57] is the highest energy synchrotron in a chain of particle accelerators operated by the European Organisation for Nuclear Research (CERN), with a primary purpose of producing proton-proton (pp) collisions at ultra-relativistic energies. The LHC is located around 50–150 m underground, in the tunnel that previously hosted the Large Electron-Positron collider (LEP) [58] which stopped operating in 2000. The tunnel has a circumference of around 26.7 km, crossing the border between Switzerland and France (see figure 2.1). The underground positioning of the tunnel provides good shielding from cosmic radiation; due to geological complications the depth varies with the shallowest point being around

50 m below the surface, near to Lake Geneva, making the plain of the LHC accelerator slightly inclined to the horizontal. At the collision points where the phenomena of interest take place, detectors are built to record the outcome of the collisions. The main LHC detectors are ATLAS [59], CMS [60], LHCb [61] and ALICE [62]. The LHCb detector, designed to study rare decays and CP-violation of b- and c-hadrons such as the $\Lambda_b^0 \to \Lambda\mu^+\mu^-$, is the detector from which data used for the present thesis were collected. In this chapter I will briefly discuss the LHC complex and the main components that make the LHCb detector [57].

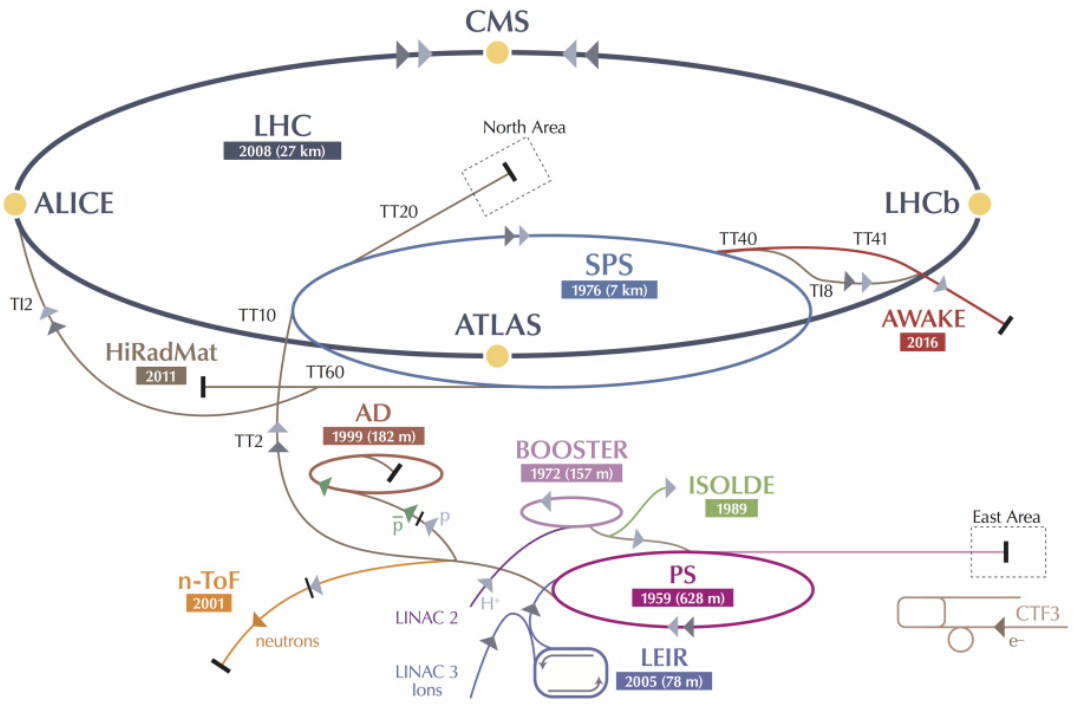

Figure 2.1: An overview of the LHC complex (adopted and modified from Ref. [63]).

2.1 The LHC complex

Before protons are injected into the LHC they pass through a series of pre-accelerators, starting with the Linear Accelerator 2 (LINAC 2). Afterwards they are passed to the Proton Synchrotron Booster (PSB) and Proton Synchrotron (PS), and finally are accelerated by the Super Proton Synchrotron (SPS) reaching a beam energy of 450 GeV, before finally being injected into the LHC, where the two proton beams are accelerated in opposite directions up to 7 TeV. The protons that are accelerated do not form a continuous beam, but are injected from the SPS as bunches, containing around 10^{11} protons, which is a direct requirement of the radio frequency (RF) cavities used to accelerate the protons; since the particles should transverse the RF cavities when the electric field has the correct phase. The beams are accelerated in opposite directions in separate vacuum tubes and maintained in an approximately circular orbit using superconducting dipole magnets that are cooled down to 1.9 K, producing a magnetic field of around 8 T. The beams are focused using quadrupole magnets before they collide, increasing the probability that protons in the two beams will interact [57].

The design instantaneous luminosity of the LHC is $\mathcal{L} = 10^{34}$ cm^{-2}s^{-1}, where beams cross each other every 25 ns. However, at LHCb in order to prevent radiation damage of the detector and retain optimum reconstruction efficiency of the primary vertices, the luminosity is decreased by a factor of ~ 20 compared to ATLAS and CMS, corresponding to around 1.5 interactions per beam crossing (for Run1). Furthermore, in order to keep trigger rates constant, the luminosity is also adjusted

("levelled") throughout each data taking run to account for reduction in beam current. These conditions are achieved by reducing the overlap of the beams at the collision point. In total, during 2011–2012 LHCb recorded 1 (2) fb^{-1} for 2011 (2012) at $\sqrt{s} = 7(8)\,\text{TeV}$ and 0.5 (1.6) fb^{-1} for 2015 (2016) at $\sqrt{s} = 13\,\text{TeV}$. In the following, data collected during the 2011, 2012 and the 2015, 2016 data-taking periods will be referred to as Run1 and Run2 data, respectively.

2.2 The LHCb detector

The LHCb is a single-arm spectrometer detector installed at IP8 of the LHC, with an angular acceptance of ∼15–250 (300) mrad in the non-bending (bending) plane, covering a pseudorapidity region of $2 < \eta < 5$. The forward geometry of LHCb is chosen to take advantage of the predominately forward or backward production of b-hadrons, which account for the studies of primary interest. The LHCb detector comprises a powerful magnet necessary for the momentum measurements of charged particles and a series of sub-detectors which mainly consist of tracking detectors (for charged particles) and particle identification (PID) systems. These are supported by a very robust trigger system, consisting of a hardware stage and a very flexible software component [64]. A schematic overview of the LHCb detector is given in figure 2.2. In the LHC the production of b-hadrons is related to the $pp \to b\bar{b}$ cross section, a process which mainly proceeds through the gluon-gluon fusion (around 85% of the times) and the hadronisation fraction, which represents the probability that a b quark is hadronised to a given hadron. The production of $b\bar{b}$ pairs in

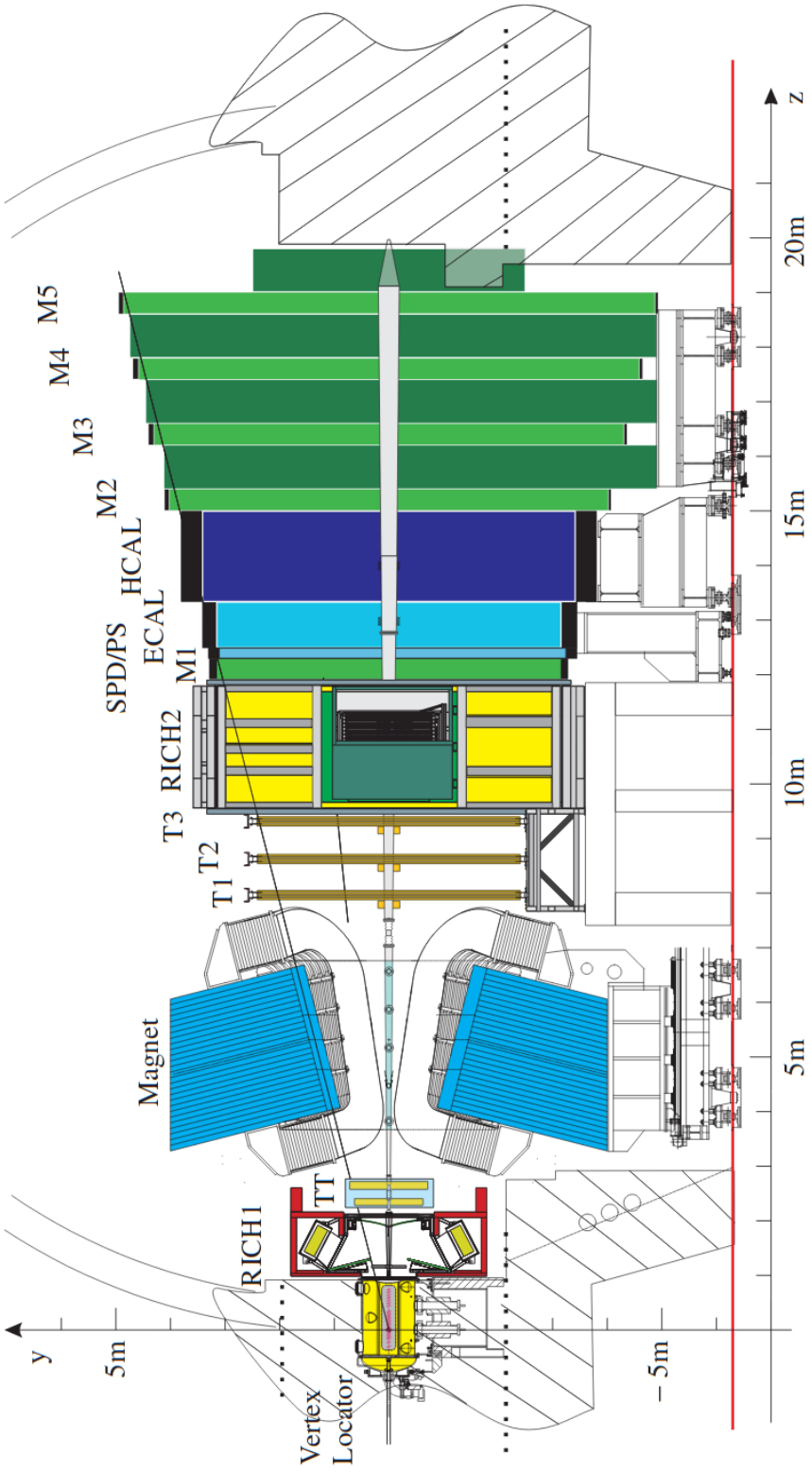

Figure 2.2: Schematic of overview of the LHCb detector and the various sub-detectors [65].

the forward and backward regions is illustrated in figure 2.3. The hadronisation fraction of Λ_b^0, *i.e.* $f_{\Lambda_b^0}$ is around 2%. Considering that hundreds of millions of $b\bar{b}$ pairs have been already produced, with more than one quarter of the total being inside the angular acceptance of LHCb, a very large sample of Λ_b^0 is available for further analysis.

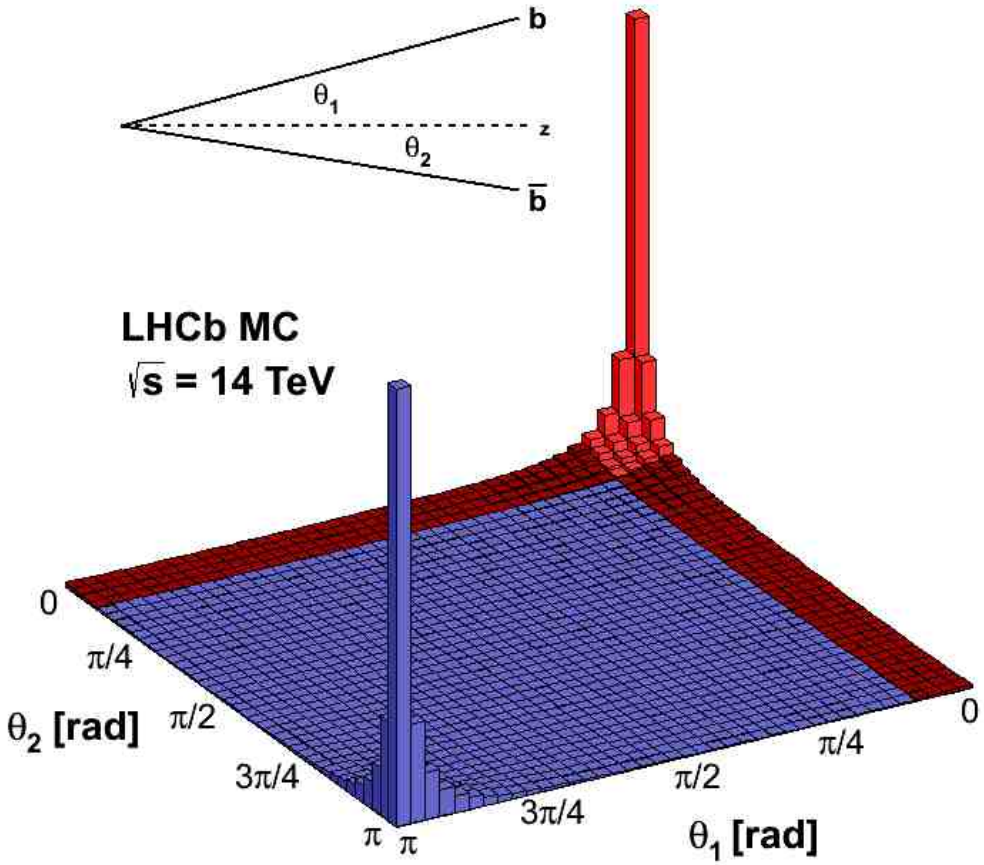

Figure 2.3: A simulation of $b\bar{b}$ production at LHCb, where the $b\bar{b}$ pairs that are produced inside the angular acceptance of LHCb are highlighted in red [66]. This asymmetry originates from the fact that the interacting partons are not symmetric in momentum. This results in a significant boost of the $b\bar{b}$ pairs, which are produced mainly through the gluon-gluon fusion, in the forward or backward region [67].

2.2.1 The beam pipe

The beam pipe of LHCb is designed to both maintain the vacuum and to minimise interactions of particles traversing it. The latter is correlated with the material and thickness of the beam pipe, the connectors and flanges between the different parts of the pipe and the support structure. The beam pipe is made of beryllium, for the first 12 m from the collision point, where the transparency is most critical, while for the remaining 7 m stainless steel in used. The LHCb beam pipe consists of four main sections that have conical shapes, connected through bellows and flanges made out of aluminium alloys, with each section supported in two different places by aluminium alloy collars that are themselves supported using stainless steel cables and rods [65].

2.2.2 The Magnet

The magnet used by the LHCb experiment is a dipole magnet, made of two coils that have a saddle shape installed in an iron yoke weighing around 1450 tonnes. The shape of the coils is such that the gap formed inside the magnet follows the angular acceptance of the detector (see figure 2.4). The polarity of the magnet is changed intermittently enabling the collection of similar integrated luminosities of data from both polarities, hence allowing the cancellation of systematic uncertainties that potentially originate from detection asymmetries. This is particularly important for searches for CP-violation. The bending power of the magnet is $\int \vec{B} d\vec{l} = 4\,\mathrm{Tm}$ for a 10 m long track [68]. This magnetic field is sufficient to produce forces that bend

highly energetic charged particles in the horizontal plane and allow their momenta to be measured, with resolutions of around 1% for charged tracks of 200 GeV/c [69]. Good momentum resolution is particularly important in obtaining the invariant-mass resolution needed to distinguish signal from combinatorial or peaking background and also for enabling the accurate determination of angles, which is vital for the extraction of parameters in the analysis presented in this thesis.

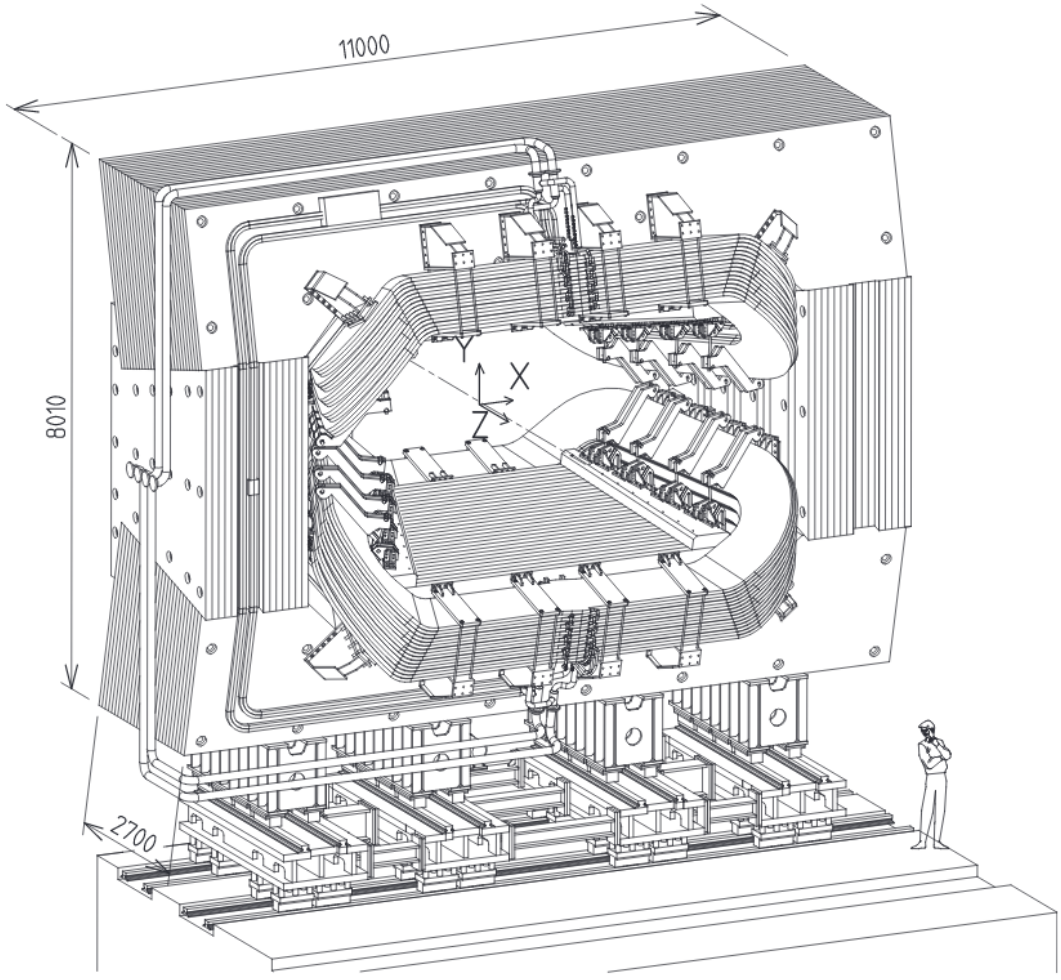

Figure 2.4: The LHCb magnet [64].

2.2.3 The Vertex Locator

The Vertex Locator (VELO) sub-detector is one of the fundamental components of the LHCb detector enabling measurements of track coordinates, used for the determination of the primary and secondary vertices with very high precision; measurements from VELO are also an important ingredient for the triggers [70]. The VELO is a retractable sub-detector, physically withdrawn during injection and acceleration; under stable, colliding beam conditions it is moved to a distance of 8 mm from the beam axis. The sub-detector consists of a series of 42 semi-circular modules, housed inside their own vacuum and shielded from the RF wakefield of the beam by a very thin aluminium foil. Each module consists of a pair of silicon mircrostrip sensors of 300 mm thickness placed back to back, each of them designed for either a radial (r) or azimuthal (ϕ) measurement, with the thickness being particularly important for the reduction of multiple scattering; an illustration of a single module is presented in figure 2.5. Furthermore, the amount of energy deposition is also measured. Combining the signals from neighbouring strips allows the reconstruction of a cluster of energy deposits and finally the determination of a weighted mean, which significantly improves the vertex resolution compared to a binary decision. The vertices in the VELO are determined with an accuracy of a few μm (depending on the plane and the occupancy), resulting in a decay time resolution of ~ 50 fs, which is much smaller that the typical lifetimes of ~ 1 ps of the b-hadrons. This feature is the key ingredient for several measurements, such as that of the CP-violating phase in the $B_s^0 \to J/\psi K^+K^-$ decays where the need to disentangle the fast oscillations

of the B_s^0-$\bar{B}_s^0$ system is paramount [71].

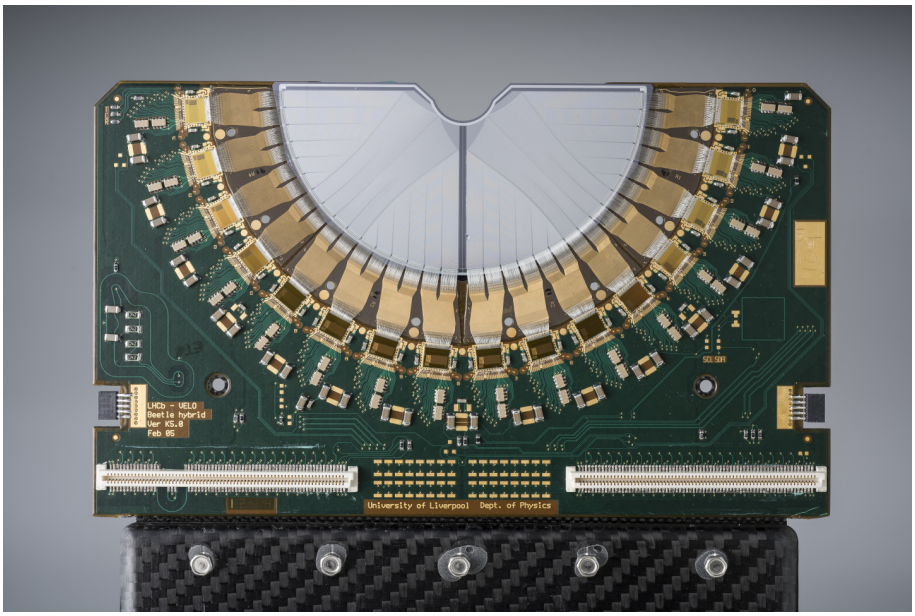

Figure 2.5: A single module from VELO [72].

2.2.4 The Silicon Trackers

The flux of particles produced in the LHCb acceptance are most concentrated in the region around the beam-pipe and consequently make the requirements for the design of the tracking stations very specific. The tracking systems employed in the LHCb detector in the regions where the flux of particles is very high, consist of the Tracker Turicensis (TT) and the Inner Tracker (IT) installed upstream and downstream of the magnet respectively. Both of these are made out of silicon strips, providing a very good spatial resolution of approximately 50 µm [73] in the $x - y$ plane.

The TT station is made out of four planes of silicon strip detectors of around 500 µm thickness, each covering an active area of approximately $8\,\mathrm{m}^2$. The first and last planes are vertical to the x-axis while the middle two have a $\pm 5^0$ orientations re-

spectively, making the so called "$xuvx$" configuration [73]. An overview of the TT station is given in figure 2.6. In contrast with the IT stations where the "$xuvx$" configuration is also adopted in the TT station the first ("xu") and the last ("vx") two pairs of layers are separated with a gap of approximately 27 cm along the z-axis. The IT is made out of three stations (T1-T3), each of them following the "$xuvx$" configuration. The IT is surrounded by the Outer Tracker (see section 2.2.5). The cross shape of the IT is placed around the beam pipe, covering an active area of around $4\,\mathrm{m}^2$; one of the IT stations is illustrated in figure 2.7. Although the IT only covers around 1.3% of the total surface of the T1–T3 stations, around 20% of charged particles pass through it [73].

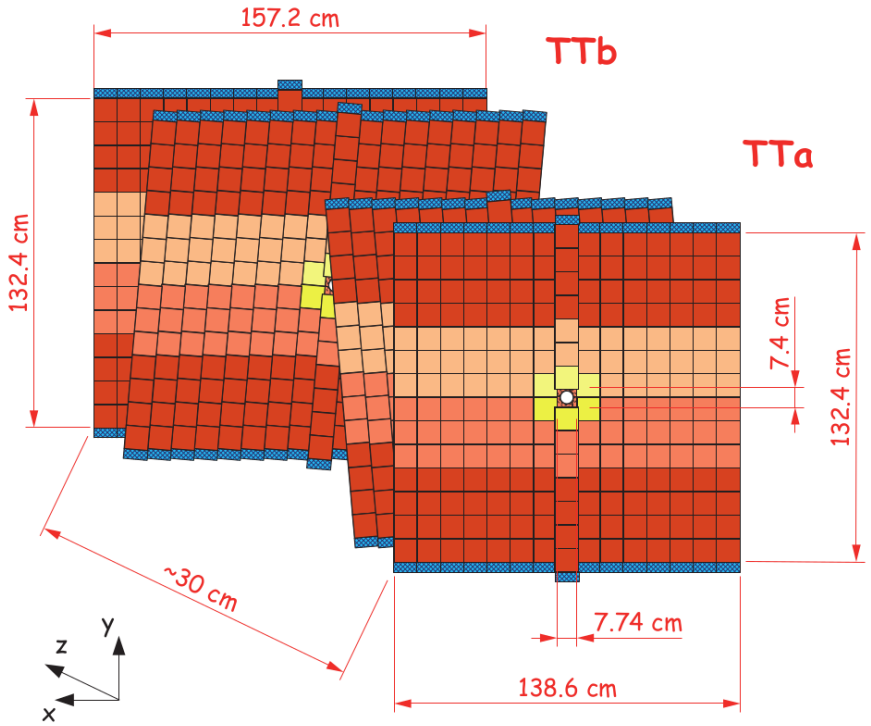

Figure 2.6: A schematic overview of the TT station, where the four layers forming the "$xuvx$" configuration.

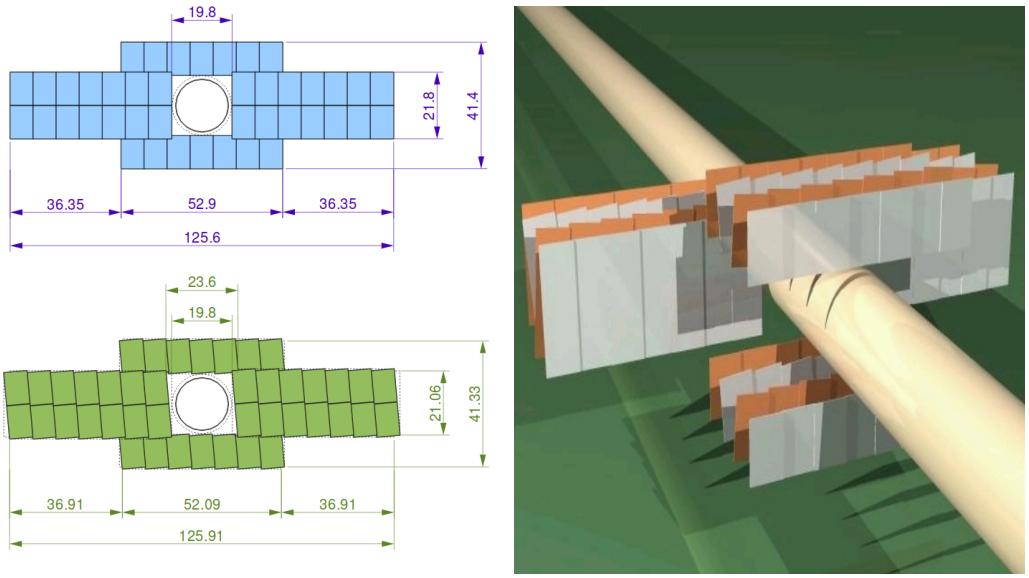

Figure 2.7: (Left) Illustration of the vertical (blue) and stereo (green) layers of the IT. (Right) An illustration of the "*xuvx*" configuration around the beam pipe for one of the IT stations [73].

2.2.5 The Outer Tracker

The three tracking stations (T1–T3) installed upstream of the magnet, where each station comprises the inner region (IT) station, while the rest of the area represent the so-called Outer Tracker (OT). Each of the OT stations is made out of four layers following the "*xuvx*" configuration. Each layer is composed of several stand-alone modules; each of them containing two layers of straw gas detectors. Each of the layers in the modules contains 64 tubes (see figure 2.8), with inner diameter of 5 mm [74]; the hit resolution provided by the straw tubes is around 200 µm.

2.2.6 The RICH detectors

Particle identification is of particular importance for the LHCb detector. Many physics analyses involve the investigation of *b*-hadrons that cascade to multi-hadronic

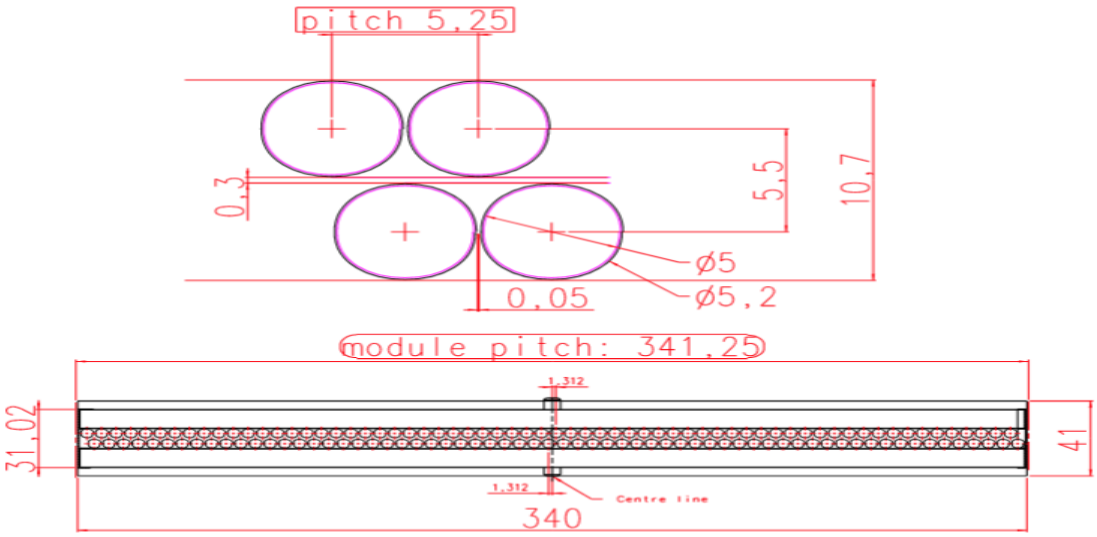

Figure 2.8: The cross section of a single OT module composed of the two layers of series of straw gas detectors [74].

final states; the correct identification of which is vital in the proper reconstruction of the invariant-mass of the decaying hadrons. This is a necessary ingredient in order to reject as much combinatorial background as possible. The particle identification system is also a very powerful tool, used for example in the separation of hadronic decays that have the same topology but different final-state hadrons; in the flavour tagging where the produced state of the heavy flavoured particle is found by identifying soft momentum kaons produced in the cascade chain; and in the high level trigger system [75].

The particle identification in LHCb is performed by two Ring Imaging Cherenkov detectors, the so-called RICH1 and RICH2. Charged particles that pass through the medium faster than the speed of light in the medium emit so-called Cherenkov radiation in the form of cones with a characteristic angle relative to the charged particle trajectory. The Cherenkov light is reflected by a set of mirrors and finally

detected by a set of Hybrid Photon Detectors (HPDs) placed outside of the detector acceptance. From the measurement of this angle, together with the knowledge of the refractive index n of the medium, using $\cos\theta = 1/n\beta$, the speed of the particle is determined. Combining this information with the measured momentum of the particle, the mass of the particle and so its identity (ID) can be inferred.

Both of the RICH detectors have very similar design. They are made of a radiator medium and a set of mirrors to reflect and focus the emitted light to a set of photo detectors. The radiator medium is C_4F_{10} and CF_4 for RICH1 and RICH2 respectively, resulting in different refractive indices, optimised to the particular momentum range for which each of them is designed to operate[1]. The RICH1 is placed after the VELO and before the magnet and covers the momentum range from 2–40 GeV/c, while RICH2 is installed after the magnet and before the tracking stations covering a momentum range of 15–100 GeV/c [76]. An overview of the design of RICH1 and RICH2 is given in figure 2.9.

In order to determine the particle ID, all tracks in both RICH detectors are treated simultaneously, where the relevant information is employed in a likelihood based algorithm and the likelihood of the event (originally all particles are treated as pions) under different mass hypotheses is computed. The same process can be performed by computing a combined likelihood (as a linear sum) using information from other sub-detectors such as the calorimeters and the muon system. Another approach is to use multivariate techniques to account for correlations between the various sub-

[1] An additional aerogel radiator was present in RICH1 during Run1, but during the first long shutdown it was removed.

systems and using additionally information from the tracks, resulting in an output of a single probability (`ProbNN`), for each mass hypothesis [77].

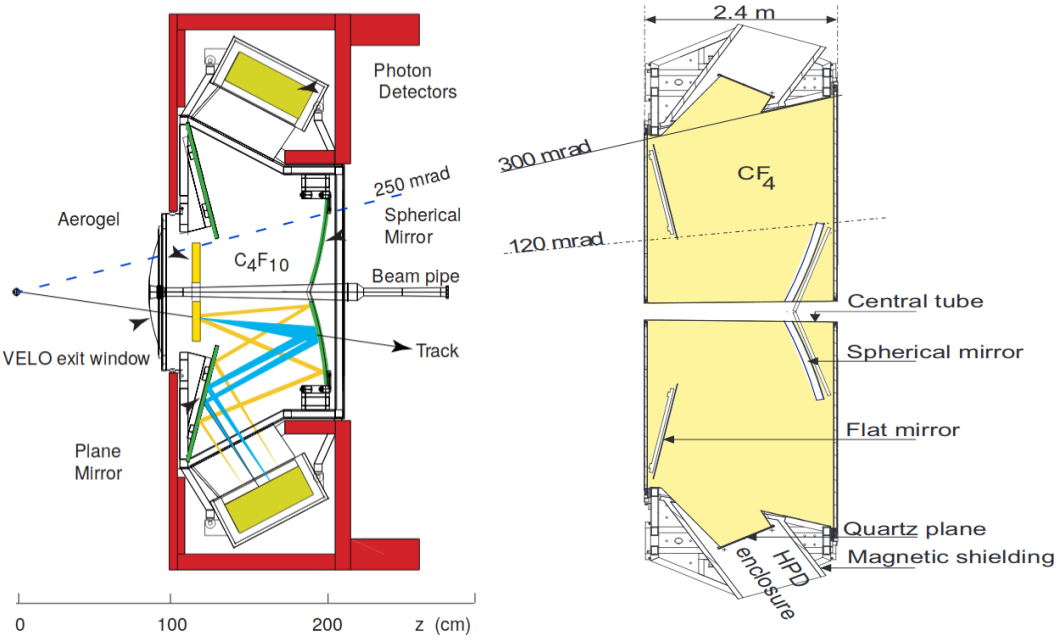

Figure 2.9: Layout of the RICH1 (left) and RICH2 (right) [64].

2.2.7 The Calorimeters

The calorimeter system in LHCb is placed after RICH2 and consists of four wall-like detectors, their purpose being to identify electrons, photons and hadrons, measure their energy and direction and provide information to the triggers and for offline analysis. The calorimeters are segmented with varying granularity in order to deal with the high flux of particles close to the beam pipe, as can be seen in figure 2.10. The four calorimeters consist of a Scintillating Pad Detector (SPD), followed by the Preshower (PS) detector, where in between these two a thin layer of lead of 2.5 radiation lengths is placed to initiate electromagnetic showers. The main purpose

of the SPD and PS detectors is to identify electrons and photons and distinguish between the two of them. Electrons produce scintillation light in SPD, unlike photons, while the thin layer of lead is sufficient to initiate electromagnetic showers for photons that will be detected by the PS, charged hadrons are not likely to initiate a shower and this provides further separation between electrons/photons and charged hadrons. The Electromagnetic (ECAL) and Hadronic (HCAL) calorimeters are placed downstream; both of them are sampling calorimeters, where the so-called Shashlik technology [78] is adopted and are made of alternating layers of scintillator and lead (ECAL) or iron (HCAL). The thickness of ECAL corresponds to 25 radiations lengths, which is enough to contain the full shower that is initiated by photons and electrons. The thickness of HCAL corresponds to only 5.6 interactions lengths (due to limited space), and the main purpose of this calorimeter is to supply the L0 trigger with useful information about high energy hadrons [64].

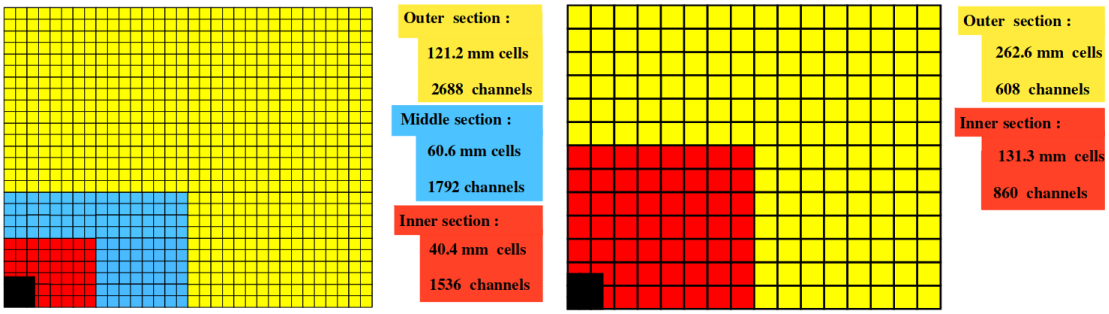

Figure 2.10: The segmentation of ECAL (left) and HCAL (right) [79].

2.2.8 The Muon stations

The last component of the LHCb detector is the Muon system, which consists of five wall-like stations. The Muon stations (M1–M5) are made using Multi-Wire Proportional Chambers (MWPC), with varying size to fit in the LHCb acceptance. The M1 is built after the RICH2 and before the calorimeters, and is the only one of the stations where the central part of the station is made out of a Triple Gas Electron Multiplier (GEM), in order to deal with the high flux of particles in this region. The MWPC are segmented in four regions each of them having different granularity, in order to have a comparable ratio of particle flux and occupancy in each channel. To stop highly penetrating particles other than muons, a 80 cm layer of iron is placed in between each of the M2–M5 stations, resulting in the minimum momentum for a muon to traverse all stations being 6 GeV/c. An illustration of the installation of M1–M5 is given in figure 2.11. The M1–M3 stations are used to reconstruct track segments and perform a measurement of p_{T} with good resolution, the p_{T} measurement is particularly improved by the presence of M1 before the calorimeters. The M4–M5 stations, due to poor spatial resolution, are mainly used for the muon identification. Overall the muon stations are an extremely valuable component in the LHCb detector, providing fast measurements of p_{T} used in the triggers and identification of muons [64].

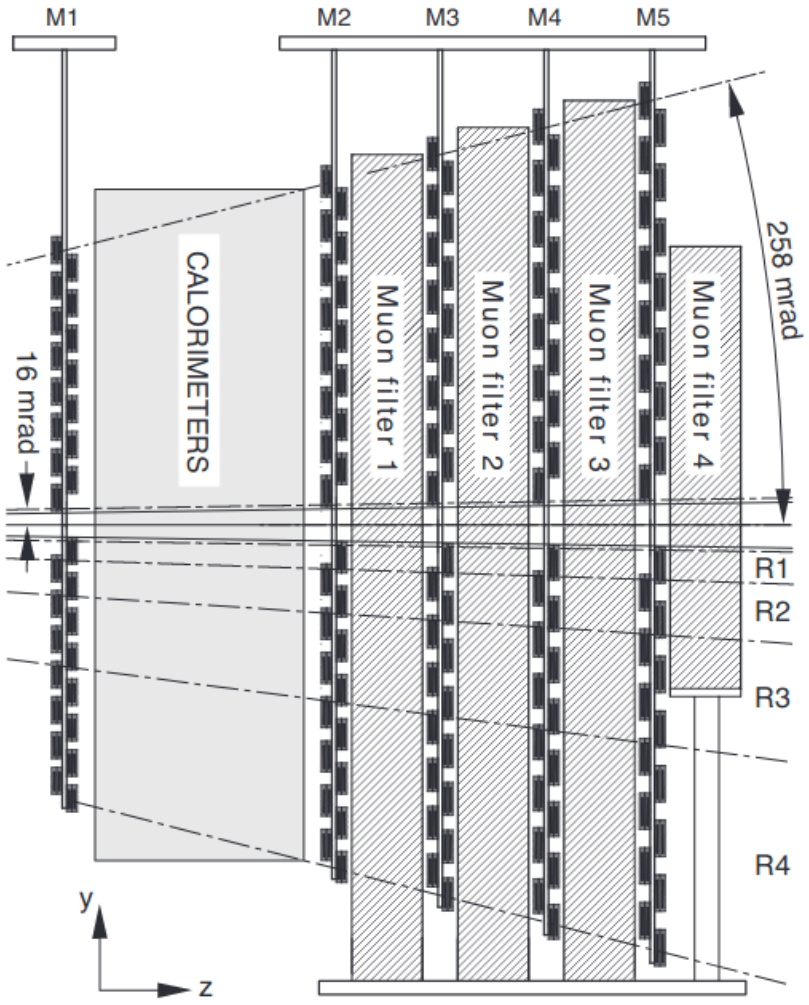

Figure 2.11: A view form the side of the M1–M5 stations [80].

2.2.9 The Trigger system

The objective of the LHCb trigger system is to reduce the enormous amount of raw information coming from the LHCb detector to a manageable level that can be permanently stored for offline analysis, while selecting interesting events for the LHCb programme with high efficiency and rejecting as much background as possible. At LHCb the rate of visible interactions is about 13 MHz (Run1) [81]; the trigger system reduces the output rate of events that are permanently stored to 3.5, 5

and 12.5 kHz for 2011, 2012 and Run2 respectively. The LHCb trigger system is composed of the Level-0 trigger (L0), a hardware-based system, and the High Level Triggers (HLT), a software-based system that is further subdivided into HLT1 and HLT2 applications. Events passing the full chain are stored with the complete information from all the sub-detectors for offline analysis. Due to the significant increase in the number of visible interactions in Run2 and the increase in cross-section of b- and c-hadrons, the trigger strategy was revised [82]. In this spirit several improvements are made, such as the online calibration and alignment and using the offline reconstruction software at trigger level, which results in an impressively good quality of data just after triggering [64, 83].

The L0 trigger is built on a hardware system and consists of custom-made electronics, whose purpose is to achieve an output rate of 1 MHz, that will be delivered to the HLT system. The main objective of the L0 system is to make a very fast decision on whether an event is interesting or not. The decision is based on looking for tracks with high p_{T} or E_T which is a distinct feature of the b- and c-hadrons decays; for this purpose, the L0-Muon and the L0-Calorimeter triggers are used. Events that are triggered from at least one of the L0 triggers are delivered to the HLT, otherwise they are removed. The L0-Muon trigger [84] starts by searching for hits in the Muon stations that point back to the interaction point, and selects muons that satisfy a p_{T} requirement. The L0-Calorimeter trigger [85] uses information from the PS, SPD, ECAL and HCAL calorimeters; candidates with E_T that exceeds a certain threshold activate the L0-Calorimeter decisions, `L0-Electron`, `L0-Hadron` and `L0-Photon` depending on the ID of the candidate. Apart from the L0-Muon

and L0-Calorimeter triggers filtering the raw data, events with a significant number of SPD hits, *i.e.* with a high multiplicity, are vetoed [64, 83].

The HLT is a software-based application, running on a CPU farm, which consists of a few thousands CPU cores. For optimisation purposes, the HLT triggers are split into two stages: starting with HLT1, which receives the 1 MHz output of L0 trigger; events are filtered and those that are triggered by HLT1 are passed to HLT2 which further reduces the rate to a few kHz. The HLT1 performs a partial reconstruction of the event. VELO tracks that are found to be interesting are propagated to the tracking and muon stations (if they are triggered by the L0-Muon) and their momentum is determined in a simplified way. Subsequently a filtering on the event is performed from the several trigger lines that compose the HLT1 by applying cuts on variables, such as the track quality, impact parameter and momentum of the tracks. At the HLT2, a complete event reconstruction is performed using a simplified version of the reconstruction software (in Run2 the reconstruction software used for offline analyses was also used in HLT2) [64, 83, 86]. The HLT2 consists of a list of inclusive and exclusive selections ("trigger lines"), based on kinematic quantities, PID variables and quality criteria.

CHAPTER 3

Simulation

In this chapter I will discuss the basis of the simulation software used in the LHCb experiment, while focusing on the description of a certain benchmarking test for the electromagnetic interactions in LHCb simulations. The purpose of this test is to validate certain steps in the simulation chain and in particular the software which is responsible for the description of the interactions of particles with the LHCb detector, the so-called GEANT4 toolkit [87–89]. The validation test that is described is an update of that presented in Ref. [90]. While the basics of the test remained intact, many other aspects are significantly changed in order for the software to be executed automatically in a periodic way and to be integrated with applications

that perform systematic regression tests.

3.1 Simulation of an event in the LHCb detector

In the LHCb experiment, as in most High Energy Physics (HEP) experiments, the modelling of the physics processes and the equivalent detector response is performed using a Monte Carlo (MC) simulation, where the phenomena to be described are parametrised in terms of probability density distributions. The latter are randomly sampled sequentially to produce instances of the phenomena of interest. The full chain of the simulation, starts with the simulation of the event, the decay of unstable particles, followed by the simulation of the response of the detector [65], where each stage of the simulation is handled by a dedicated package. The *pp* collision and the hadronisation process is simulated by a package called Pythia [91], the decay of particles then is performed by a dedicated package (EvtGen [92]), where the decay of particles is performed either in phase-space, or if the matrix element of the decay is known it can also be included and transformed into the equivalent kinematics of the decay. In addition, final state radiation (FSR) is also generated using the Photos package [93]. In the following steps, the interactions of the particles with the active and passive components of the LHCb detector, such the beam pipe, are also simulated. The simulation of the interaction of particles with the detector is performed through the Geant4 package. The way that "stable" particles[1] interact with the various materials of the detector is fully described in Geant4 by a set of

[1]Particles that have long enough lifetime to traverse a measurable distance in the detector.

physics lists, *e.g.* the electromagnetic physics lists set up all relevant information for the GEANT4 package related to the electromagnetic interactions and how different aspects of the simulation will be handled. Different physics lists may have their own set of production cuts that control the generation of secondary particles produced with very low energies, which will increase significantly the CPU required by the simulation even though the presence of these low energy particles is not expected to play any significant role. Information, such as the energy deposits and the registered points of interaction for the relevant sub-systems is taken into account and finally the collective information is digitised and processed in the same way as data. All these phases of the simulation need properly to be described in order for the MC samples to accurately describe data.

3.2 Validation of electromagnetic interaction models

Several electromagnetic physics list are already available from the GEANT4 collaboration, while a few of them are tuned by the LHCb collaboration in order to match better the needs of the detector design and physics requirements. Electromagnetic physics lists such as `Opt1`, `Opt2` are provided by the GEANT4 collaboration, while others such as `LHCb` and `NoCuts` (default list that is used in the official MC productions) are private physics lists used by the LHCb Collaboration. The purpose of the test listed below is to validate that electromagnetic interactions behave as expected, while at the same time checking for incompatibilities between results obtained among different versions of GEANT4. The test that I will describe is completely integrated

in the GAUSS [94] framework, which is a software suite integrating the full LHCb simulation chain. The results of this test are automatically generated in a periodic way and collected by a dedicated software, named LHCbPR. The latter is an application that is designed for monitoring systematically the LHCb software, since for example changes in the data bases, libraries and models may have an effect in the performance of the simulation [95].

The test consists of the generation of mono-energetic particles, of different types, such as $e^{\pm}$, $\mu^{\pm}$ and $\pi^{\pm}$; the process is repeated using different types of physics lists. The particles are "fired" (using a "particle gun") onto thin layers of silicon, specifically the VELO modules and path lengths between 290 and 310 µm are considered. The energy deposits in the thin layers of silicon form a smeared Landau distribution, the latter distribution is saved to extract parameters of interest that will be compared against expectations [7]. The number of particles used in the generation for each of the samples is the main component which determines the CPU consumption. The number of primary particles generated in each sample is tuned to allow the test to be performed rather quickly because it is performed very frequently. The most probable value (MPV) and the full width at half maximum (FWHM) are extracted from the Landau distributions by performing a parabolic fit around the peak of the distributions, an example of the energy deposit and the relevant fit from which the MPV and FWHM are extracted is illustrated in figure 3.1. The fit process is repeated for all the particles, energies and physics lists used in the test and compared against the expected values.

The results in terms of the comparison of the MPV and MPV/FWHM for all the possible combinations of particles, energies and physics lists using the GEANT4.9.6P04 version are summarised in figure 3.2. The results are found to behave in a reasonable way, *i.e.* the distributions of the MPV and MPV/FWHM from the simulation is close to what is expected from theory [7] for all physics lists; small deviations are expected due to statistical fluctuation in the simulated samples, the fact that the path length is not constant and mainly due to the parabolic fit which is very sensitive to fluctuations in the data sample. In terms of the comparison between different GEANT4 versions *e.g.*GEANT4.9.6P04 and GEANT4.10.3P02, the results for the `NoCuts` physics list are summarised in figure 3.3 and found to be compatible, small differences in MPV/FWHM between the two different GEANT4 version are understood to originate mainly due to statistical fluctuations of the simulated samples that effect the parabolic fit.

It must be noticed that the main objective of this test, in terms of comparing the results of the simulation with the theory predictions and the results obtained between the different GEANT4 versions, is to perform a qualitative monitoring of the simulation chain. Any problems identified will be further investigated and resolved in an independent process. In this spirit the specific test indicates that the results from the simulation are compatible with the theory predictions to an acceptable level and that the compatibility of the two GEANT4 versions for the default physics list is good[2].

[2]The results are classified as acceptable/good since small deviations between what is expected are well understood and not attributed to an unexpected behaviour of the simulation software.

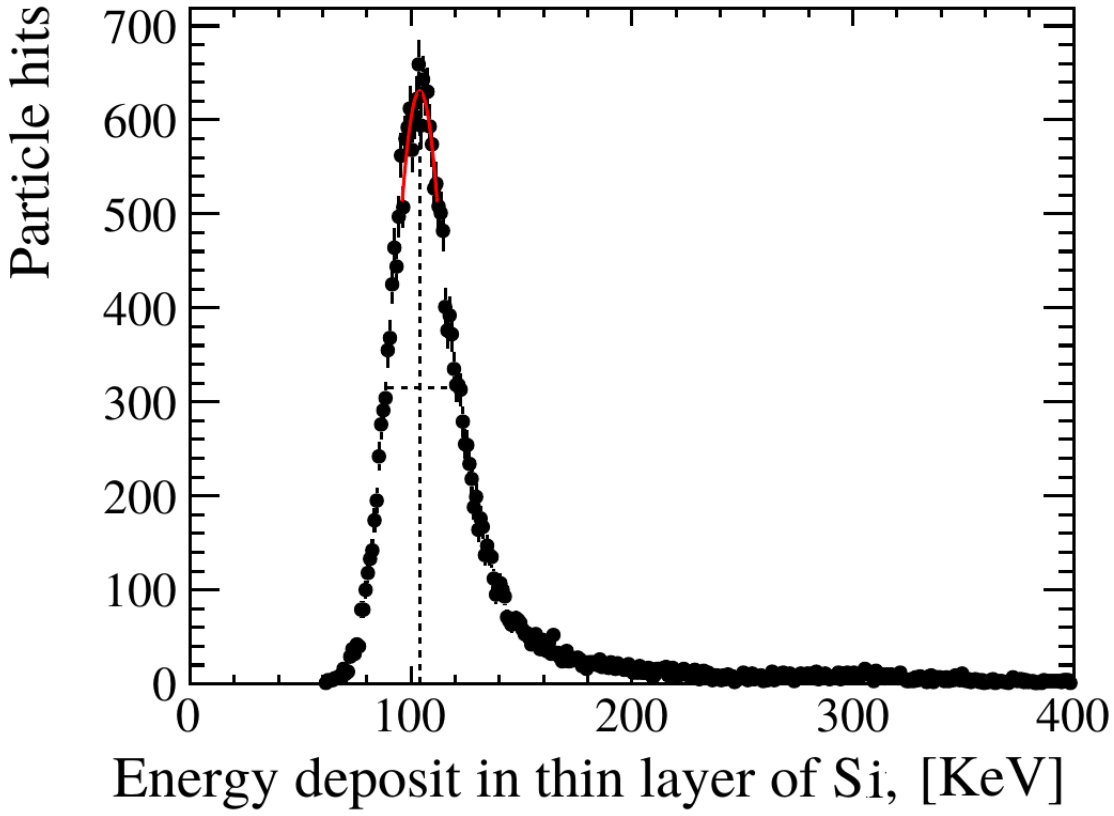

Figure 3.1: Smeared landau distribution for $e^{\pm}$, using `NoCuts` for momentum of 100 GeV/c (black). The fit around the peak (red line) is parametrised using second order polynomials. The vertical and horizontal dotted black lines represent the positions of MPV and the FWHM respectively.

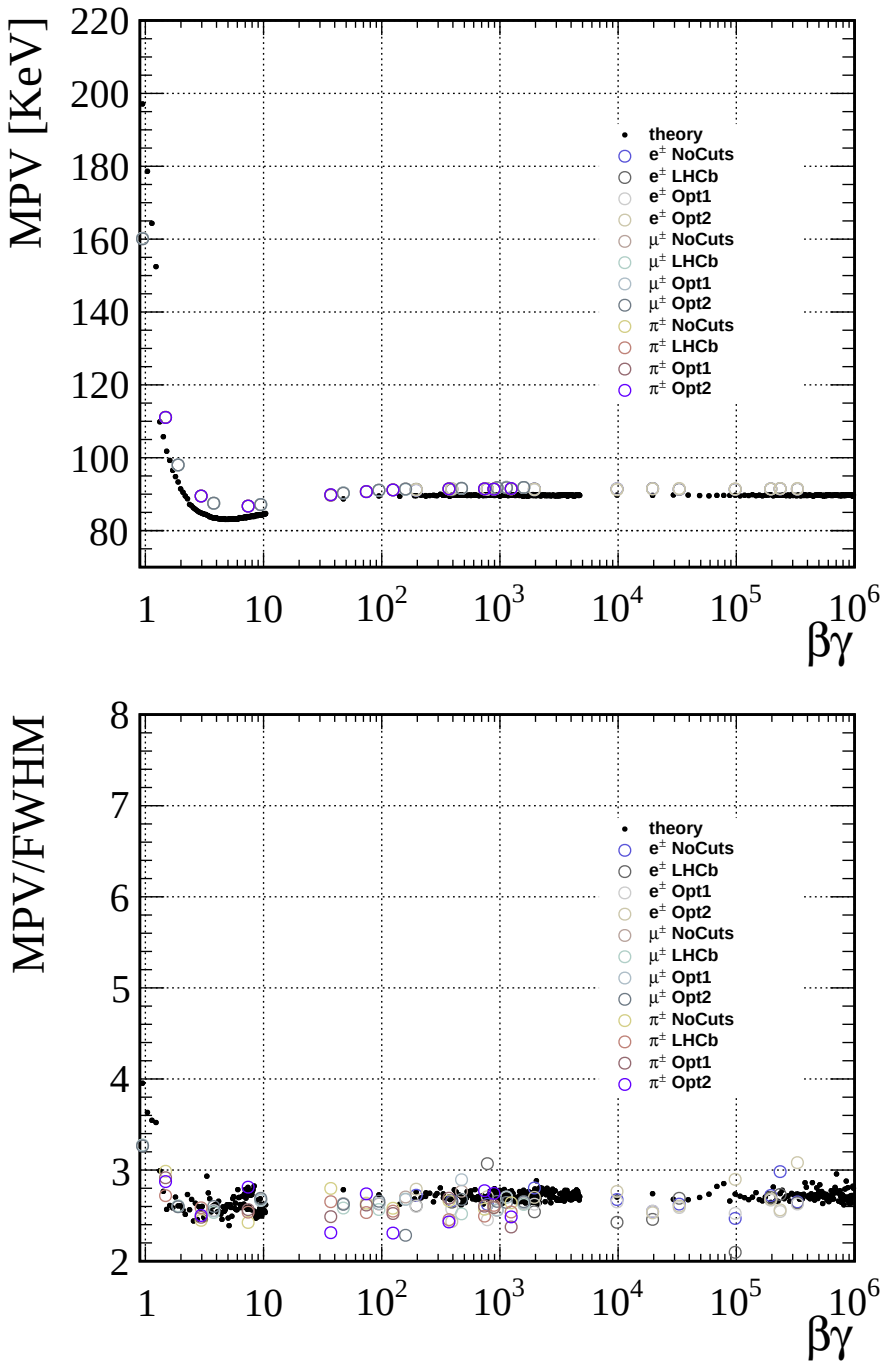

Figure 3.2: Summary of MPV (top) and MPV/FWHM (bottom) from the energy deposits for $e^{\pm}$, $\mu^{\pm}$ and $\pi^{\pm}$, using `Opt1`, `Opt2`, `LHCb` and `NoCuts`. The full test is executed using GEANT4.9.6P04 version.

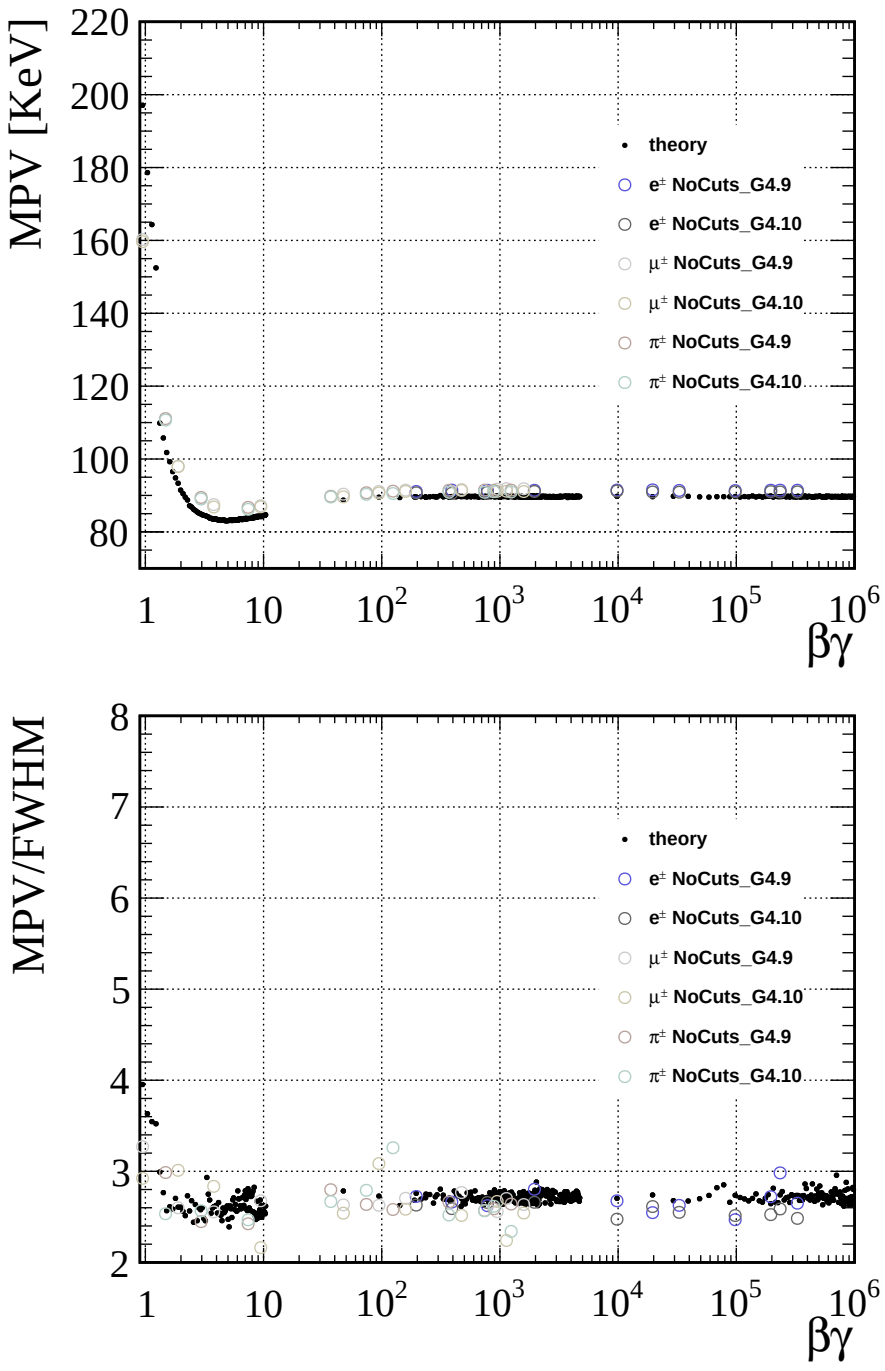

Figure 3.3: Summary of MPV (top) and MPV/FWHM (bottom) from the energy deposits using `NoCuts`, between GEANT4.9.6P04 and GEANT4.10.3P02 versions.

CHAPTER 4

Angular analysis of $\Lambda_b^0 \to \Lambda\mu^+\mu^-$

This chapter is organised as follows: section 4.1 introduces the strategy used to extract the angular observables for the $\Lambda_b^0 \to \Lambda\mu^+\mu^-$ decay; sections 4.2 and 4.3 describe the full selection that is applied in order to increase the purity of the data-samples and the strategy that is followed for the background subtraction respectively; section 4.4 presents the corrections that are applied to the Monte Carlo samples; section 4.5 outlines the parametrisation of the efficiency functions; sections 4.6 and 4.7 illustrate the resolution and validation studies respectively; the potential sources of systematic uncertainty are given in section 4.8; results are presented in section 4.9 and summarised in section 4.10, which also draws conclusions

from the analysis.

4.1 Strategy for extracting the angular observables

In this analysis, the q^2 spectrum is split into two different regions. The first one is the high-q^2 region, defined as $15 < q^2 < 20\,\mathrm{GeV}^2/c^4$, while the second one is the "control" region, defined as, $8.41 < q^2 < 9.92\,\mathrm{GeV}^2/c^4$. The latter region is dominated by the $\Lambda_b^0 \to J/\psi\,\Lambda$ decays, where the particular window is chosen in order to contain the J/ψ resonance without truncating significantly the tail of the J/ψ invariant mass distribution, which can potentially affect the reconstructed invariant mass of the $p\pi^-\mu^+\mu^-$ system, $m(p\pi^-\mu^+\mu^-)$. The control region data are used: in the tuning of the selection; in the determination of the signal parameters of the $m(p\pi^-\mu^+\mu^-)$ distribution for the $\Lambda_b^0 \to \Lambda\mu^+\mu^-$ mode; to evaluate corrections applied to simulated data and to perform several checks of the efficiency function. The low-q^2 region is not used due to the relatively small number of signal candidates, making the extraction of angular observables not meaningful in this region. The angular observables will be extracted only in one q^2 region, namely that of high-q^2. The sample size is insufficient to sub-divide the high-q^2 region.

The angular observables (K_i) are extracted using the method of moments, where a set of trigonometric functions (see table 4.1) is used to project out (see equation 4.1)

the angular observables from the differential decay rate,

$$K_i \equiv \Big\{ \int \frac{\mathrm{d}^6\Gamma}{\mathrm{d}q^2\ \mathrm{d}\cos\theta_l\ \mathrm{d}\cos\theta_b\ \mathrm{d}\cos\theta\ \mathrm{d}\phi_l\ \mathrm{d}\phi_b} \times g_i(\cos\theta_l, \cos\theta_b, \cos\theta, \phi_l, \phi_b)\ \mathrm{d}\cos\theta_l\ \mathrm{d}\cos\theta_b\ \mathrm{d}\cos\theta\ \mathrm{d}\phi_l\ \mathrm{d}\phi_b \Big\} \Big/ \Big\{ \int \frac{\mathrm{d}^6\Gamma}{\mathrm{d}q^2\ \mathrm{d}\cos\theta_l\ \mathrm{d}\cos\theta_b\ \mathrm{d}\cos\theta\ \mathrm{d}\phi_l\ \mathrm{d}\phi_b}\ \mathrm{d}\cos\theta_l\ \mathrm{d}\cos\theta_b\ \mathrm{d}\cos\theta\ \mathrm{d}\phi_l\ \mathrm{d}\phi_b \Big\}\ , \tag{4.1}$$

The moments, *i.e.* the estimates of the K_i, can be determined from data using the following expression,

$$K_i \equiv \Big\{ \sum_e^{N_{\mathrm{ev}}} w^{(e)}/\varepsilon^{(e)} \times g_i(\cos\theta_l^{(e)}, \cos\theta_b^{(e)}, \cos\theta^{(e)}, \phi_l^{(e)}, \phi_b^{(e)}) \Big\} \Big/ \Big\{ \sum_e^{N_{\mathrm{ev}}} w^{(e)}/\varepsilon^{(e)} \Big\}\ , \tag{4.2}$$

where the sum runs over all the candidates (e). The weights $w^{(e)}$ and $\varepsilon^{(e)}$ are defined as,

$$w^{(e)} \equiv w(m(p\pi^-\mu^+\mu^-)^{(e)}) \tag{4.3}$$

$$\varepsilon^{(e)} \equiv \varepsilon(\cos\theta_l^{(e)}, \cos\theta_b^{(e)}, \cos\theta^{(e)}, \phi_l^{(e)}, \phi_b^{(e)}, q^{2(e)})\ , \tag{4.4}$$

where $w^{(e)}$ and $\varepsilon^{(e)}$ represent the sWeights, extracted using the *sPlot* technique, which are weights that statistically remove the contribution of the background (see section 4.3) and the efficiency weights (see section 4.5) respectively. The latter are used to correct the angular space for distortions introduced by the event reconstruction, trigger and selection. In the case that the data sample contains only

Table 4.1: Weighting functions used in equation 4.1.

Observable	$g_i(\cos\theta_l, \cos\theta_b, \cos\theta, \phi_l, \phi_b)$
K_1	$\frac{1}{4}(3 - 5\cos^2\theta_l)$
K_2	$\frac{1}{2}(5\cos^2\theta_l - 1)$
K_3	$\cos\theta_l$
K_4	$\frac{3}{4}(3 - 5\cos^2\theta_l)\cos\theta_b$
K_5	$\frac{3}{2}(5\cos^2\theta_l - 1)\cos\theta_b$
K_6	$3\cos\theta_l\cos\theta_b$
K_7	$\frac{15}{2}\cos\theta_l\sin\theta_l\sin\theta_b\cos(\phi_l + \phi_b)$
K_8	$\frac{3}{2}\sin\theta_l\sin\theta_b\cos(\phi_l + \phi_b)$
K_9	$\frac{15}{2}\cos\theta_l\sin\theta_l\sin\theta_b\sin(\phi_l + \phi_b)$
M_{10}	$\frac{3}{2}\sin\theta_l\sin\theta_b\sin(\phi_l + \phi_b)$
K_{11}	$\frac{3}{4}(3 - 5\cos^2\theta_l)\cos\theta$
K_{12}	$\frac{3}{2}(5\cos^2\theta_l - 1)\cos\theta$
K_{13}	$3\cos\theta_l\cos\theta$
K_{14}	$\frac{9}{4}(3 - 5\cos^2\theta_l)\cos\theta_b\cos\theta$
K_{15}	$\frac{9}{2}(5\cos^2\theta_l - 1)\cos\theta_b\cos\theta$
K_{16}	$9\cos\theta\cos\theta_l\cos\theta_b$
K_{17}	$\frac{45}{2}\cos\theta_l\sin\theta_l\sin\theta_b\cos\theta\cos(\phi_l + \phi_b)$
K_{18}	$\frac{9}{2}\sin\theta_l\sin\theta_b\cos\theta\cos(\phi_l + \phi_b)$
K_{19}	$\frac{45}{2}\cos\theta_l\sin\theta_l\sin\theta_b\cos\theta\sin(\phi_l + \phi_b)$
K_{20}	$\frac{9}{2}\sin\theta_l\sin\theta_b\cos\theta\sin(\phi_l + \phi_b)$
K_{21}	$\frac{15}{2}\cos\theta_l\sin\theta_l\sin\theta\sin\phi_l$
K_{22}	$\frac{3}{2}\sin\theta\sin\theta_l\sin\phi_l$
K_{23}	$\frac{15}{2}\cos\theta_l\sin\theta_l\sin\theta\cos\phi_l$
K_{24}	$\frac{3}{2}\sin\theta\sin\theta_l\cos\phi_l$
K_{25}	$\frac{45}{2}\cos\theta_l\sin\theta_l\cos\theta_b\sin\theta\sin\phi_l$
K_{26}	$\frac{9}{2}\sin\theta\sin\theta_l\cos\theta_b\sin\phi_l$
K_{27}	$\frac{45}{2}\cos\theta_l\sin\theta_l\cos\theta_b\sin\theta\cos\phi_l$
K_{28}	$\frac{9}{2}\sin\theta\sin\theta_l\cos\theta_b\cos\phi_l$
K_{29}	$\frac{9}{4}(5\cos^2\theta_l - 1)\sin\theta_b\sin\theta\sin\phi_b$
K_{30}	$\frac{9}{8}(3 - 5\cos^2\theta_l)\sin\theta_b\sin\theta\sin\phi_b$
K_{31}	$\frac{9}{4}(5\cos^2\theta_l - 1)\sin\theta_b\sin\theta\cos\phi_b$
K_{32}	$\frac{9}{8}(3 - 5\cos^2\theta_l)\sin\theta_b\sin\theta\cos\phi_b$
K_{33}	$\frac{9}{4}\sin\theta_b\sin\theta\cos(2\phi_l + \phi_b)$
K_{34}	$\frac{9}{4}\sin\theta_b\sin\theta\sin(2\phi_l + \phi_b)$

Observable	Value	Observable	Value	Observable	Value
K_1	0.3512	K_{13}	-0.0175	K_{25}	-0.0000
K_2	0.2976	K_{14}	0.0021	K_{26}	0.0000
K_3	-0.2356	K_{15}	-0.0115	K_{27}	0.0133
K_4	-0.1953	K_{16}	0.0091	K_{28}	-0.0112
K_5	-0.1542	K_{17}	0.0061	K_{29}	0.0000
K_6	0.1872	K_{18}	0.0012	K_{30}	-0.0000
K_7	-0.0219	K_{19}	0.0000	K_{31}	0.0000
K_8	-0.0998	K_{20}	-0.0001	M_{32}	-0.0028
K_9	0.0004	K_{21}	0.0000	M_{33}	-0.0032
K_{10}	-0.0006	K_{22}	-0.0000	M_{34}	0.0000
K_{11}	-0.0038	K_{23}	-0.0179		
K_{12}	0.0144	K_{24}	0.0202		

Table 4.2: The expected central values of the angular observables evaluated using LQCD form factors from Ref [31]. This is a private evaluation and uncertainties are not calculated.

signal candidates and the efficiency function is flat, *i.e.* $w^{(e)}, \varepsilon^{(e)} \to 1$, equation 4.1 simplifies to the expression

$$K_i \equiv \sum_e^{N_{\rm ev}} g_i(\cos\theta_l^{(e)}, \cos\theta_b^{(e)}, \cos\theta^{(e)}, \phi_l^{(e)}, \phi_b^{(e)}) \Big/ N_{ev} \ . \tag{4.5}$$

The SM predictions for the K_i obtained when setting the value of the Λ_b^0 production polarisation to that of the previous LHCb measurement [46], are given in table 4.2. The SM predictions are used in the generation of pseudo-experiments in the validation studies and in the evaluation of the systematic uncertainties. The 1D angular projections of the five angles for the case of pure signal, with a flat efficiency and by setting the angular coefficients to their SM predictions for the unpolarised case, *i.e.* $P_b = 0$, are illustrated in figure 4.1.

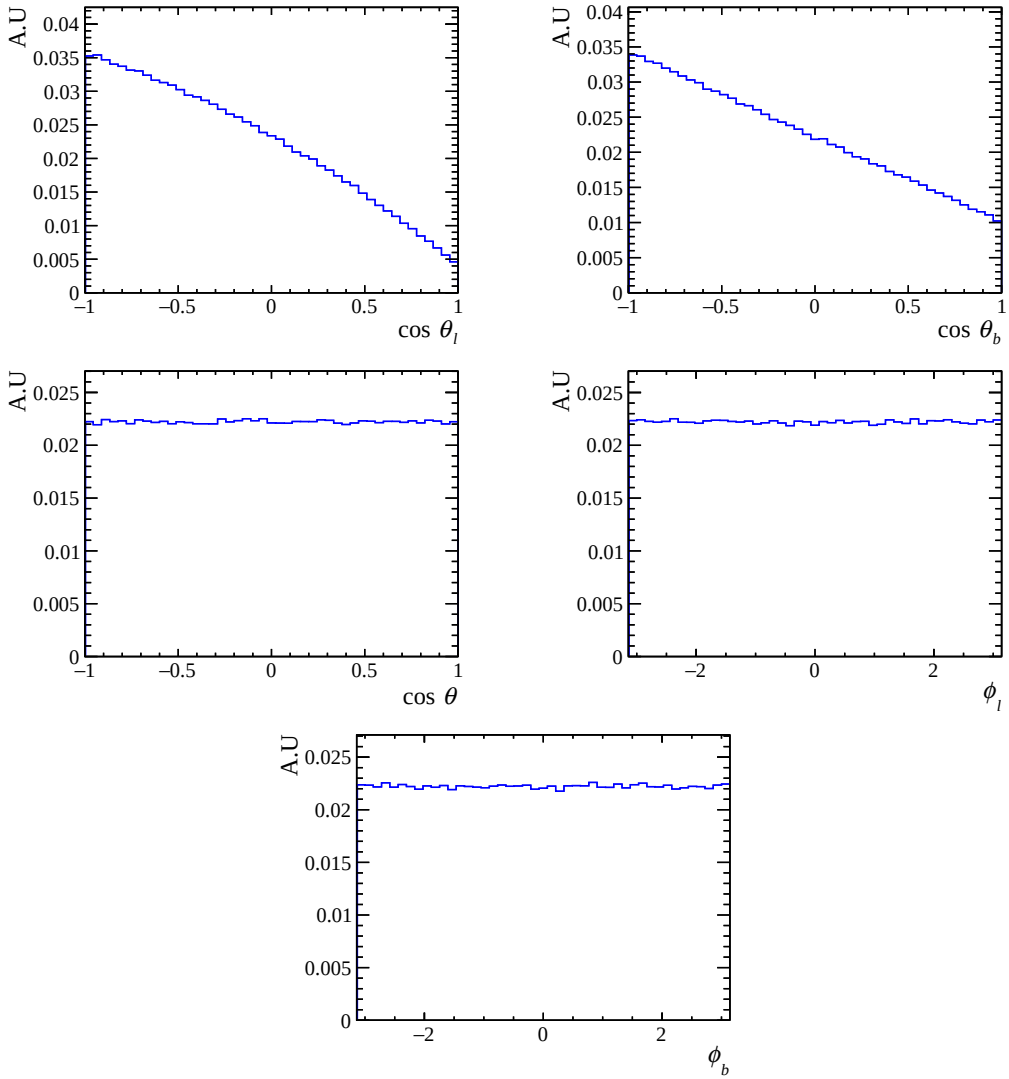

Figure 4.1: 1D angular projections of $\cos\theta_l$, $\cos\theta_b$, $\cos\theta$, ϕ_l and ϕ_b of the angular distribution of $\Lambda_b^0 \to \Lambda\mu^+\mu^-$, where the angular coefficients are set to the SM expectations for the high-q^2 region as given in table 4.2, and setting $P_b = 0$, i.e., $K_{11-34} = 0$.

4.1.1 Determination of statistical uncertainties

The statistical uncertainties of the moments are extracted using the bootstrapping technique [96]. The original data set is randomly sampled with replacement and a number of replicas of the original sample (10000 in the default analysis) are constructed and saved. For each of the replicas the sWeights and the efficiency weights are calculated and finally the moments are extracted and saved. The distributions of the moments are obtained and the RMS is used as a measure of the statistical uncertainty[1]. In the case that the data set is a mixture of many categories, *e.g.* six categories for 2011 + 2012, 2015, 2016 data with two different particle track classifications (see section 4.2.2), then for each category the bootstrapping process is performed separately. Once the sample for each category has been corrected using the sWeights and efficiency weights, it is effectively a pure signal sample, with uniform efficiency. After this, all sub-samples, *i.e.* the replicas for each category, are merged and moments from the combined sample are extracted. These are then saved and used for the determination of the statistical uncertainties.

[1] As discussed in section 4.9.1, the bootstrapping distributions are Gaussian.

4.2 Selection

The selection of candidates is performed in several stages. As a first step a selection is applied based on triggers, in the second stage a cut-based selection is performed (this stage is subdivided into two steps called "stripping" and "preselection"). The final stage uses a Neural Network, after which the extraction of the moments is performed. The same selection is applied to both the rare decay and control modes, with the exception of the q^2 selection (see section 4.1) and an additional requirement on the PID probability assigned to the proton, *i.e.* `ProbNNp>0.1`, which is only applied to the protons of the control sample; this further removes misreconstructed $B^0 \to J/\psi\, K^0_S$ decays. As the selections developed for the 2011 and 2012 data samples are so similar, these two data sets are combined and treated as one. For the 2015 and 2016 samples, there are significant differences in the trigger criteria and so these two samples are treated separately. The same approach holds also for the simulated data samples, where the 2011 and 2012 MC samples are mixed according to the recorded integrated luminosities and $b\bar{b}$ cross section.

4.2.1 Triggers

The candidates are Triggered On Signal (TOS), which essentially means that the daughters of the $\Lambda_b^0 \to \Lambda\mu^+\mu^-$ are responsible for the candidate satisfying the trigger requirements, ensuring the proper modelling of the angular acceptance from the simulated samples. Each of the three stages of the trigger system, L0, HLT1 and

HLT2 (see section 2.2.9), has its own trigger lines. In this work no absolute trigger efficiencies are extracted, however a general discussion for the performance of the triggers is given in Ref. [81]. It must be noticed that the performance depends on the decay mode and the kinematics of the particles and so efficiency values presented below are only indicative.

At the first stage of the trigger, only events that are not busy and triggered by the L0-Muon trigger are considered in this analysis. The trigger looks for muons with high p_{T}; if at least one muon is found that exceeds a given threshold the event is triggered with the `L0Muon` decision. If more that one muon candidate is present, the muon with the second largest p_{T} is also used; if ${p_{\mathrm{T}}}^{\text{largest}} \times {p_{\mathrm{T}}}^{\text{second largest}}$ exceeds a specified threshold then the event is accepted using the `L0Dimuon` decision. The performance of the single and dimuon triggers combined is measured to be $\sim 89\%$ for 2012 data-taking conditions, using $B^- \to J/\psi(\to \mu^+\mu^-)K^-$ decays [81].

At the second stage, a further filtering is applied by the HLT1; trigger lines looking for a single track with a high p_{T}, significant displacement from the PV and good track quality (trigger lines with and without requiring a muon identification are considered) are extensively used. In addition, events that contain two tracks that have good reconstruction quality, are identified as muons, form a good vertex and exceed a certain mass threshold are also triggered by a dedicated trigger line, the so-called `DiMuonHighMass`, the efficiency of which was measured to be $\sim 69\%$ for 2012 data-taking conditions, using $B^- \to J/\psi(\to \mu^+\mu^-)K^-$ decays [81, 97].

Finally in the HLT2, the main selections that are used in this analysis are the

topological trigger lines. These are exclusive lines that focus on the triggering of partially reconstructed b-hadrons, with at least two charged tracks, with or without requiring the presence of a muon in the chain. These lines base their selection on several variables of the topological candidates, such as the significance of the impact parameter, distance of closest approach, flight distance (FD) significance and $\sum p_{\mathrm{T}}$ of the formed candidate. Apart from the topological triggers, an additional trigger line called `DiMuonDetached`, which selects dimuon pairs that are significantly detached from the PV, is also used.

4.2.2 Stripping and preselection

Before discussing in more details the stripping and preselection a brief overview of the track characterisation in the LHCb detector is given.

Tracks in LHCb are classified according to the tracking stations from which data are available. The two kind of tracks that are particularly important in this analysis are those that are reconstructed using hits from the VELO and those that do not, denoted Long and Downstream tracks, respectively. This is of particular importance for long-lived particles, such as the Λ and the K_{S}^0, that can decay outside of the VELO due to their long lifetimes. A schematic overview of all tracks in LHCb and the decay length of several long-lived particles is given in figure 4.2. Other track types are: the Upstream tracks, which are reconstructed with hits from VELO and TT alone; and VELO and T tracks, which are reconstructed solely from hits in the VELO and T stations, respectively. In the following, the acronyms DD and LL will

be used to refer to a signal candidate where the Λ is reconstructed by either two Downstream or two Long tracks respectively; these are the only types of candidates that are used in this analysis.

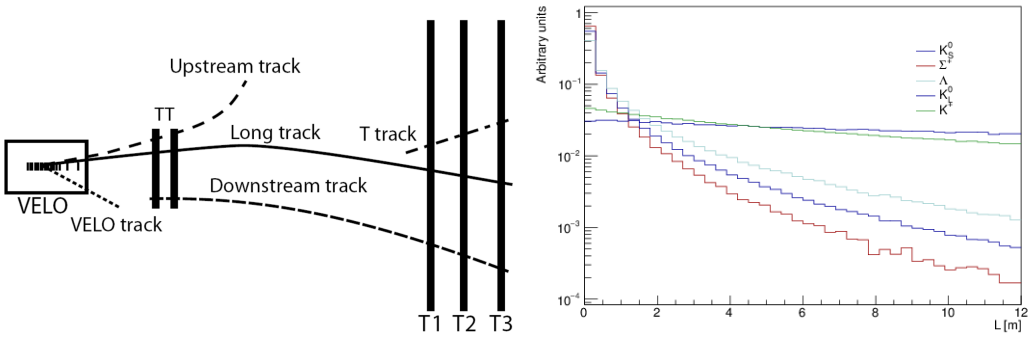

Figure 4.2: (Left) An overview of the track categories in LHCb. (Right) An overview of strange long-lived particles and their decay length (The downstream end of the VELO ends around 1 m from the pp interaction point, while TT station is located at distance of around 2 m from the PV.). [98].

After the full reconstruction of the event, the $\Lambda_b^0 \to \Lambda\mu^+\mu^-$ candidates are required to pass a set of very loose "stripping" cuts to reduce the data to a manageable level for further analysis. At this stage tracks of two oppositely charged muons are combined with a Λ to form a signal candidate. The Λ particle is reconstructed using two long (LL) or downstream (DD) oppositely charged particle tracks; a tight window around the known mass of the Λ baryon [7] is applied, and the two tracks are required to form a vertex with a good fit quality and to have a decay time of at least 2 ps. Finally, for the resulting Λ_b^0 candidates, a very loose cut on the invariant mass is applied. The Λ_b^0 candidate as defined above is required to form a vertex that is significantly detached from the PV. A directional variable, referred to as DIRA and defined as the cosine of the angle defined between the momentum vector of the Λ_b^0 and the vector between the PV and the Λ_b^0 decay vertex, is required to be close to one. In the second stage another cut-based preselection is applied which removes

pathological events, such as background originating from hadronic interactions with the detector material at the RICH1 subdetector exit which are removed by requiring the decay vertex of the Λ to have $z < 2330\,\text{mm}$.

4.2.3 Neural network

The last step in the selection of candidates is performed with a Bayesian Neural Network (NN), using the NeuroBayes package [99, 100], which is trained to separate signal from combinatorial background. For the NN training, signal decays are represented by simulated $\Lambda_b^0 \to \Lambda\mu^+\mu^-$ decays, while background events taken from the upper mass sideband (above the reconstructed Λ_b^0 mass peak) in data are used as a proxy for the combinatorial background in the signal mass interval. The variables that are used as an input are: the vertex and reconstructed decay time χ^2 (see figure 4.3); the DIRA and transverse momentum of Λ_b^0; the impact parameter χ^2 of the muon (hadron) with the highest traverse momentum; the reconstructed mass, p_{T}, vertex position and flight distance of the Λ. It must be noted that variables that are associated with the Λ, proton and pion are treated separately for the LL and DD candidates.

The requirement imposed on the NN output response, the so-called NNcut, is obtained by finding the point where the expected signal significance ($N_{sig}/\sqrt{N_{sig} + N_{bkg}}$) of the $\Lambda_b^0 \to \Lambda\mu^+\mu^-$ in the high-q^2 region is maximised, where the branching fraction of $\Lambda_b^0 \to \Lambda\mu^+\mu^-$ as measured previously by LHCb [27] is used in this estimate. Only candidates with NN response greater than the NNcut are used in the extraction of

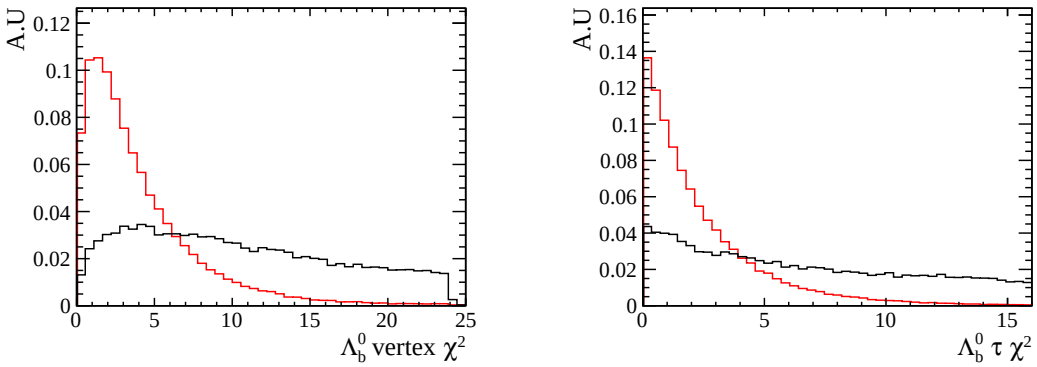

Figure 4.3: Comparison between the distributions of the signal (red) and combinatorial background (black) used in the training of the NN applied to the Run1 data, for the Λ_b^0 vertex χ^2 and Λ_b^0 τ χ^2. These two variables are among the most significant variables for the classification of the candidates.

the moments. The suppression of the combinatorial background by the NN is illustrated in figure 4.4 for the combined sample of both DD and LL track categories using Run1 data. In addition, as an example, the NN distribution, the purity plot ($N_{sig}/(N_{sig} + N_{bkg})$ in bins of the NN output) and the Receiving Operation Curve (ROC) of the NN used for Run1 are given in figure 4.5. To further check that no bias in terms of artificial peaks in the invariant mass of $m(p\pi^-\mu^+\mu^+)$ are introduced by the NN selection, the average response for the signal and background in bins of $m(p\pi^-\mu^+\mu^+)$ is examined; no significant peaks are found. It must be noted that the training and optimisation of the NN is performed separately for 2011+2012, 2015 and 2016 data samples. Equivalent results to the one illustrated in figure 4.5 for the 2015 and 2016 Neural Networks are given in Appendix A.1. For the control mode the NN trained for the rare mode is applied and a conservative cut of NNcut = 0 is finally used.

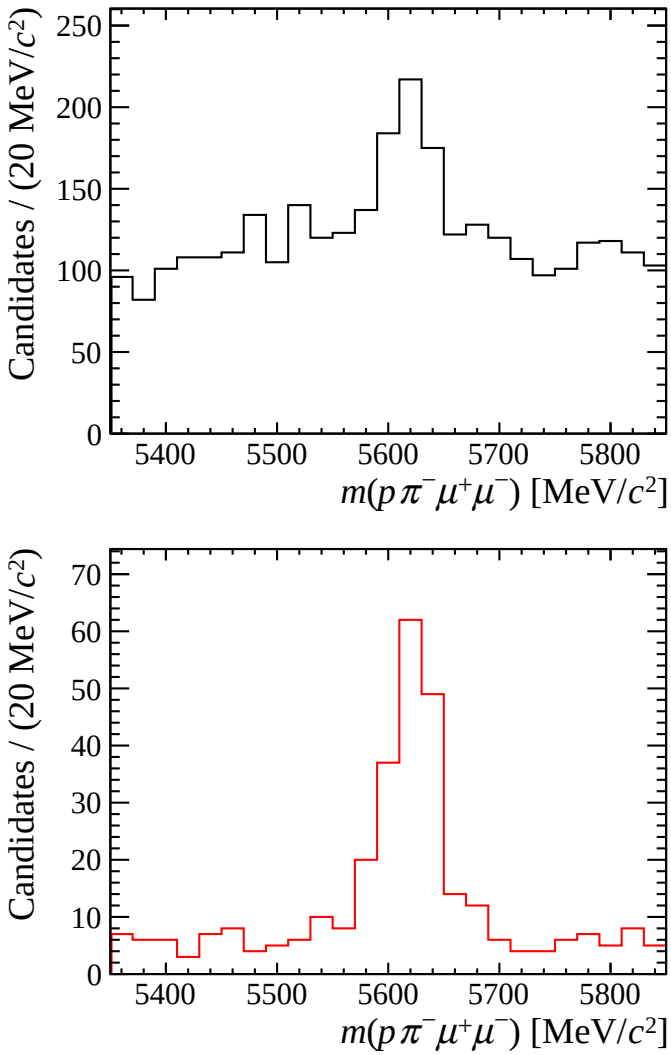

Figure 4.4: Distribution of the invariant mass of $\Lambda_b^0 \to \Lambda\mu^+\mu^-$ before (top) and after (bottom) applying the NNcut. In these figures both track categories of the Run1 sample are combined.

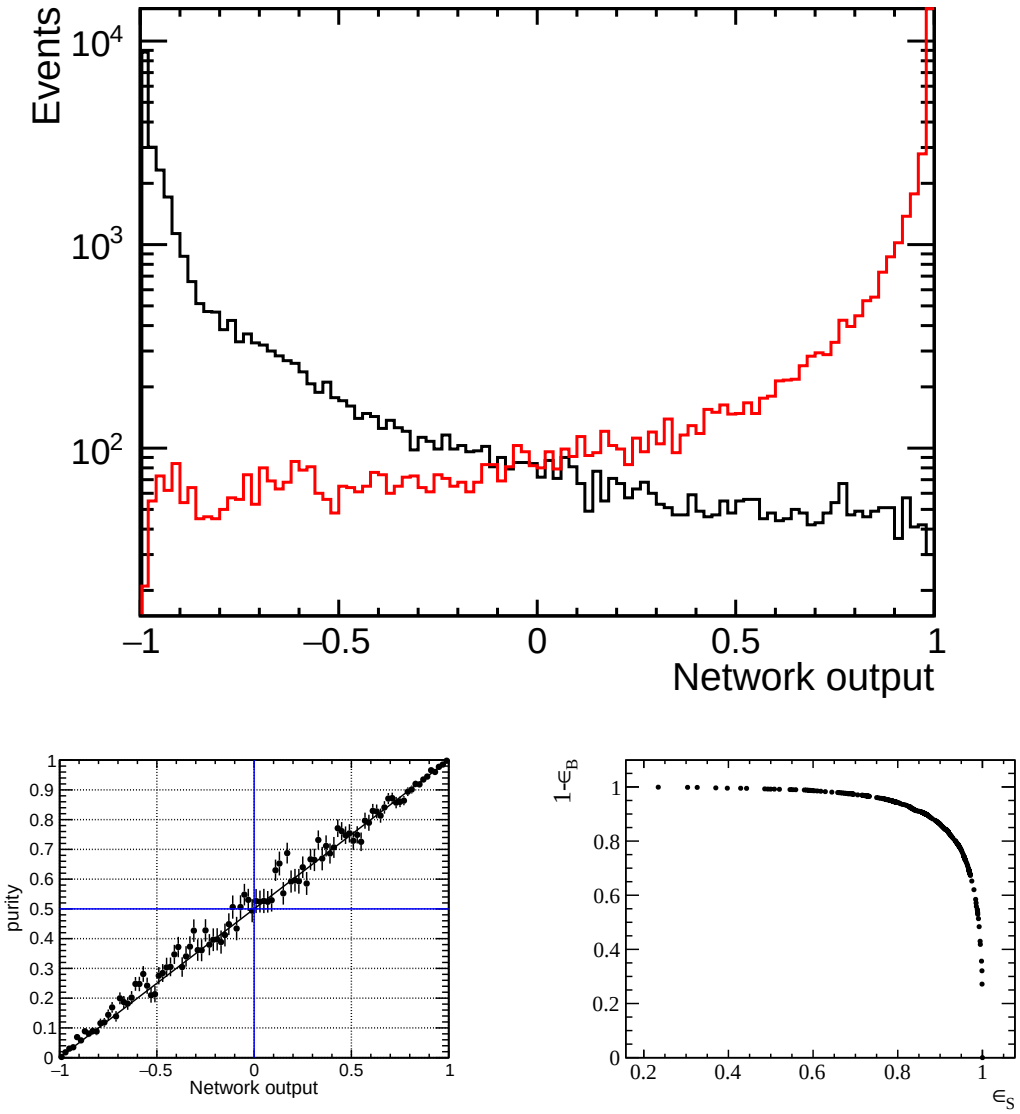

Figure 4.5: (Top) Separation of signal (red histogram) and combinatorial background (black histogram) using the NN. (Bottom left) Purity of the sample as a function of the NN output. (Bottom right) the ROC curve (black line). In the ROC curve, ϵ_B and ϵ_S represent the background and signal efficiencies. All results are obtained using the NN for the Run1 samples. The optimal point is found to be NNcut = 0.15.

4.3 Background subtraction

After the full selection is applied to data, a small fraction of background candidates still remains, which should either be removed or statistically subtracted. The statistical subtraction of background is performed by assigning appropriate weights to the candidates so that the contribution of the background cancels statistically. A simple example of this case, usually referred as sideband-subtraction, is presented below. In this simplified version of cancelling the contribution of the background, the invariant mass of the $\Lambda_b^0 \to \Lambda\mu^+\mu^-$ is divided into several regions, illustrated in figure 4.6. As a first step, a window is defined around the signal peak where most of the signal resides, *i.e.* the **D+C** region in this example, while the upper sideband, *i.e.* the **B** area, defined as the region to the right of the signal window and the lower sideband, *i.e.* the **A** area, defined as the region to the left of the signal window are dominated by combinatorial background. In order to remove statistically the contribution of the **C** band which represents the contribution of the combinatorial background in the signal window, the $m(p\pi^-\mu^+\mu^-)$ distribution which is used as discriminating variable is fitted. The parametric model that is used to describe the invariant mass distribution in this example consists of a signal and a combinatorial background component. The lineshapes of the components and the relevant yields are extracted from an unbinned likelihood fit to data, which finally leads to the determination of the number of candidates that reside in each band. Finally, in the determination of the moments, the candidates take proper weights relative to the region that they reside, *i.e.* $w^{(e)} = -N_C/(N_A + N_B)$ and $w^{(e)} = 1$ for candidates

in **A**, **B** and **C+D** bands respectively. In this analysis, the background subtraction is performed by using the *sPlot* technique [101], where the rough definition of the signal window and side bands is not used and weights are now computed in a more sophisticated way. In the *sPlot* technique, the weights are not binary-like as before, but vary depending on the likelihood of the candidate being either signal or background, allowing signal candidates that extend into side band regions to also be considered. The weights are called sWeights and have weights larger than one in the signal region that gradually become smaller when moving away from the signal peak, becoming negative in the the upper and lower sidebands. In this technique, the discriminant variable is the invariant mass of the candidates and it is assumed that there are no correlations between the angles. Both the sideband subtraction method and the *sPlot* technique are widely used to remove statistically the contribution of the background. However, since in the *sPlot* technique the sWeights are derived in a more "natural" way compared to the former method and without introducing any bias in the estimation of moments (see section 4.7), the latter technique is considered to be more appropriate and so adopted in this work.

4.3.1 Invariant mass fits

In order to compute the sWeights the Probability Density Function (PDF) that describes the invariant mass distribution of the $\Lambda_b^0 \to \Lambda\mu^+\mu^-$ in data needs to be modelled. The PDF is described using the sum of three components, which represent the contribution from the signal, the combinatorial and peaking background

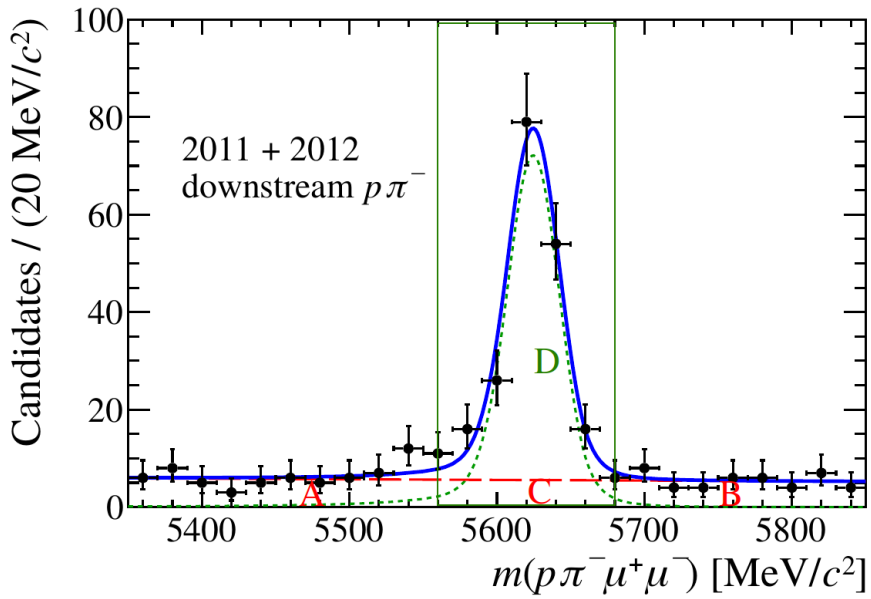

Figure 4.6: Invariant mass distribution of the rare mode for the DD category in 2011 + 2012 data. Overlaid are the projections of the fitted components. The blue solid line represents the total lineshape, while the red and green dotted lines represent the contribution of the signal and background. The signal window, *i.e.* 60 MeV/c^2 around the peak is shown by the green box. The **A**, **C** and **B** bands represent the contribution of the combinatorial background in the different regions, while the **D** region represents the contribution of the signal candidates.

candidates (the modelling of the various components is discussed in section 4.3.3). In this case, the peaking background component describes the contribution from the $B^0 \to K^0_S(\to \pi^+\pi^-)\mu^+\mu^-$ and $B^0 \to K^0_S(\to \pi^+\pi^-)J/\psi(\to \mu^+\mu^-)$ decays for the rare and control modes respectively that are misreconstructed, *i.e.* the π^+/π^- is reconstructed as a $p/\bar{p}$. The peaking background component for the rare mode is found not to contribute, the same also holds for the LL candidates of the control mode. For these cases, the peaking background component is excluded from the description of the PDF. To extract the parameters that fully describe the lineshape of the PDF[2] and the relevant yields, an extended unbinned likelihood fit is performed.

[2]As discussed in section 4.3.3, a set of these parameters is determined from a fit to MC samples and are fixed in the final fit applied to data.

The likelihood is defined as

$$\mathcal{L} \equiv e^{-(N_{\rm Sig}+N_{\rm Comb}+N_{\rm Peak})} \times \prod_{e=1}^{N} [N_{\rm Sig} P_{\rm Sig}(m^{(e)}) + N_{\rm Comb} P_{\rm Comb}(m^{(e)}) + N_{\rm Peak} P_{\rm Peak}(m^{(e)})] \ , \tag{4.6}$$

where, N_{Sig} ($P_{Sig}(m)$), N_{Comb} ($P_{Comb}(m)$) and N_{Peak} ($P_{Peak}(m)$) represent the number (PDF component) of signal, combinatorial and peaking background candidates.

4.3.2 Fit strategy

In both the rare and the control modes the parametric models that are used to describe the various contributions contain a significant number of parameters. As the values of some of these parameters are not very constrained by the data, a two-step approach is necessary. The first step uses simulated data to determine values that are then fixed in subsequent fits to data. These parameters (see section 4.3.3) are those that affect the lineshape of the signal contribution for both the rare and control modes, and all the parameters that describe the lineshape of the peaking background. In the second step, a fit to the control mode data is made to extract the rest of the parameters that describe the line shape of the invariant mass distribution. In this case, a discrepancy in the resolution of the Gaussian core between the MC and data of order 10% is observed, which can be quantified as $c \equiv \frac{\sigma_{\Lambda_b^0 \to J/\psi\,\Lambda\rm data}}{\sigma_{\Lambda_b^0 \to J/\psi\,\Lambda\rm MC}}$. Finally, for the fit of the rare mode to data, the same process as in the control mode is followed, but additionally fixing the resolution to $\sigma_{\Lambda_b^0 \to \Lambda\mu^+\mu^-\rm data} \equiv c \times \sigma_{\Lambda_b^0 \to \Lambda\mu^+\mu^-\rm MC}$

and the mean of the Gaussian core to the value obtained for the control mode. All the fits are performed using the RooFit toolkit [102].

4.3.3 Mass components

The PDF ($P_{Sig}(m)$) that describes the $m(p\pi^-\mu^+\mu^-)$ distribution of the signal candidates is modelled using the sum of two Crystal Ball (CB) functions [103, 104] with left and right tails relative to the signal peak. The CB function can be realised as a Gaussian core with a power-law tail. The exact description of the CB_l, *i.e.* with a power-law tail placed on the left side of the Gaussian core, can be expressed as,

$$CB_l(m;\alpha_l,n_l,m_0,\sigma) = \begin{cases} \exp\left(-\frac{(m-m_0)^2}{2\sigma}\right) & \text{if } \frac{(m-m_0)}{\sigma} \geq -|\alpha_l|, \\ A(n_l,\alpha_l)\left(B(n_l,\alpha_l) - \frac{(m-m_0)^2}{\sigma}\right)^{-n_l} & \text{if } \frac{(m-m_0)}{\sigma} < -|\alpha_l|, \end{cases} \tag{4.7}$$

where m is the $m(p\pi^-\mu^+\mu^-)$, σ (m_0) is the width (mean) of the Gaussian core, n_l is the power-law coefficient and α_l defines the point at which the transition between the Gaussian and the power-law behaviour takes place. The description of the functions A and B can be found in Ref. [103, 104]. The $P_{Sig}(m)$ is described as the sum of two CB functions CB_l and CB_r having a common mean and width, and can be expressed as,

$$P_{\text{Sig}}(m) = f_l\, CB_l(m;m_0,\sigma,\alpha_l,n_l) + (1-f_l)\, CB_r(m;m_0,\sigma,\alpha_r,n_r)\,, \tag{4.8}$$

where f_l represents the fractional contribution of the CB_l. The $\alpha_{l,r}$, $n_{l,r}$ (tail parameters) and f_l are fixed from fits to MC samples for both modes. An example of the fit to the MC sample of the rare mode for $2011 + 2012$ conditions using the DD candidates is illustrated in figure 4.7. The main background for

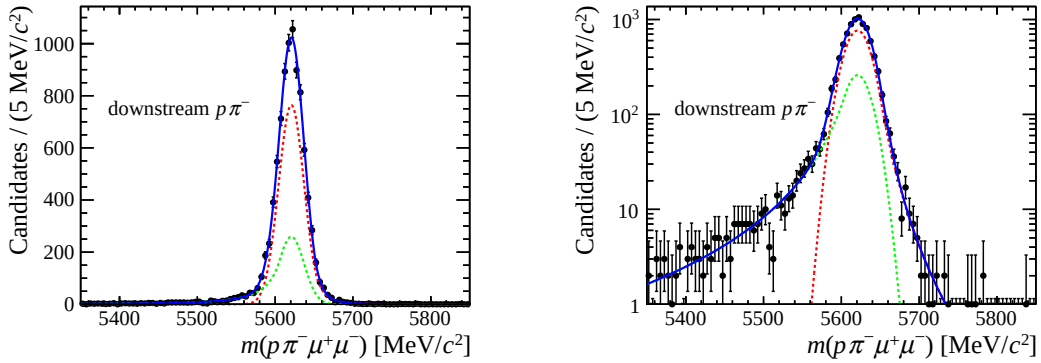

Figure 4.7: Invariant mass of the rare mode in 2011+2012 MC using DD candidates. Overlaid are the projections of the fitted components. The blue line represents the total contribution, while the red and green dotted lines present the contributions of the CB_r and CB_l respectively. The same fit is illustrated using linear (left) and logarithmic (right) scales.

both modes is the combinatorial background which is parametrised with a simple exponential function ($P_{Comb}(m)$), the slope of which is allowed to vary freely in the fits to data. For the control mode in the DD category, the misreconstructed $B^0 \to K^0_S(\to \pi^+\pi^-)J/\psi(\to \mu^+\mu^-)$ contribution is present in the data and an additional component ($P_{Peak}(m)$) is included in the total PDF. The PDF which is chosen to describe the latter contribution is a single CB function, with a power-law tail on the right side of the Gaussian core. The parameters of the CB_r are determined from a fit to MC samples and all of these are fixed in the final fit of the total PDF to the data. An example of the fit for the DD category on $2011 + 2012$ MC is illustrated in figure 4.8, while an example of a fit of the invariant mass of $\Lambda_b^0 \to J/\psi\Lambda$ to data for the DD and LL categories is illustrated in figure 4.9, using the $2011 + 2012$ data

sample for the DD and LL categories. As seen in figure 4.9 for the DD category, the peaking background component pollutes the lower sideband, forming a shoulder-like shape.

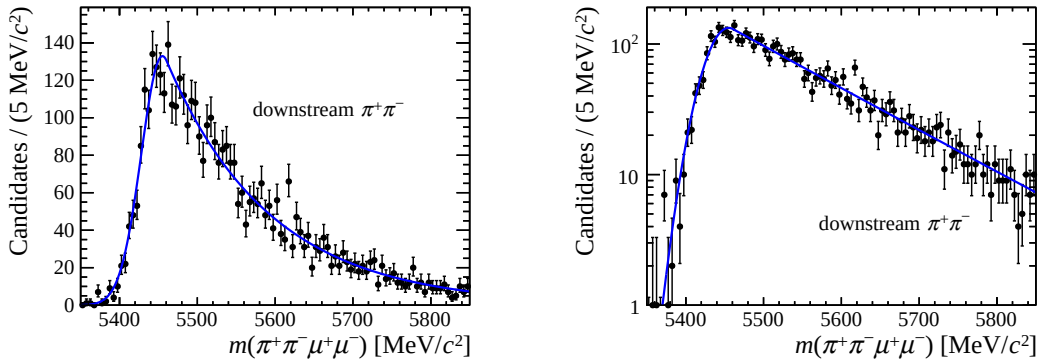

Figure 4.8: Invariant mass of misreconstructed $B^0 \to K_s^0(\to \pi^+\pi^-)J/\psi(\to \mu^+\mu^-)$ candidates in $2011+2012$ MC using DD candidates. Overlaid are the projections of the fitted components. The blue line represents the total contribution of the CB_r function. The fit is illustrated in a linear (left) and logarithmic (right) scale.

4.3.4 Fit to $\Lambda_b^0 \to \Lambda\mu^+\mu^-$ candidates

Fits to the invariant mass distributions of $\Lambda_b^0 \to \Lambda\mu^+\mu^-$ candidates for both DD and LL candidate categories are illustrated in figures 4.10, 4.11 and 4.12, while the estimates of the floating parameters in the fit are presented in table 4.3. The fit results in 610 signal candidates for the $2011+2012+2015+2016$ data set including both track categories.

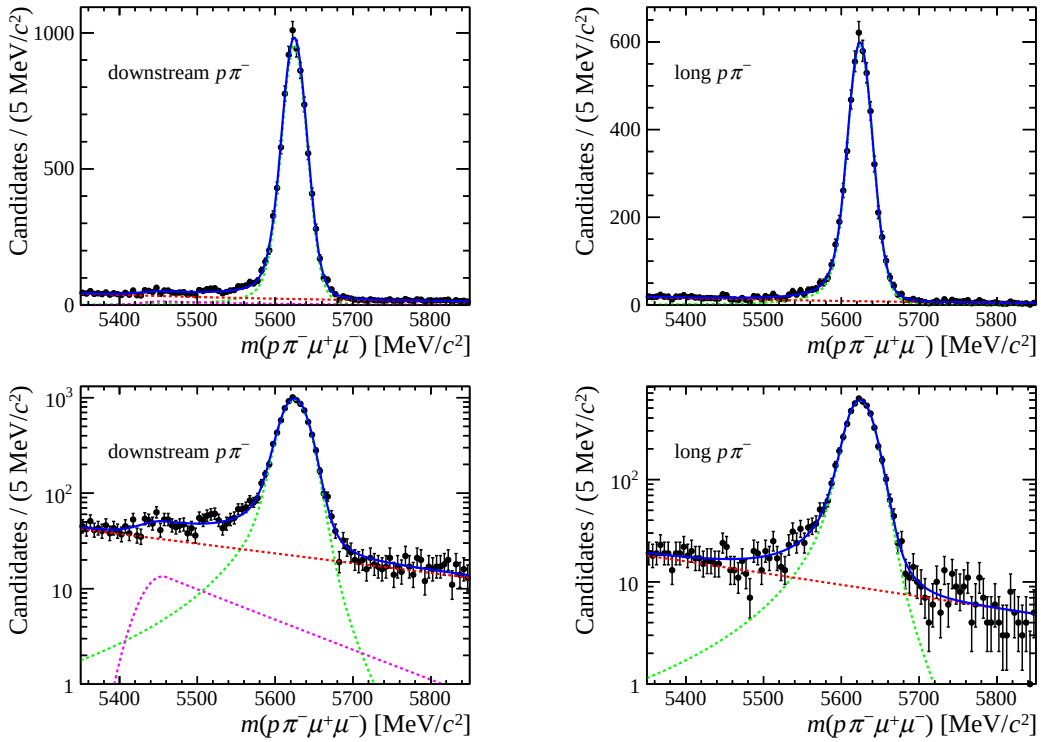

Figure 4.9: Invariant mass distribution of $\Lambda_b^0 \to J/\psi\Lambda$ for DD (top left) and LL (top right) categories in 2011 + 2012 data samples. Overlaid are the projections of the fitted components. The blue line represents the total contribution of the mass components, while the red and green dotted lines represent the contribution of the combinatorial and signal components respectively. The magenta dotted line represents the contribution from the peaking background. The same plots are illustrated in logarithmic scale in the bottom left (DD category) and right (LL category) figures.

Decay Mode (Track Type)	N_{Sig}	N_{Comb}	c_{exp}
$\Lambda\mu^+\mu^-$ (LL)(2011 + 2012)	120 $\pm$13	134 $\pm$13	0.0001 $\pm$0.0006
$\Lambda\mu^+\mu^-$ (DD)(2011 + 2012)	175 $\pm$15	140 $\pm$14	$-$0.0002 $\pm$0.0006
$\Lambda\mu^+\mu^-$ (LL)(2015)	19 $\pm$5	45 $\pm$7	$-$0.0006 $\pm$0.0010
$\Lambda\mu^+\mu^-$ (DD)(2015)	26 $\pm$6	42 $\pm$7	0.0006 $\pm$0.0010
$\Lambda\mu^+\mu^-$ (LL)(2016)	107 $\pm$12	168 $\pm$15	$-$0.0005 $\pm$0.0005
$\Lambda\mu^+\mu^-$ (DD)(2016)	163 $\pm$15	218 $\pm$17	0.0002 $\pm$0.0005

Table 4.3: Lineshape parameters of the $\Lambda_b^0 \to \Lambda\mu^+\mu^-$ mass PDF, shown separately for each of the DD and LL categories and 2011 + 2012, 2015 and 2016 samples, extracted from a likelihood fit.

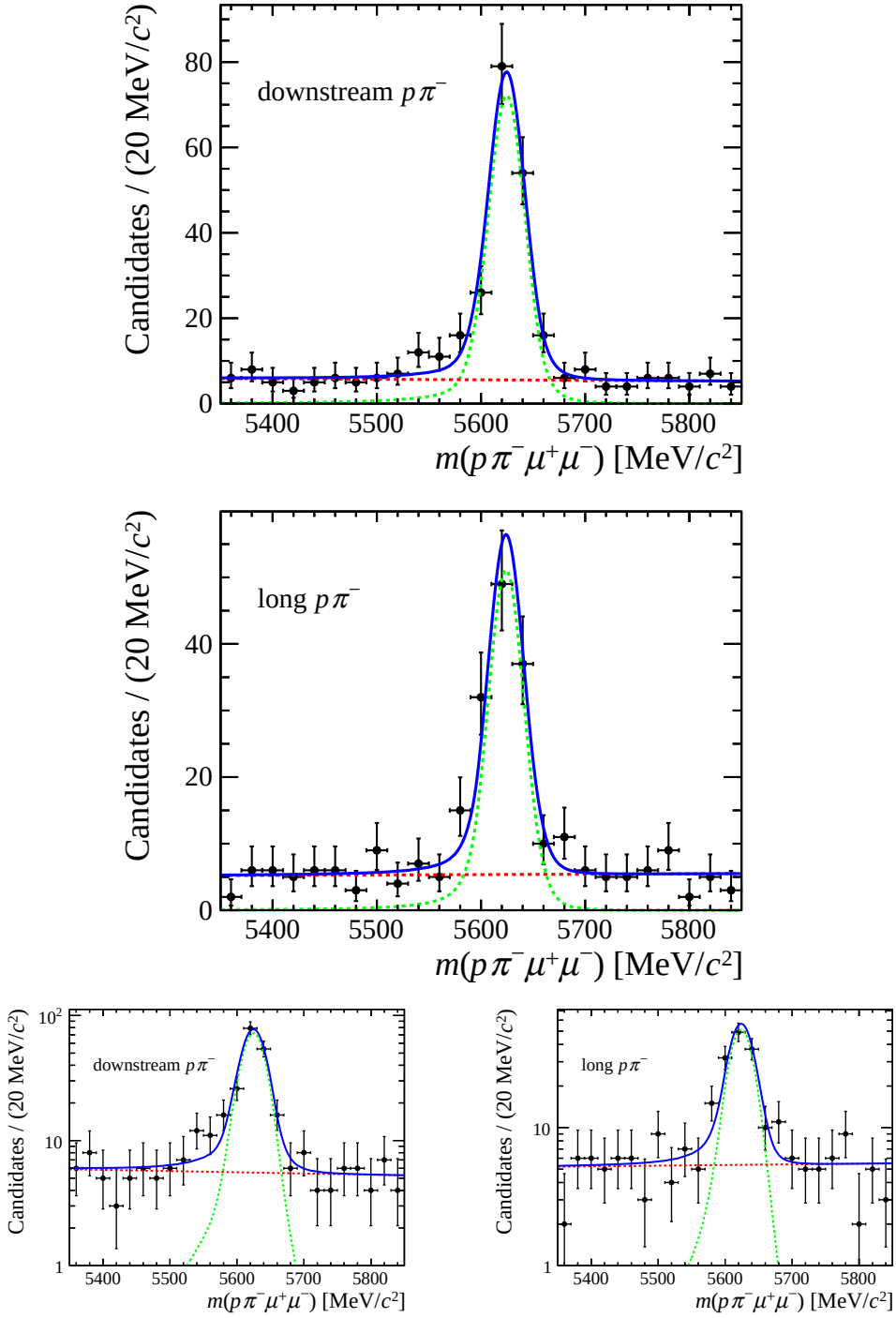

Figure 4.10: Invariant mass distribution of $\Lambda_b^0 \to \Lambda\mu^+\mu^-$ of DD (top) and LL (middle) categories in 2011+2012 data samples. Overlaid are the projections of the fitted components. The blue line represents the total contribution of the mass components, while the red and green dotted lines represent the contribution of the combinatorial and signal components respectively. The same data are presented on a logarithmic scale in the bottom left (DD category) and right (LL category) figures.

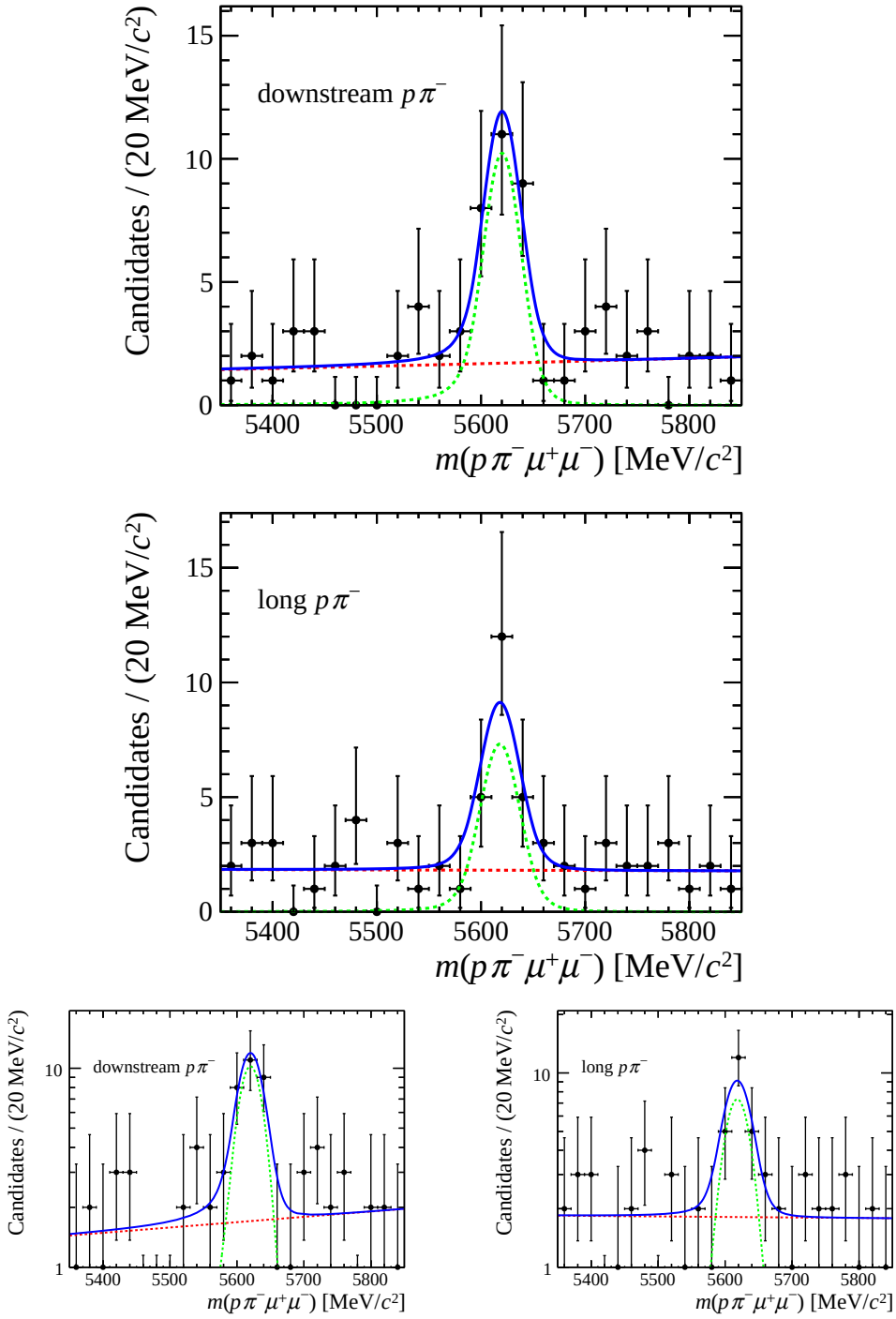

Figure 4.11: Invariant mass distribution of $\Lambda_b^0 \to \Lambda\mu^+\mu^-$ for DD (top) and LL (middle) categories in 2015 data samples. Overlaid are the projections of the fitted components. The blue line represents the total contribution of the mass components, while the red and green dotted lines represent the contribution of the combinatorial and signal components respectively. The same data are presented on a logarithmic scale in the bottom left (DD category) and right (LL category) figures. The small difference between the signal to background ratio obtained for the 2015 fits compared to Run1 is attributed to the fact that the selections are not identical, *e.g.* the NN for 2015 is trained with fewer input parameters.

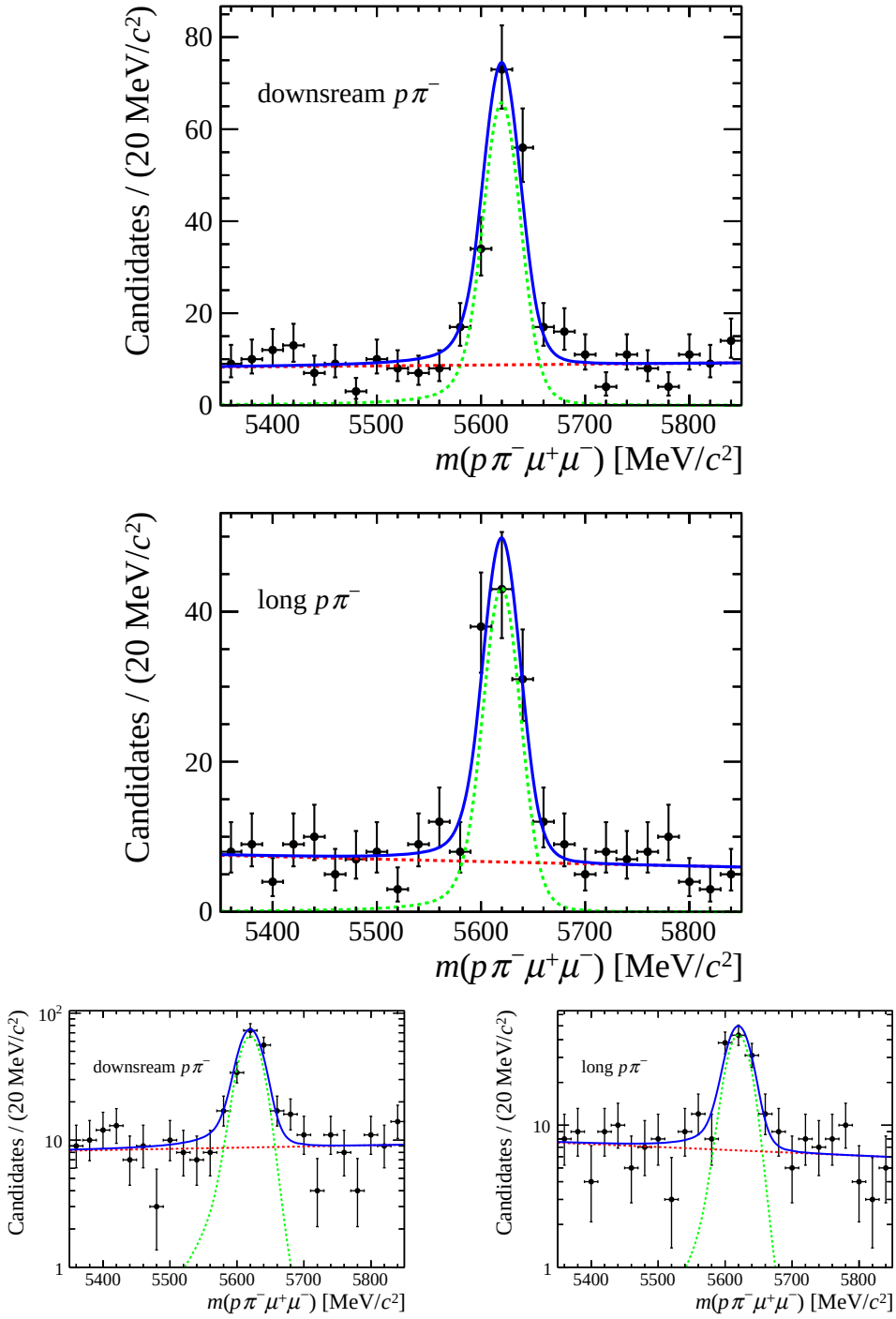

Figure 4.12: Invariant mass distribution of $\Lambda_b^0 \to \Lambda\mu^+\mu^-$ of DD (top) and LL (middle) categories in 2016 data samples. Overlaid are the projections of the fitted components. The blue line represents the total contribution of the mass components, while the red and green dotted lines represent the contribution of the combinatorial and signal components respectively. The same data are presented on a logarithmic scale in the bottom left (DD category) and right (LL category) figures. The small difference between the signal to background ratio obtained for the 2016 fits compared to Run1 is attributed to the fact that the selections are not identical, *e.g.* the NN for 2016 is trained with less input parameters.

4.4 Correction of the Monte Carlo samples

As well as being used in developing the invariant mass fits and NN training, samples of simulated data are a vital ingredient in modelling the acceptance function, which characterises the potential effects/distortions of the angular and (for the rare mode) q^2 distributions caused by the reconstruction, trigger and the subsequent selection of the candidates. In this spirit, it is particularly important to disentangle genuine distortions associated with the latter reasons from those effects due to imperfect modelling of data by the simulation. The performance of the simulation in terms of MC-data discrepancies is evaluated using a decay that has similar kinematics to the decay mode under study and where the matrix element of the decay is well known.

The MC samples used to validate and test the MC-data agreement are generated in phase-space[3], *i.e.* contain only information of the kinematics of particles and not from the matrix element that governs the decay. Since the matrix element depends on the angles and subsequently on the kinematics of the daughters, it will have an effect on the distributions of the latter. Hence, when studying the compatibility between data and MC the effect of the matrix element is investigated. The studies of the compatibility between the MC-data and the subsequent corrections are extracted using the $\Lambda_b^0 \to \Lambda(\to p\pi^-)J/\psi(\to \mu^+\mu^-)$ decay due to the large statistical size of the available samples, the similarity of their kinematics to the $\Lambda_b^0 \to \Lambda(\to p\pi^-)\mu^+\mu^-$ decay, and also due to the fact that the matrix element of the control mode is

[3]The phase-space distribution for the $\cos\theta_l$, $\cos\theta_b$, $\cos\theta$, ϕ_l and ϕ_b is flat, while the distribution of the q^2, which is relevant only for the description of the $\Lambda_b^0 \to \Lambda\mu^+\mu^-$ decay, is not (see figure 4.16).

partially known [46, 47, 56].

To correct for the observed differences between data and MC, the latter is weighted in an unbiased way to provide an accurate description of data. After identifying the variables that need to be corrected, the weights are derived in an iterative manner, *i.e.* the distribution of the N^{th} variable chosen to be corrected is weighted by the product of $N-1$ weights before an N^{th} weight that corrects the N^{th} distribution is extracted.

4.4.1 $\Lambda_b^0 \to J/\psi\,\Lambda$ decay model

The influence of the matrix element for $\Lambda_b^0 \to J/\psi\,\Lambda$ decays on the angles and subsequently the kinematics of the Λ_b^0 is studied by weighting the phase-space kinematics of the decay with the relevant decay structure. The parameters that describe the matrix element of the $\Lambda_b^0 \to J/\psi\,\Lambda$ decay are partially measured in Refs. [46, 47, 56] (in this test the LHCb measurement is used [46]). The effect of the matrix element on the kinematics of the decay is illustrated in figure 4.13.

4.4.2 MC correction

In general, reasonable agreement is found between MC and data with the main discrepancies being observed in the p_{T} of Λ_b^0, which is subsequently corrected. In addition, corrections are applied for modelling of the lifetime of Λ_b^0, the detector occupancy ($nTracks$) and the Λ_b^0 vertex χ^2. Although variables such as the lifetime

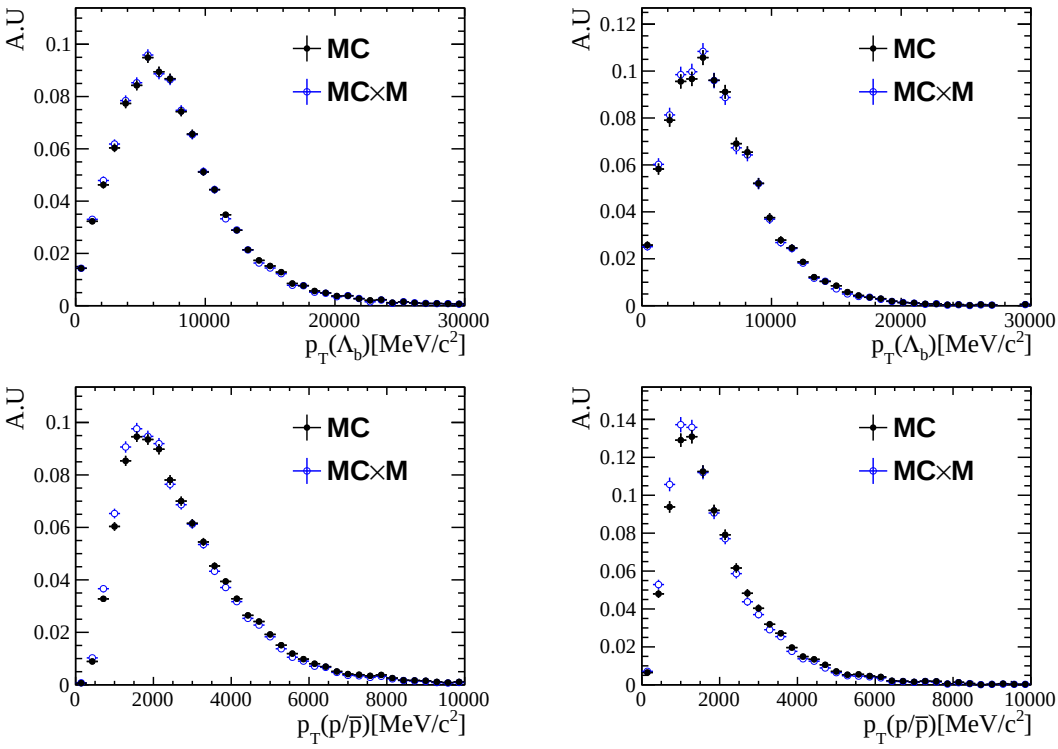

Figure 4.13: An illustration of the effect of the matrix element on the transverse momentum of Λ_b^0 (top) and proton (bottom) using DD (left) and LL (right) candidates of 2012 MC sample of the $\Lambda_b^0 \to J/\psi\Lambda$ decay. The black (blue) markers represent the transverse momentum distribution without (with) taking into account the effects of the matrix element (M).

of Λ_b^0, $nTracks$ and Λ_b^0 vertex χ^2 do not have a visible effect on angles, they are corrected to account for second order effects. In the remainder of this section I will give a brief description of the corrections extracted from the control mode and finally applied to the MC samples of the $\Lambda_b^0 \to \Lambda\mu^+\mu^-$. The corrections are determined separately for each of the track categories and data-taking periods.

In order to correct the transverse momentum of the Λ_b^0 baryon for inaccurate modelling of the production kinematics as simulated by PYTHIA, a per-event weight is

assigned to the MC events, using the following equation[4],

$$w_i^{p_{\rm T}} \equiv \frac{f_{\Lambda_b^0}}{f_d}(p_{\rm T}) \times \frac{{\rm PDF}_{\rm gen}^{B^0\to J/\psi K_{\rm S}^0}(p_{\rm T})}{{\rm PDF}_{\rm gen}^{\Lambda_b^0\to J/\psi \Lambda}(p_{\rm T})} \times \frac{{\rm PDF}_{\rm data}^{B^0\to J/\psi K_{\rm S}^0}(p_{\rm T})}{{\rm PDF}_{\rm reco}^{B^0\to J/\psi K_{\rm S}^0}(p_{\rm T})} \ . \tag{4.9}$$

Here $\frac{f_{\Lambda_b^0}}{f_d}(p_{\rm T})$ represents the $p_{\rm T}$ dependence of the fragmentation fraction. For the 2011 data-taking period, the function that describes the latter dependence is measured by LHCb [105] and takes the form,

$$\begin{aligned} \frac{f_{\Lambda_b^0}}{f_d}(p_{\rm T}) &\equiv c + \exp(d + e\cdot p_{\rm T}) \ , \\ c &= 0.151 \pm 0.016^{+0.024}_{-0.025} \ , \\ d &= -0.573 \pm 0.040^{+0.101}_{-0.097} \ , \\ e &= -0.095 \pm 0.007 \pm 0.014 \, ({\rm GeV}/c)^{-1} \ . \end{aligned} \tag{4.10}$$

The second term in equation 4.9 represents the ratio between the PDF's of $p_{\rm T}$ for the $\Lambda_b^0 \to J/\psi\Lambda$ and $B^0 \to J/\psi K_{\rm S}^0$ decays extracted using MC samples without any cuts applied. The third and final term is used to correct for the production kinematics of $p_{\rm T}$ for the B^0 meson. The correction is extracted by taking the ratio of the PDF's of $p_{\rm T}$ for background subtracted data versus MC of $B^0 \to J/\psi K_{\rm S}^0$ events. For the $B^0 \to J/\psi K_{\rm S}^0$ the matrix element is fully known and is taken into account in the MC samples. In all the cases the PDF's are described using non-parametric models, *i.e.* with 1D histograms. In this way the the production kinematics of Λ_b^0 are corrected without having to rely upon the matrix element of the $\Lambda_b^0 \to J/\psi\Lambda$ decay, which is not fully known.

[4]The definition of the abbreviations "gen" and "reco" is given in section 4.11.

The dependence of $\frac{f_{\Lambda_b^0}}{f_d}(p_{\rm T})$ in bins of transverse momentum is measured using 2011 data collected at $\sqrt{s} = 7\,\text{TeV}$. Although the lineshape of this fragmentation fraction can potentially vary with $\sqrt{s}$, the centre-of-mass-energy during 2012 data taking ($\sqrt{s} = 8\,\text{TeV}$) did not differ significantly from 2011 and so equation 4.9 can be safely used for the correction of 2012 MC samples. However, for Run2 samples the centre-of-mass-energy of the collisions almost doubled, making the applicability of equation 4.10 less obvious. To test whether equation 4.10 and the relevant values of the parameters can be used for the correction of Run2 MC samples, the ratio of efficiency corrected yields is determined in several bins of transverse momentum ($R(p_{\rm T})$) of $\Lambda_b^0 \to J/\psi\,\Lambda$ and $B^0 \to J/\psi\,K^0_{\rm S}$ decays; since $\frac{f_{\Lambda_b^0}}{f_d}(p_{\rm T}) \sim R(p_{\rm T})$, the $R(p_{\rm T})$ measurement in bins of $p_{\rm T}$ gives access to the lineshape of the fragmentation fraction as a function of $p_{\rm T}$; it is noted that only the lineshape of $\frac{f_{\Lambda_b^0}}{f_d}(p_{\rm T})$ is of interest and not the absolute scale. The $R(p_{\rm T})$ is illustrated in figure 4.14. From this study it is concluded that the $\frac{f_{\Lambda_b^0}}{f_d}(p_{\rm T})$ lineshape is compatible between Run1 and Run2 and therefore equation 4.10 can be used for the Run2 MC correction. Following the correction of the production kinematics of the Λ_b^0, the lifetime of the Λ_b^0 baryon is corrected to match the measured world-average value [7].

Remaining discrepancies observed in the $nTracks$ and the vertex χ^2 of Λ_b^0 are corrected directly using non-parametric models, *i.e.* 1D histograms obtained from the ratio of MC and background-subtracted data for the control mode. These variables are found to not have dependence on the matrix element of the decay.

An example of the effect of the MC correction on the control mode for the trans-

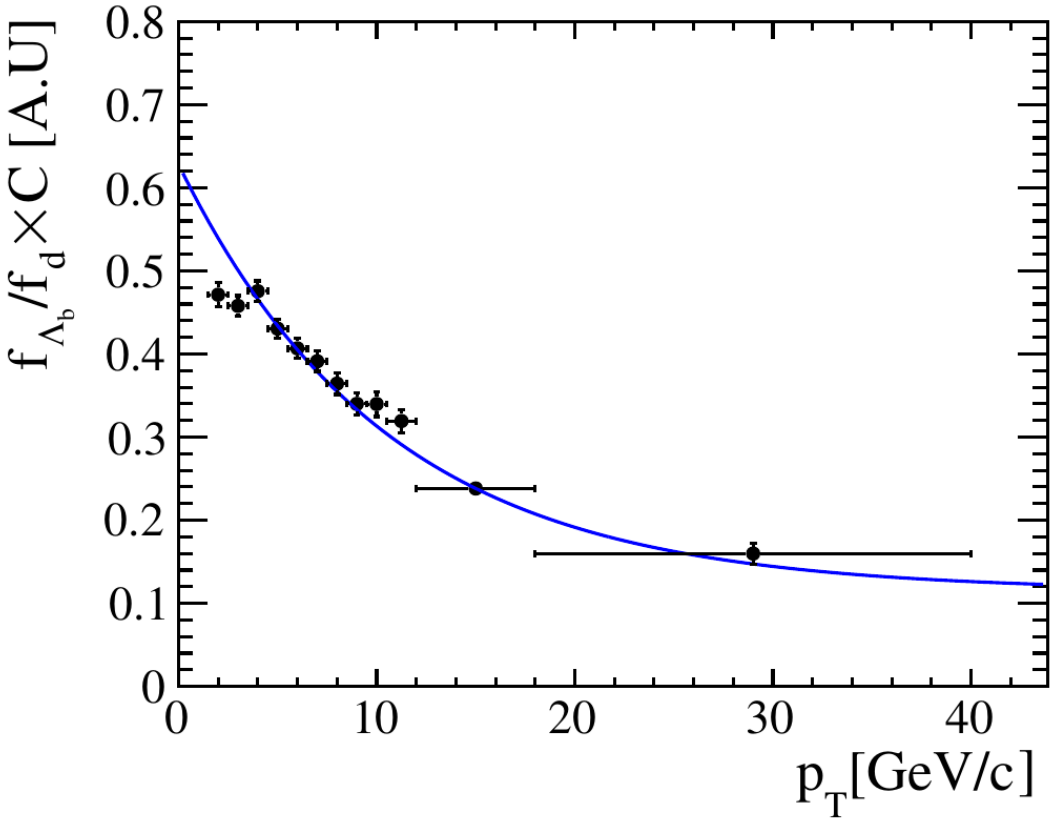

Figure 4.14: The data points represent the ratio of the efficiency corrected yields, of $\Lambda_b^0 \to J/\psi\,\Lambda$ versus $B^0 \to J/\psi\,K_S^0$ in several bins of p_T. The blue line represents equation 4.10 where the parameters are fixed to the LHCb measurement [105], but with the absolute scale floating.

verse momentum of Λ_b^0 using 2012 MC is illustrated in figure 4.15; a more detailed description is given in Appendix A.2. Other corrections related to the simulation of tracking and the muon identification are considered as potential sources of systematic uncertainty. The $\Lambda_b^0 \to J/\psi\,\Lambda$ MC samples are additionally weighted using a 2D parametric model in order to account for imperfect simulation of the `ProbNNp` variable. The parametric models are extracted using calibration samples such as $\Lambda \to p\pi^-$ and provided by a dedicated package (`PIDCalid` tool) [106].

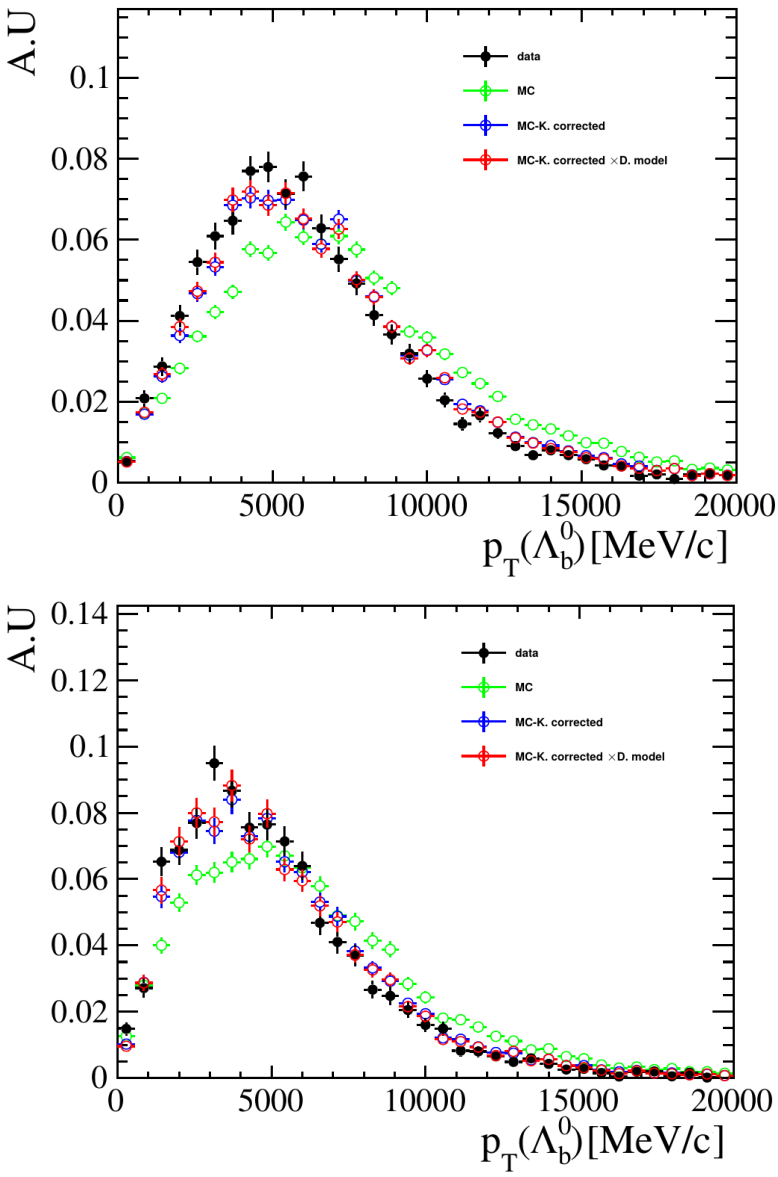

Figure 4.15: Comparison between data and MC for the $\Lambda_b^0 \to J/\psi\,\Lambda$ decay in 2012 data-taking conditions for Λ_b^0 p_{T} using the DD (top) and LL (bottom) categories. The black data points represent the background-subtracted data, the green points the MC, the blue and red markers correspond to the corrected MC and corrected MC $\times$ the decay structure of $\Lambda_b^0 \to J/\psi\,\Lambda$.

4.5 Determination of the relative efficiency

The kinematics of the decays products, through which the angles and the q^2 (for the rare mode) are reconstructed, may be distorted by the trigger, reconstruction and selections made. To correct for these effects, events are weighted with the inverse of a parametric model[5], the so-called efficiency or acceptance function. The efficiency function can be realised as a model that parametrises all of the distortions in q^2 and angles. The efficiency model is described in six-dimensions, *i.e.* the q^2 of the dimuon system and the five angles, using Legendre polynomials (LP)[6]; differences between the reconstructed kinematics of particles originating from the decay of the Λ_b^0 and $\overline{\Lambda}_b^0$ are ignored. The parameters that fully describe the shape of the efficiency model are estimated using the method of moments. The efficiency model can be described in a general way as, $\epsilon \equiv f^{reco}/f^{gen}$, where the f^{gen} and f^{reco} represent models that parametrise the angular and q^2 distributions before and after the trigger, reconstruction and selection are applied. In this spirit, parametric models can be used for the description of f^{reco} and f^{gen}; since the angular distribution of f^{gen} is flat the latter function is reduced to $f^{gen} = q^{2,gen}$, where the distribution of $q^{2,gen}$ is illustrated in figure 4.16. For simplicity, the angular and q^2 distributions after triggering, reconstruction and the full selection are weighted with the inverse of $q^{2,gen}$, resulting in a simplified description of the efficiency model, $\epsilon \equiv f^{reco}$.

To describe the efficiency model, simulated signal candidates outside of the $15 <$

[5] A non-parametric model, *i.e.* a multidimensional histogram, can also be used.

[6] It must be noted that the efficiency function can also be parametrised in terms of other orthogonal bases, such as using a combination of sine and cosine terms; this is can be useful for the $\phi_{l,b}$ but not for the rest parameters.

$q^2 < 20\,\mathrm{GeV}^2/c^4$ range are also used to increase the statistics of the MC sample and allow a more sophisticated description of the efficiency function. The disadvantage of this is that more complicated correlations between the relevant dimensions are introduced, through correlations with the q^2 distribution. A compromise between the increase of the statistical power of the MC samples and the inclusion of additional correlations is found by using candidates in the range of $11 < q^2 < 20\,\mathrm{GeV}^2/c^4$, for the parametrisation of the efficiency model. The latter is described separately for $2011 + 2012$, 2015 and 2016 data-taking years and for the different track categories. The MC samples are weighted using per-event (r) weights defined as, $w^r \equiv w^r_{MC} \times w^r_{q^{2,gen}}$, in order to include the $q^{2,gen}$ distribution and account for the MC-data discrepancies (as discussed in section 4.4).

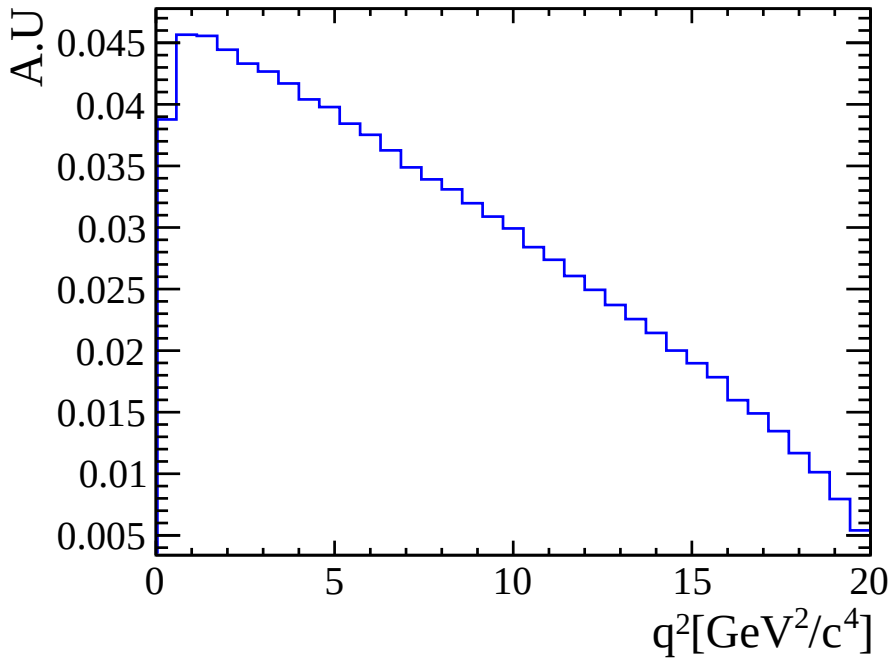

Figure 4.16: Phase-space distribution of q^2 for the $\Lambda_b^0 \to \Lambda\mu^+\mu^-$ decays, without any cuts.

4.5.1 Parametrisation of the efficiency model

The model of the efficiency function in the general case of the N dimensions can be written in terms of LP as,

$$\epsilon(x_1, ..., x_N) = \sum_i ... \sum_n c_{i,...,n} P_i(x_1) \times ... \times P_n(x_N) \ , \tag{4.11}$$

where the $P_i(x_k)$ are the LP of order i, while the x_k are defined in the domain of $-1 \leq x_k \leq 1$. The polar angles *i.e.* the $\cos\theta_l$, $\cos\theta_b$ and $\cos\theta$ are by construction defined in the range $-1 \leq x_k \leq 1$, but not the ϕ_l, ϕ_b and the q^2 parameters; the latter are transformed to match the domain defined previously. To estimate the coefficients $c_{i,...,n}$ that describe the shape of the efficiency model, the orthogonality properties of the LP, which satisfy the condition,

$$\int_{-1}^{1} P_i(x_k) P_j(x_k) dx_k = \frac{2}{2i+1} \delta_{ij} \ , \tag{4.12}$$

are exploited. The coefficients are estimated by computing the normalised moments,

$$\widetilde{M}_{i,..,n} = \frac{1}{N_e} \sum_{r=1}^{N_e} P_i(x_1^r) \times ... \times P_n(x_N^r) \, , \tag{4.13}$$

where N_e represents the total number of entries (or in the case of weighted MC, the sum of weights) in the MC sample. The estimated moments, *i.e.* $\widetilde{M}_{i,..,n}$, as defined

in equation 4.13, can be matched to the efficiency model according to

$$M_{i,..,n} = \frac{1}{\kappa}\int_{-1}^{1}...\int_{-1}^{1}\epsilon(x_1,...,x_N)P_i(x_1)\times...\times P_n(x_N)dx_1\times...\times \mathrm{d}x_N \ , \qquad (4.14)$$

where,

$$\kappa = \int_{-1}^{1}...\int_{-1}^{1}\epsilon(x_1,...,x_N)\mathrm{d}x_1\times...\times \mathrm{d}x_N = 2^N c_{0...0} \ . \qquad (4.15)$$

By expanding the $\epsilon(x_1,...,x_N)$ as defined in equation 4.11, the normalised moments can be expressed as,

$$M_{i,..,n} = \frac{1}{2^N c_{0..0}}\int_{-1}^{1}...\int_{-1}^{1}\sum_{i'}...\sum_{n'}c_{i',...,n'}P_{i'}(x_1)\times...\times P_{n'}(x_N)\times$$
$$P_i(x_1)\times...\times P_n(x_N)dx_1\times...\times \mathrm{d}x_N \ . \qquad (4.16)$$

Taking into account the orthogonality properties of the LP, equation 4.14 is finally expressed as,

$$M_{i,..,n} = \frac{c_{i,...,n}}{2^N c_{0..0}}\Big(\frac{2\delta_{i'i}}{2i+1}\times...\times\frac{2\delta_{n'n}}{2n+1}\Big) \ . \qquad (4.17)$$

The $c_{i,...,n}$, in terms of the estimated moments, then take the following form,

$$c_{i,...,n} = c_{0...0}\widetilde{M}_{i,..,n}(2i+1)\times...\times(2n+1) \ . \qquad (4.18)$$

The model that is described above can be used to parametrise a distribution of arbitrary shape in N dimensions. In the case of weighted distributions, equation 4.13,

will be transformed to,

$$\widetilde{M}_{i,..,n} = \frac{1}{\sum_{r=1}^{N_e} w^r} \sum_{r=1}^{N_e} w^r \times P_i(x_1^r) \times ... \times P_n(x_N^r), \tag{4.19}$$

Equation 4.11 for $\Lambda_b^0 \to \Lambda\mu^+\mu^-$ (six dimensions) and $\Lambda_b^0 \to J/\psi\,\Lambda$ (five dimensions, as q^2 is omitted) can be expressed as defined in equations 4.20 and 4.21 respectively. It must be noted that in the previous definition, $M_{0...0} = 1$ by definition and $c_{0...0}$ cannot be measured and so is set to the arbitrary value of one.

$$\begin{aligned}\epsilon(\cos\theta_l, \cos\theta_b, \cos\theta, \phi_l, \phi_b, q^2) = &\sum_i \sum_j \sum_k \sum_l \sum_m \sum_n c_{i,j,k,l,m,n} \\ &P_i(\cos\theta_l) \times P_j(\cos\theta_b) \times P_k(\cos\theta) \\ &\times P_l(\phi_l) \times P_m(\phi_b) \times P_n(q^2)\end{aligned} \tag{4.20}$$

$$\begin{aligned}\epsilon(\cos\theta_l, \cos\theta_b, \cos\theta, \phi_l, \phi_b) = &\sum_i \sum_j \sum_k \sum_l \sum_m c_{i,j,k,l,m} \\ &P_i(\cos\theta_l) \times P_j(\cos\theta_b) \times P_k(\cos\theta) \\ &\times P_l(\phi_l) \times P_m(\phi_b)\end{aligned} \tag{4.21}$$

In the limit of infinitely large MC samples used to estimate the coefficients that govern the shape of the efficiency function, the efficiency models described above can be used directly. However, the available MC samples have large but finite size, resulting in points of the phase-space being poorly populated, especially in regions where the efficiency is very low. Using high orders of polynomials for the description

of the efficiency model in this case can lead to points in the phase-space where the efficiency model may oscillate to negative values, resulting in both zero and negative weights, which are clearly problematic. To work around this effect, the efficiency model is built in several stages. In the first stage, the efficiency model is constructed by performing parametrisations in 1D for each of the six-dimensions and determining per-event weights defined as,

$$w(x_1, ..., x_N) = \frac{1}{\sum_i c_i P_i(x_1) \times ... \times \sum_i c_n P_n(x_N)} \ . \tag{4.22}$$

The order of the LP that are used for the first stage of modelling the efficiency are illustrated in table 4.4. The same orders are used for both the rare and control modes. For the latter, the order of polynomials for the q^2 are set to zero and the weights for the $q^{2,gen}$ are set to unity. The weights defined in equation 4.22 are then applied to the MC sample, before the second stage starts, where 2D correlations between the subspaces are identified and parametrised. The 2D corrections correspond to parametrisations between pairs of $\cos\theta_l$, $\cos\theta$, ϕ_l and q^2 using up to four orders of polynomials for each dimension. Equivalent weights are extracted for the 2D corrections in a similar way as defined in equation 4.22 and used to further weight the MC samples. Finally a 6D parametrisation using only LP of the first order for all six dimensions is performed. This procedure can be implemented as an iterative way of parametrising a multidimensional space, where in each iteration the multidimensional space becomes simpler allowing lower orders of polynomials to be used.

Variable	Orders (DD)	Orders (LL)
$\cos\theta_l$	5	5
$\cos\theta_b$	5	5
$\cos\theta$	5	5
ϕ_l	8	8
ϕ_b	8	8
q^2	5	5

Table 4.4: Orders of polynomials used to parametrise the 1D projections of the efficiency function.

4.5.2 Projections of the efficiency model

To test the robustness of the efficiency parametrisation, events are generated from the efficiency models and compared with the weighted MC sample; an example of 1D and a small collection of 2D projections of the angles and q^2 distributions are given in figures 4.17 and 4.18 respectively, using the efficiency model and MC samples from the 2011 + 2012 DD category. A more complete description of the 1D projections of the efficiency models is given in Appendix A.3. A very good agreement between the efficiency models and the weighted MC samples is observed.

As discussed previously, the angular and q^2 distributions are correlated. To further validate that correlations between the relevant dimensions are properly modelled through the efficiency function, the behaviour of the efficiency model in 1D projections for several bins of each variable is tested; as an example the 1D projections of $\cos\theta_l$ in bins of $\cos\theta$, using the same efficiency model and MC sample as before is illustrated in figure 4.19.

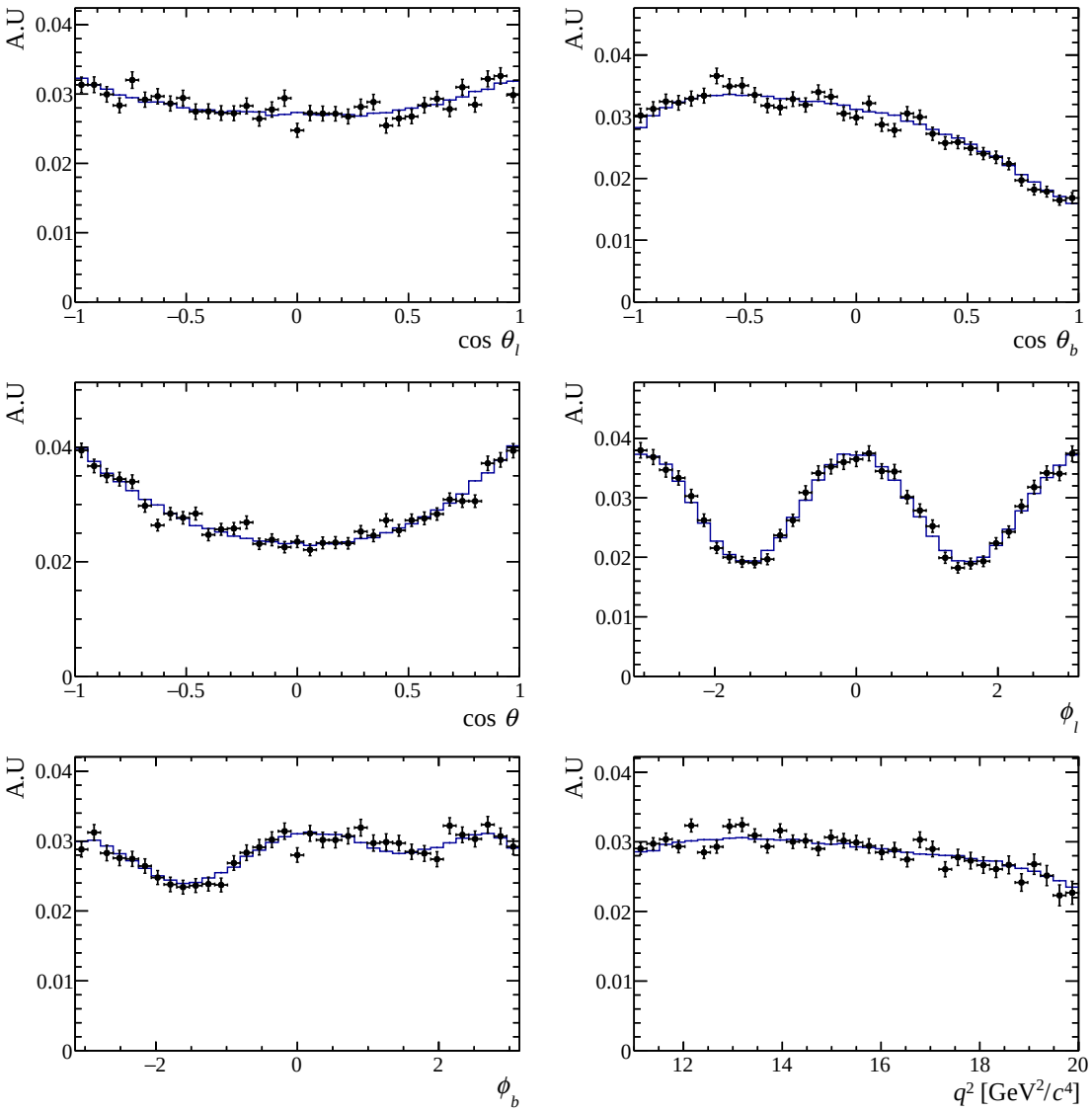

Figure 4.17: 1D efficiency projections of 2011 + 2012 MC for the DD category. The black data points represent the weighted MC sample, while the blue line the efficiency model. The dominant features, such as the oscillation in the azimuthal angles, originate mainly from momentum cuts applied to the muons and hadrons respectively, while the asymmetries observed in the hadron-related angles are due to the mass difference of the proton and pion.

4.5.3 Distribution of the efficiency weights

It is particularly important to test the distribution of the efficiency weights ($w^e \equiv 1/\epsilon(\vec{\Omega}, q^2)^e$) in the data sample. The efficiency weights enter the formula which determines the evaluation of moments, and consequently the determination of the

statistical uncertainties, through the bootstrapping distributions. Events with extremely large weights, which can result from points in the phase-space that have an efficiency very close to zero, are, in principle, extremely unlikely to appear in data. However, it is not so unlikely that background events will acquire large weights. These events can cause a significant bias in the determination of the moments and the associated statistical uncertainties. The study showed that the RMS of the distribution of the efficiency weights is very small and no events with extreme weights appear, an example of the efficiency weights for the DD and LL categories of the $2011 + 2012$ data is illustrated in figure 4.20.

4.5.4 Testing the efficiency model with phase-space Monte Carlo

As discussed earlier, the efficiency models are built using phase-space MC samples after the full selection is applied, corrected for MC-data discrepancies as described in section 4.4 and additionally weighted with the inverse of the phase-space of the $q^{2,gen}$ distribution, evaluated using the 1D histogram illustrated in figure 4.16 (see section 4.5 for how the phase-space of the $q^{2,gen}$ enters the determination of the efficiency model for the rare mode). By construction, if the efficiency model perfectly describes the MC used to extract the coefficients of the acceptance function, weighting additionally the MC with the inverse of the efficiency function will transform the MC into a 6D uniform distribution. To test this method, a 6D uniform distribution is generated from which the 34 K_i moments are extracted. The extraction of moments is then also performed using the weighted MC used to extract

the efficiency models, which is additionally weighted with $w^e \equiv 1/\epsilon(\vec{\Omega}, q^2)^e$. Finally the moments evaluated from the two different samples are compared. The results of this test using the 2011 + 2012 MC samples for the DD and LL categories are presented in figure 4.21. The test showed that the moments extracted from the two different samples are compatible, indicating that the efficiency models are properly parametrised.

4.5.5 Testing the efficiency model with $B^0 \to J/\psi\, K_S^0$ decays

To validate both the procedure used to model the efficiency function and the framework through which the moments and the statistical uncertainties are evaluated, the $B^0 \to J/\psi\, K_S^0$ decay is used. This decay mode has a similar topology to the $\Lambda_b^0 \to \Lambda\mu^+\mu^-$ but a simpler differential decay rate, which depends only on $\cos\theta_l$ and is defined as

$$\frac{\mathrm{d}\Gamma}{\mathrm{d}\cos\theta_l} = \frac{3}{4}(1 - \cos^2\theta_l) \ , \tag{4.23}$$

while the rest of the angles exhibit a uniform distribution. This results in all the K_i moments being equal to zero except for K_1 which is equal to one half.

Before extracting the angular observables, the MC samples corresponding to 2011 + 2012, 2015 and 2016 for the DD and LL categories are corrected for MC-data discrepancies and finally the relevant efficiency functions are extracted in 5D, using equation 4.21. The $m(\pi^+\pi^-\mu^+\mu^-)$ distribution is used to subtract statistically the contribution of the background by assigning appropriate weights determined using

the *sPlot* technique [101].

In the fits to the invariant mass distributions, the signal component is parametrised using a double-sided Crystal Ball function [103, 104], where the tail parameters and the relevant fractional contributions of the $CB_{r,l}$ are extracted from a fit to the MC samples. The combinatorial background is parametrised by a simple exponential function, while the peaking background in this case is the contribution from the $B_s^0 \to J/\psi K_S^0$ decays. The latter contribution is parametrised with the same Crystal Ball functions used for the signal component, where the mean is shifted by the known B^0 and B_s^0 mass difference [7], while the width is shared between the signal components.

The results of the moments extraction from the combined data set of 2011 + 2012, 2015 and 2016 using both track categories are presented in table 4.5. The results for the moments are compatible with expectation. The 1D angular projections and the invariant mass distribution are illustrated in figure 4.22. It is noted that the sWeights and efficiency weights are extracted separately for each of the track categories and the data-taking periods.

4.5.6 Testing the efficiency model with the $\Lambda_b^0 \to J/\psi\Lambda$ decay

The moments can also be extracted for the $\Lambda_b^0 \to J/\psi\Lambda$ decays, which have a very similar topology to the $\Lambda_b^0 \to \Lambda\mu^+\mu^-$ decays. The background subtraction is performed using the *sPlot* technique, where the $m(p\pi^-\mu^-\mu^+)$ distribution is used as

Obs.	Numerical value	Obs.	Numerical value
K_1	0.5018 ± 0.0010	K_{21}	0.0159 ± 0.0061
K_2	-0.0037 ± 0.0020	K_{22}	0.0067 ± 0.0037
K_3	0.0004 ± 0.0015	K_{23}	-0.0092 ± 0.0049
K_4	-0.0005 ± 0.0036	K_{24}	-0.0031 ± 0.0025
K_5	0.0039 ± 0.0036	K_{25}	-0.0069 ± 0.0123
K_6	0.0014 ± 0.0032	K_{26}	-0.0005 ± 0.0067
K_7	0.0042 ± 0.0052	K_{27}	-0.0032 ± 0.0085
K_8	0.0002 ± 0.0027	K_{28}	-0.0107 ± 0.0046
K_9	-0.0028 ± 0.0043	K_{29}	-0.0009 ± 0.0051
K_{10}	0.0017 ± 0.0025	K_{30}	-0.0020 ± 0.0045
K_{11}	-0.0019 ± 0.0027	K_{31}	-0.0052 ± 0.0050
K_{12}	-0.0002 ± 0.0026	K_{32}	-0.0008 ± 0.0050
K_{13}	0.0007 ± 0.0022	K_{33}	0.0030 ± 0.0042
K_{14}	-0.0009 ± 0.0047	K_{34}	0.0061 ± 0.0043
K_{15}	-0.0009 ± 0.0042		
K_{16}	-0.0047 ± 0.0042		
K_{17}	-0.0069 ± 0.0064		
K_{18}	0.0018 ± 0.0038		
K_{19}	-0.0011 ± 0.0059		
K_{20}	-0.0033 ± 0.0034		

Table 4.5: Results for the moments using the combined $B^0 \to J/\psi K_S^0$ data set for both track categories in $2011 + 2012$, 2015 and 2016 data-taking periods. Moments that are by construction zero are highlighted with red colour.

the discriminating variable (see section 4.3.1 for the mass models). The efficiency functions are extracted in 5D using MC samples corrected for MC-data discrepancies. The 1D projections of the angles for the combined data sets of $2011 + 2012$, 2015 and 2016, using both track categories are illustrated in figure 4.24. The results are illustrated in figure 4.23 and found to be well behaved. In terms of the angular observables, moments $K_{3,6,8,10,13,16,18,20,22,24,26,28,29,31}$ are found to be in agreement with zero as expected, while moments K_{11}-K_{34} are found to be compatible between $2011 + 2012$, 2015 and 2016 data-taking periods and consistent with zero, pointing to a production polarisation of Λ_b^0 close to zero without any obvious trend with the $\sqrt{s}$.

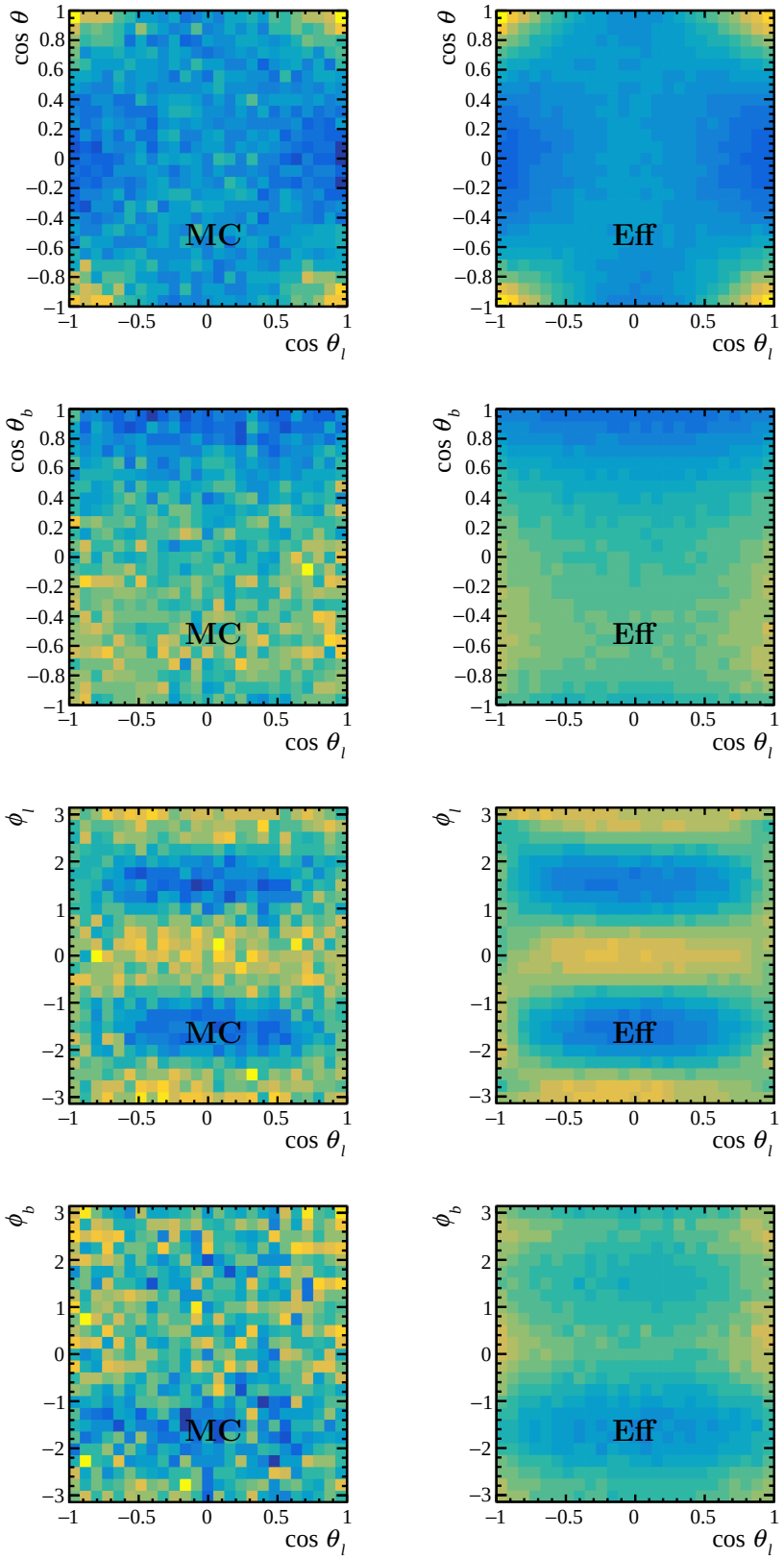

Figure 4.18: A small collection of 2D projections between $\cos\theta_l$ and the other angles, using the efficiency model and 2011 + 2012 MC for the DD category. The colour scheme is an arbitrary scale.

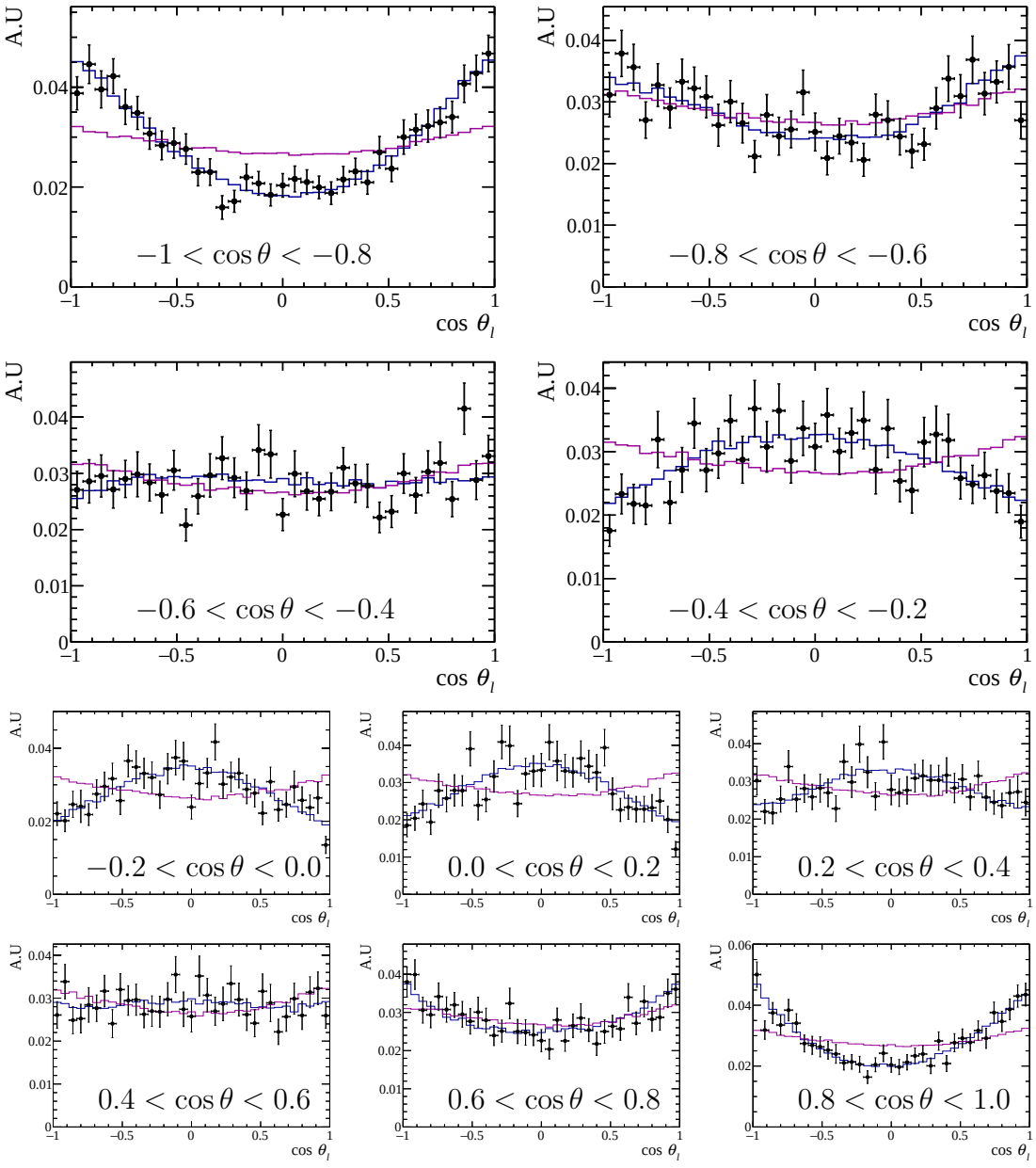

Figure 4.19: 1D efficiency projections of $\cos\theta_l$ in bins of $\cos\theta$ using 2011 + 2012 MC for the DD category. The black data points correspond to the weighted MC. The blue line represents the default efficiency model, while the magenta line the efficiency model assuming no correlations, *i.e.* using only the first step of the efficiency parametrisation.

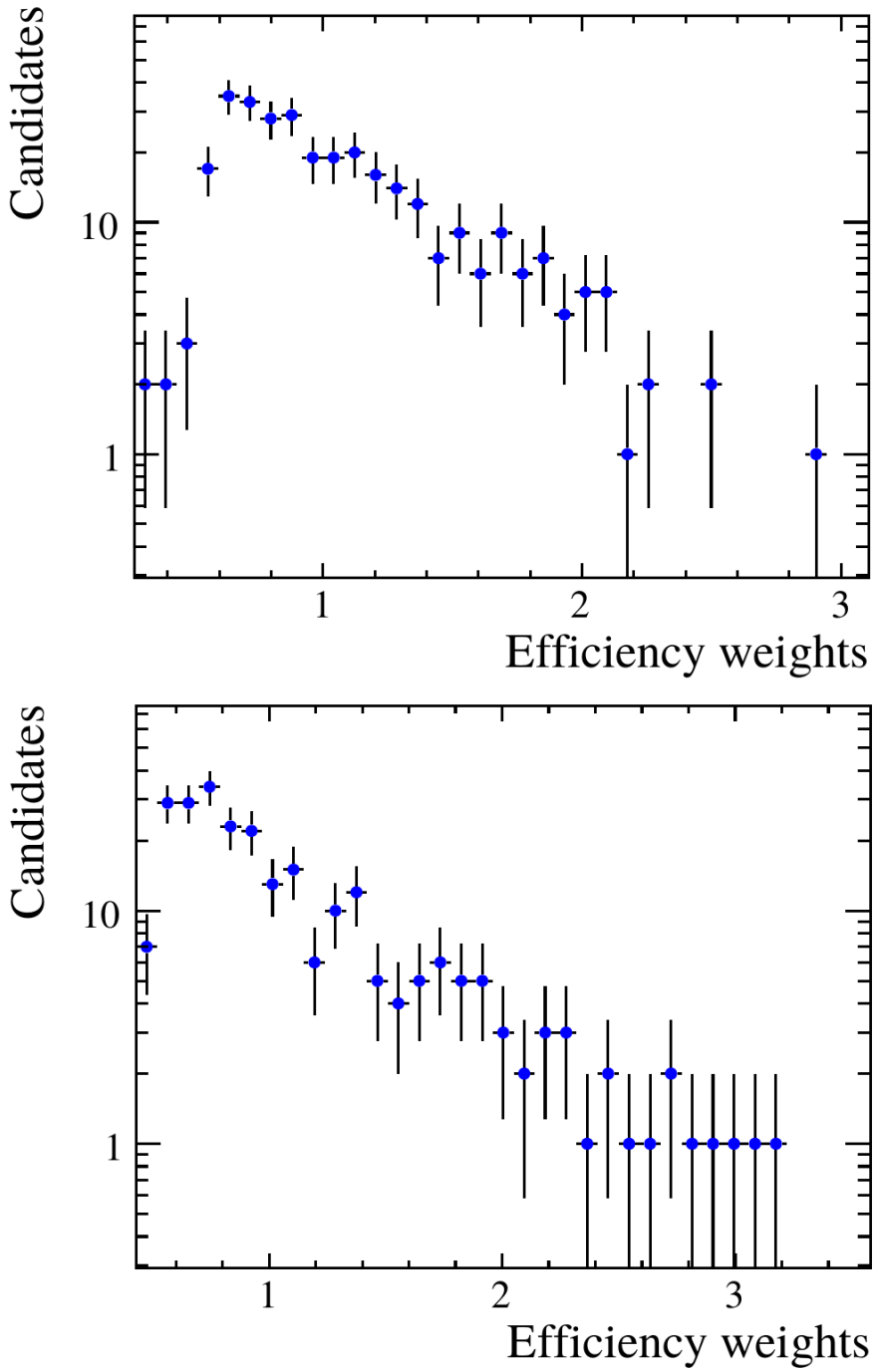

Figure 4.20: Efficiency weights for DD (left) and LL (right) $\Lambda_b^0 \to \Lambda\mu^+\mu^-$ candidates in 2011 + 2012 data.

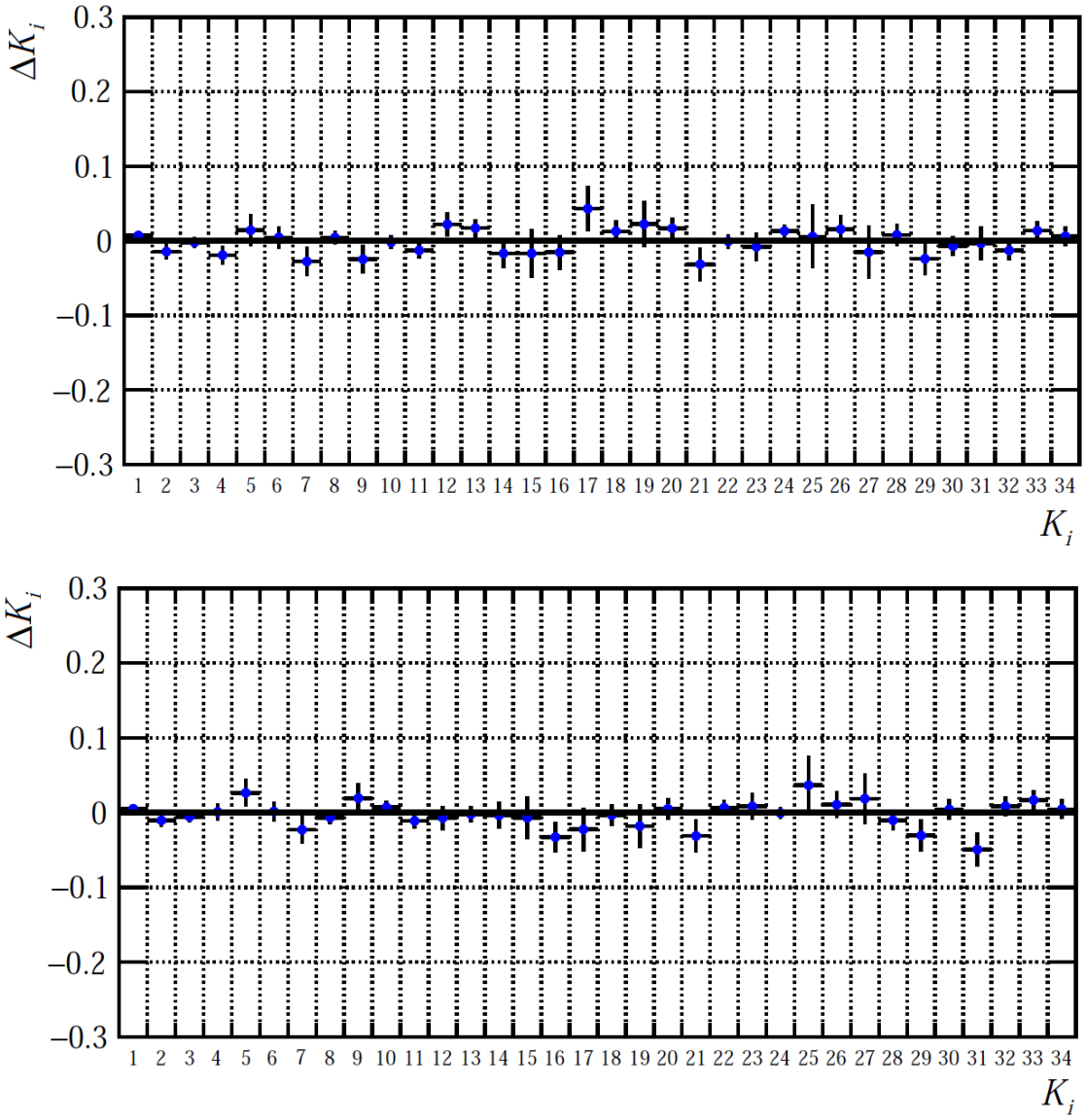

Figure 4.21: Distribution of the differences ($\Delta K_i \equiv K_i^{\text{Uniform}} - K_i^{\text{MC/eff}}$) of the K_i moments extracted from the 6D uniform distribution and the MC additionally weighted by the inverse of the efficiency model, using 2011 + 2012 MC samples of the DD (top) and LL (bottom) category.

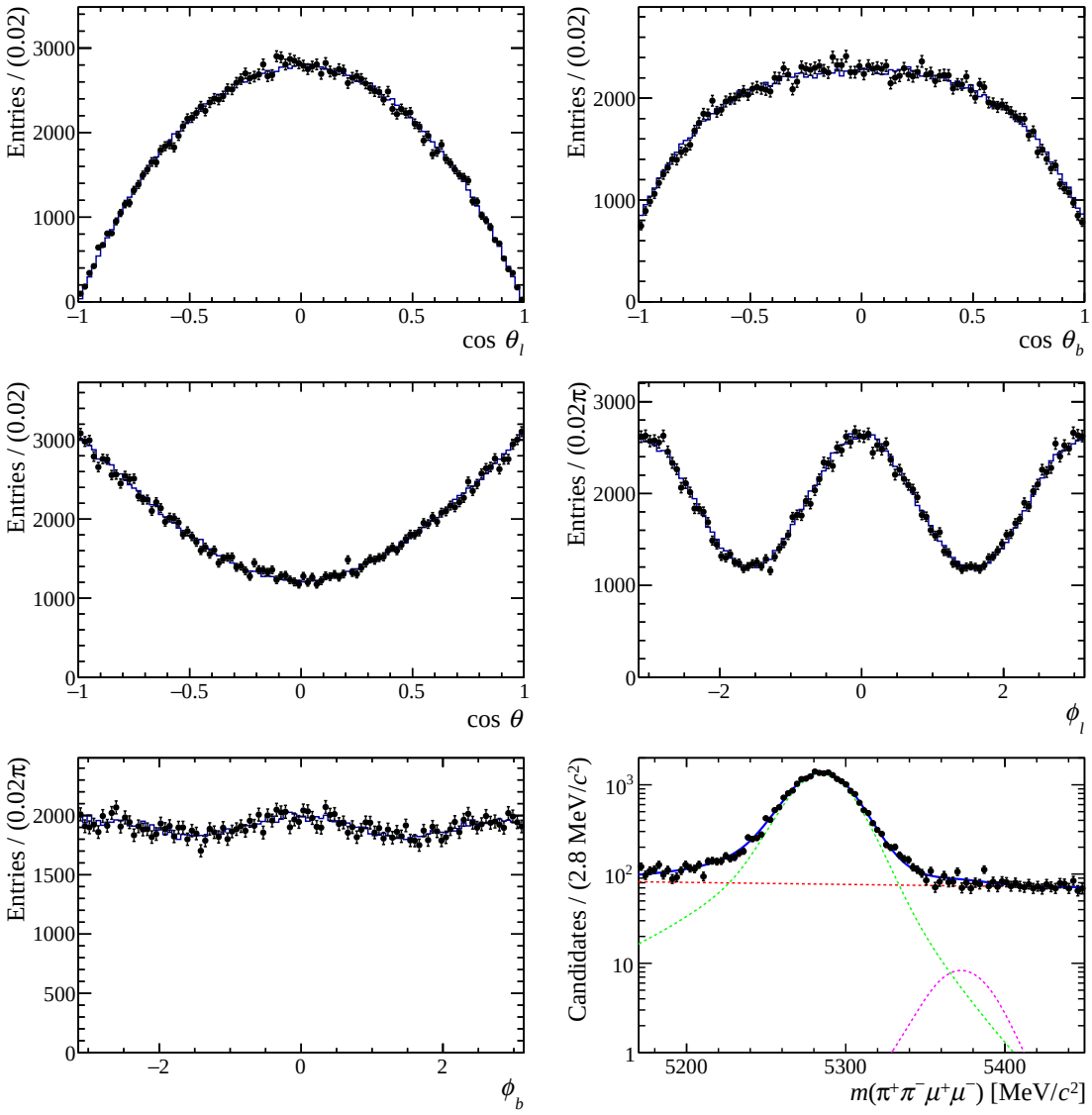

Figure 4.22: 1D angular projections of $\cos\theta_l$, $\cos\theta_b$, $\cos\theta$, ϕ_l and ϕ_b together with the invariant mass distribution for the $B^0 \to J/\psi K^0_S$ analysis. For the angular projections the blue line represents the angular distribution where the moments are set to the values extracted from the full data set, combining both track categories and data-taking years, multiplied by the relevant efficiency functions. The black markers represent the data candidates, weighted with the sWeights, but not with the efficiency weights. For the invariant mass distribution, the projections of the fitted components are overlaid. The blue solid line represents the total contribution, the green line represents the contribution of the signal component, while the red and magenta dotted lines present the contribution of the combinatorial and B^0_s components respectively. The black markers represent the data candidates.

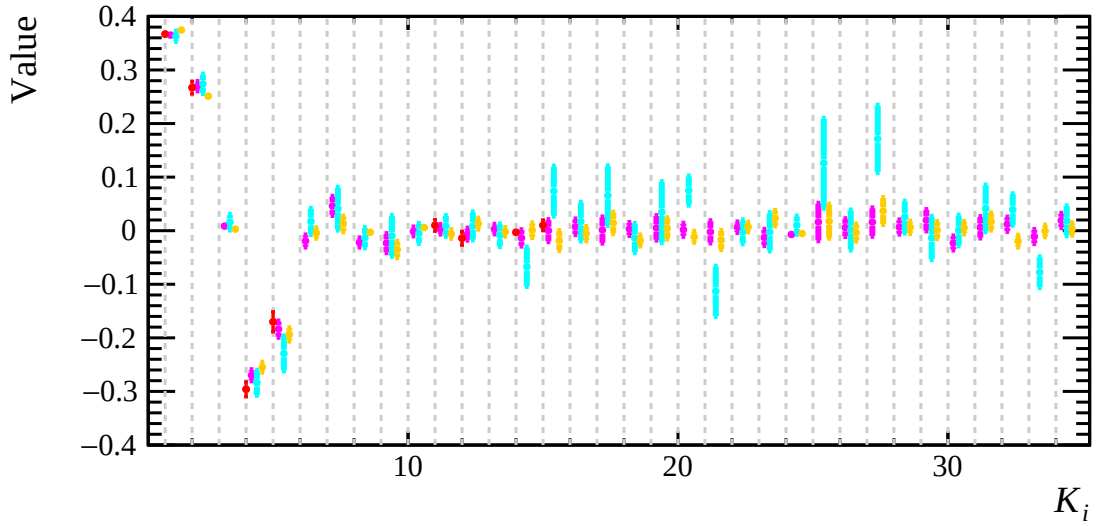

Figure 4.23: Distribution of the moments as obtained from the 2011 + 2012 (magenta), 2015 (cyan) and 2016 (orange) data sets combining both track categories for the $\Lambda_b^0 \to J/\psi\,\Lambda$ analysis. The red marker represent the averaged measurement of LHCb and CMS. Moments without a red marker correspond to those where neither LHCb [46] nor CMS [47] measuring moments that depend on the phases. The central values of the moments are shifted in the horizontal axis for illustration purposes. The moments extracted using the different data sets have a good agreement; a reasonable agreement is found with the $K_i^{<LHCb,CMS>}$.

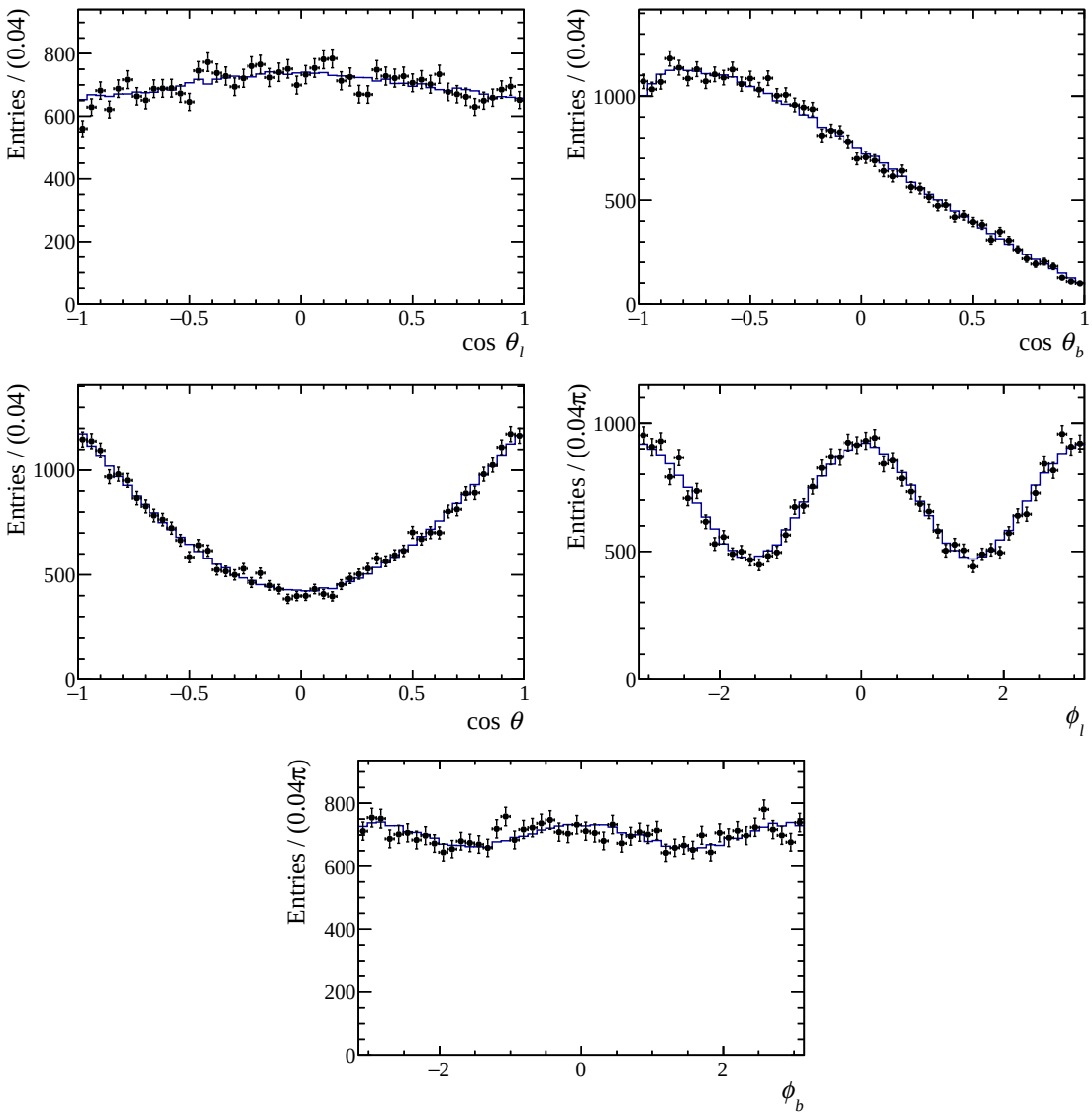

Figure 4.24: 1D angular projections of $\cos\theta_l$, $\cos\theta_b$, $\cos\theta$, ϕ_l and ϕ_b for the $\Lambda_b^0 \to J/\psi\,\Lambda$ analysis. The blue line presents the the angular distribution where moments are set to the values extracted from data, multiplied by the relevant efficiency functions. The black markers represent the data candidates for the combined 2011 + 2012, 2015, 2016 data set, weighted with the sWeights, but not with the efficiency weights.

4.6 Resolution studies

In this section a study of the resolution of the q^2 and the angles is reported. The effect that the latter will have on the evaluation of moments depends on the size of the resolution with respect to how rapidly the angular PDF and the efficiency functions oscillate.

The resolution is studied in terms of the differences between generated ($true$) and reconstructed ($reco$) angles and q^2. The resolution effects are found to be very small and so neglected in the default analysis. The resolution models described below are only used to evaluate the effect of neglecting the resolution in the default analysis (see section 4.8.4). The resolutions of the angles and q^2 are described in terms of 1D non-parametric models (*i.e.* 1D histograms), assuming that the total resolution can be written as the product of the individual ones. In addition, the resolution of each variable is assumed to be non-conditional, *i.e.* the resolution of each parameter does not depend on the value of the parameter.

An example of the 1D projections of the resolution of the angles and the invariant mass squared of the two muons for the 2011 + 2012 MC using the DD and LL categories is illustrated in figure 4.25. As expected, the angular resolution for the DD category for θ_b, θ and ϕ_b is poorer than for the LL category; this is due to the fact that the momentum resolution is inversely proportional to the length of the tracks. The resolution is found to be around 0.006, 0.092, 0.010 (0.006, 0.019, 0.006) rad for θ_l, θ_b, θ and 0.006, 0.142 (0.006, 0.026) rad for the ϕ_l, ϕ_b, while for

q^2 the resolution is found to be approximately 0.125 (0.125) GeV^2/c^4 for the DD (LL) category. The resolution is found to be consistent between all the data-taking years. These values are extracted from a fit to the Gaussian core of the resolutions. As seen from figure 4.25, the resolutions form a Gaussian core and have extended tails; no attempt is made to find a parametric description of a model that describes these distributions. Hence, the 1D histograms are directly saved and used in the evaluation of the systematics.

In principle, the distributions illustrated in figure 4.25 can be parametrised using the sum of many Gaussian functions or a combination of Gaussians and double sided Crystal Ball functions. However the parameters that determine the shape and the fractional contribution of each component become highly correlated, resulting in an extremely unstable and unreliable fit.

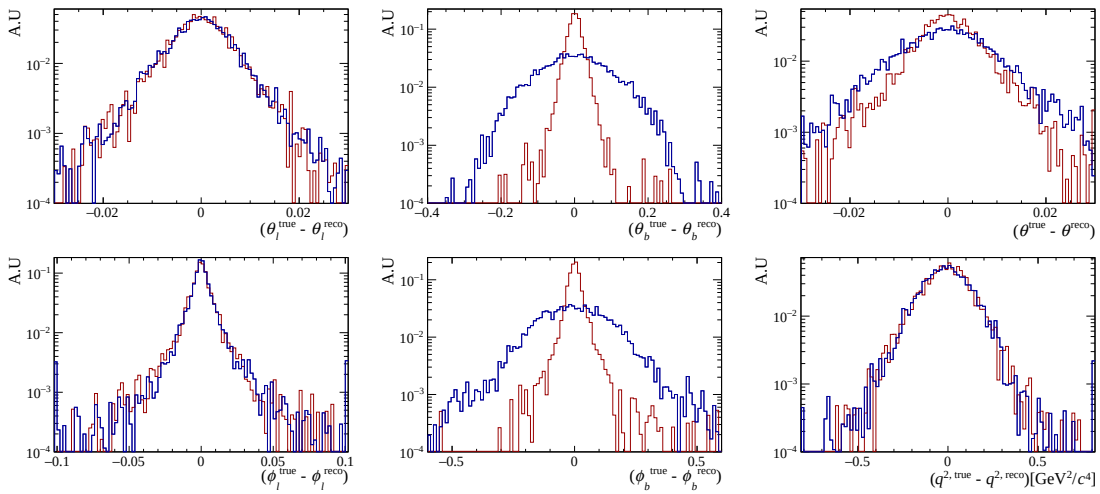

Figure 4.25: 1D projections of the the angular and q^2 resolutions for the DD (blue line) and LL (red line) categories using the 2011 + 2012 MC samples.

4.7 Validation studies

To validate the robustness of the framework used to estimate the moments and the associated statistical uncertainties, validation studies are performed in terms of pseudo-experiments ("toys"). The pseudo-experiments are performed separately for the data-sets of $2011 + 2012$, $2015 + 2016$ and $2011 + 2012 + 2015 + 2016$ combining in all cases the DD and LL track categories. The toys are generated with the equivalent statistics observed in the relevant data-sets (see table 4.3). In the pseudo-experiments the signal contribution is simulated by generating angles from a PDF defined as the product of the differential decay rate described in equation 1.7, where the K_i coefficients are set to the SM values (see table 4.2), times the equivalent efficiency model. The invariant mass component is generated using a double sided Crystal Ball function, where the tail parameters and the fractional contributions of the $CB_{l,r}$ functions are set to the values obtained from a fit to the relevant simulated samples, while the rest of the parameters are set to the values obtained from the fit on data (see table 4.3). To simulate the contribution of the combinatorial background, the angular distribution of the latter needs to be parametrised. This is done using LP,

$$\begin{aligned}\mathrm{PDF}_{\mathrm{bkg}}(\cos\theta_l, \cos\theta_b, \cos\theta, \phi_l, \phi_b) = &\sum_i \sum_j \sum_k \sum_l \sum_m c_i \times c_j \times c_k \times c_l \times c_m \times \\ &P_i(\cos\theta_l) \times P_j(\cos\theta_b) \times P_k(\cos\theta) \times \\ &P_l(\phi_l) \times P_m(\phi_b) \ , \end{aligned} \tag{4.24}$$

where due to low statistics of the samples used, the factorisation between each dimension is assumed. The events that are used to determine the shape of $\mathrm{PDF}_{\mathrm{bkg}}$ originate form the right sideband. The parametrisation for the angular distribution of the combinatorial background is performed separately for $2011 + 2012$, 2015 and 2016 data-taking periods and for each track category, while the orders of LP used in the parametrisation are up to second order. The invariant mass distribution of the combinatorial background is generated from an exponential function, where the slope is taken from the fit to the data (see table 4.3). An example of a toy is illustrated in figure 4.26.

In total 1000 pseudo-experiments are generated, where in each toy the moments and the corresponding statistical uncertainties are extracted, the results are saved and the distribution of the pulls is reconstructed. The pulls are defined as,

$$\mathrm{pull}_i \equiv \frac{K_i^{\mathrm{reco}} - K_i^{\mathrm{gen}}}{\sigma_i} \ , \tag{4.25}$$

where the K_i^{gen} represents the value of the moment used for the generation of the toys, while the K_i^{reco} corresponds to the estimated value in each of the toys, the σ_i finally is the associated statistical uncertainty. In the case that there is no bias the pulls over the pseudo-experiments should be centred on zero and have a width of one. A shift in the mean of the pull will indicate a bias in the estimates of the moments, while a width smaller or bigger that one, means that the statistical uncertainty is overestimated or underestimated respectively. The resulting pulls from the toys are well behaved, a small collection is illustrated in figure 4.27.

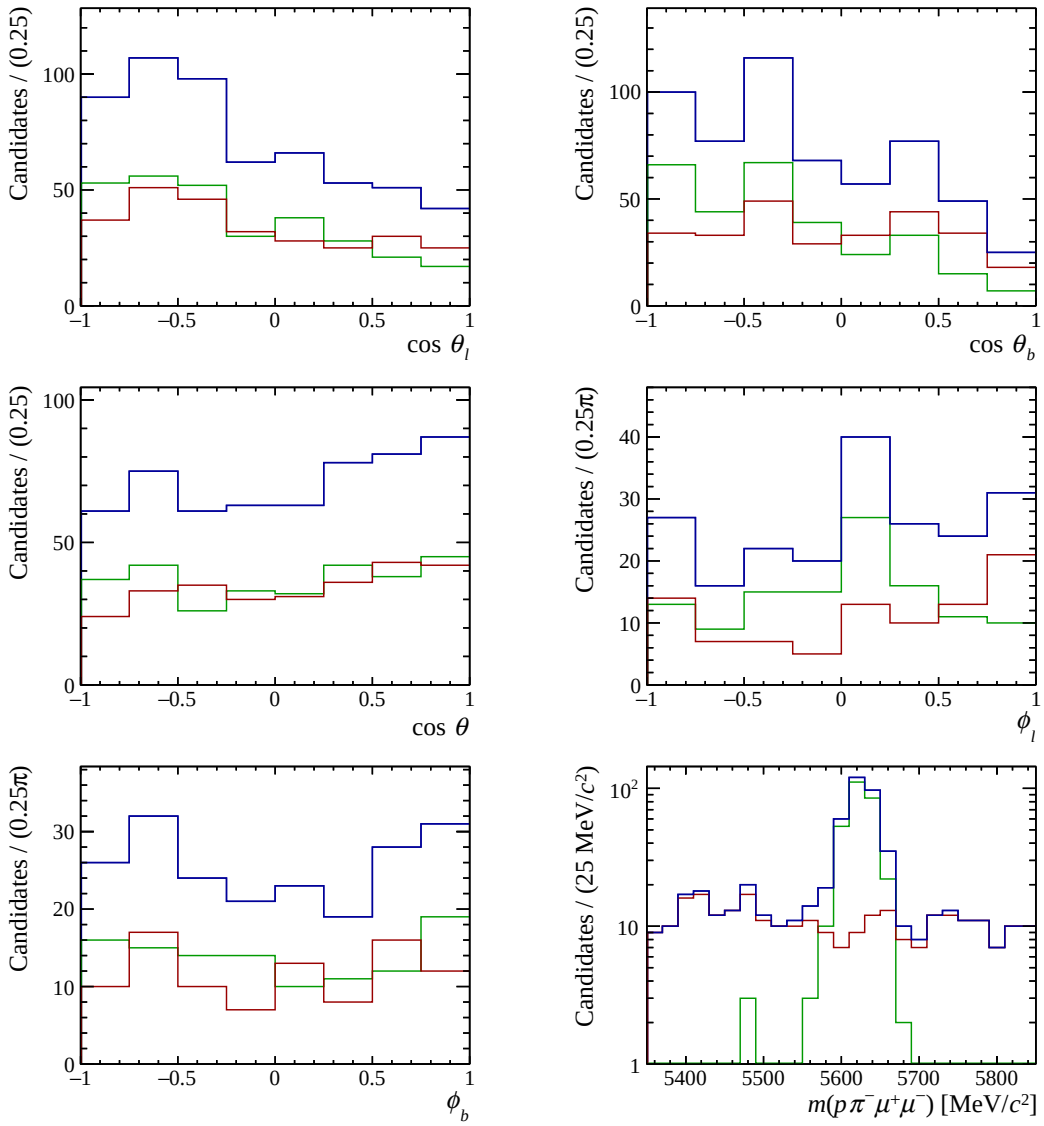

Figure 4.26: 1D projections of the angles and the invariant mass distribution as generated in a single pseudo-experiment. In all cases the green and red lines represent the contribution of signal and combinatorial background, while the blue line represents the combined contribution. In this pseudo-experiment the distributions are generated for the $2011 + 2012$ conditions, including both DD and LL categories. It is noted that the angular distributions are not weighted with the sWeights or the efficiency weights.

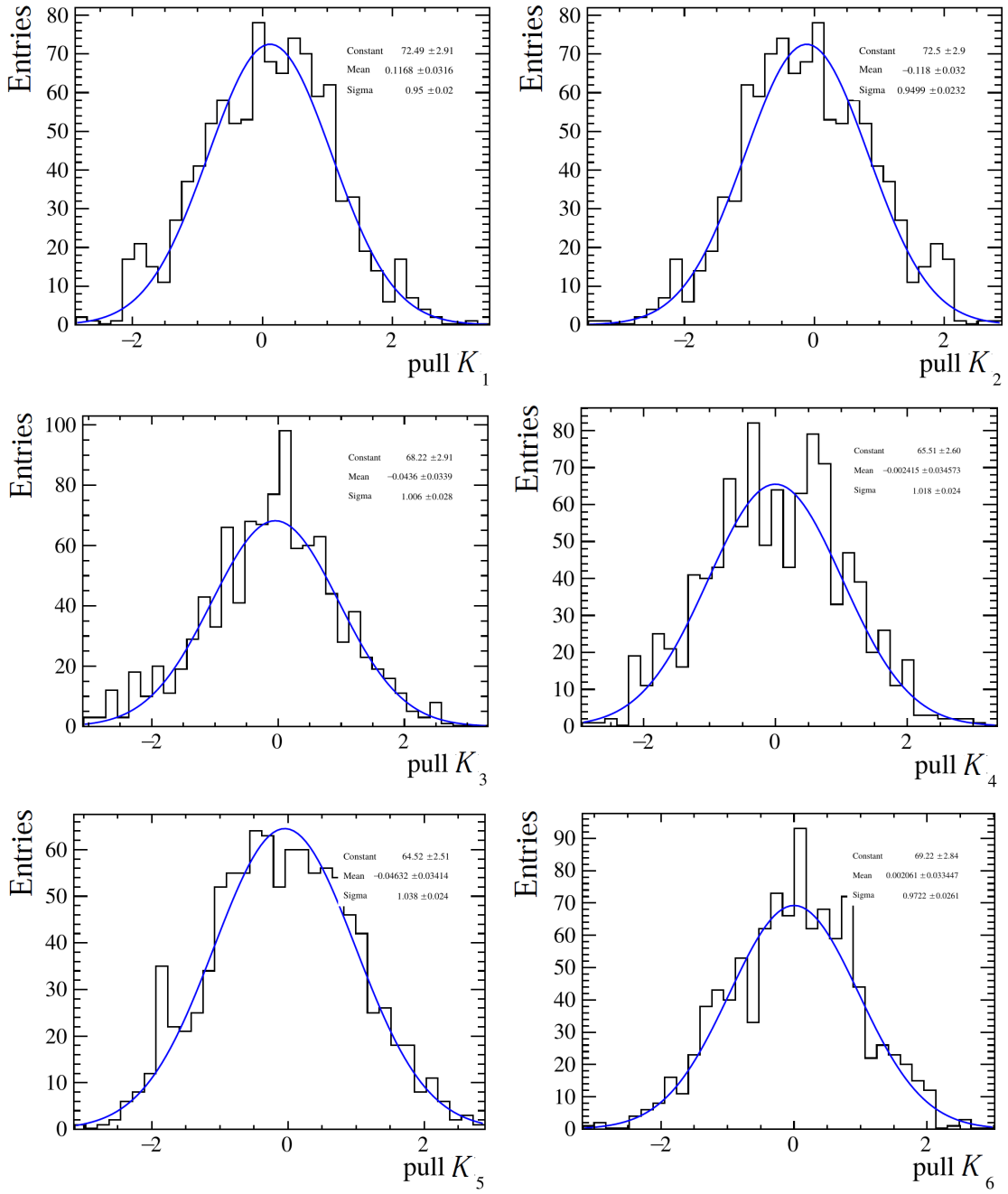

Figure 4.27: A small collection of pulls for the first six moments from which several interesting parameters, such as the asymmetry parameters are extracted. The pulls are obtained from the validation studies performed for the Run2 samples. The blue solid line represents the fit with a Gaussian function.

4.8 Systematic uncertainties

The systematic uncertainties are evaluated with one of the two following strategies. The first method is with pseudo-experiments[7], where the samples are generated as described in section 4.7, with the exception that depending on the systematic error source under investigation, a variation is applied in the model used in the generation of the samples. Finally for the extraction of the moments the default analysis is used; the bias on the mean of the angular observables from the toys is used as an estimate of the systematic uncertainty. The second approach used to evaluate the systematic uncertainties is to perform a systematic variation in the analysis and re-extract the moments from the data, this approach is used only when the first strategy is not applicable.

4.8.1 Data-simulation differences

Residual differences between data and MC, after the corrections discussed in section 4.4 are applied, are resolved by including an extra correction in p_{T} and η of Λ_b^0. This correction is extracted by taking the ratio of histograms (including correlations of p_{T} and η) of the sWeighted data of the $\Lambda_b^0 \to J/\psi\,\Lambda$ versus the MC samples weighted with the correction[8] discussed in section 4.4. After the additional correction is applied to the MC samples, new efficiency models are extracted. The pseudo-experiments are generated with the new efficiency models, while moments

[7] In the generation of the toys the K_i are set to the SM predictions, presented in table 4.2.

[8] The MC samples are additionally weighted with the relevant matrix element, the parameters of which are set to the previous LHCb measurement [46].

are extracted using the default analysis.

The effect of not correcting the MC for the muon identification and tracking efficiencies (see section 4.4.2) in the default analysis is evaluated by including a proper correction in the MC samples and extracting new efficiency models. The evaluation of the systematic uncertainties is performed in the same manner as before.

4.8.2 Parametrisation of efficiency

The orders of the LP used to model the angular efficiencies are chosen to describe accurately the MC samples in 6D, using the minimal order of polynomial possible. To investigate the effect of using this particular model in the default analysis, *i.e.* with this specific choice of the orders of LP, a new set of efficiency models is extracted using higher order corrections, where the LP are increased by up to a further two orders. The higher order efficiency models are found to describe well the MC, with no negative weights in the data. The effect of this choice of order of LP on the extraction of moments is investigated in terms of toy studies in a similar way as defined is section 4.8.1.

4.8.3 Size of the simulated samples

The shape of the efficiency model is fully described by the set of c_{ijklmn} coefficients, which are extracted with the method of moments from the MC samples. To investigate the effect of the statistical uncertainties on the c_{ijklmn} coefficients, in the final

extraction of the K_i moments a systematic study is performed. In this study the MC samples are bootstrapped (see section 4.1.1 for the definition of the bootstrapping) and a new efficiency parametrisation is extracted; this process is repeated 1000 times. For each of the efficiency models the K_i moments are evaluated from data and the results are saved. Finally the RMS distribution of the K_i moments is used as a measure of the systematic uncertainty.

4.8.4 Resolution model

As discussed in section 4.6, the angular and q^2 resolutions are not included in the default analysis. To evaluate the effect of neglecting the angular resolution a toy study is performed. In each toy the angles and the q^2 are generated with the default models but, before the efficiency weights and the extraction of moments is performed, the angles and the q^2 are smeared according to 1D non-parametric models (see section 4.6).

4.8.5 Mass model

The background subtraction is performed using the *sPlot* technique, where the factorisation of the angles with the invariant mass is assumed. To test that this assumption is correct the $m(p\pi^-\mu^+\mu^-)$ invariant mass in several bins of each angle is compared with the the invariant mass distribution obtained from the full domain. As no significant or systematic variations in the lineshape of the $m(p\pi^-\mu^+\mu^-)$ are

found with the current sample size, any systematic uncertainty must be negligible and hence none is assigned for this potential source. Another source of systematic uncertainty associated with the mass model is related to the parameters that are fixed in the mass models, which are used finally in the fit on data, through which the extraction of the sWeights is performed. To investigate this effect, the parameters that are fixed in the fit on data are smeared according to their uncertainties and a new fit is performed, followed by a new extraction of sWeights, which are finally used in the determination of the moments. This process is repeated 1000 times on data and the extracted moments are saved. The RMS distribution of the moments is used as a measure of the systematic error.

4.8.6 Beam direction

To calculate the angles that are used in the analysis the momentum of the incident proton in the laboratory frame is used in order to calculate the unit vector $\vec{n}$; the small crossing angle of the proton beams in the interaction point is neglected in the default analysis. To investigate the effect of this choice pseudo-experiments are performed where angles are generated with the correct crossing angle, while neglecting the latter before calculating the moments.

4.8.7 Summary of systematics

In total the systematic errors are found to be small compared to the statistical uncertainties (around 10–20% of the statistical uncertainty). The systematic errors are extracted separately for the 2011+2012, 2015+2016 and 2011+2012+2015+2016 data samples. A summary of the sources of the systematic errors for $2011 + 2012 + 2015 + 2016$ data sample is presented in table 4.6. The systematic uncertainties for each of the moments are finally defined as the square root of the quadrature sum of all the sources.

In principle the extraction of the moments from the combined sample of 2011+2012+2015+2016 and the determination of the corresponding systematic uncertainties can be avoided, by performing a χ^2 fit between the 2011+2012 and 2015+2016 moments. In this case however a correlation between the systematics should be assigned. The correlation coefficient between the systematics for simplicity is usually assumed (in the case of small systematic errors) to be either 1, -1 or 0, using some meaningful arguments. For example the correlation coefficient between the Run1 and Run2 systematics related to the mass model can be set to zero, since the samples used to fix the relevant parameters in the mass models are independent. However, to avoid the last step and also having all the results for the moments for all the samples obtained with the same method, the χ^2 combination of the Run1 and Run2 moments is avoided and is used only as validation of the default method, where the samples for Run1 and Run2 are merged and the full chain of extracting the moments, the statistical and systematic uncertainties is repeated.

Table 4.6: Systematic uncertainties for the combined samples of the data-taking years using both track categories. The range of systematic uncertainties that are assigned to the various K_i moments and the mean of these uncertainties are also presented. The variation of the systematic uncertainties in the moments between the different sources depends mainly on the correlation of the systematic sources between the weighting functions and the angular efficiency [1].

Sources of systematic uncertainties	Uncertainty $[10^{-3}]$	
	Range of K_i	Mean
Size of the simulated samples	3–22	9
Parametrisation of efficiency	1–13	4
Data-simulation differences	2–16	6
Resolution model	1–11	4
Beam direction	1–8	4
Mass model	1–4	2

4.9 Results

The moments are extracted separately for the 2011 + 2012 and 2015 + 2016 data samples[9]. Since the P_b can potentially depend on $\sqrt{s}$, the combination of 2011+2012 and 2015 + 2016 samples is valid only for the first ten moments. In section 4.5.6 the moments extracted for the control mode are found to be compatible between the different data-taking years, with a $\chi^2/ndof = 1.01$. As there is no evidence for $\sqrt{s}$ dependence of the Λ_b^0 production polarisation in the current $\Lambda_b^0 \to \Lambda\mu^+\mu^-$ data, the Run1 and Run2 samples are merged and a single set of moments is determined. The default method used to combine Run1 and Run2 samples merges the Run1 and Run2 samples, where the sWeights and efficiency weights are extracted independently for 2011 + 2012, 2015, 2016 data sets and for each track category.

The combination of Run1 and Run2 can also be carried out by performing a χ^2 fit between the moments extracted from these two data sets. In this spirit a χ^2 fit is performed, taking into account correlations between the systematics to obtain the combined moments. The resulting moments are found to be compatible with those obtained from the default method (see figure 4.33), while the χ^2 fit yields a $\chi^2/ndof = 1.06$, indicating good compatibility between Run1 and Run2 moments. This further supports the absence of any significant trend of the Λ_b^0 production polarisation with $\sqrt{s}$.

[9]If not stated otherwise the results for 2011 + 2012 (Run1), 2015 + 2016 (Run2) and 2011 + 2012 + 2015 + 2016 (Run1+Run2) correspond to samples in which the DD and LL categories are combined.

4.9.1 Numerical results

Before results are presented, the behaviour of the bootstrapping distributions is tested. In figure 4.28 the bootstrapping distributions for the first ten moments are illustrated, where the Most Probable Value (MPV), median and mean of the distributions are compared and found to be compatible, indicating that the distributions are Gaussian and so the statistical uncertainties are symmetric.

Numerical results for Run1, Run2 and Run1+Run2 samples combining both track categories are given in tables 4.7, 4.8 and 4.9. The associated correlation matrices are documented in section A.4. The correlations between the moments are generally small but they can take values of up to 40% in a few cases. Figures 4.29, 4.30 and 4.31 illustrate the 1D angular projections of the five angles. Using the measured values of the angular observables the well-known asymmetry parameters are constructed (see section 1.6.2). Moments are also extracted separately for the DD and LL categories, the results are compared and found to be consistent (see figure A.14), while a summary plot of the pull distributions is given in figure 4.32. In the following, the discussion will be focused mainly on the results obtained from the Run1+Run2 data set.

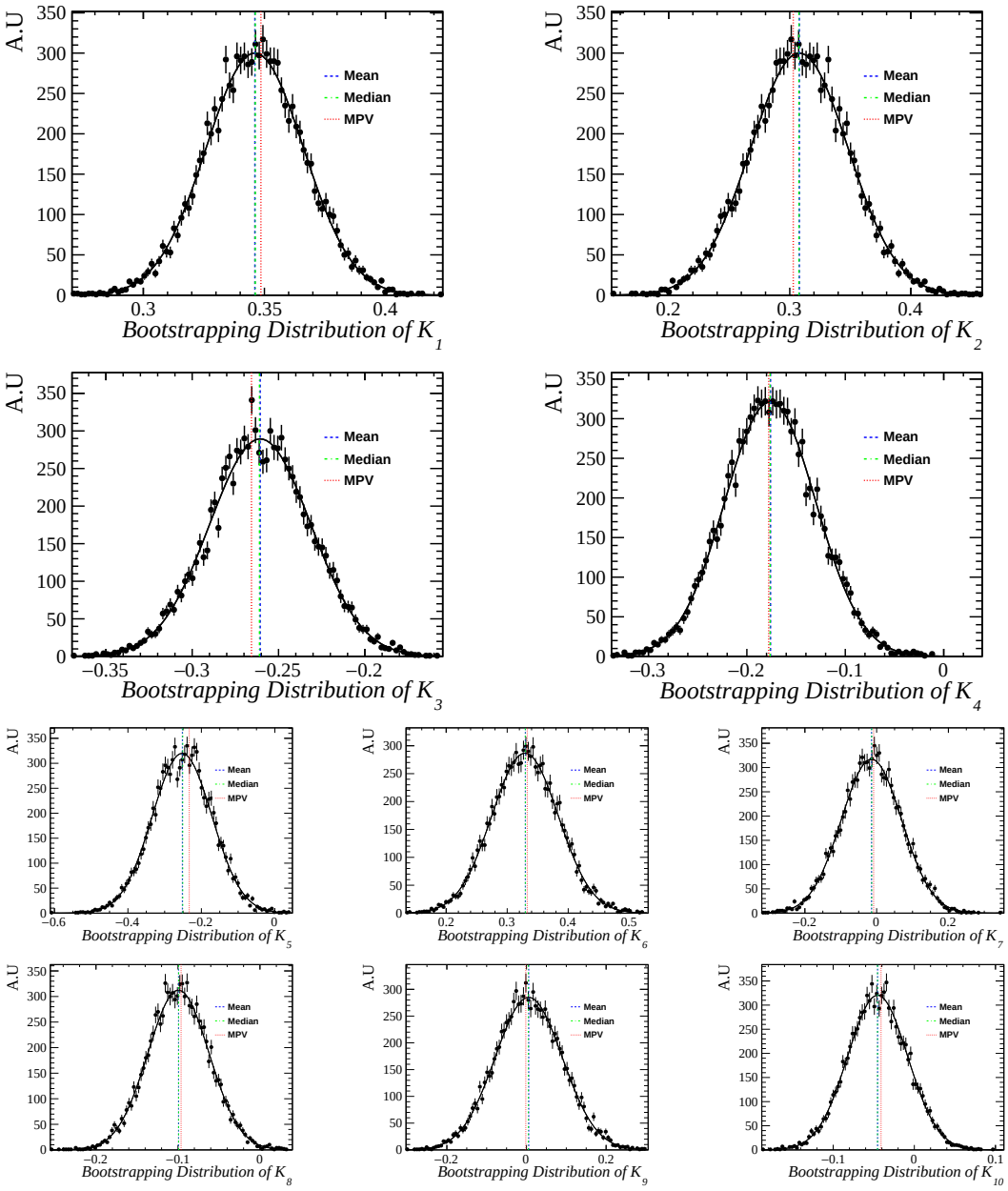

Figure 4.28: Bootstrapping distributions of the first ten moments obtained from the evaluation of moments from the Run1+Run2 data set. Characteristics of the distributions such as the mean (blue dotted line), median (green dotted line) and most probable value (red dotted line) are illustrated. Mean, median and MPV are compatible with each other, as it is expected for a Gaussian distribution. The black curves represents a fit using a Gaussian function where the width is fixed to the RMS of the distributions. The MPV is estimated using Kernel Density Estimation.

Table 4.7: Measured values of the moments extracted for the combined DD+LL sample for Run1. The first and second uncertainties represent the statistical and systematic errors respectively [1].

Obs.	Value	Obs.	Value
K_1	$0.376 \pm 0.029 \pm 0.006$	K_{18}	$-0.081 \pm 0.081 \pm 0.015$
K_2	$0.248 \pm 0.057 \pm 0.012$	K_{19}	$-0.023 \pm 0.165 \pm 0.031$
K_3	$-0.241 \pm 0.041 \pm 0.008$	K_{20}	$-0.156 \pm 0.078 \pm 0.019$
K_4	$-0.212 \pm 0.070 \pm 0.013$	K_{21}	$-0.050 \pm 0.150 \pm 0.032$
K_5	$-0.123 \pm 0.117 \pm 0.020$	K_{22}	$0.032 \pm 0.064 \pm 0.014$
K_6	$0.247 \pm 0.079 \pm 0.017$	K_{23}	$0.038 \pm 0.104 \pm 0.018$
K_7	$-0.027 \pm 0.124 \pm 0.022$	K_{24}	$0.004 \pm 0.047 \pm 0.008$
K_8	$-0.081 \pm 0.054 \pm 0.010$	K_{25}	$-0.107 \pm 0.254 \pm 0.046$
K_9	$-0.123 \pm 0.115 \pm 0.018$	K_{26}	$0.130 \pm 0.106 \pm 0.024$
K_{10}	$0.021 \pm 0.051 \pm 0.009$	K_{27}	$-0.200 \pm 0.190 \pm 0.035$
K_{11}	$-0.030 \pm 0.062 \pm 0.014$	K_{28}	$0.058 \pm 0.084 \pm 0.015$
K_{12}	$-0.114 \pm 0.092 \pm 0.022$	K_{29}	$-0.172 \pm 0.142 \pm 0.027$
K_{13}	$0.059 \pm 0.064 \pm 0.016$	K_{30}	$-0.060 \pm 0.088 \pm 0.014$
K_{14}	$0.122 \pm 0.126 \pm 0.026$	K_{31}	$0.252 \pm 0.126 \pm 0.022$
K_{15}	$0.247 \pm 0.171 \pm 0.042$	K_{32}	$-0.074 \pm 0.075 \pm 0.011$
K_{16}	$-0.193 \pm 0.116 \pm 0.029$	K_{33}	$-0.010 \pm 0.081 \pm 0.014$
K_{17}	$-0.119 \pm 0.178 \pm 0.033$	K_{34}	$0.140 \pm 0.088 \pm 0.012$

Table 4.8: Measured values of the moments extracted for the combined DD+LL sample for Run2. The first and second uncertainties represent the statistical and systematic errors respectively [1].

Obs.	Value	Obs.	Value
K_1	$0.318 \pm 0.028 \pm 0.007$	K_{18}	$-0.134 \pm 0.081 \pm 0.014$
K_2	$0.364 \pm 0.056 \pm 0.013$	K_{19}	$-0.273 \pm 0.178 \pm 0.040$
K_3	$-0.279 \pm 0.042 \pm 0.010$	K_{20}	$-0.078 \pm 0.082 \pm 0.017$
K_4	$-0.143 \pm 0.063 \pm 0.012$	K_{21}	$-0.033 \pm 0.142 \pm 0.023$
K_5	$-0.372 \pm 0.113 \pm 0.024$	K_{22}	$-0.058 \pm 0.062 \pm 0.008$
K_6	$0.407 \pm 0.076 \pm 0.017$	K_{23}	$-0.082 \pm 0.111 \pm 0.018$
K_7	$-0.004 \pm 0.114 \pm 0.018$	K_{24}	$0.005 \pm 0.046 \pm 0.008$
K_8	$-0.116 \pm 0.051 \pm 0.011$	K_{25}	$-0.339 \pm 0.243 \pm 0.042$
K_9	$0.126 \pm 0.124 \pm 0.017$	K_{26}	$0.150 \pm 0.101 \pm 0.017$
K_{10}	$-0.108 \pm 0.054 \pm 0.008$	K_{27}	$0.221 \pm 0.203 \pm 0.036$
K_{11}	$0.014 \pm 0.060 \pm 0.009$	K_{28}	$0.008 \pm 0.083 \pm 0.015$
K_{12}	$0.091 \pm 0.085 \pm 0.023$	K_{29}	$-0.085 \pm 0.135 \pm 0.025$
K_{13}	$-0.009 \pm 0.063 \pm 0.016$	K_{30}	$0.079 \pm 0.084 \pm 0.014$
K_{14}	$-0.096 \pm 0.105 \pm 0.019$	K_{31}	$0.113 \pm 0.140 \pm 0.021$
K_{15}	$0.073 \pm 0.159 \pm 0.046$	K_{32}	$0.053 \pm 0.080 \pm 0.012$
K_{16}	$0.280 \pm 0.120 \pm 0.034$	K_{33}	$0.052 \pm 0.088 \pm 0.011$
K_{17}	$0.112 \pm 0.166 \pm 0.033$	K_{34}	$-0.015 \pm 0.079 \pm 0.012$

Table 4.9: Measured values of the moments extracted from the combined samples of Run1 and Run2, using both track categories. The first and second uncertainties represent the statistical and systematic errors respectively [1].

Obs.	Value	Obs.	Value
K_1	$0.346 \pm 0.020 \pm 0.004$	K_{18}	$-0.108 \pm 0.058 \pm 0.008$
K_2	$0.308 \pm 0.040 \pm 0.008$	K_{19}	$-0.151 \pm 0.122 \pm 0.022$
K_3	$-0.261 \pm 0.029 \pm 0.006$	K_{20}	$-0.116 \pm 0.056 \pm 0.008$
K_4	$-0.176 \pm 0.046 \pm 0.016$	K_{21}	$-0.041 \pm 0.105 \pm 0.020$
K_5	$-0.251 \pm 0.081 \pm 0.016$	K_{22}	$-0.014 \pm 0.045 \pm 0.007$
K_6	$0.329 \pm 0.055 \pm 0.012$	K_{23}	$-0.024 \pm 0.077 \pm 0.012$
K_7	$-0.015 \pm 0.084 \pm 0.013$	K_{24}	$0.005 \pm 0.033 \pm 0.005$
K_8	$-0.099 \pm 0.037 \pm 0.012$	K_{25}	$-0.226 \pm 0.176 \pm 0.030$
K_9	$0.005 \pm 0.084 \pm 0.012$	K_{26}	$0.140 \pm 0.074 \pm 0.014$
K_{10}	$-0.045 \pm 0.037 \pm 0.006$	K_{27}	$0.016 \pm 0.140 \pm 0.025$
K_{11}	$-0.007 \pm 0.043 \pm 0.009$	K_{28}	$0.032 \pm 0.058 \pm 0.009$
K_{12}	$-0.009 \pm 0.063 \pm 0.014$	K_{29}	$-0.127 \pm 0.097 \pm 0.016$
K_{13}	$0.024 \pm 0.045 \pm 0.010$	K_{30}	$0.011 \pm 0.061 \pm 0.011$
K_{14}	$0.010 \pm 0.082 \pm 0.013$	K_{31}	$0.180 \pm 0.094 \pm 0.015$
K_{15}	$0.158 \pm 0.117 \pm 0.027$	K_{32}	$-0.009 \pm 0.055 \pm 0.008$
K_{16}	$0.050 \pm 0.084 \pm 0.023$	K_{33}	$0.022 \pm 0.060 \pm 0.009$
K_{17}	$-0.000 \pm 0.120 \pm 0.022$	K_{34}	$0.060 \pm 0.058 \pm 0.009$

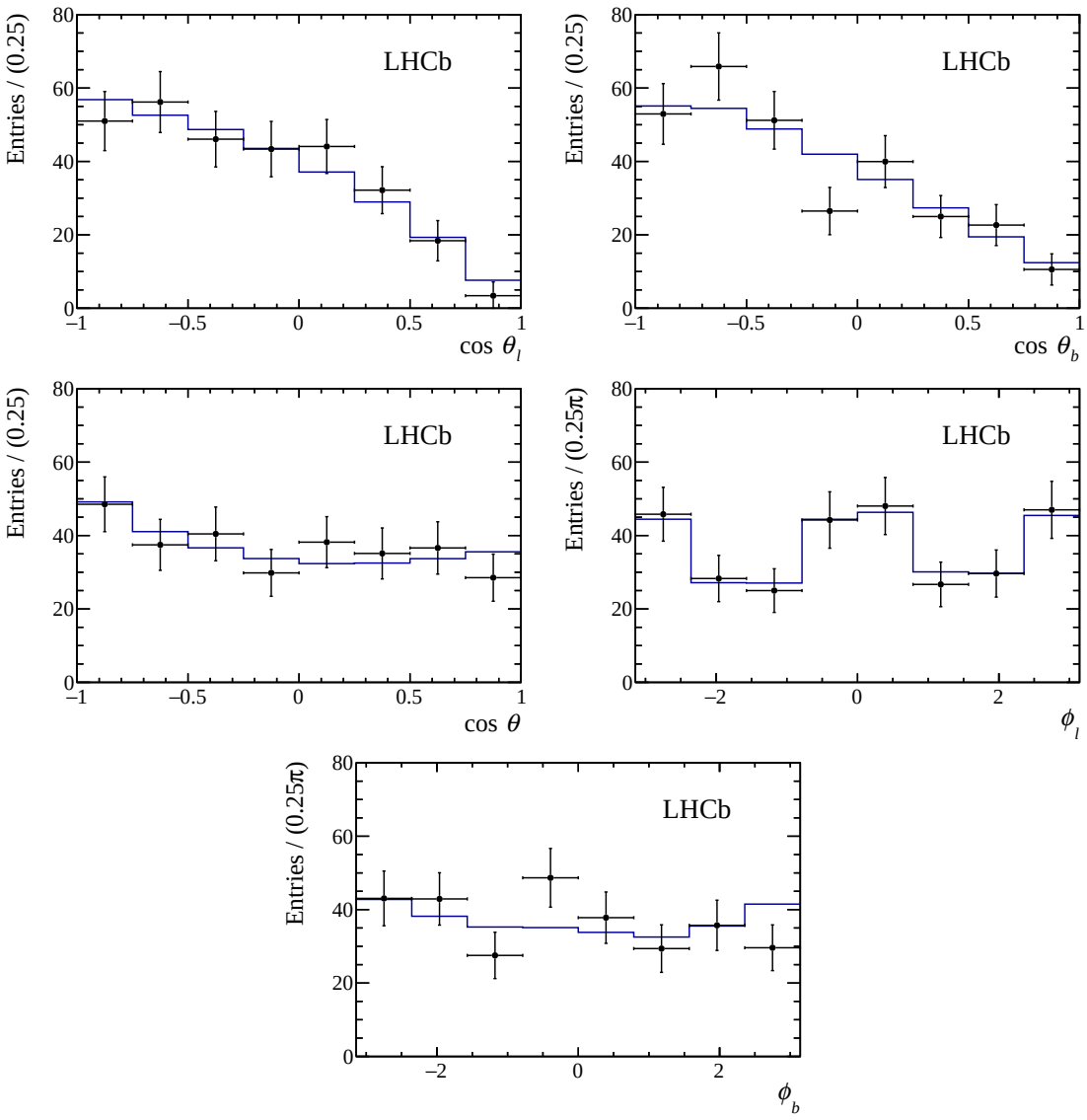

Figure 4.29: 1D projections of the angular PDF, where the moments are set to the values extracted from the Run1 data set, using both track categories. The candidates illustrated with the black markers are weighted by the sWeights but not with the efficiency weights. The angular PDF is multiplied finally by the efficiency functions and represented as a blue line [1].

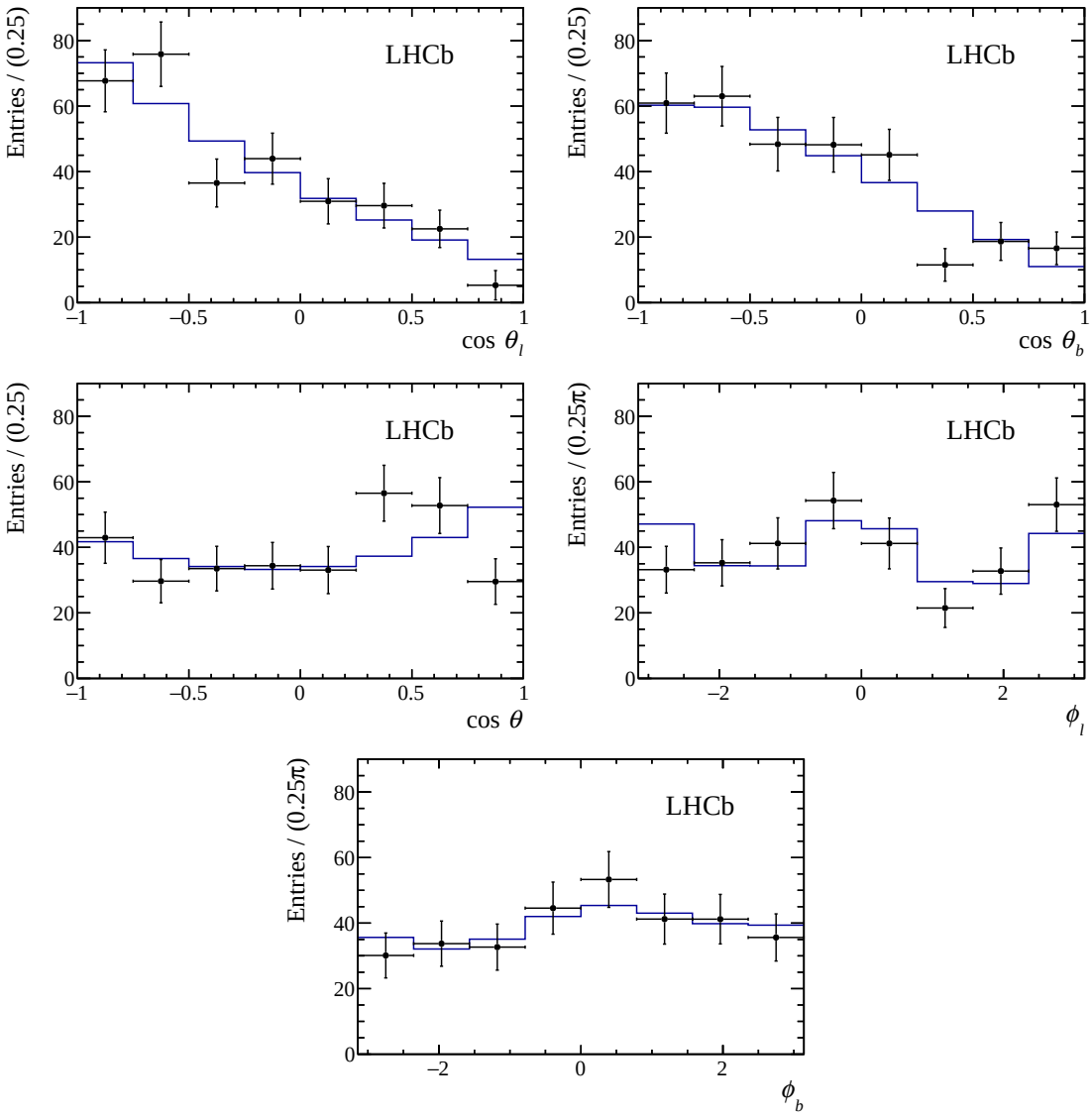

Figure 4.30: 1D projections of the angular PDF, where the moments are set to the values extracted from the Run2 data set, using both track categories. The candidates illustrated with the black markers are weighted by the sWeights but not with the efficiency weights. The angular PDF is multiplied finally by the efficiency functions and represented as a blue line [1].

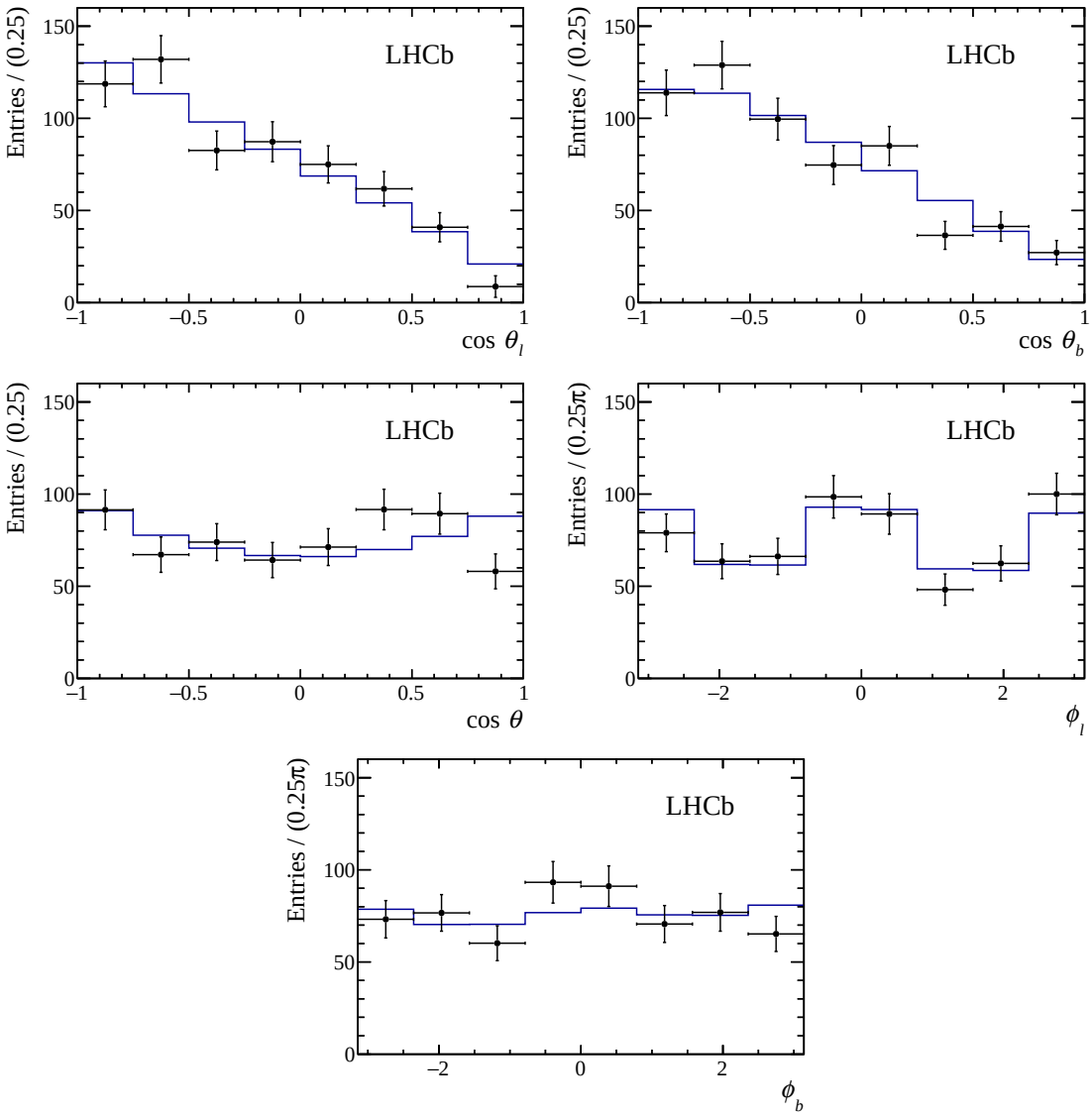

Figure 4.31: 1D projections of the angular PDF, where the moments are set to the values extracted from the combined data set of Run1 and Run2, using both track categories. The candidates illustrated by the black markers are weighted by the sWeights but not with the efficiency weights. The angular PDF is multiplied finally by the efficiency functions and represented as a blue line [1].

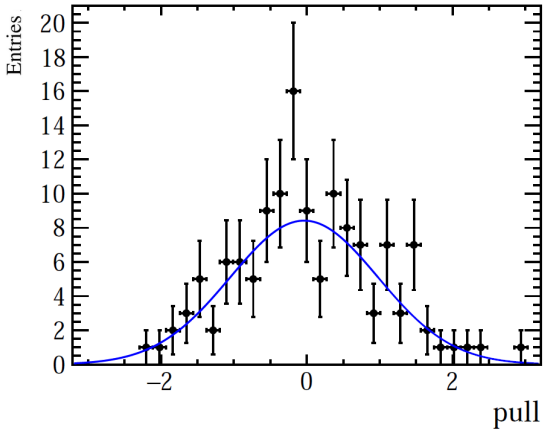

Figure 4.32: Pull distribution of moments between Run1 and Run2 data sets, keeping DD and LL candidates as separate samples. The pull is calculated with respect to the combination of all subsamples.

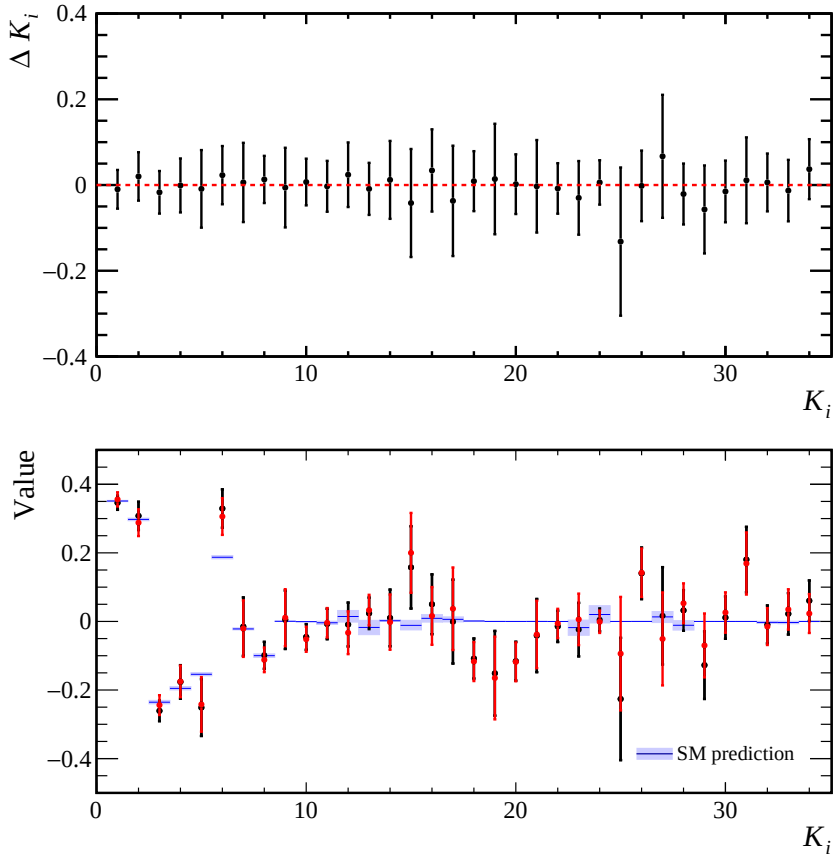

Figure 4.33: (Top) Distribution of $\Delta K_i \equiv K_i^{\text{default}} - K_i^{\chi^2}$, where the uncertainties are obtained from error propagation; it must be noted that for simplicity correlations are not included in the error determination of ΔK_i. (Bottom) Comparison of moments obtained with the default method (black markers) and the χ^2 fit (red markers). The SM predictions are also illustrated by the blue solid line, with the light-blue band corresponding to the uncertainty of the SM predictions [1].

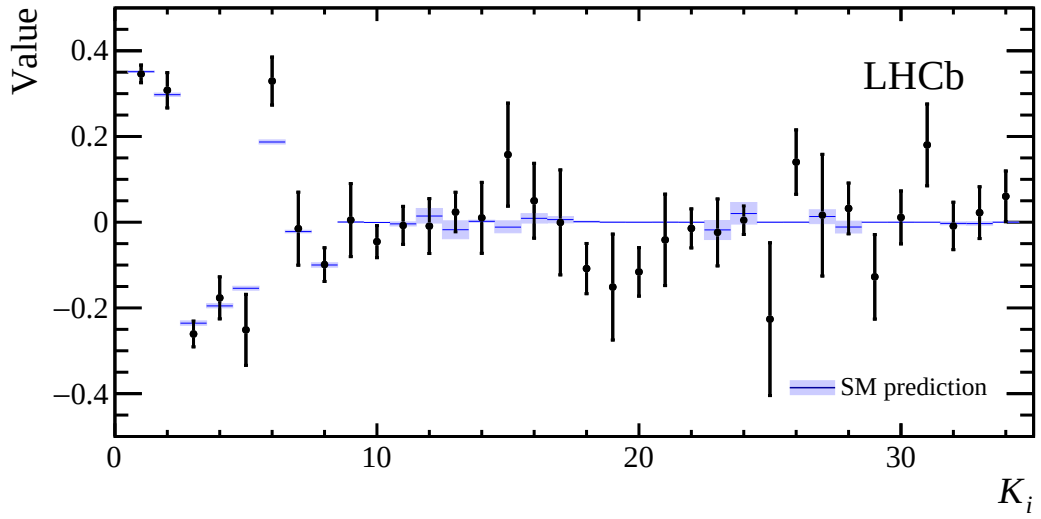

Figure 4.34: Angular moments from the combined Run1 and Run2 data sets using both track types (black markers). The moments are compared with the SM predictions, illustrated by the blue solid line, with the light-blue band corresponding to the uncertainty of the SM predictions. For P_b the previous LHCb measurement [46] is used [1].

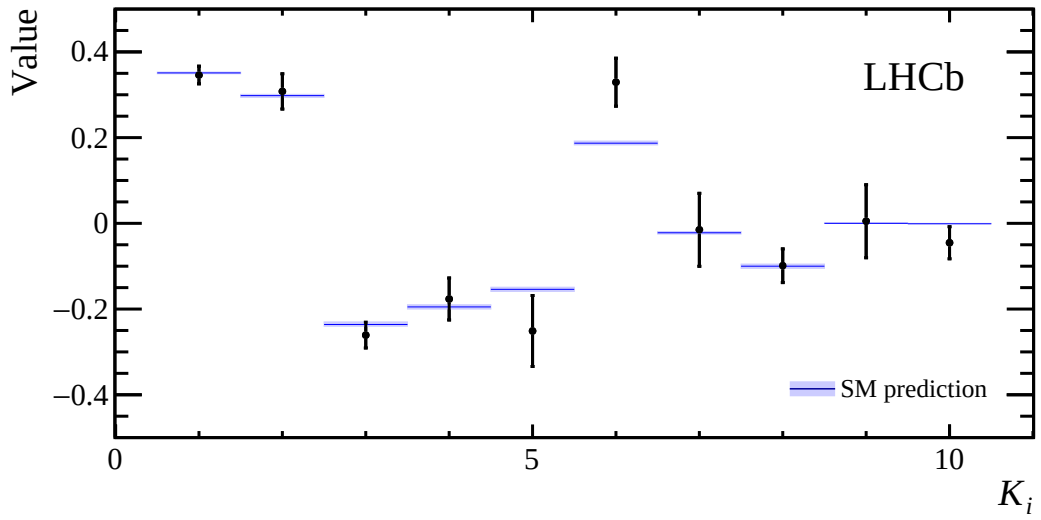

Figure 4.35: Angular moments from the combined samples of Run1 and Run2 data sets using both track types (black markers). The moments are compared with the SM predictions, illustrated by the blue solid line, with the light-blue band corresponding to the uncertainty of the SM predictions [1].

4.10 Summary and conclusion

This is the first time that the full set of angular observables for the $\Lambda_b^0 \to \Lambda\mu^+\mu^-$ decay, together with their correlations, is measured for the low-hadronic recoil region, *i.e.* high-q^2 defined as $15 < q^2 < 20\,\mathrm{GeV}^2/c^4$. The results are found to be generally consistent with the SM predictions (see figures 4.34 and 4.35). They are also compatible with popular New Physics scenarios (see section 1.6.3), as shown in figure 4.36. A small deviation on the order of 2.6 σ with respect to the SM prediction is observed for K_6, which translates into an equivalent deviation for the $A_{FB}^{\ell h}$. In addition, moments from $K_{11} - K_{34}$ are compatible with zero as expected for a measured Λ_b^0 production polarisation close to zero. From the measured moments, well-known asymmetry parameters are determined [1],

$$\begin{aligned} A_{FB}^{\ell} &\equiv \frac{3}{2}K_3 = -0.39 \pm 0.04 \pm 0.01\ , \\ A_{FB}^{\mathrm{h}} &\equiv K_4 + \frac{1}{2}K_5 = -0.30 \pm 0.05 \pm 0.02\ , \\ A_{FB}^{\ell\mathrm{h}} &\equiv \frac{3}{4}K_6 = \quad 0.25 \pm 0.04 \pm 0.01\ . \end{aligned}$$

The result for A_{FB}^{h} is also consistent with the previous measurement [27], while A_{FB}^{ℓ} is not directly comparable with the previous LHCb measurement due to an inconsistency in the definition of the polar angle of the muon system used in Ref. [27].

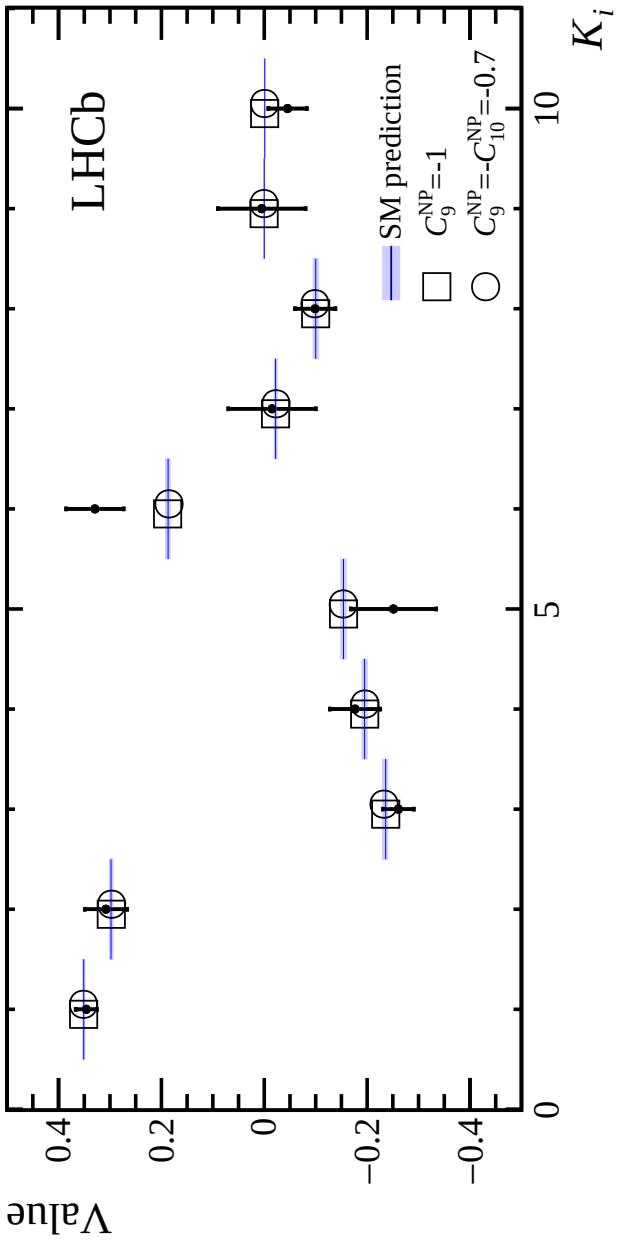

Figure 4.36: The first ten moments as extracted from the combined data set of Run1 and Run2, using both track types (black markers) are presented together with the SM prediction (blue line) and its uncertainties (light-blue coloured band). The predictions of the first ten moments for two different New Physics scenarios are also illustrated. The first scenario is for $C_9^{NP} = -C_{10}^{NP} = -0.7$ (circles) and the second one for $C_9^{NP} = -1$ (rectangles). For illustration purposes the central value of the prediction for the moments for the two NP scenario are horizontally shifted [1]. It must be noted that for these two NP scenarios in the high-q^2 bin, effects from NP cannot be distinguished from the SM contributions; in this spirit, results are consistent with the SM and also with potential effects from NP with $C_9^{NP} = -1$ or $C_9^{NP} = C_{10}^{NP} = 0.7$.

CHAPTER 5

Angular analysis of $\Lambda_b^0 \to J/\psi\,\Lambda$

In this chapter I will discuss the angular analysis of the $\Lambda_b^0 \to J/\psi\Lambda$ decay. The results are preliminary and correspond to the current status of the analysis. The strategy followed for the extraction of the angular observables shares many similarities with that presented in chapter 4, hence the description of previously discussed steps will be omitted. This chapter is organised in the following way: in section 5.1 the strategy for extracting the angular observables of the $\Lambda_b^0 \to J/\psi\,\Lambda$ decay is presented; sections 5.2 and 5.3 outline the selection and background subtraction respectively; in section 5.4 the description of the angular efficiency is presented; sections 5.5 and 5.6 illustrate the resolution and validation studies respectively; systematic

uncertainties are presented in section 5.7; results are presented in section 5.8 and summarised in section 5.9, which also draws conclusions from the analysis.

5.1 Strategy for extracting the angular observables

In the angular analysis of $\Lambda_b^0 \to J/\psi\,\Lambda$, angular observables in terms of moments are extracted following the methods described in section 4.1. The angular coefficients that are by construction zero (see section 1.7.1) are also extracted for validation purposes. The moments are measured using MC integration and the statistical uncertainties are estimated using the bootstrapping technique [96] (see section 4.1.1). After the extraction of the moments and the associated covariance matrix, the results are interpreted in terms of the Λ_b^0 production polarisation and the decay amplitudes (see table 1.1). In this analysis, the Run1 samples are now treated separately due to the small difference in $\sqrt{s}$ between 2011 and 2012 data-taking conditions.

Figure 5.1 shows an example of the 1D angular projections obtained when using similar values for the magnitudes of the decay amplitudes[1] and the Λ_b^0 production polarisation to those of Ref. [46]

[1] All phases are set to zero.

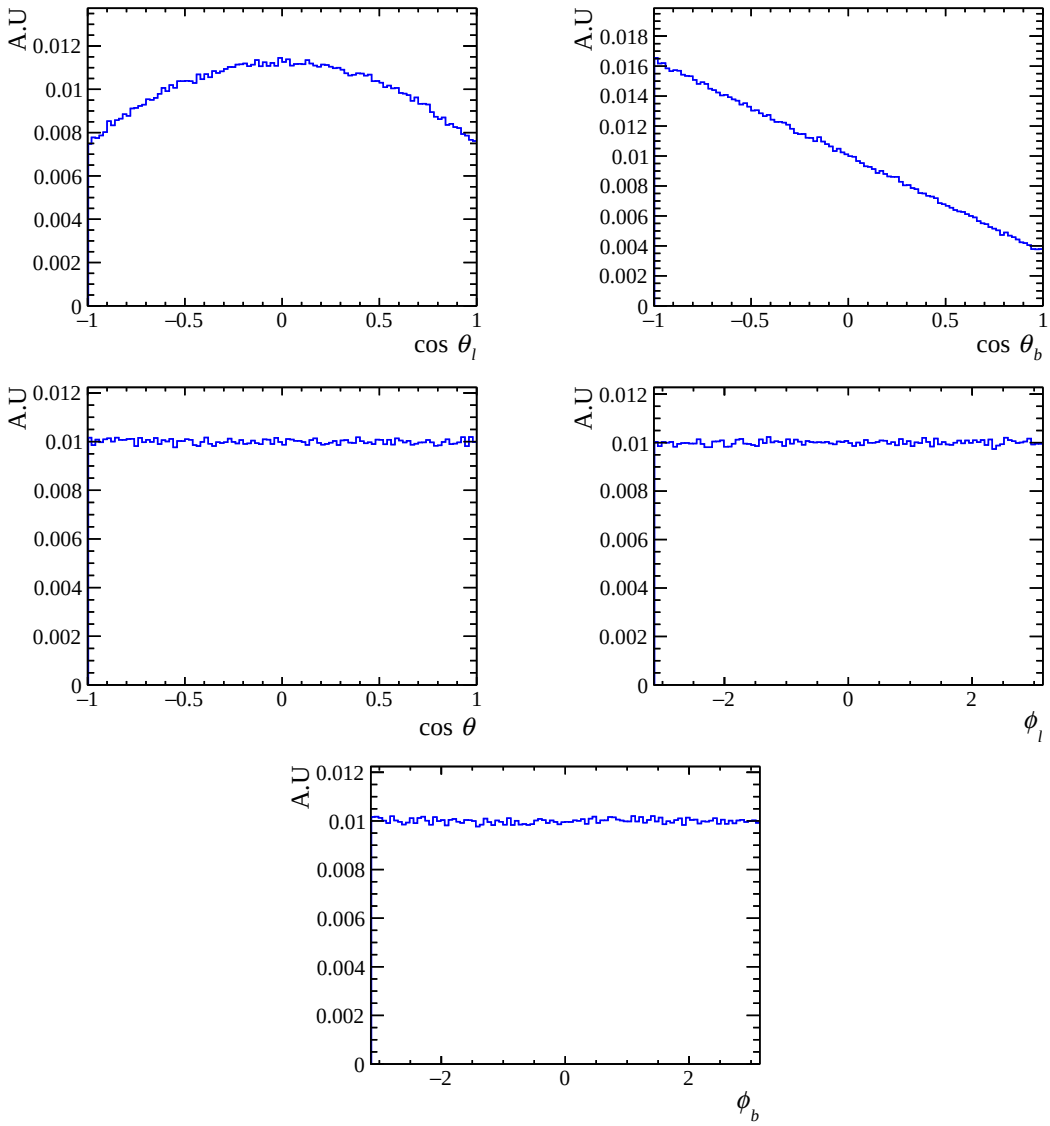

Figure 5.1: 1D angular projections for a pure signal sample with flat angular efficiency. The magnitudes of the decay amplitudes are set to values close to the LHCb measurement [46] and all the phases are set to zero, while the Λ_b^0 production polarisation is set to zero. For this particular set of values for the production polarisation and the decay amplitudes, J_7, J_9 and J_{11-34} are zero, resulting in $\cos\theta$, ϕ_l and ϕ_b being flat. The symmetric and asymmetric shapes of $\cos\theta_l$ and $\cos\theta_b$ originate from the fact that J_3 is zero and $J_{4,5}$ is negative, respectively in this particular example.

5.2 Selection

The trigger and stripping selection in this analysis is identical to that described in section 4.2. The preselection is as for the $\Lambda_b^0 \to \Lambda\mu^+\mu^-$ analysis, with the difference that now the dimuon invariant mass window used to define the J/ψ resonance is defined by the q^2 region $9.18 < q^2 < 9.92\,\mathrm{GeV}^2/c^4$. In addition, the PID requirement applied to the protons is removed and fiducial requirements on the transverse momentum ($1000 < p_\mathrm{T}(\Lambda_b^0 < 20000\,\mathrm{MeV}/c$) and pseudorapidity ($2 < \eta(\Lambda_b^0) < 5$) of the Λ_b^0 are applied to ensure that the Λ_b^0 production polarisation is performed in a well-defined region. The Neural Network is also very similar to that of the $\Lambda_b^0 \to \Lambda\mu^+\mu^-$ analysis with the main difference being the training samples employed.

A major difference with respect to the previous analysis is the splitting of the data samples. For the Run2 samples corresponding to the 2015 and 2016 data-taking periods the strategy is identical: the 2015 and 2016 samples are analysed separately before combined moments for these samples are extracted. In contrast, the 2011 and 2012 conditions are treated separately from each other since one of the objectives of the measurement is to investigate potential differences of the production polarisation of Λ_b^0 with $\sqrt{s}$.

In addition, a further small, technical difference with respect to the $\Lambda_b^0 \to \Lambda\mu^+\mu^-$ analysis, is that the particle momenta are obtained from a kinematic fit where certain constraints are imposed [107]. These are that the momentum vector of the Λ_b^0 is constrained to point back to the PV, and the invariant masses of the J/ψ and Λ

are constrained to their measured values [7]. This approach results in a significant improvement in the resolution of the signal peak, as shown in figure 5.2, which compares the invariant mass of the Λ_b^0 with and without use of the constrained fit. Although there is a clear improvement in the signal mass resolution, the substantial improvement in the resolution of the measured angles (see section 5.5) has a greater impact on the final measured results.

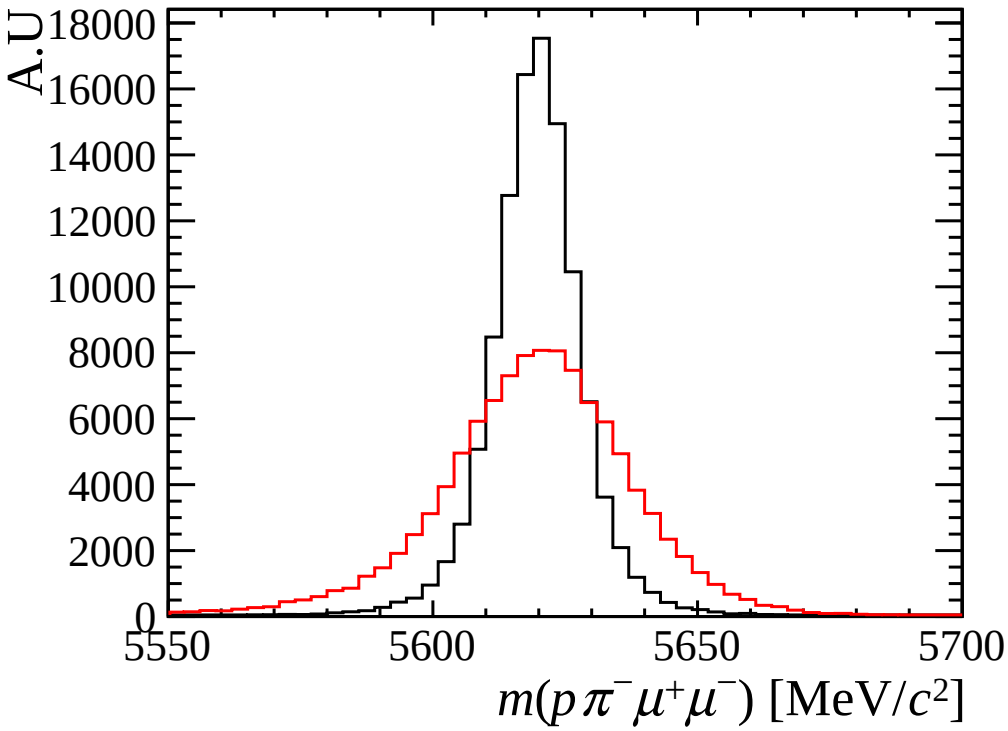

Figure 5.2: Invariant mass distribution of Λ_b^0, with (black histogram) and without (red histogram) the constrained kinematic fit, using 2011 MC combining both track categories.

5.3 Background subtraction

The statistical subtraction of the background is a necessary step towards the extraction of the angular observables of the $\Lambda_b^0 \to J/\psi\,\Lambda$ decay and it is performed with the same *sPlot* technique [101]) that is used in the $\Lambda_b^0 \to \Lambda\mu^+\mu^-$ analysis discussed in section 4.3.

5.3.1 Invariant mass fits

As in section 4.3.1, to compute the sWeights the lineshape that describes the invariant mass distribution of the data needs to be modelled. There are three components that define the total lineshape and need to be characterised, namely the contributions from the signal, the combinatorial background and the peaking background. The peaking background is dominated by misreconstructed $B^0 \to K_s^0(\to \pi^+\pi^-)J/\psi(\to \mu^+\mu^-)$ decays. In contrast to the treatment of the control mode in the $\Lambda_b^0 \to \Lambda\mu^+\mu^-$ analysis, no PID cut is applied to the protons which increases the contribution of the peaking background, now present in both track categories. The likelihood function that is used to estimate the contribution of the relevant components is given in equation 4.6.

5.3.2 Fit strategy

In the same way as for the mass fits in the $\Lambda_b^0 \to \Lambda\mu^+\mu^-$ analysis, several parameters that describe the lineshape of the signal component (see section 5.3.3) are fixed

using simulated samples. The parameters that describe the lineshape of peaking background candidates originating from $B^0 \to K_s^0(\to \pi^+\pi^-)J/\psi(\to \mu^+\mu^-)$ decays are all estimated from a fit to simulated samples of $B^0 \to K_s^0(\to \pi^+\pi^-)J/\psi(\to \mu^+\mu^-)$ reconstructed as $\Lambda_b^0 \to J/\psi\,\Lambda$ and are finally fixed in the fit of the total PDF to data. All the fits are performed using the RooFit toolkit [102].

5.3.3 Mass components

The components that describe the PDF which characterises the $m(p\pi^-\mu^+\mu^-)$ distribution are identical to those described for the control mode in section 4.3.3. The only difference is the change in the description of the signal shape where now, rather than using a two-sided CB function, the sum of a Gaussian with a CB_l and a CB_r is used, where the Gaussian and the double-sided CB function share the same mean but not width. The signal PDF is expressed as,

$$\begin{aligned} P_{\text{Sig}}(M) = f_g G(m; m_0, \sigma_g) + f_l C_l(m; m_0, \sigma_f, \alpha_l, n_l) \\ + (1 - f_l - f_g) C_r(m; m_0, \sigma_f, \alpha_r, n_r), \end{aligned} \tag{5.1}$$

where the f_l and f_g correspond to the fractional contribution of the CB_l and the Gaussian functions respectively. The tail parameters of the CB together with their fractional contribution are fixed from a fit to MC. The fraction that the Gaussian contributes to the signal component is also fixed from a fit on MC samples.

5.3.4 Fit to $\Lambda_b^0 \to J/\psi\,\Lambda$ candidates

Fits to the invariant mass distribution of $\Lambda_b^0 \to J/\psi\,\Lambda$ for both track categories and for each of the data-taking years are illustrated in figures 5.3, 5.4, 5.5 and 5.6, while the results of the parameters that are floating in the fit are presented in table 5.1.

Decay Mode (Track Type)	M_0 (MeV/c^2)	σ_f (MeV/c^2)	σ_g (MeV/c^2)	N_{Sig}	N_{Comb}	N_{Peak}	c_{exp}
$\Lambda_b^0 \to J/\psi\,\Lambda$ (LL)(2011)	5621.04 $\pm$0.22	6.42 $\pm$0.27	12.20 $\pm$1.00	1792 $\pm$46	1528 $\pm$71	283 $\pm$60	$-$0.0020 $\pm$0.0002
$\Lambda_b^0 \to J/\psi\,\Lambda$ (DD)(2011)	5621.31 $\pm$0.18	7.40 $\pm$0.22	12.47 $\pm$0.99	3027 $\pm$59	2142 $\pm$85	858 $\pm$75	$-$0.0021 $\pm$0.0002
$\Lambda_b^0 \to J/\psi\,\Lambda$ (LL)(2012)	5621.02 $\pm$0.15	6.32 $\pm$0.14	13.35 $\pm$1.10	4086 $\pm$73	3580 $\pm$110	970 $\pm$91	$-$0.0018 $\pm$0.0001
$\Lambda_b^0 \to J/\psi\,\Lambda$ (DD)(2012)	5621.14 $\pm$0.11	7.56 $\pm$0.13	13.85 $\pm$0.69	7907 $\pm$97	5333 $\pm$1365	2236 $\pm$122	$-$0.0021 $\pm$0.0001
$\Lambda_b^0 \to J/\psi\,\Lambda$ (LL)(2015)	5619.82 $\pm$0.31	6.31 $\pm$0.35	12.92 $\pm$1.60	929 $\pm$34	772 $\pm$54	261 $\pm$49	$-$0.0021 $\pm$0.0003
$\Lambda_b^0 \to J/\psi\,\Lambda$ (DD)(2015)	5619.78 $\pm$0.25	7.15 $\pm$0.29	13.91 $\pm$1.24	1721 $\pm$48	1600 $\pm$74	513 $\pm$67	$-$0.0019 $\pm$0.0002
$\Lambda_b^0 \to J/\psi\,\Lambda$ (LL)(2016)	5619.95 $\pm$0.12	6.40 $\pm$0.16	11.49 $\pm$0.62	6291 $\pm$88	6131 $\pm$146	1378 $\pm$127	$-$0.0017 $\pm$0.0001
$\Lambda_b^0 \to J/\psi\,\Lambda$ (DD)(2016)	5619.57 $\pm$0.09	7.11 $\pm$0.11	12.70 $\pm$0.44	12812 $\pm$125	10719 $\pm$161	3940 $\pm$185	$-$0.0020 $\pm$0.0001

Table 5.1: Mass parameters for the $\Lambda_b^0 \to J/\psi\,\Lambda$ lineshape, that are floating in the fit on data. The values are extracted from a fit on the 2011, 2012, 2015 and 2016 data samples. As expected, the estimated yields vary between the different data-taking years mainly due to the differences in the recorded luminosity and the increase of the $b\bar{b}$ cross section with $\sqrt{s}$. The main source of background is the combinatorial background.

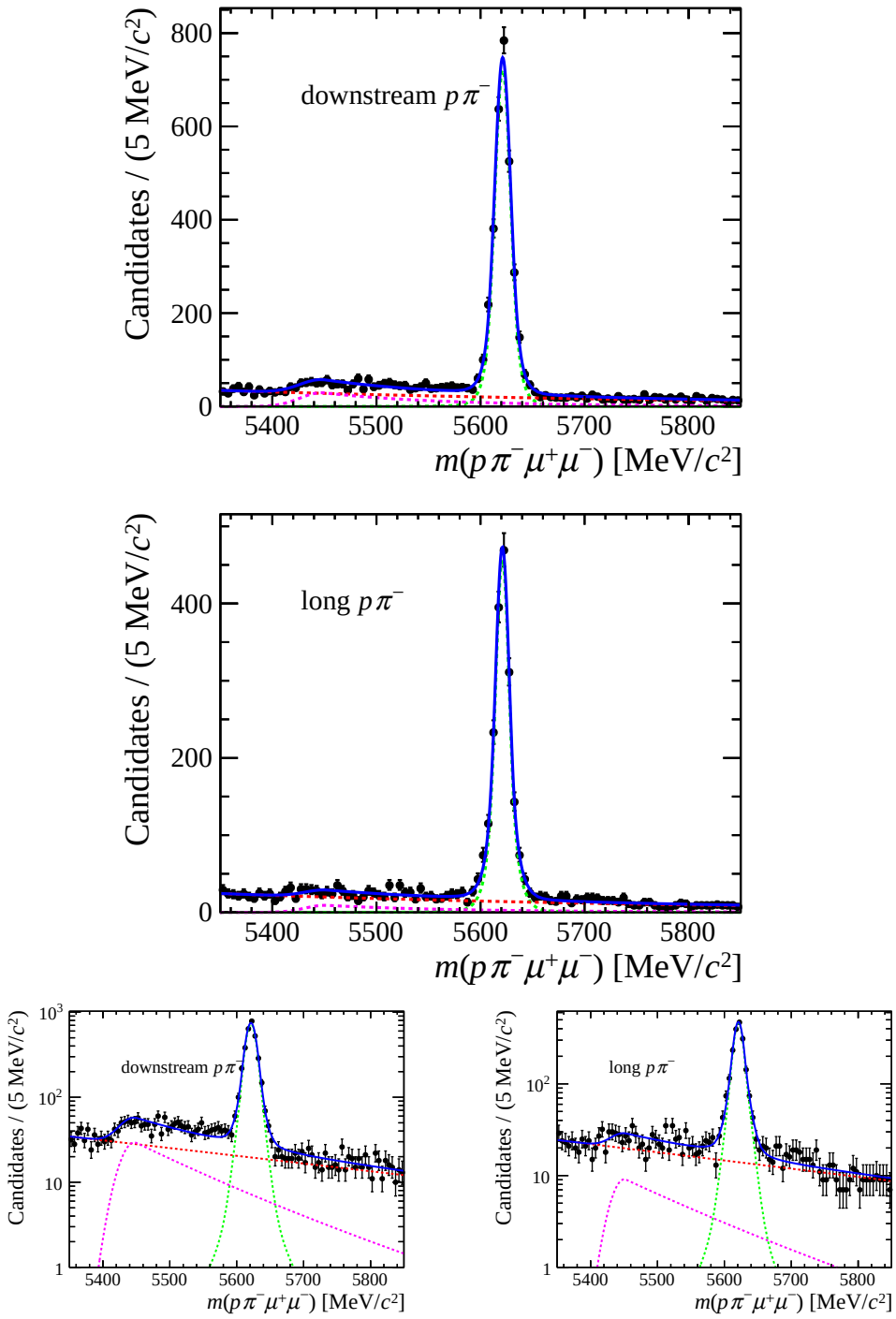

Figure 5.3: Invariant mass distribution of $\Lambda_b^0 \to J/\psi\,\Lambda$ for DD (top) and LL (middle) categories in 2011 data samples. Overlaid are the projections of the fitted components. The blue line represents the total contribution of the mass components, while the red and green dotted lines represent the contribution of the combinatorial and signal components respectively. The magenta dotted line represents the contribution from the peaking background. The same plots are illustrated in logarithmic scale in the bottom left (DD category) and right (LL category) figures.

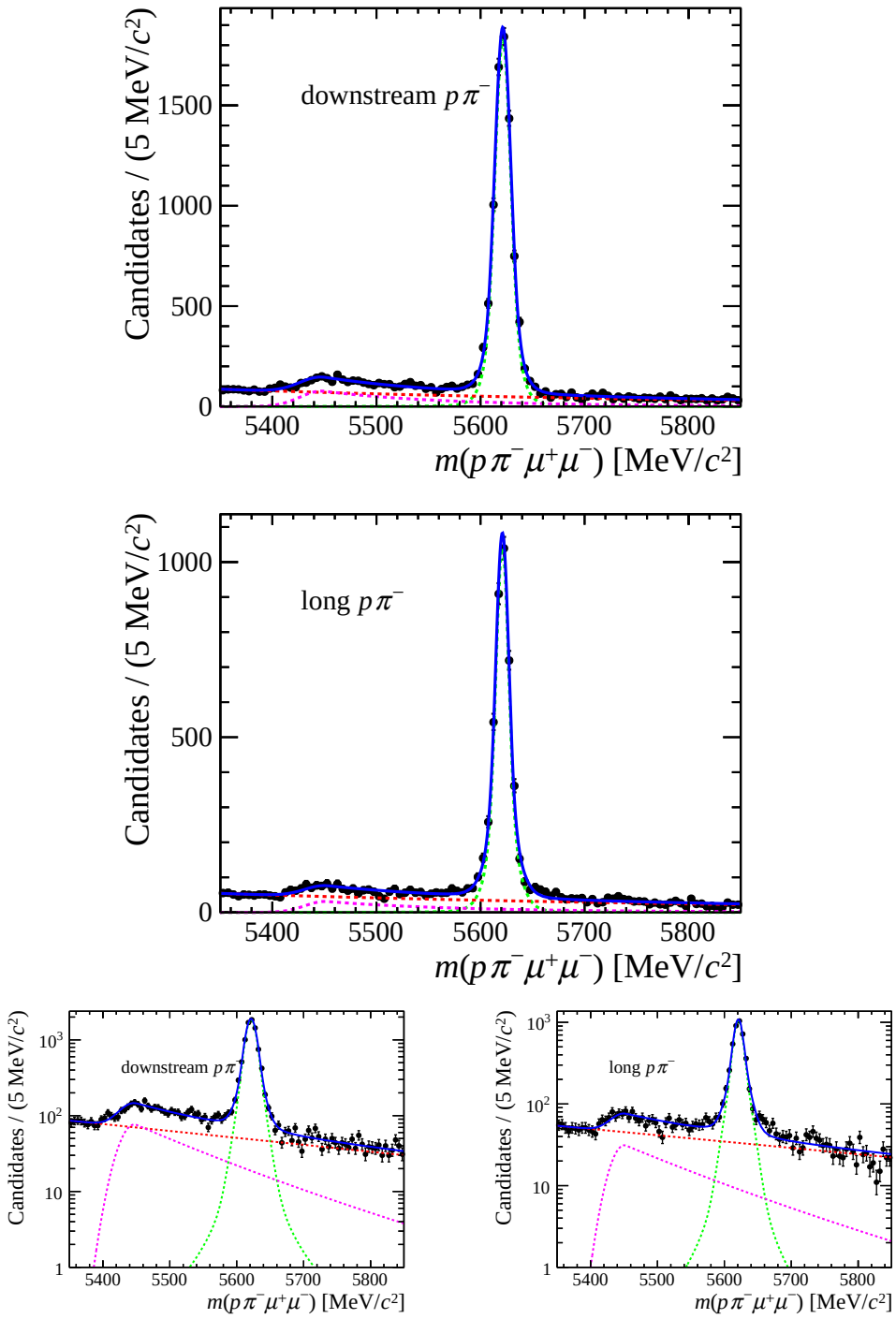

Figure 5.4: Invariant mass distribution of $\Lambda_b^0 \to J/\psi\,\Lambda$ for DD (top) and LL (middle) categories in 2012 data samples. Overlaid are the projections of the fitted components. The blue line represents the total contribution of the mass components, while the red and green dotted lines represent the contribution of the combinatorial and signal components respectively. The magenta dotted line represents the contribution from the peaking background. The same plots are illustrated in logarithmic scale in the bottom left (DD category) and right (LL category) figures.

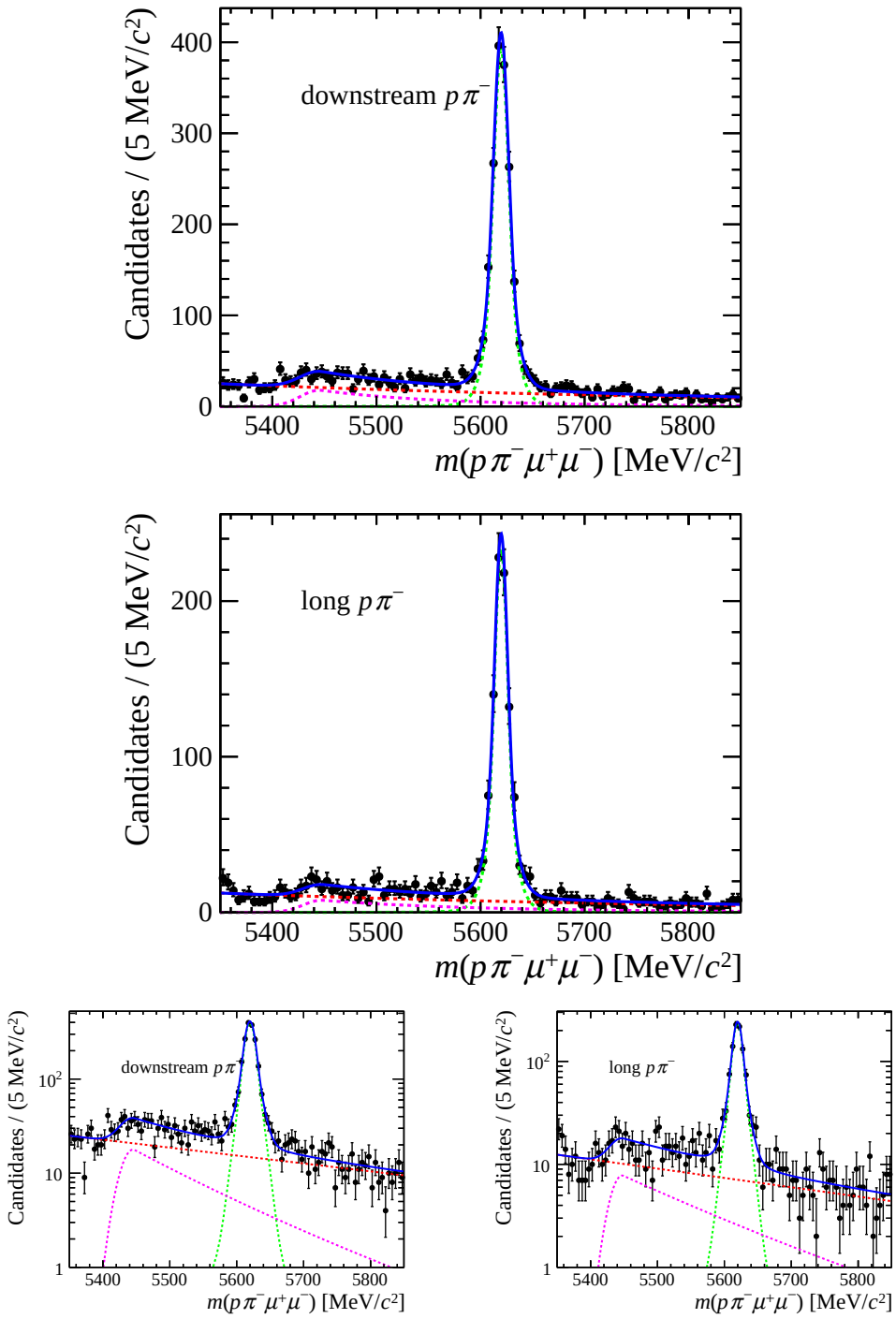

Figure 5.5: Invariant mass distribution of $\Lambda_b^0 \to J/\psi\,\Lambda$ for DD (top) and LL (middle) categories in 2015 data samples. Overlaid are the projections of the fitted components. The blue line represents the total contribution of the mass components, while the red and green dotted lines represent the contribution of the combinatorial and signal components respectively. The magenta dotted line represents the contribution from the peaking background. The same plots are illustrated in logarithmic scale in the bottom left (DD category) and right (LL category) figures.

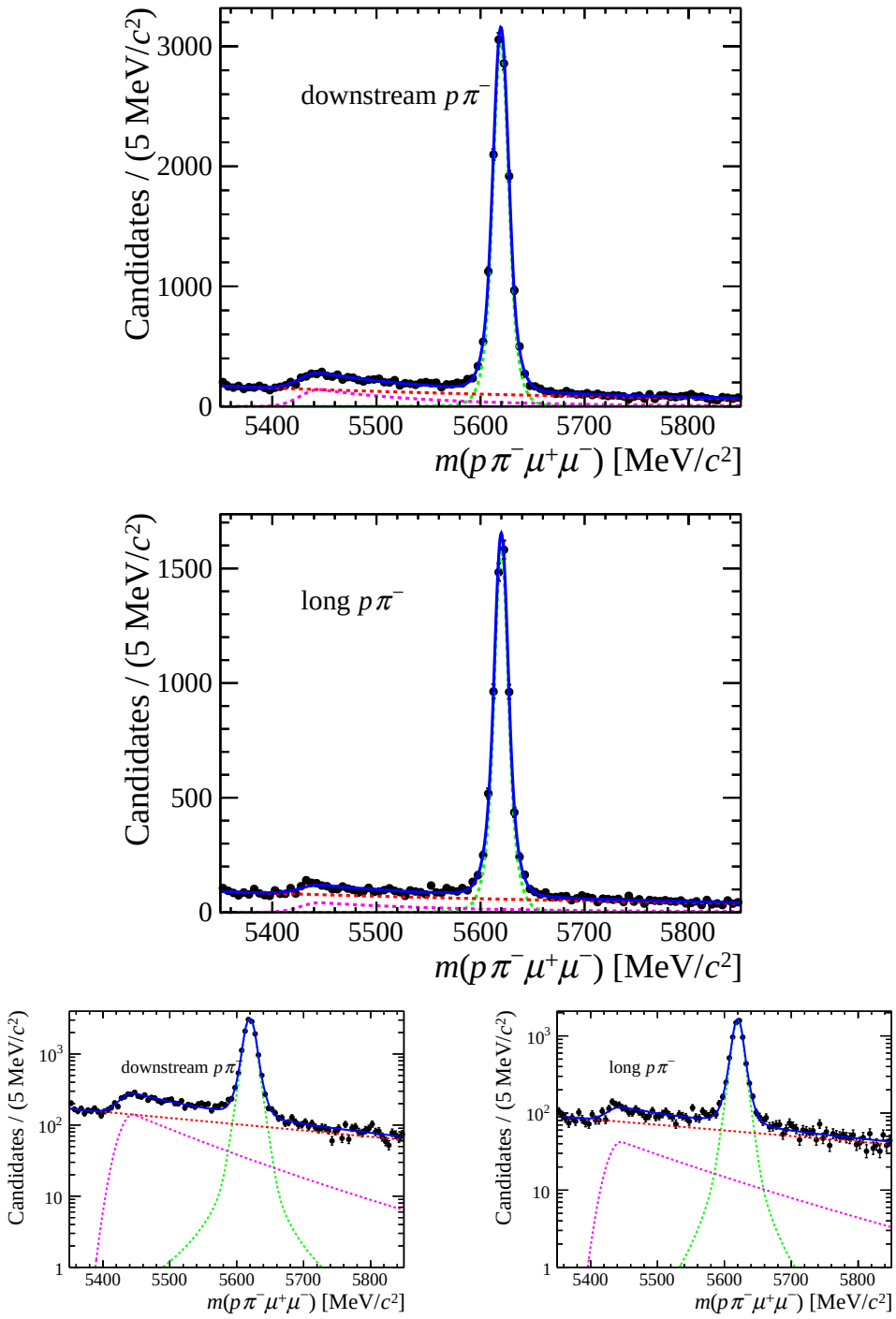

Figure 5.6: Invariant mass distribution of $\Lambda_b^0 \to J/\psi\,\Lambda$ for DD (top) and LL (middle) categories in 2016 data samples. Overlaid are the projections of the fitted components. The blue line represents the total contribution of the mass components, while the red and green dotted lines represent the contribution of the combinatorial and signal components respectively. The magenta dotted line represents the contribution from the peaking background. The same plots are illustrated in logarithmic scale in the bottom left (DD category) and right (LL category) figures.

5.4 Determination of the relative efficiency

The angular efficiency is parametrised in 5D using Legendre Polynomials as described by equation 4.21, using samples of simulated $\Lambda_b^0 \to J/\psi\,\Lambda$ decays, after being corrected for imperfections in simulation. These corrections follow those of the $\Lambda_b^0 \to \Lambda\mu^+\mu^-$ analysis (see section 4.4), differing in the preselection and NN applied to the $\Lambda_b^0 \to J/\psi\,\Lambda$ samples. The MC correction is extracted separately for each of the four years of data-taking and for each track category. After these corrections, good agreement between background-corrected data and MC is obtained. The efficiency models are extracted in an iterative way following section 4.5, where the orders of polynomials used for the 1D and the 2D corrections are similar to those used for the $\Lambda_b^0 \to \Lambda\mu^+\mu^-$ efficiency models[2]. Small additional corrections related to correlations observed between the $\cos\theta$ and ϕ_b are also included.

The angular efficiency is described separately for the 2011, 2012, 2015 and 2016 data samples and for each track category, in contrast to $\Lambda_b^0 \to \Lambda\mu^+\mu^-$ analysis, where the 2011 + 2012 MC samples were merged and a single efficiency model was derived. An example of the 1D angular projections of the downstream category for the 2012 MC sample is illustrated in figure 5.7. The angular efficiencies of $\Lambda_b^0 \to J/\psi\,\Lambda$ and $\Lambda_b^0 \to \Lambda\mu^+\mu^-$ are very similar, as expected; small differences exist due to the correlation of the q^2 with the angles. The quality of the efficiency modelling in terms of 1D, 2D and 1D projections in several bins of the angles is tested and found to be very good. In addition, the distribution of the efficiency weights in data do not

[2]The dimension for the q^2 is removed and the weights relevant for $q^{2,gen}$ are set to one.

contain extreme values that can potentially bias the estimates of the moments and their associated statistical uncertainties.

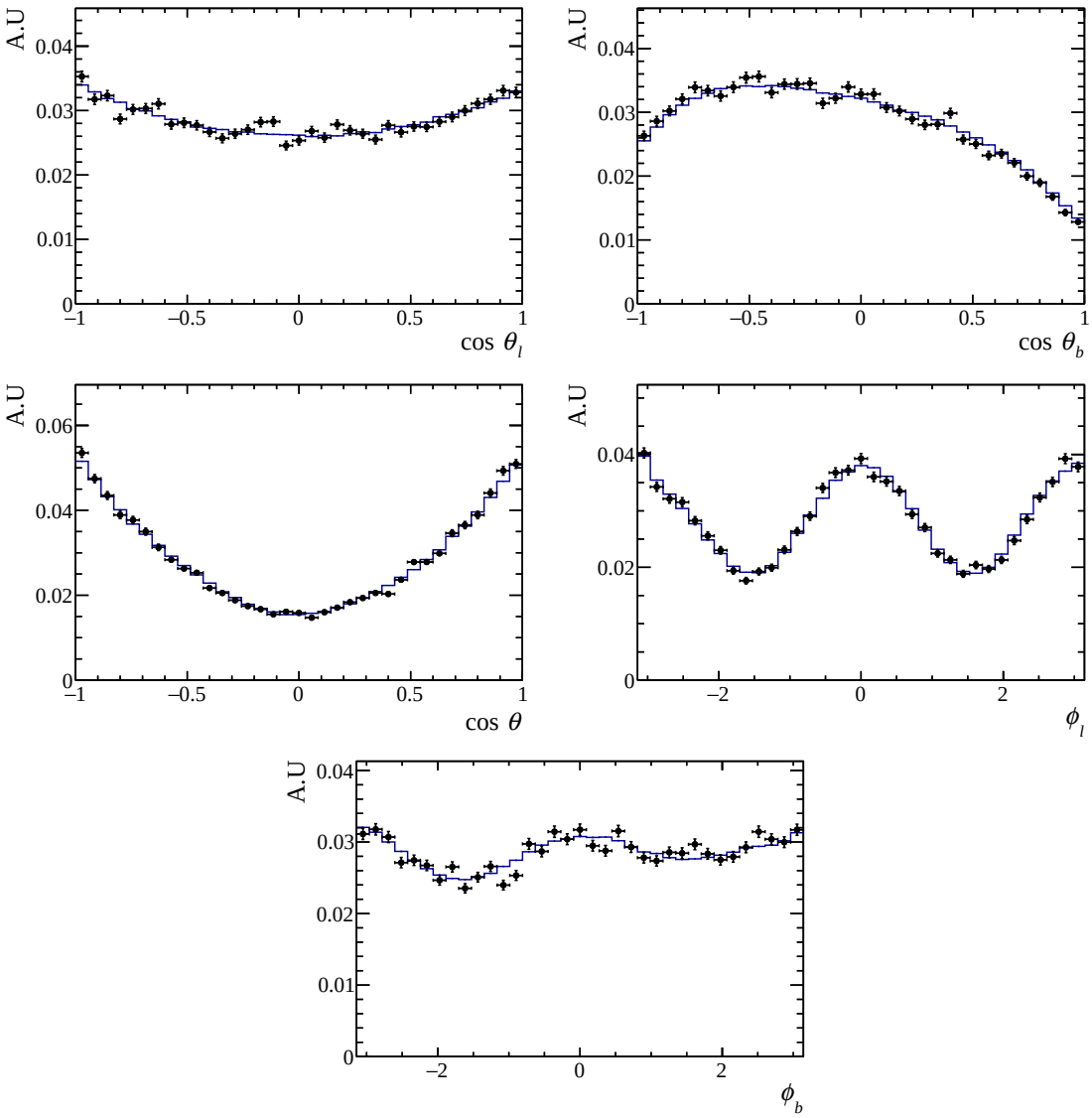

Figure 5.7: 1D efficiency projections for the 2012 MC using the DD category. The black data points represent the weighted MC sample, while the blue line the efficiency model. The dominant features such as the oscillation in the azimuthal angles, originate mainly due to momentum requirements imposed on the muons and hadrons respectively, while the asymmetries observed in the hadron-related angles are due to the different masses of the proton and pion.

5.5 Resolution studies

Resolution studies are performed in the same manner as those conducted in section 4.6. In this analysis the usage of momentum computed by removing certain degrees of freedom (see section 5.2) improves the angular resolution. The latter is particularly improved in the DD category for the azimuthal and polar angles of the proton, as highlighted in figure 5.8, where a comparison between the angular resolutions obtained with and without using the constraints for the 2011 MC sample is presented. The angular resolutions are extracted separately for each of the four years of data taken and for each track category.

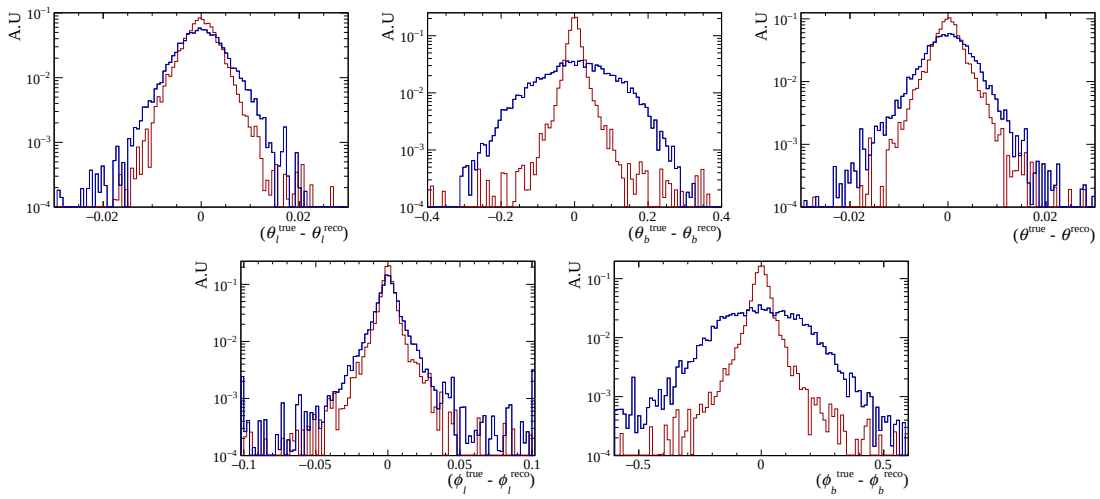

Figure 5.8: Comparison of angular resolution for the 2011 MC using DD tracks, with (red histogram) and without (blue histogram) the constraints.

5.6 Validation studies

To validate the robustness of the framework used to estimate the moments, validation studies are performed in a similar way to those introduced in section 4.7. The pseudo-experiments are generated as follows: the invariant mass distributions of the signal, combinatorial and peaking background components are generated using the models described in section 5.3. The parameters that describe the lineshape of the various components are fixed to the values presented in table 5.1, with the exception of the tail parameters of the double-sided CB and the fractional contribution of the Gaussians to the signal component and all the parameters that describe the lineshape of the peaking background component, which are fixed by performing a fit to the relevant MC samples (see section 5.3). The angular distribution of the combinatorial background is generated in a similar way to that of section 4.7; the angular distribution of the peaking background is modelled using LP and assuming factorisation of the angles using MC samples of $B^0 \to J/\psi\,K^0_{\rm S}$ decays reconstructed as $\Lambda_b^0 \to J/\psi\,\Lambda$ where the full selection of the default analysis is applied first. The angular distribution of the signal component is generated using the decay rate of the $\Lambda_b^0 \to J/\psi\,\Lambda$, where the angular coefficients are set to values that correspond to the following set of P_b and decay amplitudes; $|\alpha_-| = |b_+|$, $|\alpha_+| = |\beta_-| = 0$ and $P_b = 0$. The choice of the magnitudes of the decay amplitudes and the production polarisation of Λ_b^0 is driven from the previous measurements and also from what is observed in data in terms of moments (see section 5.8). It must be noted that for this choice of the magnitudes and P_b, the values of the phases are irrelevant. In the

case that $P_b = 0$, the only coefficients that are sensitive to the phases are:

$$\begin{aligned} J_7 \equiv & \frac{\alpha_\Lambda}{\sqrt{2}}\mathrm{Re}(-b_+^* a_+ + b_- a_-^*) \\ = & \frac{\alpha_\Lambda}{\sqrt{2}}(-|b_+||\alpha_+|\cos(\theta_{\alpha_+} - \theta_{b_+}) + |b_-||\alpha_-|\cos(-\theta_{\alpha_-} + \theta_{b_-}))\ , \\ J_9 \equiv & \frac{\alpha_\Lambda}{\sqrt{2}}\mathrm{Im}(b_+^* a_+ - b_- a_-^*) \\ = & \frac{\alpha_\Lambda}{\sqrt{2}}(|b_+||\alpha_+|\sin(\theta_{\alpha_+} - \theta_{b_+}) - |b_-||\alpha_-|\sin(-\theta_{\alpha_-} + \theta_{b_-}))\ , \end{aligned}$$

where the phases appear only as a product of $|\alpha_\pm||b_\pm|$; the latter become zero since in the toys the $|\alpha_+| = |b_-| = 0$. This results in the angular PDF not having sensitivity to the phases. An example of the angular and invariant mass distributions in a single pseudo-experiment is given in figure 5.9. Toy studies are performed separately for the 2011, 2012 and 2015 + 2016 conditions, with both track categories in each case. From the toy studies, no significant biases in the mean or width of the pull distributions (see equation 4.25) of the K_i moments is observed.

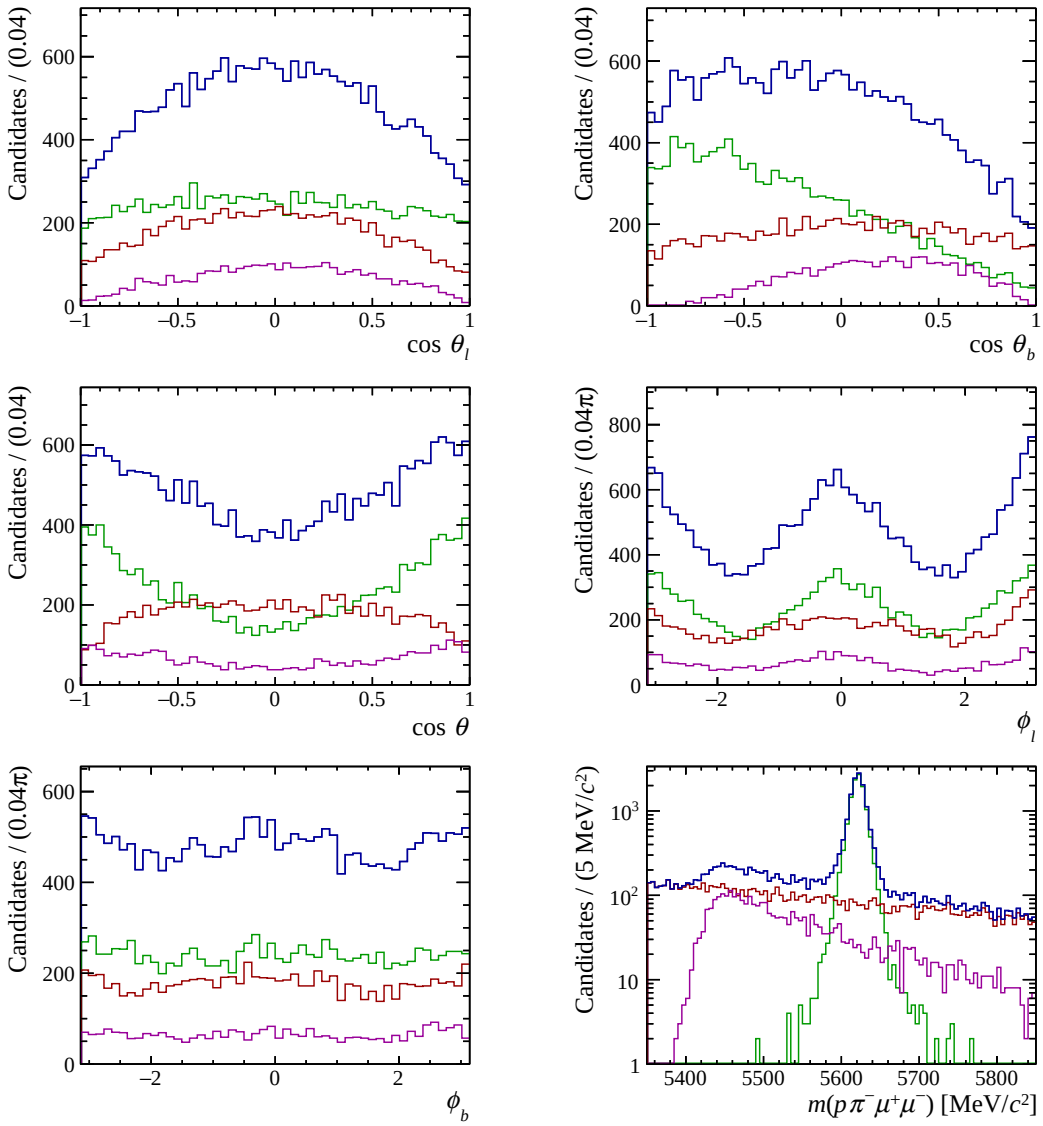

Figure 5.9: 1D projections of the angles and the invariant mass distribution as generated in a single pseudo-experiment. In all the cases, the red and magenta lines represent the contribution of the combinatorial and peaking background, the green line represents the signal contribution while the blue line corresponds to the combined contribution. In this pseudo-experiment the distributions are generated as a representation of the 2012 sample, including both DD and LL categories. The distributions are not corrected using the sWeights or the efficiency weights.

5.7 Systematic uncertainties

The sources of potential systematic uncertainty for the moments are considered and evaluated separately for the 2011, 2012 and $2015 + 2016$ data samples. The sources considered in this analysis are closely related to those discussed in section 4.8 and are evaluated following a similar methodology. When the systematic uncertainties are evaluated using toy studies, the generation of the pseudo-experiments is performed in the same way as outlined in section 5.6, with the difference that the samples are generated with systematic variations introduced in the models corresponding to the source of systematic uncertainty under study.

5.7.1 Summary of systematic uncertainties

The systematic uncertainties are extracted separately for the four data-taking years. The overall systematic uncertainty for each of the moments is defined as the square root of the sum in quadrature of all sources considered[3]. The systematic uncertainties are found to be uncorrelated between each data set. The estimated size of systematic uncertainties are typically found to be relatively small compared to the statistical uncertainties. The largest effect attributed is due to the finite size of the simulated samples used in the study, which on average contributes at the level of 20% of the statistical uncertainty.

[3]Due to the relatively small size of the MC samples for the 2011 and 2012 data sets, systematic uncertainties that depend of the size of the latter are larger for these samples compared to those extracted for the $2015 + 2016$ data sample; for this reason additional MC samples are requested, although not yet available.

5.8 Results

The moments are extracted separately for the 2011, 2012 and 2015 + 2016 data samples but combining both track types. Moments are also extracted separately for the DD and LL categories and are found to be consistent. A comparison of the moments from the DD and LL categories for the 2011, 2012 and 2015 + 2016 data samples is illustrated in figure B.2. Moments that are extracted from a combined data set, *e.g.* a data sample with both track categories and multiple data-taking years, are extracted as follows: the sWeights and the efficiency weights are extracted for each track category and each data-taking year separately; the weighted samples are combined and moments are extracted from the combined data set. For the determination of the statistical uncertainties the latter process is repeated for each of the bootstrapping iterations.

5.8.1 Numerical results

Before results in terms of the moments of the distribution are presented, the bootstrapping distributions are tested, with the latter found to have a Gaussian shape and so the statistical uncertainties can be considered symmetric. Numerical results and 1D angular projections for 2011, 2012 and 2015 + 2016 data samples combining both track categories are presented in table 5.2 and figures 5.10, 5.11, 5.12 respectively. The correlation matrices are given in Appendix B.2; in general the correlations between the moments are found to be small but may be as large as 40%

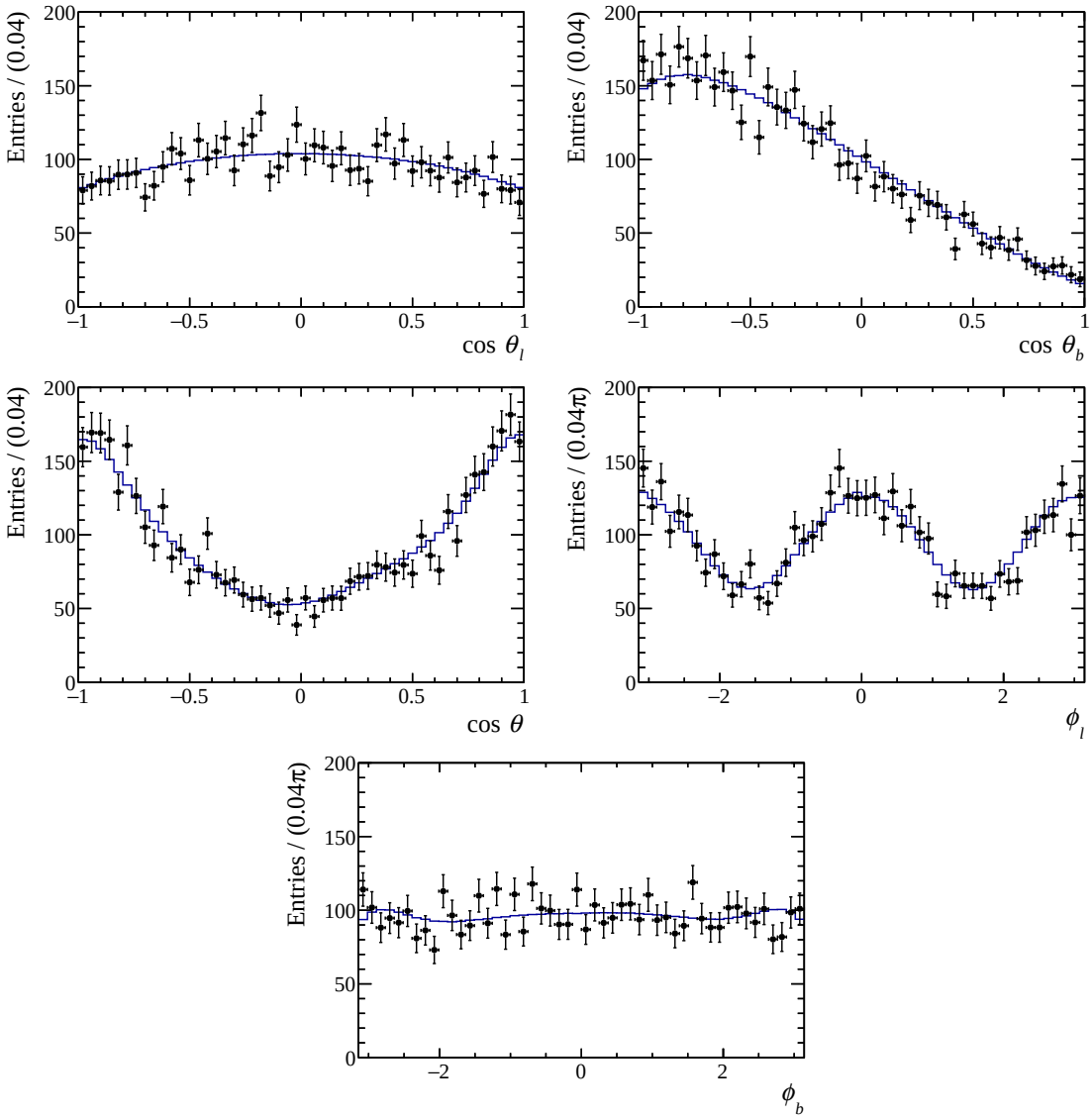

Figure 5.10: 1D projections of the angular PDF, where the moments are set to the values extracted from the 2011 data set, using both track categories. The candidates represented by the black markers are weighted with the sWeights but not with the efficiency weights. The angular PDF is multiplied finally by the efficiency functions and illustrated by the blue line.

in some cases. Moments that are zero by construction and negligible in the massless limit are found to be consistent with zero, as summarised in table B.1.

Table 5.2: Measured values of the moments extracted from the combined samples of 2011 (top), 2012 (middle), 2015+2016 (bottom) samples, using both track categories. The first and second uncertainties represent the statistical and systematic errors respectively. Moments that are by construction zero and negligible in the massless ($\beta_l = 1$) limit are omitted.

Obs.	Value	Obs.	Value
K_1	$0.3733 \pm 0.0068 \pm 0.0035$	K_{17}	$-0.0046 \pm 0.0384 \pm 0.0112$
K_2	$0.2534 \pm 0.0137 \pm 0.0069$	K_{19}	$-0.0008 \pm 0.0378 \pm 0.0065$
K_4	$-0.2788 \pm 0.0171 \pm 0.0069$	K_{21}	$-0.0208 \pm 0.0355 \pm 0.0076$
K_5	$-0.1590 \pm 0.0254 \pm 0.0081$	K_{23}	$0.0033 \pm 0.0276 \pm 0.0135$
K_7	$0.0446 \pm 0.0285 \pm 0.0077$	K_{25}	$-0.0159 \pm 0.0642 \pm 0.0113$
K_9	$-0.0202 \pm 0.0280 \pm 0.0047$	K_{27}	$0.0499 \pm 0.0502 \pm 0.0118$
K_{11}	$0.0119 \pm 0.0140 \pm 0.0082$	K_{30}	$0.0022 \pm 0.0214 \pm 0.0037$
K_{12}	$-0.0154 \pm 0.0185 \pm 0.0103$	K_{32}	$0.0010 \pm 0.0208 \pm 0.0090$
K_{14}	$0.0069 \pm 0.0257 \pm 0.0124$	K_{33}	$0.0172 \pm 0.0205 \pm 0.0040$
K_{15}	$0.0000 \pm 0.0336 \pm 0.0125$	K_{34}	$0.0167 \pm 0.0209 \pm 0.0031$

Obs.	Value	Obs.	Value
K_1	$0.3693 \pm 0.0043 \pm 0.0016$	K_{17}	$0.0030 \pm 0.0246 \pm 0.0044$
K_2	$0.2615 \pm 0.0086 \pm 0.0031$	K_{19}	$-0.0168 \pm 0.0246 \pm 0.0035$
K_4	$-0.2607 \pm 0.0108 \pm 0.0046$	K_{21}	$0.0112 \pm 0.0215 \pm 0.0041$
K_5	$-0.1983 \pm 0.0164 \pm 0.0048$	K_{23}	$-0.0251 \pm 0.0166 \pm 0.0058$
K_7	$0.0148 \pm 0.0176 \pm 0.0032$	K_{25}	$-0.0052 \pm 0.0378 \pm 0.0072$
K_9	$-0.0149 \pm 0.0175 \pm 0.0021$	K_{27}	$0.0171 \pm 0.0300 \pm 0.0055$
K_{11}	$0.0055 \pm 0.0090 \pm 0.0040$	K_{30}	$-0.0249 \pm 0.0134 \pm 0.0030$
K_{12}	$0.0068 \pm 0.0118 \pm 0.0046$	K_{32}	$0.0174 \pm 0.0131 \pm 0.0040$
K_{14}	$-0.0169 \pm 0.0161 \pm 0.0054$	K_{33}	$-0.0211 \pm 0.0131 \pm 0.0017$
K_{15}	$0.0082 \pm 0.0213 \pm 0.0055$	K_{34}	$0.0308 \pm 0.0130 \pm 0.0014$

Obs.	Value	Obs.	Value
K_1	$0.3769 \pm 0.0030 \pm 0.0008$	K_{17}	$0.0138 \pm 0.0179 \pm 0.0022$
K_2	$0.2462 \pm 0.0059 \pm 0.0017$	K_{19}	$-0.0077 \pm 0.0178 \pm 0.0020$
K_4	$-0.2694 \pm 0.0081 \pm 0.0039$	K_{21}	$-0.0297 \pm 0.0160 \pm 0.0050$
K_5	$-0.1957 \pm 0.0111 \pm 0.0031$	K_{23}	$0.0192 \pm 0.0124 \pm 0.0029$
K_7	$0.0090 \pm 0.0129 \pm 0.0018$	K_{25}	$0.0433 \pm 0.0283 \pm 0.0049$
K_9	$-0.0260 \pm 0.0128 \pm 0.0012$	K_{27}	$0.0361 \pm 0.0225 \pm 0.0031$
K_{11}	$-0.0042 \pm 0.0065 \pm 0.0018$	K_{30}	$0.0074 \pm 0.0098 \pm 0.0010$
K_{12}	$0.0058 \pm 0.0085 \pm 0.0022$	K_{32}	$-0.0173 \pm 0.0092 \pm 0.0016$
K_{14}	$-0.0067 \pm 0.0119 \pm 0.0024$	K_{33}	$-0.0099 \pm 0.0094 \pm 0.0013$
K_{15}	$-0.0102 \pm 0.0158 \pm 0.0026$	K_{34}	$0.0084 \pm 0.0093 \pm 0.0012$

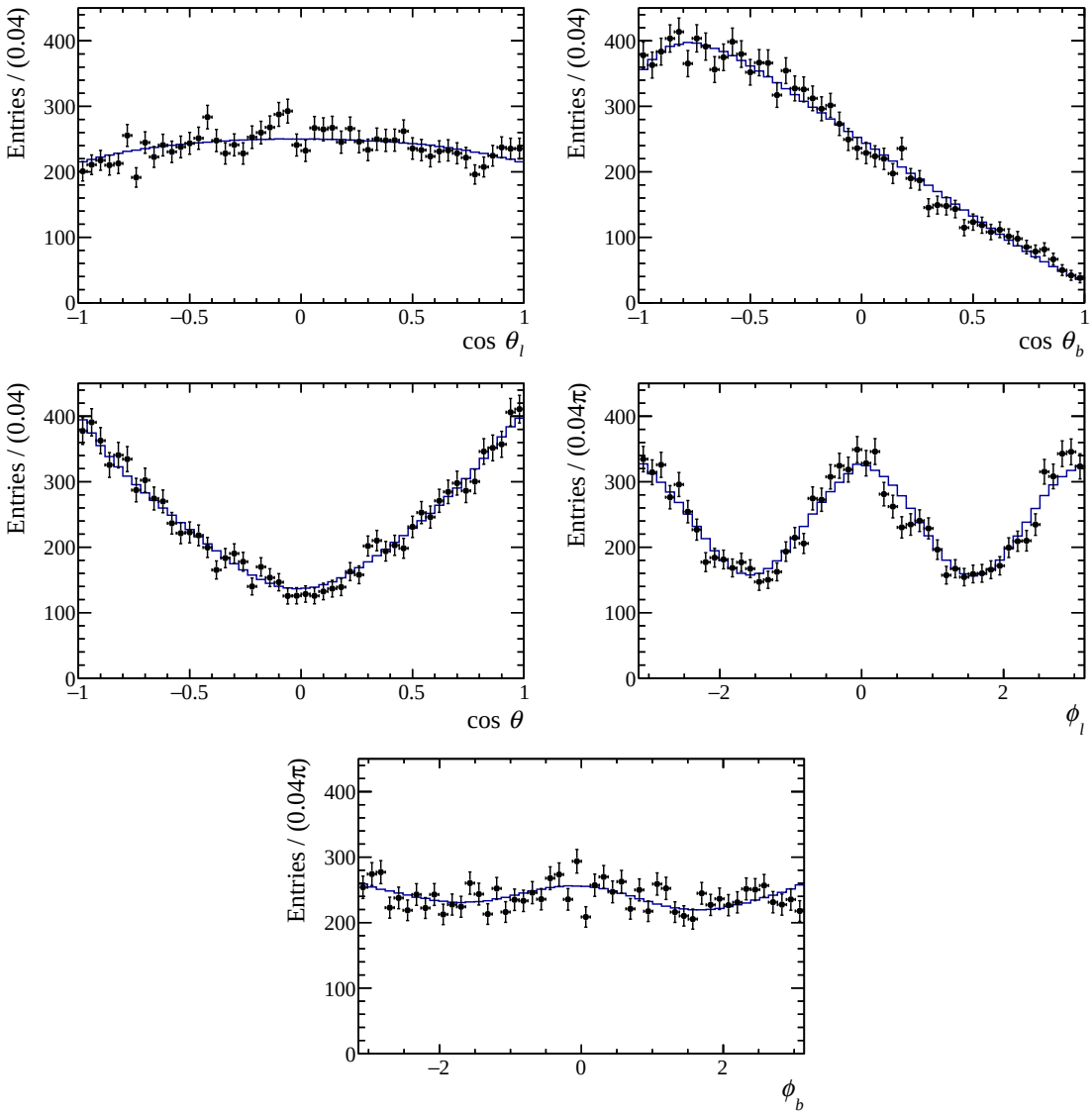

Figure 5.11: 1D projections of the angular PDF, where the moments are set to the values extracted from the 2012 data set, using both track categories. The candidates represented by the black markers are weighted with the sWeights but not with the efficiency weights. The angular PDF is multiplied finally by the efficiency functions and illustrated by the blue line.

5.8.2 Interpretation of the results

The moments extracted from all years are summarised in figure 5.13. Moments K_{11}-K_{34} are found to be compatible with zero pointing to a Λ_b^0 production polarisation that is consistent with zero and compatible with previous measurements [46, 47].

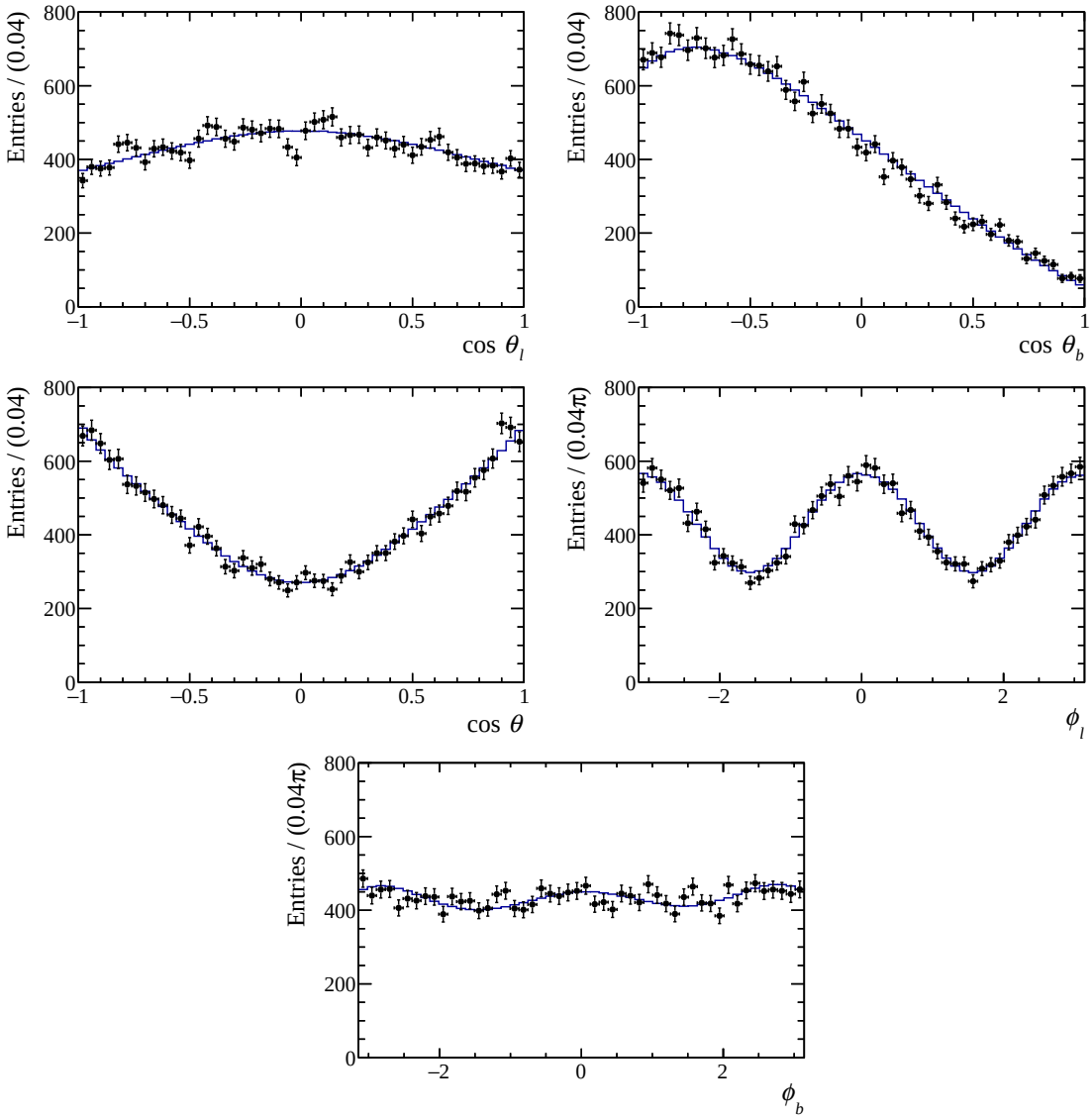

Figure 5.12: 1D projections of the angular PDF, where the moments are set to the values extracted from the combined data set of 2015 + 2016, using both track categories. The candidates represented by the black markers are weighted with the sWeights but not with the efficiency weights. The angular PDF is multiplied finally by the efficiency functions and illustrated by the blue line.

In addition, as the latter moments are compatible between the 2011, 2012 and 2015 + 2016 data-taking years, there is no strong evidence for a P_b that varies with $\sqrt{s}$ in the range 7–13 TeV. The previous measurements [46, 47, 56] found that the $|b_+| \approx |\alpha_-|$ and $|b_-| \approx |\alpha_+| \approx 0$, which will lead to $\alpha_b \equiv (|\alpha_+|^2 - |\alpha_-|^2 + |b_+|^2 - |b_-|^2)/(|\alpha_+|^2 + |\alpha_-|^2 + |b_+|^2 + |b_-|^2) \equiv (2K_4 - 3K_5)/\alpha_\Lambda \approx 0$, which is compatible

with the moments measured in this analysis. This configuration of amplitudes also agrees with the value for K_7 and K_9 which are consistent with zero, since in these moments the phases appear as a product of $|\alpha_\pm||b_\pm|$.

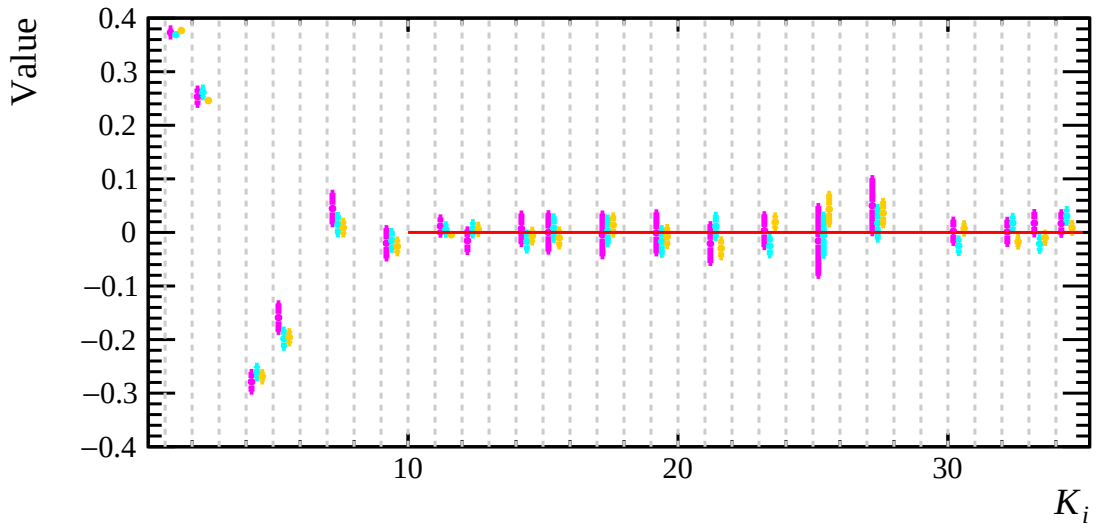

Figure 5.13: Distribution of moments extracted from the 2011 (magenta), 2012 (cyan) and 2015 + 2016 (orange) data sets, where systematic uncertainties are also included. Moments that are by construction zero and negligible in the $\beta_l = 1$ limit are omitted. Moments are displaced horizontally for illustration purposes.

A measurement of the physics parameters can be made using various methods. However, due to the fact that the production polarisation of the Λ_b^0 is compatible with zero, most of the moments have limited sensitivity to the decay amplitudes making a rigorous simultaneous extraction of P_b and the decay amplitudes very difficult. At the present moment, although the framework for the extraction of the latter parameters is not completely finalised, a prototype framework for extracting the physics parameters exists and is presented below.

The simplest way to estimate the physics parameters is by performing a χ^2 fit, where the parameters of interest for the 2011, 2012 and 2015+2016 data sets are extracted simultaneously, by keeping the magnitudes and the phases common between the

three data sets but using different P_b. The χ^2 can then be written as,

$$\chi^2 \equiv \sum_i \vec{T_i}^T C_i^{-1} \vec{T_i} + (\alpha_\Lambda - \widetilde{\alpha_\Lambda})^2/\sigma(\widetilde{\alpha_\Lambda})^2 \ , \tag{5.2}$$

where i runs for each of the data sets of the measured moments, and $\vec{T_i}$ is defined as, $\vec{T_i} \equiv \widetilde{\vec{K_i}} - \vec{K_i}(P_{b,i}, \text{decay amplitudes})$. In equation 5.2 the $\widetilde{\vec{K_i}}$ represent the measured values of the moments, while C_i the covariance matrix, where the systematic uncertainties are also included. It must be noted that since K_1 and K_2 are 100% correlated one of them must be omitted in the χ^2 minimisation. The moments that are zero for the $\Lambda_b^0 \to J/\psi\,\Lambda$ considering also the $\beta_l = 1$ are removed (see section 1.7.1), while the α_Λ asymmetry parameter is fixed with a Gaussian constraint to its measured value ($\widetilde{\alpha_\Lambda} \pm \sigma(\widetilde{\alpha_\Lambda})$) [7]. The results of the fit are illustrated in table 5.3. Due to the normalisation condition and the fact that only phase differences can be measured, the magnitude and the phase of the b_+ are fixed to one and zero respectively.

Observable	Value	$[\sigma^-,\sigma^+]$	Observable	Value	$[\sigma^-,\sigma^+]$
$\lvert\alpha_+\rvert$	0.043	$[-0.042,\ \ 0.041]$	P_b^{2011}	-0.025	$[-0.058,\ \ 0.059]$
$\lvert\alpha_-\rvert$	0.990	$[-0.019,\ \ 0.019]$	P_b^{2012}	-0.022	$[-0.035,\ \ 0.037]$
$\lvert b_-\rvert$	0.041	$[-0.040,\ \ 0.039]$	$P_b^{2015+2016}$	0.046	$[-0.026,\ \ 0.026]$

Table 5.3: Estimates for the magnitudes of the decay amplitudes and the production polarisation of Λ_b^0, extracted from the χ^2 fit. The fit includes both the statistical and the systematic uncertainties on the moments.

A Bayesian approach using the Markov Chain Monte Carlo (MCMC) method is also adopted to estimate the production polarisation of Λ_b^0 and the decay amplitudes. In this method, the posterior distribution is sampled with a Markov Chain Monte Carlo technique, using information of the $L \propto (\prod_i e^{(-1/2\vec{T_i}^T C_i^{-1}\vec{T_i})}) e^{-(\alpha_\Lambda - \widetilde{\alpha_\Lambda})^2/(2\sigma(\widetilde{\alpha_\Lambda})^2)}$ to pivot between points in the Markov Chain. It must be noted that a flat prior is

used for the physics parameters. In a simplified way, this process can be realised as follows: in the first step of the chain the parameters are set to a random value; in the second step, a proposal for the parameters is generated using the parameters from the first step as inputs, then evaluating the ratio of the likelihoods between the first and second steps to decide whether to accept or reject the new proposal of the parameters. The process is continued with a sequential generation of proposals where, in each step, a decision is made whether to accept or reject the latter. After multiple steps, this results in a chain that corresponds to the posterior distribution. Before the posterior distribution is used, the first part of the chain is rejected (approximately 5% of the chain); this is done in order to remove the influence of the starting point in the Markov Chain. Finally the MPV and the credibility intervals of the 1D projections of the posterior distribution for each of the physics parameters are used as an estimate of the latter. The credibility interval is defined in this case as the shortest interval that contains the MPV and the 68% of the distribution. The 1D projections of the posterior distribution of the P_b and of the magnitudes of the decay amplitudes are given in figure 5.14. The characteristics of the 1D projections of the posterior distributions for the P_b and the magnitudes of the decay amplitudes in terms of MPV and credibility intervals are presented in table 5.4.

Observable	MPV	Interval	Observable	MPV	Interval
$\lvert\alpha_+\rvert$	0.026	[0.000, 0.065]	P_b^{2011}	-0.034	[-0.096, 0.028]
$\lvert\alpha_-\rvert$	0.990	[0.971, 1.010]	P_b^{2012}	-0.010	[-0.046, 0.042]
$\lvert b_-\rvert$	0.000	[0.000, 0.058]	$P_b^{2015+2016}$	0.034	[-0.011, 0.064]

Table 5.4: Estimates for the magnitudes of the decay amplitudes and the production polarisation of Λ_b^0, extracted using the MCMC approach. This accounts for both the statistical and the systematic uncertainties on the moments.

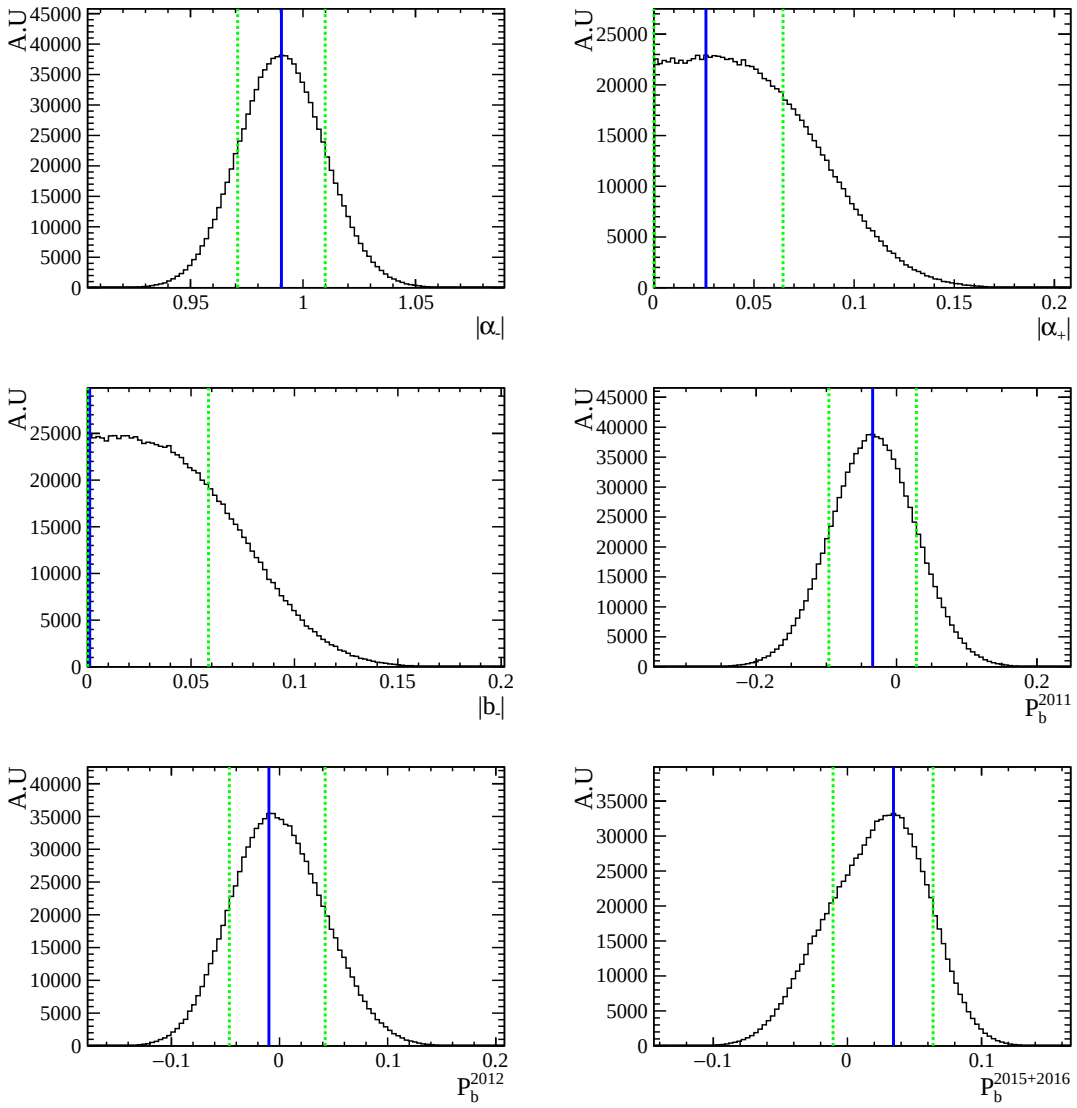

Figure 5.14: Markov Chain distributions for the magnitude of the decay amplitudes and the production polarisation. The black histograms represent the 1D projections of the posterior distribution, the blue line the MPVs and the green dotted lines the credibility intervals. The MCMC takes into account the statistical and systematic uncertainties on the moments. The small asymmetry in the distribution of the P_b for different $\sqrt{s}$, especially for those obtained from the samples with the higher statistics is related to an approximate symmetry generated between the P_b and the sign of the θ_{α_-}, when $|\alpha_-| = |b_+| = 1$ and $|\alpha_+| = |b_+| = 0$ and having fixed θ_{b_+} to zero.

The results from both methods are compatible; due to the lack of sensitivity in the phases, results for the latter are not presented. From both methods the results point to a production polarisation that is compatible with zero and shows no obvious trend

with $\sqrt{s}$; while the magnitudes of the decay amplitudes are found to be compatible with $|\alpha_-| \approx |b_+|$ and $|\alpha_+| \approx |b_-| \approx 0$[4]. The preliminary results presented in this section are largely compatible with previous measurements [108–110]; the latter use different parametrisation of the decay rate, which can finally be translated to magnitudes of the amplitudes and production polarisation of Λ_b^0. These results are preliminary; other formulations, such as parametrising the decay amplitudes in terms of Real and Imaginary part, or removing the phases completely, are also considered.

[4]It must be noted that in this work the magnitudes of the decay amplitudes are not normalised to the sum of the squared magnitudes of the decay amplitudes; these results can also be presented as: $|\alpha_\pm|^2 \equiv |\alpha_\pm|^2/N$, $|b_\pm|^2 \equiv |b_\pm|^2/N$, or $|\alpha_\pm| \equiv |\alpha_\pm|/\sqrt{N}$, $|b_\pm| \equiv |b_\pm|/\sqrt{N}$, where $N \equiv |\alpha_+|^2 + |\alpha_-|^2 + |b_+|^2 + |b_-|^2$, translating the measurements presented in this thesis to, $|\alpha_-|^2 \approx |b_+|^2 \approx 0.5$, $|\alpha_+| \approx |b_-| \approx 0$ and $|\alpha_-| \approx |b_+| \approx 0.71$, $|\alpha_+| \approx |b_-| \approx 0$ for the first and second redefinition respectively.

5.9 Summary and conclusion

This is the first time that the complete set of the angular observables of the $\Lambda_b^0 \to J/\psi\,\Lambda$ decay are measured. An interpretation of these measurements in terms of P_b and the magnitudes of the decay amplitudes is performed. The production polarisation of the Λ_b^0 baryon is found to be close to zero, while no evidence of a trend for P_b with $\sqrt{s}$ is found in the interval between 7 and 13 TeV. The magnitudes of the decay amplitudes are found to be $|\alpha_-| \approx |b_+|$ and $|\alpha_+| \approx |b_-| \approx 0$, while for this set of magnitudes and production polarisation of P_b there is no sensitivity to the phases. Since α_-, b_+ and α_+,b_- correspond to amplitudes with one half and minus one half helicities of the Λ, the results point to a preference for the Λ to be produced with a dominant minus one half helicity, which is consistent with what is expected [50]. Finally it must be noticed that the results obtained for this measurement use Λ_b^0 baryons produced directly from the pp collision and from heavier b-baryons [108–110], which are difficult to disentangle and therefore contribute to the final measurement.

CHAPTER 6

Conclusions

In this work the angular analysis of the two baryon decays of the $\Lambda_b^0 \to \Lambda\mu^+\mu^-$ and $\Lambda_b^0 \to J/\psi\,\Lambda$ is presented, using data from pp collisions collected by the LHCb detector between 2011 and 2016, corresponding to an integrated luminosity of approximately $5\,\text{fb}^{-1}$.

The angular analysis of the $\Lambda_b^0 \to \Lambda\mu^+\mu^-$ is performed in the high-q^2 region, where most of the signal resides. The angular observables are extracted with the method of moments and from the measured observables the forward-backward asymmetries A_{FB}^{ℓ}, A_{FB}^{h} and $A_{FB}^{\ell\text{h}}$ are determined. This is the first time that the complete set of

the angular observables has been measured. The results are found to be consistent with the SM predictions and published in Ref. [1].

In addition an angular analysis is of the $\Lambda_b^0 \to J/\psi\,\Lambda$ is also performed, where the angular observables are extracted with the method of moments. This is the first time that the complete set of angular observables has been measured. Finally an interpretation of the results in terms of the productions polarisation of Λ_b^0 and the decay amplitudes is made. The results are found to be in general consistent with previous measurements [108–110] and point to a production polarisation of Λ_b^0 close to zero, with no obvious trend on $\sqrt{s}$ while the magnitudes of the decay amplitudes are consistent with what is expected [50]. It must be noted that the results presented in this work are only preliminary and correspond to the current status of the analysis.

Interesting prospects for both decays modes are available for the near future using the Run1 and the full Run2 data. For the $\Lambda_b^0 \to J/\psi\,\Lambda$ decay the branching fraction can be updated. The latter measurement can then be used as an input for the update of the branching fraction of the $\Lambda_b^0 \to \Lambda\mu^+\mu^-$ decay, since the latter use the $\Lambda_b^0 \to J/\psi\,\Lambda$ as a normalisation mode, which is one of the dominant source of uncertainty especially in the high-q^2 bin (see figure 1.12). In addition the complete set of angular observables in the low-q^2 region can also potentially be extracted.

REFERENCES

[1] LHCb Collaboration, R. Aaij *et al.*, *Angular moments of the decay* $\Lambda_b^0 \to \Lambda\mu^+\mu^-$ *at low hadronic recoil*, JHEP **09** (2018) 146, arXiv:1808.00264.

[2] M. B. Gavela, P. Hernandez, J. Orloff, and O. Pene, *Standard model CP violation and baryon asymmetry*, Mod. Phys. Lett. **A9** (1994) 795, arXiv:hep-ph/9312215.

[3] F. Zwicky, *Republication of: The redshift of extragalactic nebulae*, General Relativity and Gravitation **41** (2009) 207.

[4] J. L. Rosner, *The Standard model in 2001*, in *Heavy flavor physics: Theory and experimental results in heavy quark physics and CP violation. Proceedings, 55th Scottish Universities Summer School in Physics, SUSSP 2001, St. Andrews, UK, August 7-23, 2001*, pp. 1–56, 2001. arXiv:hep-ph/0108195.

[5] R. M. Godbole, *Field Theory and the Electro-Weak Standard Model*, in *Proceedings, 2nd Asia-Europe-Pacific School of High-Energy Physics (AEPSHEP 2014): Puri, India, November 0417, 2014*, pp. 1–61, 2017. arXiv:1703.04978. doi: 10.23730/CYRSP-2017-002.1.

[6] M. Herrero, *The Standard model*, NATO Sci. Ser. C **534** (1999) 1, arXiv:hep-ph/9812242.

[7] Particle Data Group, P. D. G. Collaboration, *Review of particle physics*, Phys. Rev. D **98** (2018) 030001, Phys. Rev. D **98**, 030001.

[8] LHCb Collaboration, R. Aaij *et al.*, *Observation of the resonant character of the* $Z(4430)^-$ *state*, Phys. Rev. Lett. **112** (2014), no. 22 222002, arXiv:1404.1903.

[9] LHCb Collaboration, R. Aaij *et al.*, *Observation of $J/\psi p$ Resonances Consistent with Pentaquark States in $\Lambda_b^0 \to J/\psi K^- p$ Decays*, Phys. Rev. Lett. **115** (2015) 072001, arXiv:1507.03414.

[10] A. Salam and J. C. Ward, *Gauge theory of elementary interactions*, Phys. Rev. **136** (1964) B763.

[11] S. Weinberg, *A Model of Leptons*, Phys. Rev. Lett. **19** (1967) 1264.

[12] S. L. Glashow, *Partial Symmetries of Weak Interactions*, Nucl. Phys. **22** (1961) 579.

[13] C. S. Wu *et al.*, *Experimental test of parity conservation in beta decay*, Phys. Rev. **105** (1957) 1413.

[14] P. W. Higgs, *Broken symmetries and the masses of gauge bosons*, Phys. Rev. Lett. **13** (1964) 508.

[15] F. Englert and R. Brout, *Broken symmetry and the mass of gauge vector mesons*, Phys. Rev. Lett. **13** (1964) 321.

[16] G. S. Guralnik, C. R. Hagen, and T. W. B. Kibble, *Global conservation laws and massless particles*, Phys. Rev. Lett. **13** (1964) 585.

[17] ATLAS Collaboration, G. Aad *et al.*, *Observation of a new particle in the search for the Standard Model Higgs boson with the ATLAS detector at the LHC*, Phys. Lett. **B716** (2012) 1, arXiv:1207.7214.

[18] CMS Collaboration, S. Chatrchyan *et al.*, *Observation of a new boson at a mass of 125 GeV with the CMS experiment at the LHC*, Phys. Lett. **B716** (2012) 30, arXiv:1207.7235.

[19] S. Lee and H. Serdio, *Flavour physics and cp violation*, CERN Yellow Reports: School Proceedings **2** (2017), no. 0 125.

[20] P. Kooijman and N. Tuning, *Lectures on CP-violation*.

[21] K. G. Wilson and W. Zimmermann, *Operator product expansions and composite field operators in the general framework of quantum field theory*, Commun. Math. Phys. **24** (1972) 87.

[22] P. Koppenburg, Z. Dolezal, and M. Smizanska, *Rare decays of b hadrons*, Scholarpedia **11** (2016) 32643, arXiv:1606.00999.

[23] M. Blanke, *Introduction to flavour physics and cp violation*, CERN Yellow Reports: School Proceedings.

[24] A. J. Buras, *Weak Hamiltonian, CP violation and rare decays*, in *Probing the standard model of particle interactions. Proceedings, Summer School in Theoretical Physics, NATO Advanced Study Institute, 68th session, Les Houches, France, July 28-September 5, 1997. Pt. 1, 2*, pp. 281–539, 1998. arXiv:hep-ph/9806471.

[25] S. L. Glashow, J. Iliopoulos, and L. Maiani, *Weak Interactions with Lepton-Hadron Symmetry*, Phys. Rev. **D2** (1970) 1285.

[26] HFLAV Collaboration, Y. Amhis *et al.*, *Averages of b-hadron, c-hadron, and τ-lepton properties as of summer 2016*, Eur. Phys. J. **C77** (2017), no. 12 895, arXiv:1612.07233.

[27] LHCb Collaboration, R. Aaij *et al.*, *Differential branching fraction and angular analysis of $\Lambda_b^0 \to \Lambda\mu^+\mu^-$ decays*, JHEP **06** (2015) 115, arXiv:1503.07138, [Erratum: JHEP **09**,145 (2018)].

[28] LHCb Collaboration, R. Aaij *et al.*, *Angular analysis and differential branching fraction of the decay $B_s^0 \to \phi\mu^+\mu^-$*, JHEP **09** (2015) 179, arXiv:1506.08777.

[29] LHCb Collaboration, R. Aaij *et al.*, *Differential branching fractions and isospin asymmetries of $B \to K^{(*)}\mu^+\mu^-$ decays*, JHEP **06** (2014) 133, arXiv:1403.8044.

[30] LHCb Collaboration, R. Aaij *et al.*, *Measurements of the S-wave fraction in $B^0 \to K^+\pi^-\mu^+\mu^-$ decays and the $B^0 \to K^*(892)^0\mu^+\mu^-$ differential branching fraction*, JHEP **11** (2016) 047, arXiv:1606.04731, [Erratum: JHEP **04**,142 (2017)].

[31] W. Detmold and S. Meinel, *$\Lambda_b \to \Lambda\ell^+\ell^-$ form factors, differential branching fraction, and angular observables from lattice QCD with relativistic b quarks*, Phys. Rev. **D93** (2016), no. 7 074501, arXiv:1602.01399.

[32] LHCb Collaboration, R. Aaij *et al.*, *Test of lepton universality using $B^+ \to K^+\ell^+\ell^-$ decays*, Phys. Rev. Lett. **113** (2014) 151601, arXiv:1406.6482.

[33] LHCb Collaboration, R. Aaij *et al.*, *Test of lepton universality with $B^0 \to K^{*0}\ell^+\ell^-$ decays*, JHEP **08** (2017) 055, arXiv:1705.05802.

[34] LHCb Collaboration, R. Aaij *et al.*, *Angular analysis of the $B^0 \to K^{*0}\mu^+\mu^-$ decay using 3 fb^{-1} of integrated luminosity*, JHEP **02** (2016) 104, arXiv:1512.04442.

[35] CMS Collaboration, A. M. Sirunyan *et al.*, *Measurement of angular parameters from the decay $\mathrm{B}^0 \to \mathrm{K}^{*0}\mu^+\mu^-$ in proton-proton collisions at $\sqrt{s} = 8$ TeV*, Phys. Lett. **B781** (2018) 517, arXiv:1710.02846.

[36] ATLAS Collaboration, *Angular analysis of $B_d^0 \to K^*\mu^+\mu^-$ decays in pp collisions at $\sqrt{s} = 8$ TeV with the ATLAS detector*, Tech. Rep. ATLAS-CONF-2017-023, CERN, Geneva, Apr, 2017.

[37] Belle Collaboration, S. Wehle *et al.*, *Lepton-Flavor-Dependent Angular Analysis of $B \to K^*\ell^+\ell^-$*, Phys. Rev. Lett. **118** (2017), no. 11 111801, arXiv:1612.05014.

[38] S. Descotes-Genon, L. Hofer, J. Matias, and J. Virto, *Global analysis of $b \to s\ell\ell$ anomalies*, JHEP **06** (2016) 092, arXiv:1510.04239.

[39] B. Capdevila *et al.*, *Patterns of New Physics in $b \to s\ell^+\ell^-$ transitions in the light of recent data*, JHEP **01** (2018) 093, arXiv:1704.05340.

[40] W. Altmannshofer and D. M. Straub, *New physics in $b \to s$ transitions after LHC run 1*, Eur. Phys. J. **C75** (2015), no. 8 382, arXiv:1411.3161.

[41] G. Hiller and I. Nisandzic, *R_K and R_{K^*} beyond the standard model*, Phys. Rev. **D96** (2017), no. 3 035003, arXiv:1704.05444.

[42] M. Ciuchini *et al.*, *On Flavourful Easter eggs for New Physics hunger and Lepton Flavour Universality violation*, Eur. Phys. J. **C77** (2017), no. 10 688, arXiv:1704.05447.

[43] W. Altmannshofer, P. Stangl, and D. M. Straub, *Interpreting Hints for Lepton Flavor Universality Violation*, Phys. Rev. **D96** (2017), no. 5 055008, arXiv:1704.05435.

[44] T. Blake and M. Kreps, *Angular distribution of polarised Λ_b baryons decaying to $\Lambda\ell^+\ell^-$*, JHEP **11** (2017) 138, arXiv:1710.00746.

[45] G. Hiller, M. Knecht, F. Legger, and T. Schietinger, *Photon polarization from helicity suppression in radiative decays of polarized Λ_b to spin-3/2 baryons*, Phys. Lett. **B649** (2007) 152, arXiv:hep-ph/0702191.

[46] LHCb Collaboration, R. Aaij *et al.*, *Measurements of the $\Lambda_b^0 \to J/\psi\Lambda$ decay amplitudes and the Λ_b^0 polarisation in pp collisions at $\sqrt{s} = 7$ TeV*, Phys. Lett. **B724** (2013) 27, arXiv:1302.5578.

[47] CMS Collaboration, A. M. Sirunyan *et al.*, *Measurement of the Λ_b polarization and angular parameters in $\Lambda_b \to J/\psi\,\Lambda$ decays from pp collisions at $\sqrt{s} = 7$ and 8 TeV*, Phys. Rev. **D97** (2018), no. 7 072010, arXiv:1802.04867.

[48] P. Ber, T. Feldmann, and D. van Dyk, *Angular Analysis of the Decay $\Lambda_b \to \Lambda(\to N\pi)\ell^+\ell^-$*, JHEP **01** (2015) 155, arXiv:1410.2115.

[49] T. Gutsche *et al.*, *Rare baryon decays $\Lambda_b \to \Lambda l^+ l^- (l = e, \mu, \tau)$ and $\Lambda_b \to \Lambda\gamma$: differential and total rates, lepton- and hadron-side forward-backward asymmetries*, Phys. Rev. **D87** (2013) 074031, arXiv:1301.3737.

[50] T. Gutsche *et al.*, *Polarization effects in the cascade decay $\Lambda_b \to \Lambda(\to p\pi^-) + J/\psi(\to \ell^+\ell^-)$ confined quark model*, Phys. Rev. **D88** (2013), no. 11 114018, arXiv:1309.7879.

[51] Z. J. Ajaltouni, E. Conte, and O. Leitner, *Λ_b decays into Lambda-vector*, Phys. Lett. **B614** (2005) 165, arXiv:hep-ph/0412116.

[52] Fayyazuddin and Riazuddin, *Two-body nonleptonic Λ_b decays in quark model with factorization ansatz*, Phys. Rev. **D58** (1998) 014016, arXiv:hep-ph/9802326.

[53] R. Mohanta *et al.*, *Hadronic weak decays of Λ_b baryon in the covariant oscillator quark model*, Prog. Theor. Phys. **101** (1999) 959, arXiv:hep-ph/9904324.

[54] C.-H. Chou, H.-H. Shih, S.-C. Lee, and H.-n. Li, *$\Lambda_b \to \Lambda J/\psi$ decay in perturbative QCD*, Phys. Rev. **D65** (2002) 074030, arXiv:hep-ph/0112145.

[55] Z.-T. Wei, H.-W. Ke, and X.-Q. Li, *Evaluating decay Rates and Asymmetries of Lambda$_b$ into Light Baryons in LFQM*, Phys. Rev. **D80** (2009) 094016, arXiv:0909.0100.

[56] ATLAS Collaboration, G. Aad *et al.*, *Measurement of the parity-violating asymmetry parameter α_b and the helicity amplitudes for the decay $\Lambda_b^0 \to J/\psi + \Lambda^0$ with the ATLAS detector*, Phys. Rev. **D89** (2014), no. 9 092009, arXiv:1404.1071.

[57] L. Evans and P. Bryant, *LHC machine*, Journal of Instrumentation **3** (2008) S08001.

[58] S. Myers, *The LEP Collider, from design to approval and commissioning*, John Adams' Lecture, CERN, Geneva, 1991. Delivered at CERN, 26 Nov 1990, doi: 10.5170/CERN-1991-008.

[59] ATLAS Collaboration, *ATLAS: letter of intent for a general-purpose pp experiment at the large hadron collider at CERN*, Tech. Rep. CERN-LHCC-92-004, 1992.

[60] CMS Collaboration, *CMS: letter of intent by the CMS Collaboration for a general purpose detector at LHC*, Tech. Rep. CERN-LHCC-92-003, 1992.

[61] H. Dijkstra, H. J. Hilke, T. Nakada, and T. Ypsilantis, *LHCb Letter of Intent, LHCb Collaboration*, Tech. Rep. LHCb-95-001, 1995.

[62] ALICE Collaboration, *Letter of Intent for A Large Ion Collider Experiment [ALICE]*, Tech. Rep. CERN-LHCC-93-016, 1993.

[63] J. Haffner, *The CERN accelerator complex. Complexe des accélérateurs du CERN*, General Photo.

[64] LHCb Collaboration, A. A. Alves *et al.*, *The LHCb Detector at the LHC*, JINST **3** (2008), no. LHCb-DP-2008-001. CERN-LHCb-DP-2008-001 S08005, Also published by CERN Geneva in 2010.

[65] LHCb Collaboration, R. Antunes-Nobrega *et al.*, *LHCb reoptimized detector design and performance: Technical Design Report*, Technical Design Report LHCb, CERN, Geneva, 2003.

[66] LHCb Collaboration, *$b\bar{b}$ pair production at the LHCb,* http : //lhcb.web.cern.ch/lhcb/speakersbureau/html/bb_ProductionAngles.html, General Photo.

[67] M. Pepe Altarelli and F. Teubert, *B Physics at LHCb*, Int. J. Mod. Phys. **A23** (2008) 5117, arXiv:0802.1901, [299 (2008)].

[68] LHCb Collaboration, S. Amato *et al.*, *LHCb magnet: Technical Design Report*, Technical Design Report LHCb, CERN, Geneva, 2000.

[69] LHCb Collaboration, R. Aaij *et al.*, *LHCb Detector Performance*, Int. J. Mod. Phys. **A30** (2015), no. 07 1530022, arXiv:1412.6352.

[70] L. Collaboration, *LHCb VELO Upgrade Technical Design Report*, Tech. Rep. CERN-LHCC-2013-021. LHCB-TDR-013, Nov, 2013.

[71] LHCb Collaboration, R. Aaij *et al.*, *Precision measurement of CP violation in $B_s^0 \to J/\psi K^+K^-$ decays*, Phys. Rev. Lett. **114** (2015), no. 4 041801, arXiv:1411.3104.

[72] M. Brice, *Part of the VELO (VErtex LOcator) of the LHCb experiment*, General Photo.

[73] LHCb Collaboration, P. R. Barbosa-Marinho, I. Bediaga, F. Barbosa-Ademarlaudo, and Cernicchiaro, *LHCb inner tracker: Technical Design Report*, Technical Design Report LHCb, CERN, Geneva, 2002.

[74] LHCb Collaboration, P. R. Barbosa-Marinho *et al.*, *LHCb outer tracker: Technical Design Report*, Technical Design Report LHCb, CERN, Geneva, 2001.

[75] LHCb RICH Group, M. Adinolfi *et al.*, *Performance of the LHCb RICH detector at the LHC*, Eur. Phys. J. **C73** (2013) 2431, arXiv:1211.6759.

[76] LHCb Collaboration, S. Amato *et al.*, *LHCb RICH: Technical Design Report*, Technical Design Report LHCb, CERN, Geneva, 2000.

[77] L. Anderlini *et al.*, *Computing strategy for PID calibration samples for LHCb Run 2*, Tech. Rep. LHCb-PUB-2016-020. CERN-LHCb-PUB-2016-020, CERN, Geneva, Jul, 2016.

[78] J. Badier *et al.*, *Shashlik calorimeter: Beam test results*, Nucl. Instrum. Meth. **A348** (1994) 74.

[79] LHCb Collaboration, S. Amato *et al.*, *LHCb calorimeters: Technical Design Report*, Technical Design Report LHCb, CERN, Geneva, 2000.

[80] LHCb Collaboration, A. A. Alves, Jr. *et al.*, *Performance of the LHCb muon system*, JINST **8** (2013) P02022, arXiv:1211.1346.

[81] LHCb, J. Albrecht, *The LHCb Trigger System: Present and Future*, J. Phys. : Conf. Ser. **623** (2015), no. 1 012003. 5 p.

[82] LHCb, F. Dordei, *LHCb detector and trigger performance in Run II*, EPJ Web Conf. **164** (2017) 01016. 10 p.

[83] B. Sciascia, *LHCb Run 2 trigger performance*, PoS (**BEAUTY2016**) 029 .

[84] E. Aslanides *et al.*, *The level-0 muon trigger for the lhcb experiment*, Nuclear Instruments and Methods in Physics Research Section A: Accelerators, Spectrometers, Detectors and Associated Equipment **579** (2007), no. 3 989 .

[85] A. Martin Sanchez, P. Robbe, and M.-H. Schune, *Performances of the LHCb L0 Calorimeter Trigger*, Tech. Rep. LHCb-PUB-2011-026. CERN-LHCb-PUB-2011-026, CERN, Geneva, Jun, 2012.

[86] R. Aaij *et al.*, *Performance of the LHCb trigger and full real-time reconstruction in Run 2 of the LHC*, `arXiv:1812.10790`.

[87] S. Agostinelli *et al.*, *Geant4a simulation toolkit*, Nuclear Instruments and Methods in Physics Research Section A: Accelerators, Spectrometers, Detectors and Associated Equipment **506** (2003), no. 3 250 .

[88] J. Allison *et al.*, *Geant4 developments and applications*, IEEE Trans. Nucl. Sci. **53** (2006) 270.

[89] J. Allison *et al.*, *Recent developments in geant4*, Nuclear Instruments and Methods in Physics Research Section A: Accelerators, Spectrometers, Detectors and Associated Equipment **835** (2016) 186 .

[90] P. N. Griffith, *First observation and branching fraction measurement of the rare decay $\Lambda_b^0 \to pK^-\mu^+\mu^-$ at the LHCb experiment, CERN*, PhD thesis, University of Birmingham, 2017.

[91] T. Sjostrand, L. Lonnblad, and S. Mrenna, *PYTHIA 6.2: Physics and manual*, `arXiv:hep-ph/0108264`.

[92] D. J. Lange, *The EvtGen particle decay simulation package*, Nucl. Instrum. Meth. **A462** (2001) 152.

[93] P. Golonka and Z. Was, *PHOTOS Monte Carlo: A Precision tool for QED corrections in Z and W decays*, Eur. Phys. J. **C45** (2006) 97, `arXiv:hep-ph/0506026`.

[94] I. Belyaev *et al.*, *Handling of the generation of primary events in Gauss, the LHCb simulation framework*, in *Proceedings, 2010 IEEE Nuclear Science Symposium and Medical Imaging Conference (NSS/MIC 2010): Knoxville, Tennessee, October 30-November 6, 2010*, pp. 1155–1161, 2010. doi: 10.1109/NSSMIC.2010.5873949.

[95] A. Mazurov, B. Couturier, D. Popov, and N. Farley, *Microservices for systematic profiling and monitoring of the refactoring process at the LHCb experiment*, Journal of Physics: Conference Series **898** (2017) 072037.

[96] B. Efron, *Bootstrap methods: Another look at the jackknife*, Ann. Statist. **7** (1979) 1.

[97] LHCb HLT project, J. Albrecht, V. V. Gligorov, G. Raven, and S. Tolk, *Performance of the LHCb High Level Trigger in 2012*, J. Phys. Conf. Ser. **513** (2014) 012001, arXiv:1310.8544.

[98] A. A. Alves Junior *et al.*, *Prospects for Measurements with Strange Hadrons at LHCb*, arXiv:1808.03477.

[99] M. Feindt, *A Neural Bayesian Estimator for Conditional Probability Densities*, arXiv:physics/0402093.

[100] M. Feindt and U. Kerzel, *The NeuroBayes neural network package*, Nucl. Instrum. Meth. **A559** (2006) 190.

[101] M. Pivk and F. R. Le Diberder, *SPlot: A Statistical tool to unfold data distributions*, Nucl. Instrum. Meth. **A555** (2005) 356, arXiv:physics/0402083.

[102] W. Verkerke and D. P. Kirkby, *The RooFit toolkit for data modeling*, eConf **C0303241** (2003) MOLT007, arXiv:physics/0306116, [186 (2003)].

[103] M. Oreglia, *A Study of the Reactions $\psi' \to \gamma\gamma\psi$*, PhD thesis, SLAC, 1980.

[104] T. Skwarnicki, *A study of the radiative CASCADE transitions between the Upsilon-Prime and Upsilon resonances*, PhD thesis, Cracow, INP, 1986.

[105] LHCb Collaboration, R. Aaij *et al.*, *Study of the kinematic dependences of Λ_b^0 production in pp collisions and a measurement of the $\Lambda_b^0 \to \Lambda_c^+ \pi^-$ branching fraction*, JHEP **08** (2014) 143, arXiv:1405.6842.

[106] L. Anderlini *et al.*, *The PIDCalib package*, Tech. Rep. LHCb-PUB-2016-021. CERN-LHCb-PUB-2016-021, CERN, Geneva, Jul, 2016.

[107] W. D. Hulsbergen, *Decay chain fitting with a kalman filter*, Nuclear Instruments and Methods in Physics Research Section A: Accelerators, Spectrometers, Detectors and Associated Equipment **552** (2005), no. 3 566 .

[108] CDF Collaboration, T. Aaltonen *et al.*, *First observation of heavy baryons Σ_b and Σ_b^**, Phys. Rev. Lett. **99** (2007) 202001, arXiv:0706.3868.

[109] CDF Collaboration, T. Aaltonen *et al.*, *Measurement of the masses and widths of the bottom baryons Σ_b^{+-} and Σ_b^{*+-}*, Phys. Rev. **D85** (2012) 092011, arXiv:1112.2808.

[110] LHCb Collaboration, R. Aaij *et al.*, *Observation of excited Λ_b^0 baryons*, Phys. Rev. Lett. **109** (2012) 172003, arXiv:1205.3452.

APPENDIX A

Angular analysis of $\Lambda_b^0 \to \Lambda \mu^+ \mu^-$

A.1 Neural Network

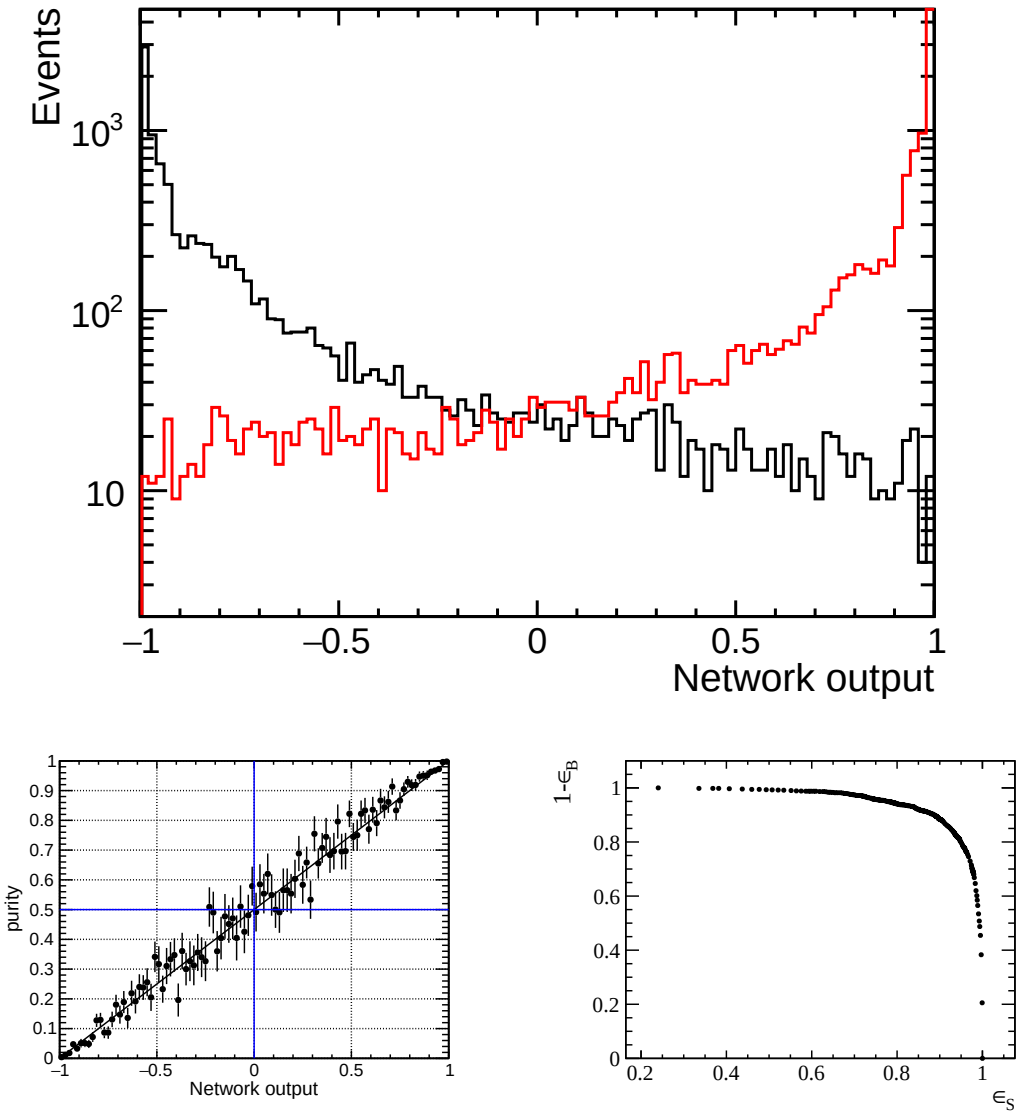

Figure A.1: (Top) Separation of signal (red histogram) and combinatorial background (black histogram) from the NN. (Bottom left) Purity of the sample as a function of the NN output. (Bottom right) the ROC curve (black line). In the ROC curve the ϵ_B and ϵ_S represent the background and signal efficiencies. All results are obtained using the NN for the 2015 samples. The optimal point is found to be NNcut $= -0.20$.

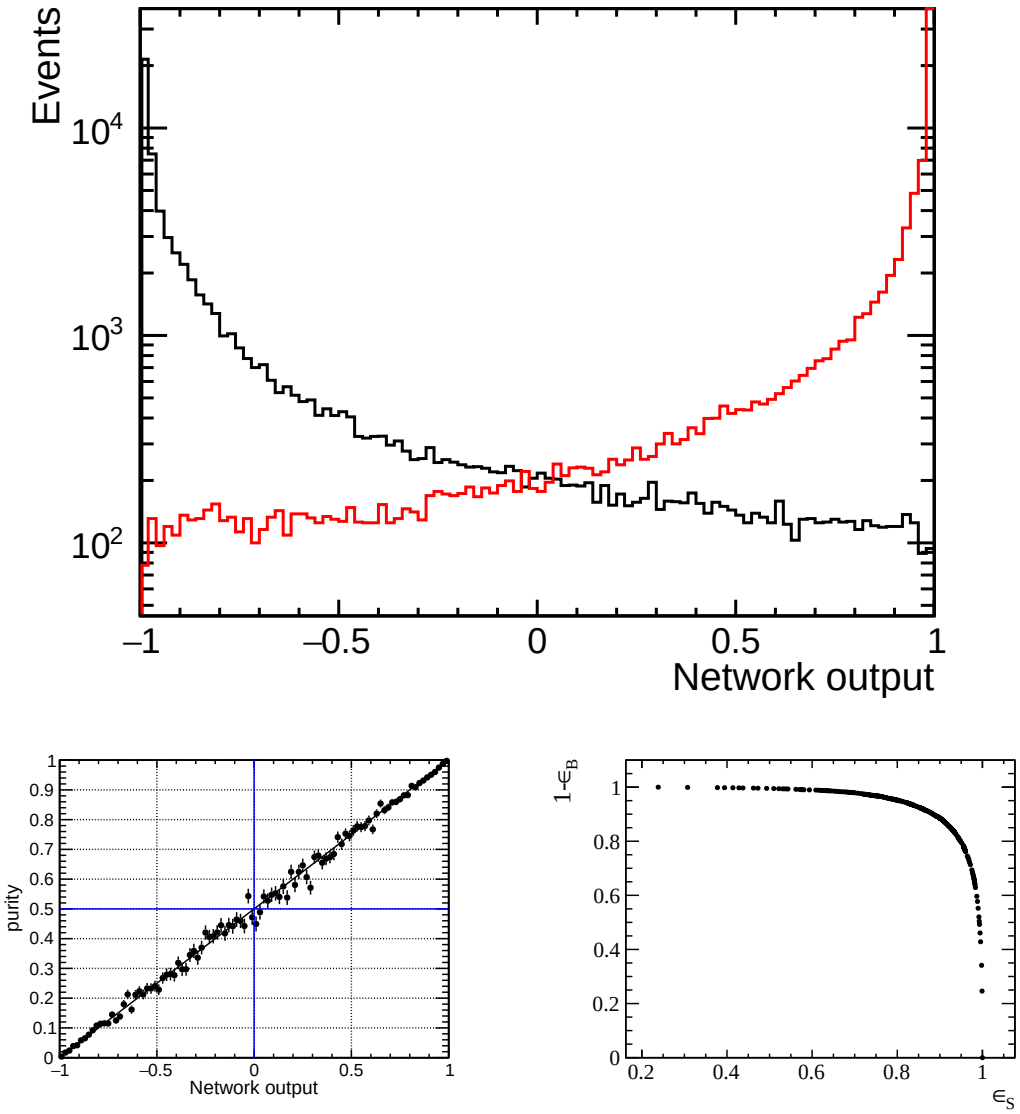

Figure A.2: (Top) Separation of signal (red histogram) and combinatorial background (black histogram) from the NN. (Bottom left) Purity of the sample as a function of the NN output. (Bottom right) the ROC curve (black line). In the ROC curve the ϵ_B and ϵ_S represent the background and signal efficiencies. All results are obtained using the NN for the 2016 samples. The optimal point is found to be NNcut = 0.30.

A.2 MC Correction

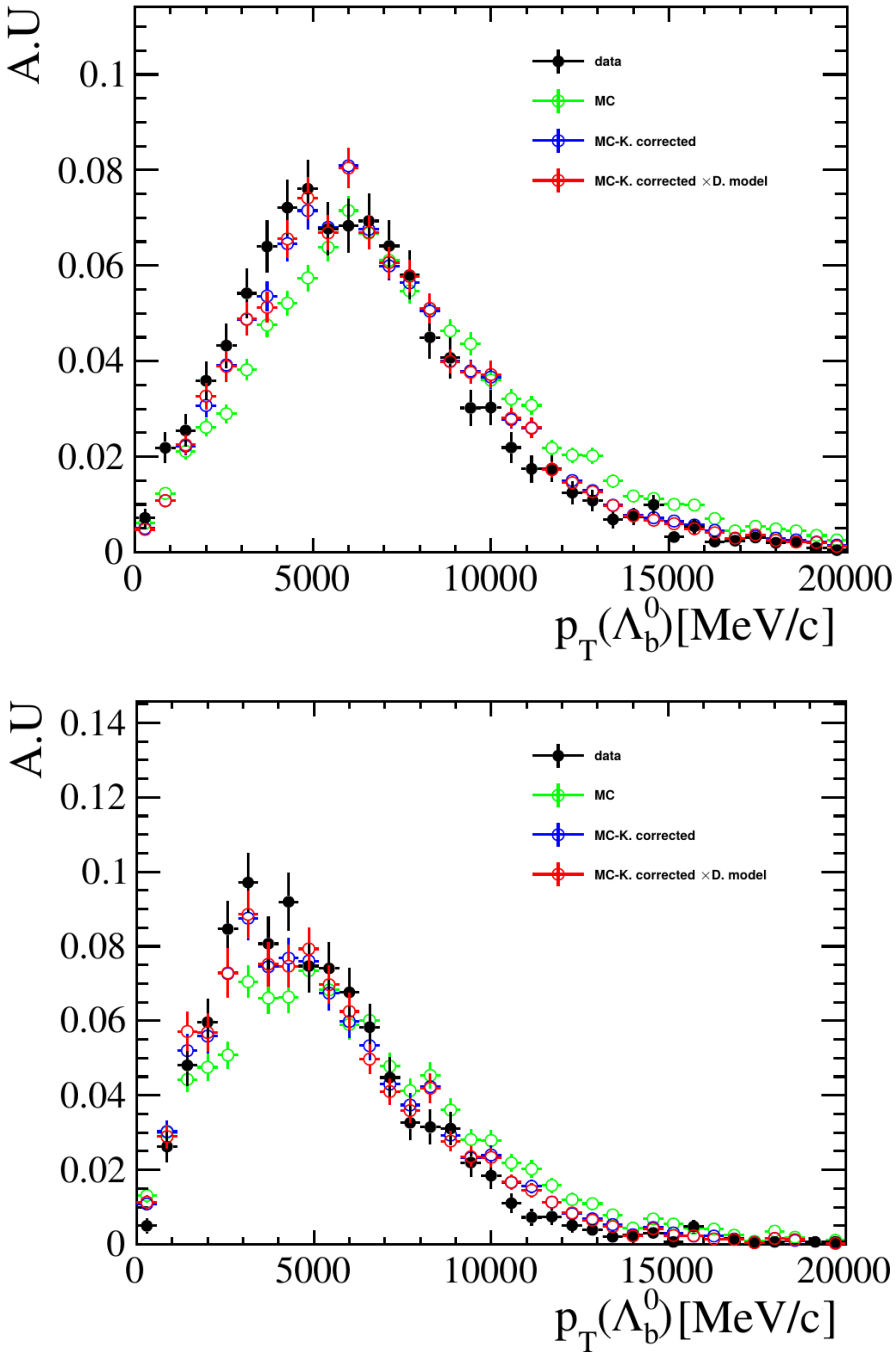

Figure A.3: Comparison between data and MC of the $\Lambda_b^0 \to J/\psi\,\Lambda$ decay for 2011 data-taking conditions for the transverse momentum of Λ_b^0 using the DD (left) and LL (right) categories. The black data points represent the background-subtracted data, the green data points the MC, the blue and red markers correspond to the corrected MC and corrected MC × the decay structure of $\Lambda_b^0 \to J/\psi\,\Lambda$.

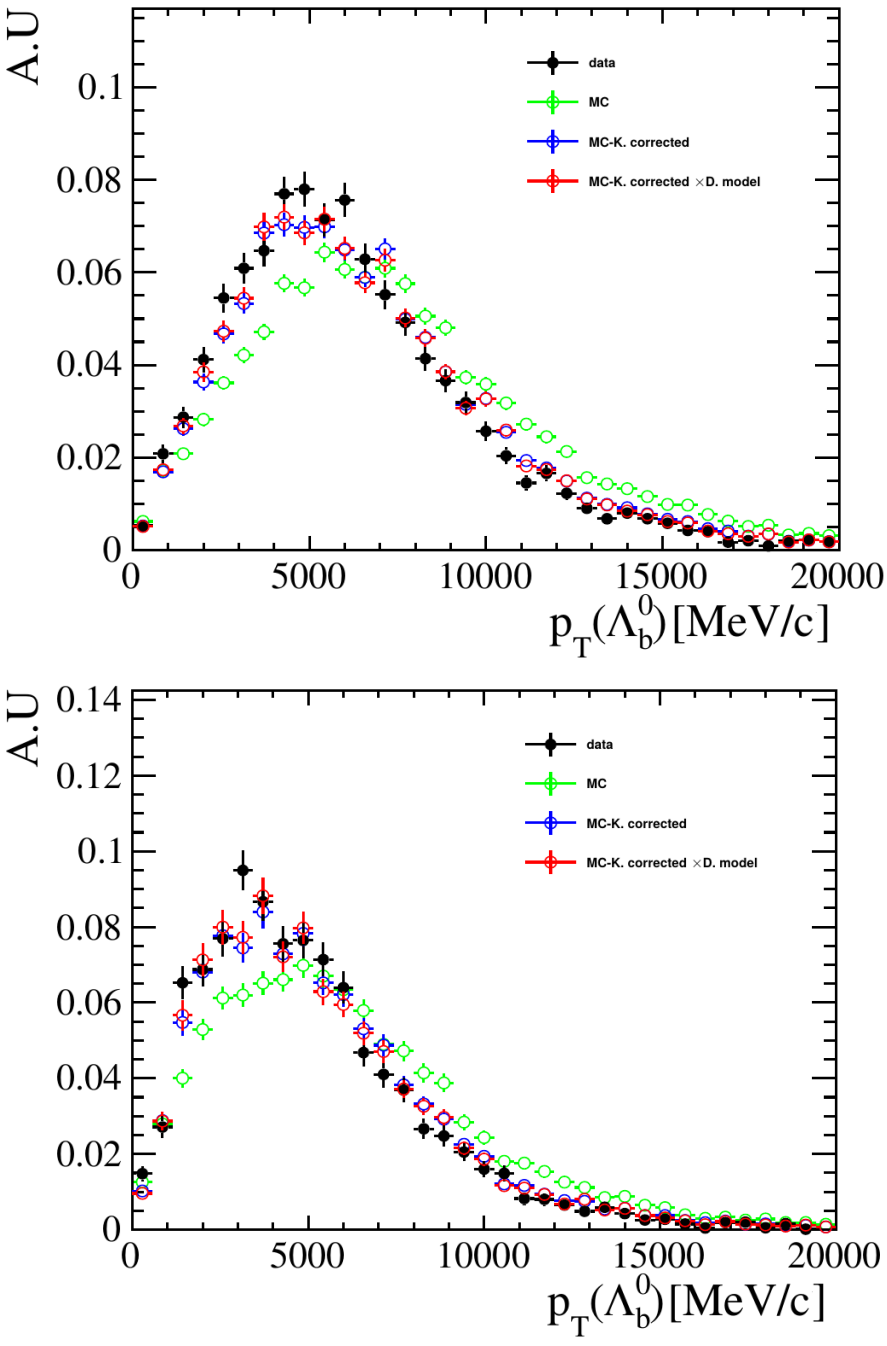

Figure A.4: Comparison between data and MC of the $\Lambda_b^0 \to J/\psi\,\Lambda$ decay for 2012 data-taking conditions for the transverse momentum of Λ_b^0 using the DD (left) and LL (right) categories. The black data points represent the background-subtracted data, the green data points the MC, the blue and red markers correspond to the corrected MC and corrected MC $\times$ the decay structure of $\Lambda_b^0 \to J/\psi\,\Lambda$.

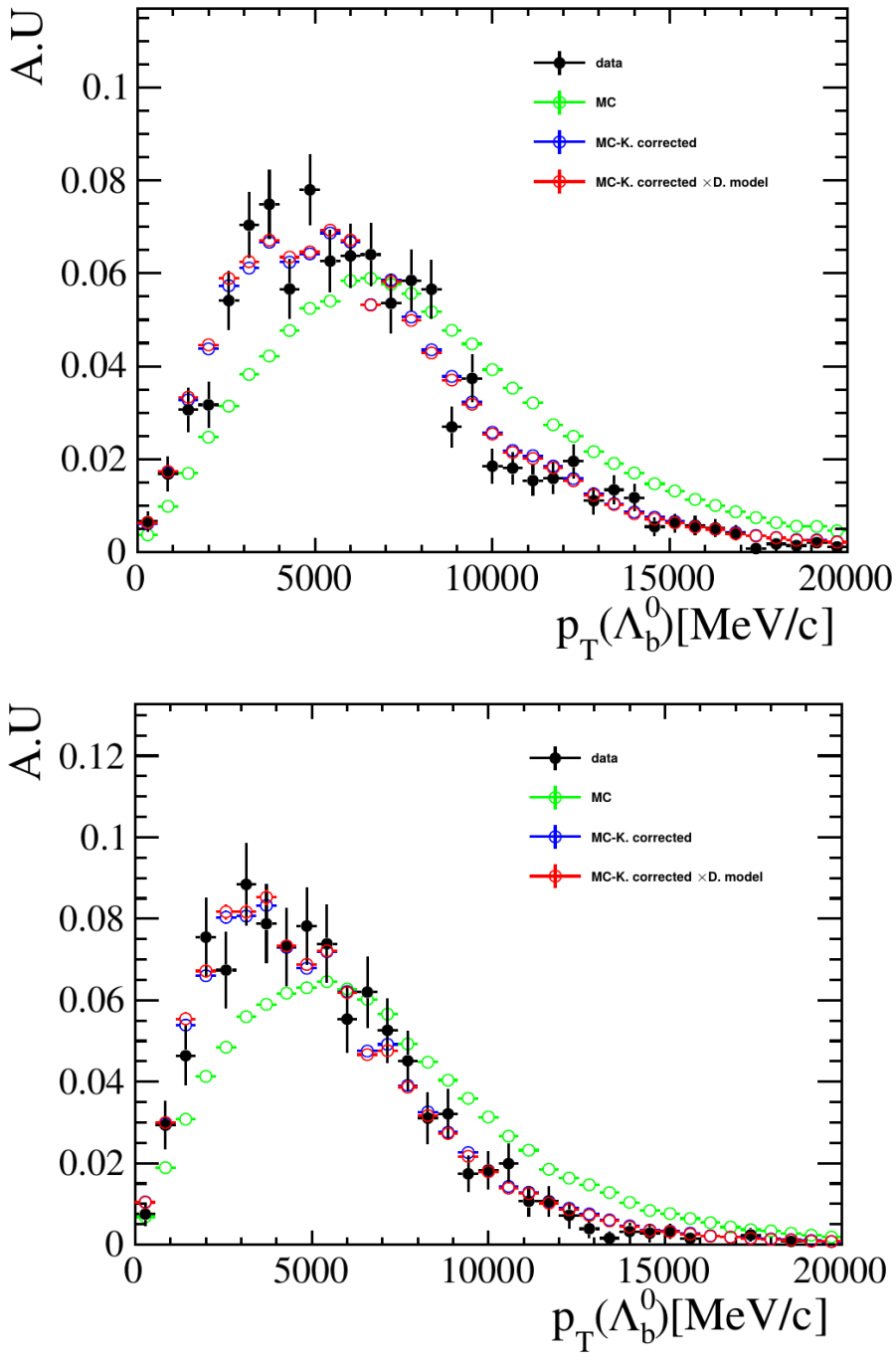

Figure A.5: Comparison between data and MC of the $\Lambda_b^0 \to J/\psi\,\Lambda$ decay for 2015 data-taking conditions for the transverse momentum of Λ_b^0 using the DD (left) and LL (right) categories. The black data points represent the background-subtracted data, the green data points the MC, the blue and red markers correspond to the corrected MC and corrected MC × the decay structure of $\Lambda_b^0 \to J/\psi\,\Lambda$.

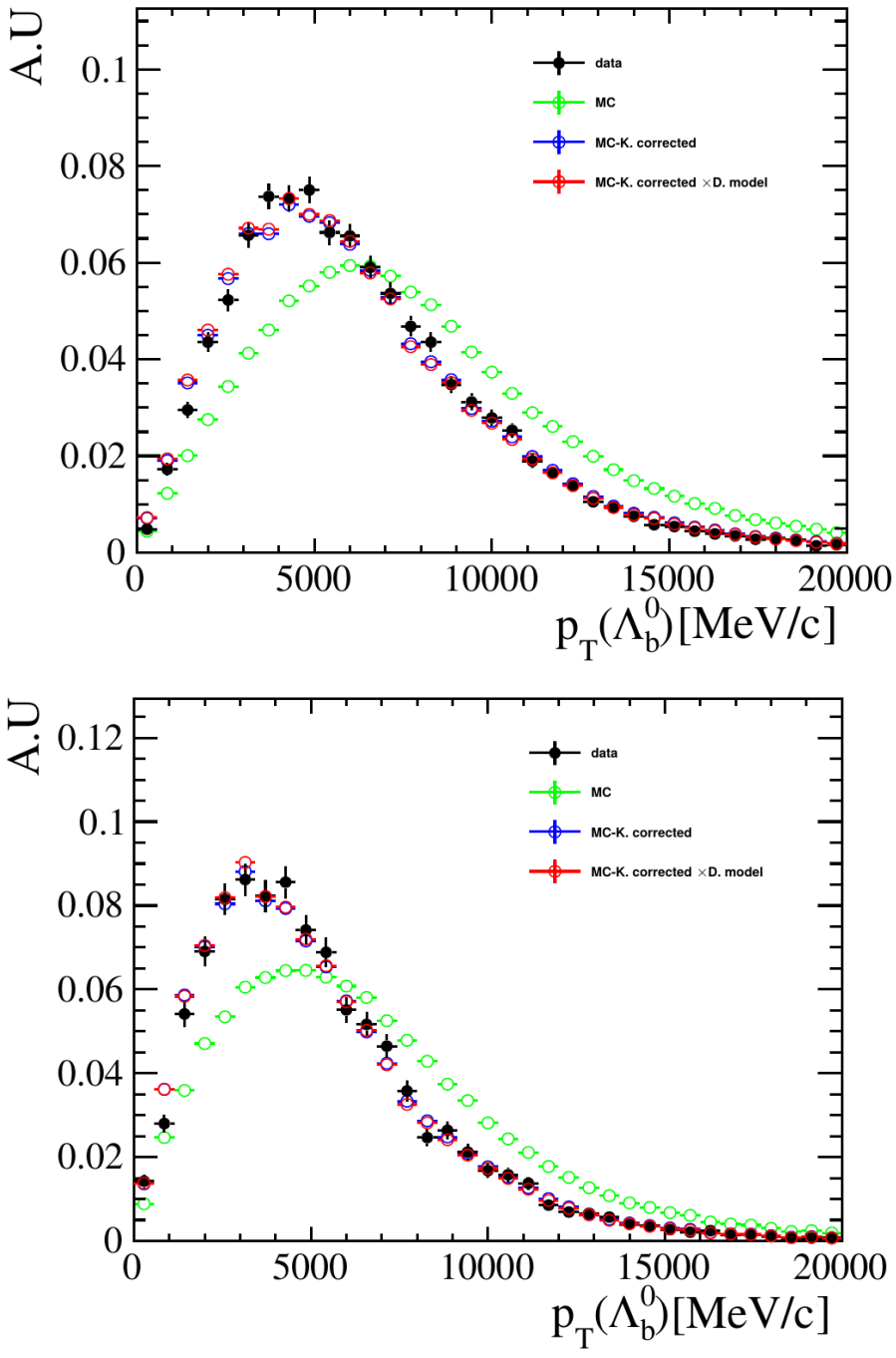

Figure A.6: Comparison between data and MC of the $\Lambda_b^0 \to J/\psi\,\Lambda$ decay for 2016 data-taking conditions for the transverse momentum of Λ_b^0 using the DD (left) and LL (right) categories. The black data points represent the background-subtracted data, the green data points the MC, the blue and red markers correspond to the corrected MC and corrected MC $\times$ the decay structure of $\Lambda_b^0 \to J/\psi\,\Lambda$.

A.3 Efficiency projections

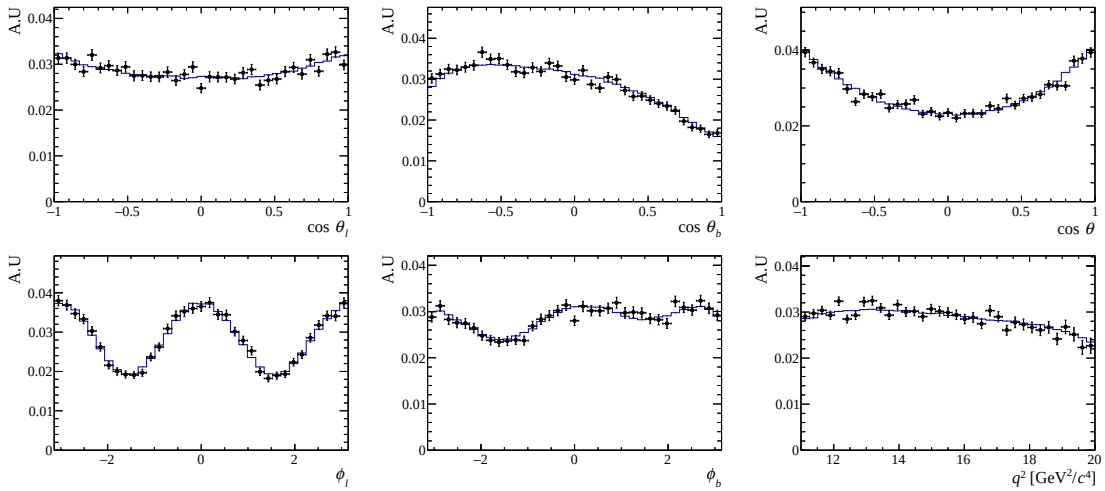

Figure A.7: 1D efficiency projections of 2011 + 2012 MC for the DD category. The black data points represent the weighted MC sample, while the blue line the efficiency model.

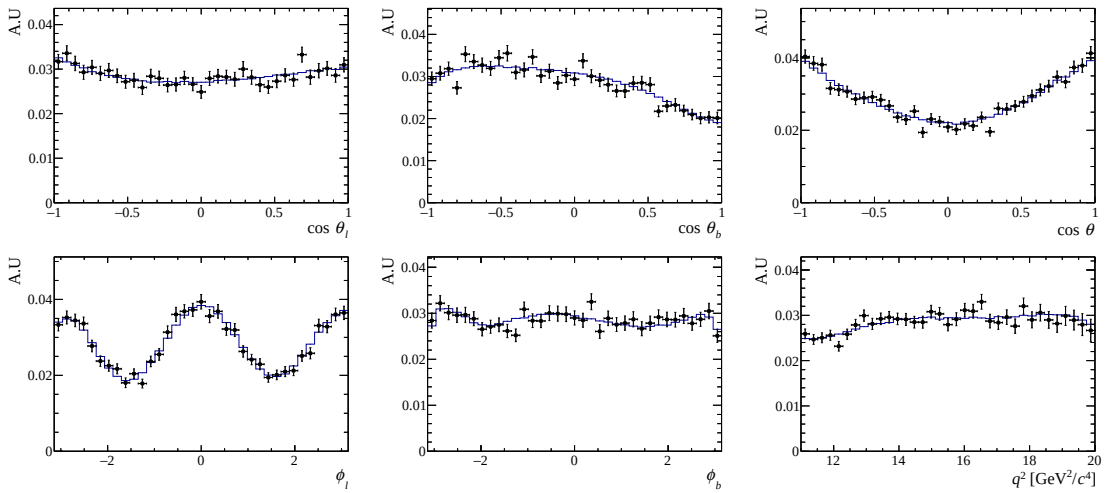

Figure A.8: 1D efficiency projections of 2011 + 2012 MC for the LL category. The black data points represent the weighted MC sample, while the blue line the efficiency model.

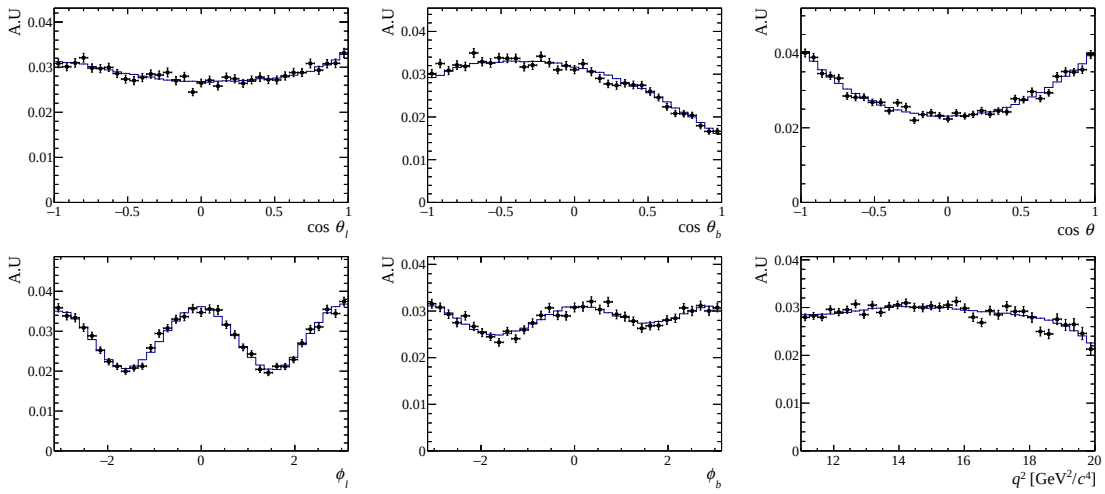

Figure A.9: 1D efficiency projections of 2015 MC for the DD category. The black data points represent the weighted MC sample, while the blue line the efficiency model.

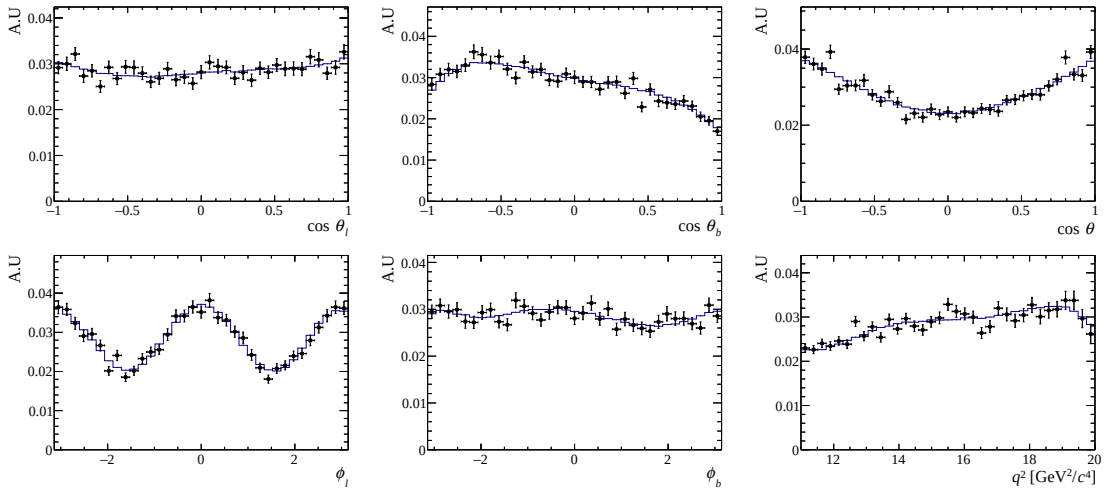

Figure A.10: 1D efficiency projections of 2015 MC for the LL category. The black data points represent the weighted MC sample, while the blue line the efficiency model.

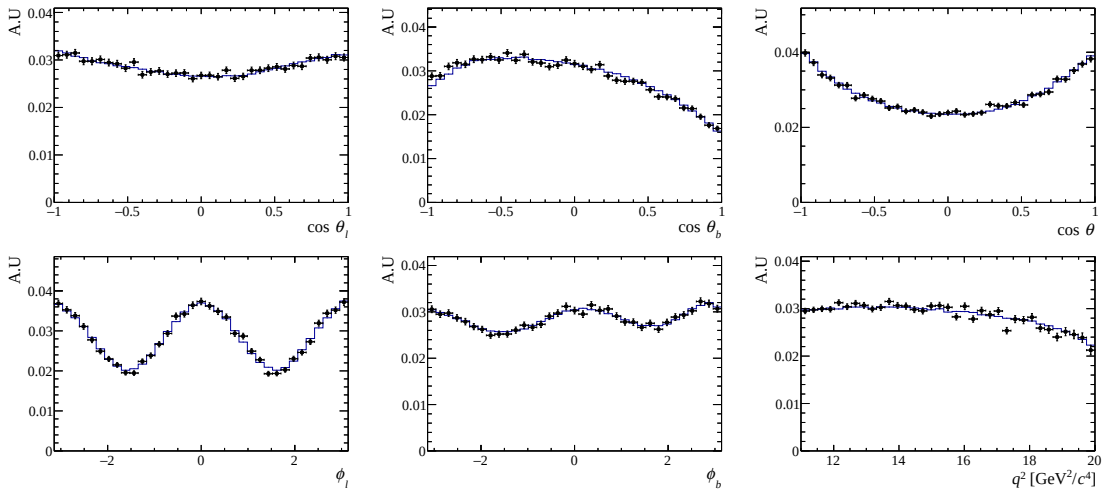

Figure A.11: 1D efficiency projections of 2016 MC for the DD category. The black data points represent the weighted MC sample, while the blue line the efficiency mode.

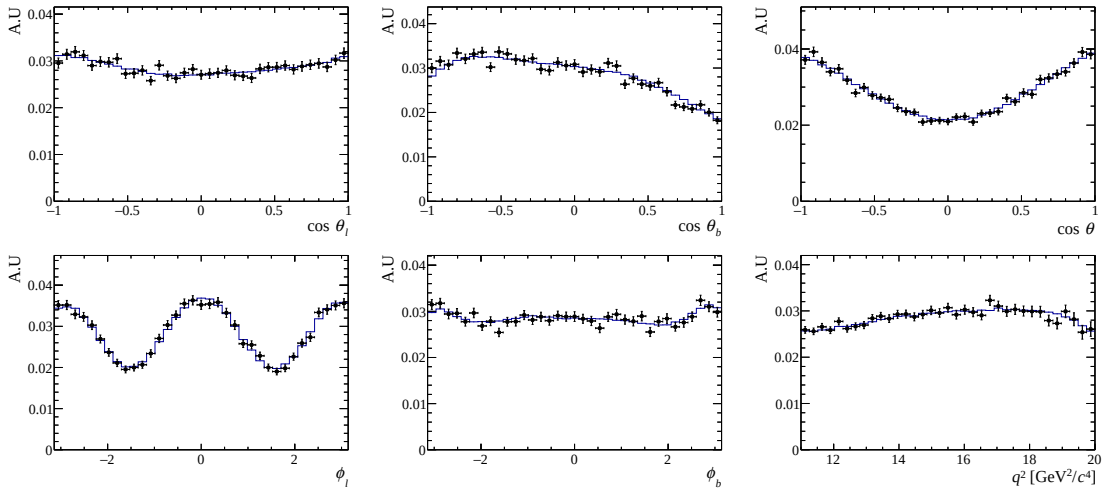

Figure A.12: 1D efficiency projections of 2016 MC for the LL category. The black data points represent the weighted MC sample, while the blue line the efficiency mode.

A.4 Correlation matrices

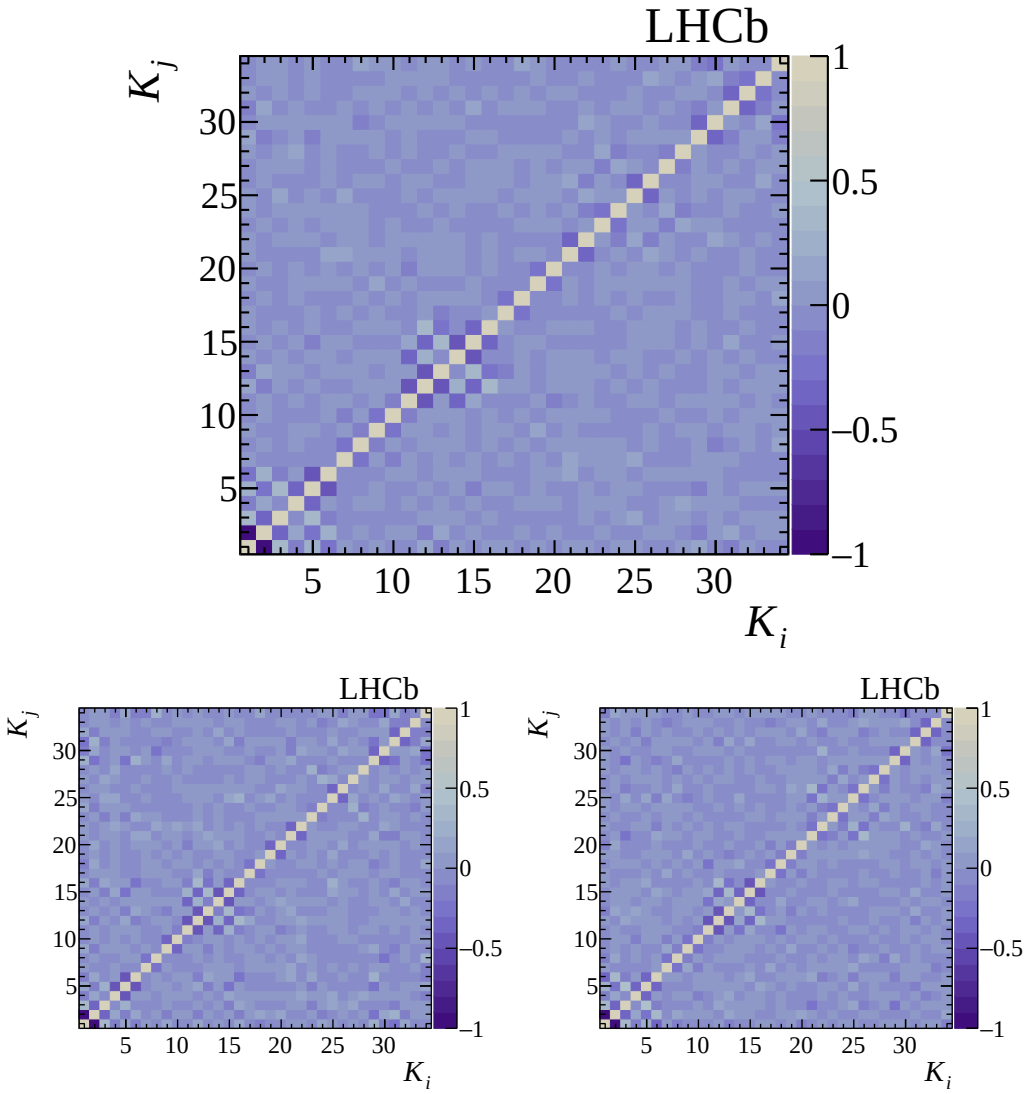

Figure A.13: Correlation matrices for the Run1+Run2 (top), Run1 (bottom left) and Run2 (bottom right) samples [1].

A.5 Comparison of moments for DD and LL categories

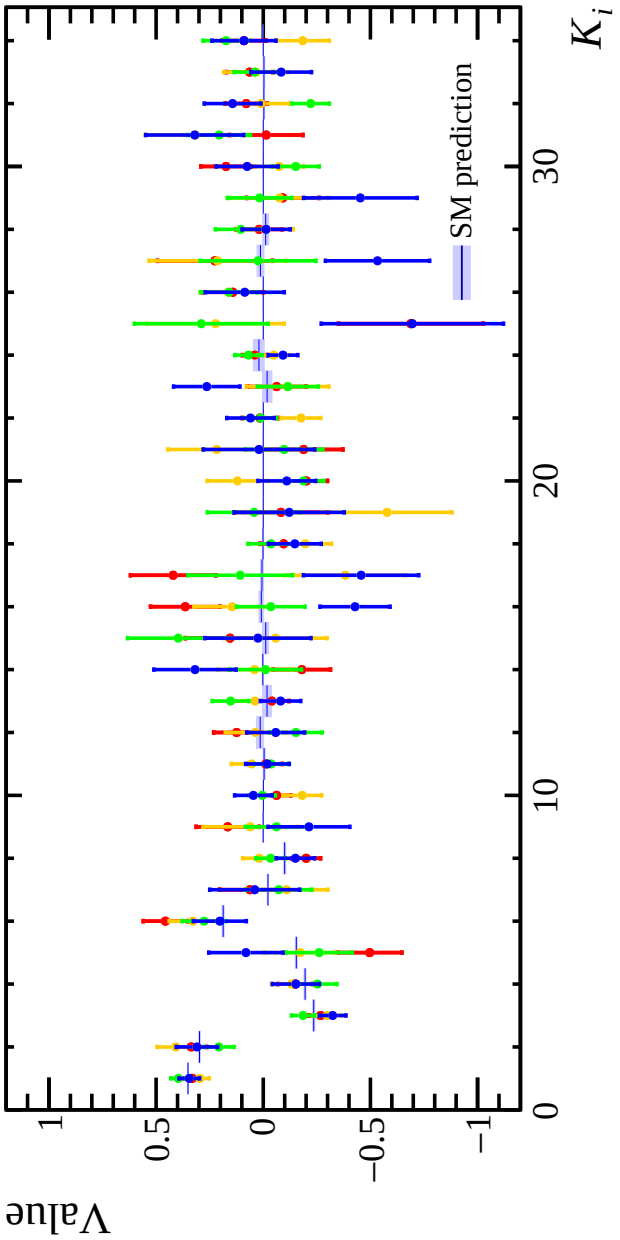

Figure A.14: The angular observables of DD, 2011+2012 (orange marker), LL, 2011+2012 (red marker), DD, 2015+2016 (blue marker) and LL, 2015+2016 (green marker) are compared. The SM predictions are also illustrated by a blue line, where the light-blue colour band represent the uncertainty on the SM predictions.

APPENDIX B

Angular analysis of $\Lambda_b^0 \to J/\psi\,\Lambda$

B.1 Complete numerical results

Table B.1: Measured values of the moments extracted from the combined samples of 2011 (top), 2012 (middle), 2015+2016 (bottom) samples, using both track categories. The first and second uncertainties represent the statistical and systematic errors respectively. Moments that are zero by construction and negligible in the massless ($\beta_l = 1$) limit are highlighted with a red colour.

Obs.	Value	Obs.	Value
K_1	$0.3733 \pm 0.0068 \pm 0.0035$	K_{18}	-0.0184 ± 0.0189
K_2	$0.2534 \pm 0.0137 \pm 0.0069$	K_{19}	$-0.0008 \pm 0.0378 \pm 0.0065$
K_3	-0.0024 ± 0.0104	K_{20}	-0.0008 ± 0.0184
K_4	$-0.2788 \pm 0.0171 \pm 0.0069$	K_{21}	$-0.0208 \pm 0.0355 \pm 0.0076$
K_5	$-0.1590 \pm 0.0254 \pm 0.0081$	K_{22}	-0.0104 ± 0.0158
K_6	-0.0053 ± 0.0184	K_{23}	$0.0033 \pm 0.0276 \pm 0.0135$
K_7	$0.0446 \pm 0.0285 \pm 0.0077$	K_{24}	$0.0074 \pm 0.0125 \pm 0.0016$
K_8	-0.0070 ± 0.0132	K_{25}	$-0.0159 \pm 0.0642 \pm 0.0113$
K_9	$-0.0202 \pm 0.0280 \pm 0.0047$	K_{26}	0.0245 ± 0.0285
K_{10}	-0.0078 ± 0.0127	K_{27}	$0.0499 \pm 0.0502 \pm 0.0118$
K_{11}	$0.0119 \pm 0.0140 \pm 0.0082$	K_{28}	0.0002 ± 0.0228
K_{12}	$-0.0154 \pm 0.0185 \pm 0.0103$	K_{29}	0.0064 ± 0.0363
K_{13}	0.0060 ± 0.0135	K_{30}	$0.0022 \pm 0.0214 \pm 0.0037$
K_{14}	$0.0069 \pm 0.0257 \pm 0.0124$	K_{31}	0.0401 ± 0.0312
K_{15}	$0.0000 \pm 0.0336 \pm 0.0125$	K_{32}	$0.0010 \pm 0.0208 \pm 0.0090$
K_{16}	-0.0125 ± 0.0246	K_{33}	$0.0172 \pm 0.0205 \pm 0.0040$
K_{17}	$-0.0046 \pm 0.0384 \pm 0.0112$	K_{34}	$0.0167 \pm 0.0209 \pm 0.0031$

Obs.	Value	Obs.	Value
K_1	$0.3693 \pm 0.0043 \pm 0.0016$	K_{18}	0.0016 ± 0.0121
K_2	$0.2615 \pm 0.0086 \pm 0.0031$	K_{19}	$-0.0168 \pm 0.0246 \pm 0.0035$
K_3	0.0030 ± 0.0065	K_{20}	0.0110 ± 0.0122
K_4	$-0.2607 \pm 0.0108 \pm 0.0046$	K_{21}	$0.0112 \pm 0.0215 \pm 0.0041$
K_5	$-0.1983 \pm 0.0164 \pm 0.0048$	K_{22}	0.0024 ± 0.0098
K_6	-0.0101 ± 0.0115	K_{23}	$-0.0251 \pm 0.0166 \pm 0.0058$
K_7	$0.0148 \pm 0.0176 \pm 0.0032$	K_{24}	-0.0065 ± 0.0076
K_8	-0.0254 ± 0.0082	K_{25}	$-0.0052 \pm 0.0378 \pm 0.0072$
K_9	$-0.0149 \pm 0.0175 \pm 0.0021$	K_{26}	-0.0035 ± 0.0173
K_{10}	-0.0106 ± 0.0080	K_{27}	$0.0171 \pm 0.0300 \pm 0.0055$
K_{11}	$0.0055 \pm 0.0090 \pm 0.0040$	K_{28}	0.0053 ± 0.0137
K_{12}	$0.0068 \pm 0.0118 \pm 0.0046$	K_{29}	0.0175 ± 0.0210
K_{13}	0.0004 ± 0.0086	K_{30}	$-0.0249 \pm 0.0134 \pm 0.0030$
K_{14}	$-0.0169 \pm 0.0161 \pm 0.0054$	K_{31}	0.0111 ± 0.0211
K_{15}	$0.0082 \pm 0.0213 \pm 0.0055$	K_{32}	$0.0174 \pm 0.0131 \pm 0.0040$
K_{16}	-0.0073 ± 0.0154	K_{33}	$-0.0211 \pm 0.0131 \pm 0.0017$
K_{17}	$0.0030 \pm 0.0246 \pm 0.0044$	K_{34}	$0.0308 \pm 0.0130 \pm 0.0014$

Obs.	Value	Obs.	Value
K_1	$0.3769 \pm 0.0030 \pm 0.0008$	K_{18}	-0.0093 ± 0.0087
K_2	$0.2462 \pm 0.0059 \pm 0.0017$	K_{19}	$-0.0077 \pm 0.0178 \pm 0.0020$
K_3	-0.0033 ± 0.0046	K_{20}	-0.0046 ± 0.0086
K_4	$-0.2694 \pm 0.0081 \pm 0.0039$	K_{21}	$-0.0297 \pm 0.0160 \pm 0.0050$
K_5	$-0.1957 \pm 0.0111 \pm 0.0031$	K_{22}	0.0023 ± 0.0073
K_6	-0.0132 ± 0.0082	K_{23}	$0.0192 \pm 0.0124 \pm 0.0029$
K_7	$0.0090 \pm 0.0129 \pm 0.0018$	K_{24}	-0.0072 ± 0.0057
K_8	-0.0035 ± 0.0060	K_{25}	$0.0433 \pm 0.0283 \pm 0.0049$
K_9	$-0.0260 \pm 0.0128 \pm 0.0012$	K_{26}	-0.0055 ± 0.0134
K_{10}	0.0037 ± 0.0059	K_{27}	$0.0361 \pm 0.0225 \pm 0.0031$
K_{11}	$-0.0042 \pm 0.0065 \pm 0.0018$	K_{28}	0.0107 ± 0.0104
K_{12}	$0.0058 \pm 0.0085 \pm 0.0022$	K_{29}	0.0139 ± 0.0141
K_{13}	-0.0007 ± 0.0063	K_{30}	$0.0074 \pm 0.0098 \pm 0.0010$
K_{14}	$-0.0067 \pm 0.0119 \pm 0.0024$	K_{31}	0.0226 ± 0.0138
K_{15}	$-0.0102 \pm 0.0158 \pm 0.0026$	K_{32}	$-0.0173 \pm 0.0092 \pm 0.0016$
K_{16}	-0.0095 ± 0.0116	K_{33}	$-0.0099 \pm 0.0094 \pm 0.0013$
K_{17}	$0.0138 \pm 0.0179 \pm 0.0022$	K_{34}	$0.0084 \pm 0.0093 \pm 0.0012$

B.2 Correlation matrices

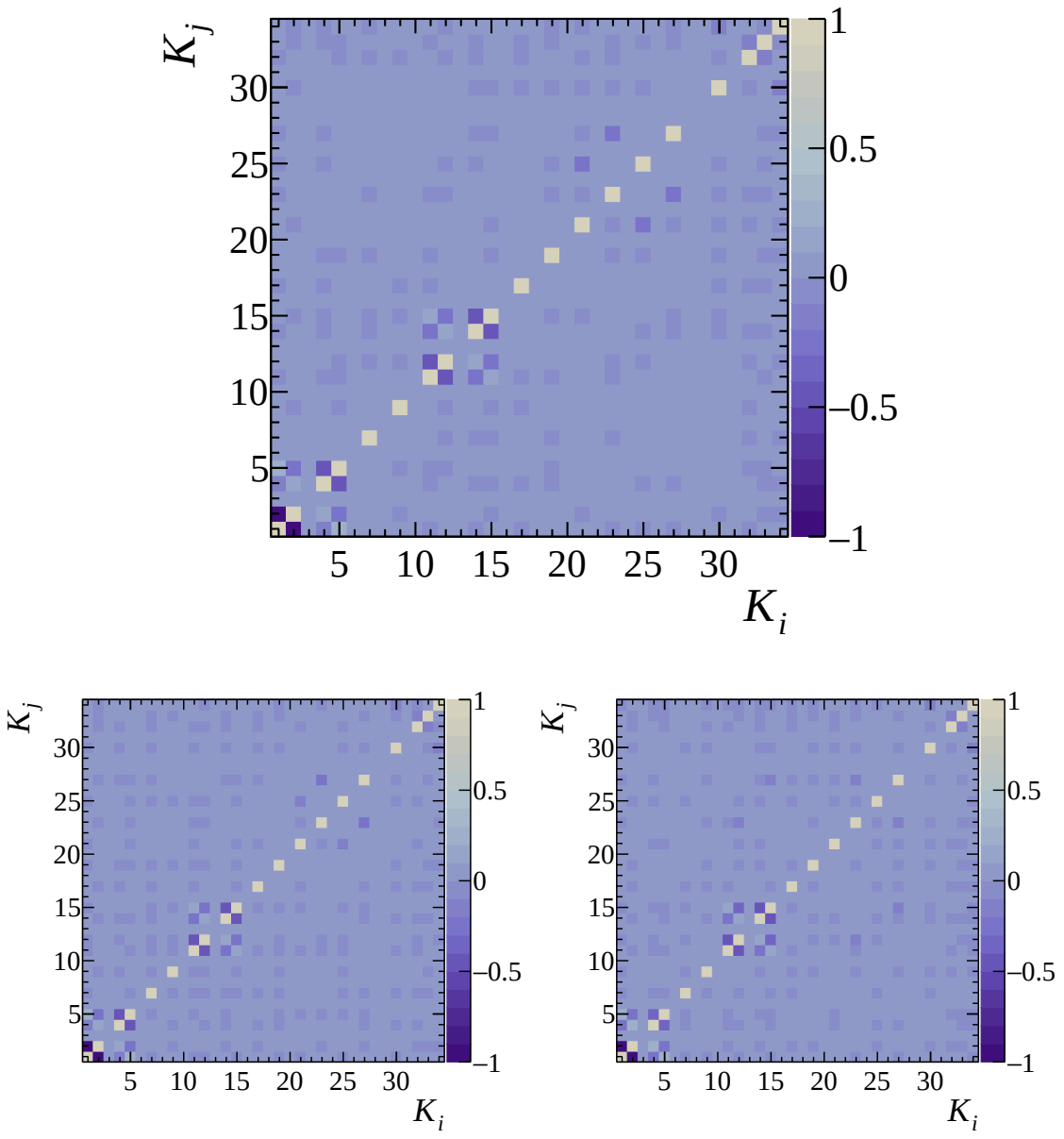

Figure B.1: Correlation matrices for moments extracted from 2015 + 2016 (top), 2011 (bottom right) and 2012 (bottom left) data sets, where both track categories are combined. In general, correlations are small but it can be as large as 40% in some cases. The correlation coefficients for the moments that are zero for $\Lambda_b^0 \to J/\psi\,\Lambda$ in the massless limit are set to zero.

B.3 Comparison of moments for DD and LL categories

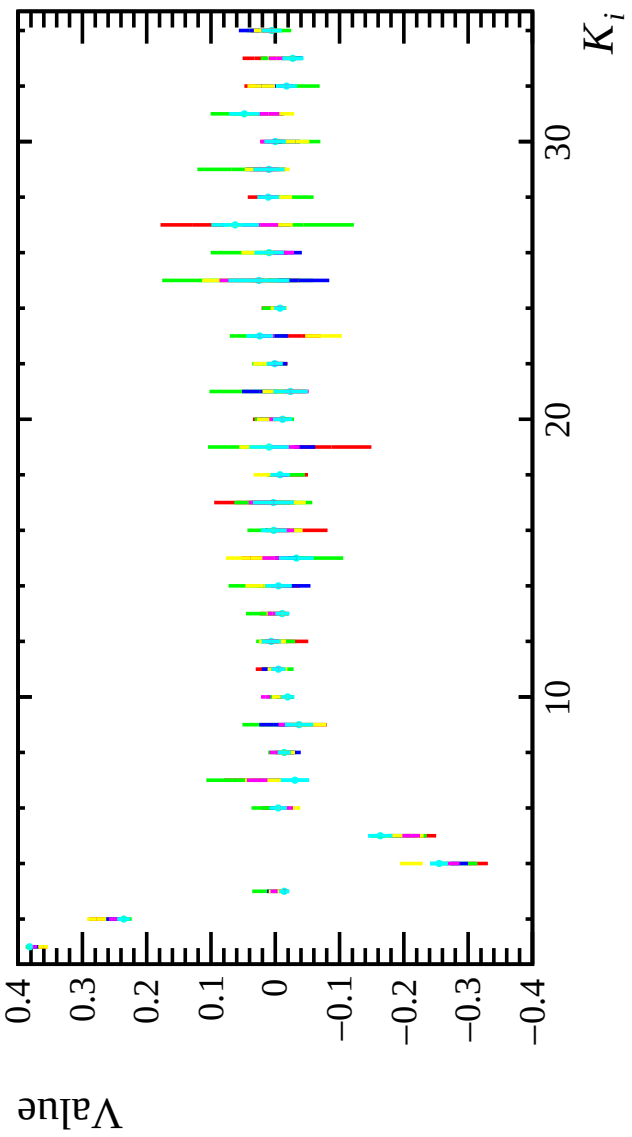

Figure B.2: Comparison between moments obtained from the 2011, DD (red), 2011, LL (green), 2012, DD (blue), 2012, LL (yellow), 2015 + 2016, DD (magenta) and 2015 + 2016, LL (cyan) data sets.